

---

Electrical tests of silicon detector modules  
for the ATLAS experiment and a study of  
the discovery potential of the  
 $t\bar{t}H, H \rightarrow W^+W^-$  process

---

Inga Ludwig



---

FAKULTÄT FÜR MATHEMATIK UND PHYSIK  
ALBERT-LUDWIGS-UNIVERSITÄT FREIBURG

---



Electrical tests of silicon detector modules for the  
ATLAS experiment and a study of the discovery  
potential of the  $t\bar{t}H$ ,  $H \rightarrow W^+W^-$  process

**DISSERTATION**  
zur Erlangung des Doktorgrades  
der Fakultät für Mathematik und Physik  
der Albert-Ludwigs-Universität  
Freiburg im Breisgau

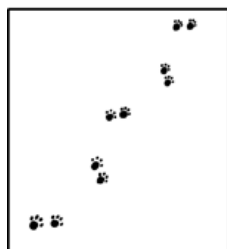
vorgelegt von  
Inga Ludwig  
aus Aschaffenburg

Oktober 2011

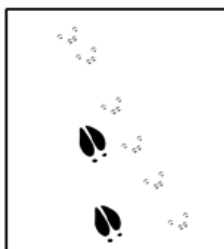
Dekan:	Prof. Dr. Kay Königsmann
Leiter der Arbeit:	Prof. Dr. Karl Jakobs
Referent:	Prof. Dr. Karl Jakobs
Korreferent:	Prof. Dr. Markus Schumacher

Datum der mündlichen Prüfung: 15. November 2011

BACKYARD SNOW TRACKING GUIDE



CAT



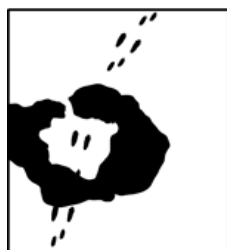
MOOSE AND SQUIRREL



LONGCAT



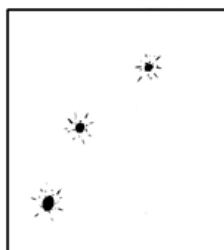
MOUSE RIDING BICYCLE



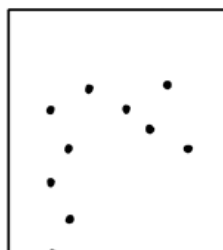
RABBIT STOPPING  
TO USE HAIR DRYER



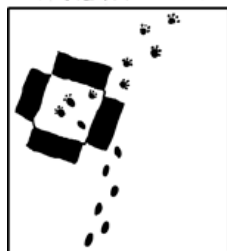
LEGOLAS



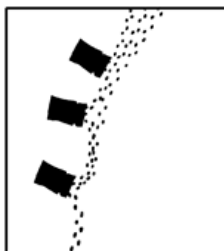
BOBCAT ON POGO STICK



KNIGHT



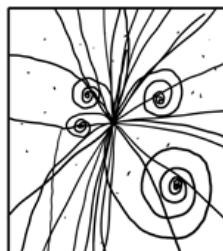
KID WITH  
TRANSMOGRIFIER



KID WITH DUPLICATOR



PRIUS



HIGGS BOSON



# Contents

<b>Introduction</b>	<b>1</b>
<b>1 The Standard Model and the Higgs boson</b>	<b>3</b>
1.1 The Standard Model of elementary particle physics . . . . .	3
1.1.1 Particle content of the Standard Model . . . . .	3
1.1.2 Quantum chromodynamics . . . . .	4
1.1.3 Electroweak theory . . . . .	5
1.2 The Higgs mechanism . . . . .	7
1.2.1 Spontaneous symmetry breaking . . . . .	7
1.2.2 Fermion masses . . . . .	8
1.2.3 The Higgs boson . . . . .	9
1.3 Bounds on the Higgs boson mass . . . . .	9
1.4 Higgs boson searches at the LHC . . . . .	11
1.4.1 Production modes and decay channels . . . . .	11
1.4.2 Associated Higgs boson production with top quark pairs . . . . .	13
1.4.3 Discovery potential of the ATLAS experiment . . . . .	15
1.4.4 Recent exclusion limits . . . . .	15
1.5 Coupling measurements at the LHC . . . . .	16
<b>2 Phenomenology of hadron collider experiments</b>	<b>19</b>
2.1 Luminosity . . . . .	19
2.2 Cross sections . . . . .	19
2.2.1 Partonic cross sections . . . . .	20
2.2.2 Hadronic cross sections . . . . .	21
2.2.3 Uncertainties in cross section calculations . . . . .	22
2.3 Monte Carlo event generation . . . . .	24
2.3.1 Hard scattering . . . . .	24
2.3.2 Parton shower . . . . .	25
2.3.3 Parton shower in higher order Monte Carlo generators . . . . .	25
2.3.4 Particle Decays . . . . .	26
2.3.5 Hadronization . . . . .	26
2.3.6 Underlying event an multiple interactions . . . . .	27
2.3.7 Pile-up . . . . .	27
<b>3 The ATLAS experiment at the LHC</b>	<b>29</b>
3.1 Large Hadron Collider . . . . .	29
3.2 The ATLAS experiment . . . . .	31
3.2.1 Inner Detector . . . . .	33
3.2.2 Calorimetry . . . . .	37
3.2.3 Muon spectrometer . . . . .	40
3.2.4 Forward detectors . . . . .	41
3.2.5 Trigger system and data flow . . . . .	41

3.3	Event reconstruction and ATLAS detector simulation . . . . .	43
3.3.1	Track reconstruction and vertexing . . . . .	43
3.3.2	Muon reconstruction . . . . .	45
3.3.3	Electrons and photons . . . . .	46
3.3.4	Jet finding and calibration . . . . .	47
3.3.5	$b$ -tagging . . . . .	48
3.3.6	Detector simulation . . . . .	49
<b>4</b>	<b>Electrical tests of ATLAS SCT endcap modules</b>	<b>51</b>
4.1	The SCT endcap modules . . . . .	51
4.1.1	Module layout . . . . .	52
4.1.2	Sensors . . . . .	54
4.1.3	Hybrids . . . . .	58
4.2	Testing system . . . . .	61
4.3	ATLAS SCT endcap module testing . . . . .	63
4.3.1	$I - V$ curves . . . . .	64
4.3.2	Digital functionality tests . . . . .	65
4.3.3	Analogue functionality tests . . . . .	68
4.4	Results . . . . .	75
4.4.1	Performance after assembly on the disk . . . . .	75
4.4.2	Summary of the results from tests during construction . . . . .	76
4.5	Summary . . . . .	77
<b>5</b>	<b>Projective likelihood estimator for electron isolation</b>	<b>79</b>
5.1	Monte Carlo samples . . . . .	79
5.2	Discriminating variables . . . . .	84
5.3	The projective likelihood estimator . . . . .	88
5.4	Variable selection and separation power of the likelihood output . . . . .	91
5.5	Summary and outlook . . . . .	99
<b>6</b>	<b>Prospects for the search for <math>t\bar{t}H, H \rightarrow W^+W^-</math></b>	<b>101</b>
6.1	Introduction . . . . .	101
6.2	Generation of Monte Carlo samples for $t\bar{t}H, H \rightarrow W^+W^-$ . . . . .	104
6.3	Monte Carlo samples for background studies . . . . .	106
6.3.1	Backgrounds for $t\bar{t}H, H \rightarrow W^+W^-$ production . . . . .	107
6.3.2	Top quark pair production . . . . .	109
6.3.3	Associated production of weak bosons with a top quark pair . . . . .	110
6.3.4	$t\bar{t}\bar{t}$ production . . . . .	111
6.3.5	$W$ boson production in association with jets . . . . .	112
6.4	Event selection . . . . .	114
6.4.1	Jet and lepton selection . . . . .	114
6.4.2	Kinematic event selection . . . . .	119
6.4.3	Triggers and trigger efficiencies . . . . .	121
6.5	Estimation of the additional contributions to the $t\bar{t}$ background . . . . .	124
6.5.1	$t\bar{t}$ background generated by “fake” leptons . . . . .	124
6.5.2	Lepton charge mismeasurement . . . . .	129
6.5.3	Discussion of the total $t\bar{t}$ background . . . . .	130

6.6	Estimation of the $W$ +jet background . . . . .	132
6.6.1	Validation of the description of the event properties in the release 12 and 14 datasets . . . . .	132
6.6.2	Factorization of the event selection . . . . .	133
6.6.3	Limit on the accepted $W$ +jet cross section . . . . .	135
6.7	Summary of the accepted signal and background cross sections . . . . .	137
6.8	Impact of pile-up on the signal and background selection . . . . .	141
6.9	Estimation of systematic uncertainties . . . . .	146
6.9.1	Detector performance uncertainties . . . . .	146
6.9.2	Luminosity . . . . .	149
6.9.3	Theory uncertainties . . . . .	149
6.9.4	Summary of systematic uncertainties . . . . .	150
6.9.5	Impact of systematic uncertainties on the signal significance . . . . .	151
6.10	Summary and Outlook . . . . .	153
6.10.1	Summary . . . . .	153
6.10.2	Further suppression of the $t\bar{t}W$ and $t\bar{t}Z$ backgrounds . . . . .	154
6.10.3	The three lepton final state . . . . .	155
6.10.4	High-luminosity run at the LHC . . . . .	155
6.11	Comparison with previous studies . . . . .	157
6.12	Measuring the top Yukawa coupling . . . . .	159
6.12.1	Accuracy of a $\sigma_{t\bar{t}H} \times \text{BR}(H \rightarrow W^+W^-)$ measurement . . . . .	159
6.12.2	Coupling measurements . . . . .	160
	<b>Summary</b> . . . . .	<b>163</b>
	<b>A Addendum on the electron isolation</b> . . . . .	<b>167</b>
A.1	Additional discriminating variables . . . . .	167
A.2	Pile-up conditions . . . . .	169
A.3	Correlations . . . . .	173
A.4	Overview of the discriminating variables . . . . .	174
A.5	Choice of the “default” and “highJetMulti” variable sets . . . . .	175
A.6	Signal and background separation without ID efficiencies . . . . .	177
A.7	Choice of the training samples . . . . .	182
	<b>B Addendum on the <math>t\bar{t}H, H \rightarrow W^+W^-</math> study</b> . . . . .	<b>185</b>
B.1	Impact of the use of the <code>WZtoLeptonFilter</code> . . . . .	185
B.2	Calculation of results obtained with MC@NLO datasets . . . . .	187
B.2.1	Cross sections . . . . .	187
B.2.2	Efficiencies . . . . .	187
B.2.3	Limits . . . . .	188
B.3	Event selection and cross sections in the published study . . . . .	190
B.4	Details on the estimation of the $W$ +jet background contribution . . . . .	193
B.4.1	Comparison of the lepton and jet $p_T$ spectra in 10 TeV and 14 TeV . . . . .	193
B.4.2	Event selection for the release 14 analysis . . . . .	196
B.4.3	Correction of the centre-of-mass energy . . . . .	199
B.4.4	Combined limit on the $W$ +jet background . . . . .	200
B.5	Calculation of significance expectations . . . . .	202
B.5.1	$p$ -value and significance . . . . .	202
B.5.2	Treatment of background uncertainties: profile likelihood ratio . . . . .	203

---

B.5.3	Wilks' approximation . . . . .	204
B.5.4	Expected significances . . . . .	205
B.6	Signal expectations and significances for different Higgs boson masses . . . . .	206
B.7	Details on the estimation of detector systematics uncertainties . . . . .	207
B.8	Outlook on a reconstruction of the signal . . . . .	209
B.8.1	Analytic reconstruction of the final state . . . . .	209
B.8.2	Combinatorial background . . . . .	210
B.8.3	Suppression of irreducible backgrounds . . . . .	212
B.8.4	Multivariate methods . . . . .	213
B.8.5	Summary . . . . .	214
<b>List of Figures</b>		<b>220</b>
<b>List of Tables</b>		<b>221</b>
<b>Bibliography</b>		<b>228</b>

# Introduction

The Large Hadron Collider (LHC) at the European particle physics laboratory CERN is the world's largest and highest energy particle collider, successfully colliding proton beams since late in 2009. The collisions are recorded by the four LHC experiments ATLAS, CMS, LHCb and ALICE. Almost  $4\text{fb}^{-1}$  of data have been collected by each of the two multi-purpose experiments ATLAS and CMS at a centre-of-mass energy of 7 TeV so far. The analysis of these data has resulted in a variety of first results, which have been published during the last months. But this is just the beginning: during its lifetime, the LHC aims at collecting up to several hundred  $\text{fb}^{-1}$  of data at centre-of-mass energies up to 14 TeV. The results from the analysis of these data are expected to give new insights into the fundamental laws of nature and to reveal the limits of today's knowledge of particle physics, which is condensed in the Standard Model.

The Standard Model has been very successful in describing elementary particles, their properties and interactions and almost all predicted particles have been discovered over the last decades. Nevertheless, a few puzzling aspects of particle physics still remain unexplained. Among these, the question for the origin of the mass of the elementary particles is one of the most important. A possible solution is the Higgs mechanism, which, in its simplest implementation, requires the existence of one more elementary particle. The quest for this "Higgs boson" is one of the main goals of the LHC. Moreover, theorists have proposed many different theoretical models to describe potential physics beyond the Standard Model, among them supersymmetry, technicolour or extra dimensions, just to name a few. Theoretical considerations of more general nature imply that any successful theory must contain new particles below the 1 TeV mass scale. This is within the energy range accessible at the LHC and hence, most probably, new physics must be discovered by the LHC experiments. If nothing is found, this will perhaps be the most stunning result the LHC could produce. Thus, it is expected that the LHC will push particle physics a big step forward within the next few years.

This thesis is dedicated to the preparation of the ATLAS experiment for data taking. It comprises three different subjects, including contributions to the construction of the ATLAS detector, the development of electron identification strategies and the evaluation of the discovery significance for the search for a Standard Model Higgs boson in the  $t\bar{t}H$ ,  $H \rightarrow W^+W^-$  channel. The latter two tasks were related to a major publication effort by the ATLAS collaboration finished in 2009. For this purpose, dedicated releases of the ATLAS reconstruction software were issued and corresponding Monte Carlo datasets were produced by the collaboration, together with recommendations on e.g. cross sections to be used for the published studies. These were kept, wherever possible, for the study in this thesis, which implies the assumption of data taking at a centre-of-mass energy of 14 TeV at a low instantaneous luminosity in the first three years, as originally planned before the magnet failure accident in 2008.

Most of the searches for new particles rely on efficient identification of electrons, muons or  $\tau$  leptons and a precise knowledge of their kinematics, as well as on an accurate reconstruction and classification of jets. Excellent track reconstruction performance, guaranteeing high

reconstruction efficiency and precision at the same time, is a key ingredient to achieve all of these. In the ATLAS experiment, high quality track reconstruction is ensured by an Inner Detector, consisting of layers of silicon pixel and strip detectors and a straw tube transition radiation detector. All Inner Detector components need to be fast, radiation hard and very stable in operation. The Semiconductor Tracking detector (SCT) is built from more than 4000 detector modules, of which about 200 were assembled, tested and characterized at the University of Freiburg. The responsibility for the validation of the electrical functionality of the completed modules within the specifications required for operation in the ATLAS detector was the first part of this thesis.

A large part of the work performed in the course of this thesis was dedicated to a Monte Carlo study with the aim to evaluate the discovery significance for the search for the Higgs boson in the  $t\bar{t}H$ ,  $H \rightarrow W^+W^-$  channel. The cross section for this process is much smaller than that of the designated discovery channels  $gg \rightarrow H$  and weak boson fusion, which are approximately two and one order of magnitude larger, respectively. Nevertheless, once a Higgs boson has been found, it will be important to determine its properties and the  $t\bar{t}H$ ,  $H \rightarrow W^+W^-$  channel is considered a candidate to give access to the top Yukawa coupling constant. With four  $W$  bosons, two from the decay of the Higgs boson and two from the top quark decays, and additional jets involved, the channel requires the study of very complex final states. The most promising among them is the final state consisting of a pair of leptons of equal charge and six jets. The feasibility of an observation of a significant amount of  $t\bar{t}H$ ,  $H \rightarrow W^+W^-$  signal events in this final state with an integrated luminosity of  $30 \text{ fb}^{-1}$  of data was studied with a full simulation of the ATLAS detector.

Effective suppression of the major backgrounds is crucial for the measurement of this channel. Especially backgrounds with leptons from semi-leptonic heavy quark decays need to be taken care of. Part of this thesis was therefore also dedicated to lepton isolation studies. These resulted in a likelihood estimator algorithm for the separation of isolated electrons from non-isolated real electron background originating from heavy quark decays. The algorithm was contributed to the electron reconstruction software package of the ATLAS analysis framework Athena.

The outline of this thesis is the following: Chapters 1 and 2 give an overview on the Standard Model, the physics of the Higgs boson and the theoretical description of particle collisions at hadron colliders. The layouts of the LHC and the ATLAS experiment are described in Chapter 3, whereas the design of the SCT modules, the electrical tests and a summary of the characteristics of the modules are dealt with in Chapter 4. Chapter 5 covers the studies on electron isolation. The prospects to observe a Standard Model Higgs boson in the  $t\bar{t}H$ ,  $H \rightarrow W^+W^-$  channel are discussed in Chapter 6. Finally, a brief summary of the most important achievements of all three parts of this thesis is given.

# 1 The Standard Model and the Higgs boson

Today’s knowledge on particle physics is summarized in the so-called “Standard Model”, a gauge theory based on the  $SU(3)_C \times SU(2)_L \times U(1)_Y$  symmetry [1, 2, 3]. It describes all elementary particles known to date and three of the four known fundamental forces: the electromagnetic (EM) and weak forces, which are unified in the electroweak (EW) interaction, and the strong force of quantum chromodynamics (QCD)<sup>1</sup>. The dynamics of the particles and the three mentioned forces is represented by a renormalizable Lagrangian

$$\mathcal{L}_{\text{SM}} = \mathcal{L}_{\text{QCD}} + \mathcal{L}_{\text{EW}} \quad , \quad (1.1)$$

which is a function of the matter and force fields. The requirement of local gauge invariance of this Lagrangian fully determines the interactions of these particles. The Standard Model is, however, not complete, since the QCD and electroweak theories themselves fail to describe all experimentally observed massive particles in a way preserving the local gauge invariance. A possible solution to this problem is the Higgs mechanism, which extends the Standard Model Lagrangian to

$$\mathcal{L}_{\text{SM}} = \mathcal{L}_{\text{QCD}} + \mathcal{L}_{\text{EW}} + \mathcal{L}_{\text{Higgs}} + \mathcal{L}_{\text{Yukawa}} \quad (1.2)$$

and generates particle masses through the mechanism of “spontaneous symmetry breaking” of the underlying symmetry down to a  $SU(3)_C \times U(1)_Q$  symmetry.

## 1.1 The Standard Model of elementary particle physics

The following sections briefly summarize the most important aspects of the Standard Model particle content and the QCD and electroweak theories. More comprehensive introductions into quantum field theories and the fundamentals of particle physics can be found in numerous textbooks [4, 5] or lecture notes [6].

### 1.1.1 Particle content of the Standard Model

The Standard Model describes the dynamics of a set of elementary particles, which to the current knowledge are point-like and cannot be divided into smaller constituents. These particles are either fermions with spin  $\frac{1}{2}$ , which are the matter particles, or bosons with spin 1, which are the carriers of the fundamental forces. Each particle is characterized by a unique set of quantum numbers. Furthermore, many of them carry a mass, and it is so far unknown, how these masses are generated.

The fermions are grouped into three families of particles of increasing mass. Except for the “flavour” quantum number, which characterizes the family membership, each family consists of a set of particles with identical quantum numbers. All known stable matter is made up of

---

<sup>1</sup>The fourth force, gravity, is described by the theory of general relativity and could not yet successfully be incorporated in a quantum field theory. Nevertheless, gravity is very weak compared with the other forces and hence does not influence the short-scale dynamics of particle physics.

fermions of the first generation. The massive particles of the other generations are unstable and decay into lighter particles. Table 1.1 gives an overview on the Standard Model fermions and their masses<sup>2</sup>. The fermions are furthermore divided into leptons, which participate only in electroweak interactions and quarks, which in addition also take part in strong interactions. The Standard Model treats half of the leptons, the neutrinos, as massless particles. Experiments since the turn of the millennium have shown that neutrinos indeed do have a mass [7, 8]. Nevertheless, these masses are tiny and the Standard Model predictions referring to the vanishing neutrino masses still describe the experimental reality to a very high precision. Furthermore, it is so far unclear, how a theoretical description of neutrino masses in the Standard Model could look like. In the following, neutrinos are assumed to be massless. Finally, an anti-particle exists for each fermion, with identical mass and the same multiplicative quantum numbers but opposite additive quantum numbers.

Name	Symbol	Generation	Mass
<b>Leptons</b>			
Electron neutrino	$\nu_e$	1	$< 2 \text{ eV}$
Electron	$e$	1	0.511 MeV
Muon neutrino	$\nu_\mu$	2	$< 0.19 \text{ MeV}$
Muon	$\mu$	2	105.7 MeV
Tau neutrino	$\nu_\tau$	3	$< 18.2 \text{ MeV}$
Tau	$\tau$	3	1.777 GeV
<b>Quarks</b>			
Up	$u$	1	1.7 to 3.1 MeV
Down	$d$	1	4.1 to 5.7 MeV
Strange	$s$	2	80 to 130 MeV
Charm	$c$	2	1.18 to 1.34 GeV
Bottom	$b$	3	4.1 to 4.4 GeV
Top	$t$	3	172.9 GeV

**Table 1.1:** Overview on the Standard Model fermions and their masses according to Ref. [9]. Quarks cannot be observed as free particles. Hence, the given masses are model dependent and have a large uncertainty (details are given in Ref. [9]).

The fermions' interactions are mediated by gauge bosons, which carry spin 1 (see Table 1.2). Eight massless gluons are responsible for the strong force. The gauge boson for the electromagnetic force is the massless photon. The weak interactions are mediated by three gauge bosons, called the  $W^+$ ,  $W^-$  and  $Z$  boson. Experiments showed that the  $W$  and  $Z$  bosons are massive and decay into fermion pairs [10, 11].

All above discussed fermions and gauge bosons have been discovered in astroparticle and high energy physics experiments over the last decades. Should the Higgs mechanism turn out to be valid, the particle content is completed by another, so far unobserved bosonic member – the Higgs particle  $H$ .

### 1.1.2 Quantum chromodynamics

The  $SU(3)_C$  part of the Standard Model describes the interaction of coloured particles (hence the index “ $C$ ”). Quarks are colour space triplets and come along in three colours with corresponding anti-colours for the anti-quarks, such that colour–anti-colour states are colour-neutral singlets. All other fermions are colourless  $SU(3)_C$  singlets and hence remain unaf-

<sup>2</sup>Throughout this thesis the convention  $c \equiv 1$  is used. Masses and momenta are therefore given in eV.

Name	Symbol	Interaction	$Q$ [ $e$ ]	Mass	Couples to
Photon	$\gamma$	EM	$< 5 \cdot 10^{-30}$	$< 10^{-18}$ eV	charged particles
$Z$ boson	$Z$	EW	0	$(91.1876 \pm 0.0021)$ GeV	all fermions, $W, Z, H$
$W$ boson	$W^\pm$	weak	$\pm 1$	$(80.399 \pm 0.023)$ GeV	all fermions, $W, Z, \gamma, H$
Gluon	$g$	strong	0	0 (theoretical)	quarks and gluons

**Table 1.2:** Overview on the Standard Model gauge bosons, their electrical charges (in units of the absolute value of the electron charge  $e$ ) and masses according to Ref. [9].

acted under the actions of the  $SU(3)_C$  group. The eight generators  $\lambda^a$  of the  $SU(3)_C$  group require eight different gauge fields  $G_\mu^a$  ( $a = 1 \dots 8$ ), the gluons. Each of them carries a specific superposition of colour–anti-colour combinations. The QCD Lagrangian is given by

$$\mathcal{L}_{\text{QCD}} = \sum_f \bar{q}_f (i\gamma^\mu D_\mu - m_f) q_f - \frac{1}{4} G_a^{\mu\nu} G_{\mu\nu}^a, \quad (1.3)$$

with  $q_f$  denoting the quark fields and  $m_f$  the corresponding quark masses. The gluon fields enter the Lagrangian via their corresponding field strength tensors

$$G_a^{\mu\nu} = \partial^\mu G_a^\nu - \partial^\nu G_a^\mu - g_s f^{abc} G_b^\mu G_c^\nu, \quad (1.4)$$

where  $g_s$  denotes the strong coupling constant. The covariant derivatives

$$D_\mu = \partial_\mu + ig_s \frac{\lambda_a}{2} G_\mu^a \quad (1.5)$$

are chosen such that they ensure local gauge invariance. This requirement also enforces massless gluons. The  $SU(3)_C$  structure constants  $f^{abc}$  determine the commutators of the generating Gell-Mann matrices  $\lambda^a$ . The theory is non-abelian and the non-zero commutators generate cubic and quartic self-coupling terms of the gluon fields. The self-interactions give rise to the phenomena of “asymptotic freedom”, i.e. the observation that at small length scales quarks and gluons can be regarded as free particles, and “confinement”, which implies that all observable particles are colour singlets and free quarks and gluons cannot be observed.

### 1.1.3 Electroweak theory

The  $SU(2)_L \times U(1)_Y$  part of the Standard Model unifies the electromagnetic and weak interactions. Electroweak interactions partly distinguish between fermions with left- and right-handed chirality. The left-handed fermions appear as doublets of the two leptons or quarks of the respective generation under actions of the  $SU(2)_L$  symmetry group of the weak isospin, which is indicated by the index “L”. The right-handed fermions are  $SU(2)_L$  singlets and hence remain unaffected by actions of the  $SU(2)_L$  group of the weak isospin. The index “Y” in the  $U(1)_Y$  part of the gauge group stands for the hypercharge that is introduced in correspondence to the electrical charge  $e$  in quantum electrodynamics. The corresponding quantum numbers that characterize the transformation behaviour of the fermions are the absolute value  $T$  and third component  $T_3$  of the weak isospin and the weak hypercharge  $Y$ . The hypercharge and  $T_3$  are related to the particle’s electrical charge  $Q$  via  $Q = T_3 + \frac{Y}{2}$ . A summary of all Standard Model fermions and their electroweak quantum numbers is given in Table 1.3. The quark weak eigenstates  $d', s', b'$  are not identical with the mass eigenstates  $d, s, b$  but are

			$Q [e]$	$Y$	$ \vec{T} $	$T_3$
$\begin{pmatrix} \nu_e \\ e^- \end{pmatrix}_L$	$\begin{pmatrix} \nu_\mu \\ \mu^- \end{pmatrix}_L$	$\begin{pmatrix} \nu_\tau \\ \tau^- \end{pmatrix}_L$	0	-1	$\frac{1}{2}$	$\frac{1}{2}$
$e^-_R$	$\mu^-_R$	$\tau^-_R$	-1	-1	$\frac{1}{2}$	$-\frac{1}{2}$
$e^-_R$	$\mu^-_R$	$\tau^-_R$	-1	-2	0	0
$\begin{pmatrix} u \\ d' \end{pmatrix}_L$	$\begin{pmatrix} c \\ s' \end{pmatrix}_L$	$\begin{pmatrix} t \\ b' \end{pmatrix}_L$	$\frac{2}{3}$	$\frac{1}{3}$	$\frac{1}{2}$	$\frac{1}{2}$
$d'_L$	$s'_L$	$b'_L$	$-\frac{1}{3}$	$\frac{1}{3}$	$\frac{1}{2}$	$-\frac{1}{2}$
$u_R$	$c_R$	$t_R$	$\frac{2}{3}$	$\frac{4}{3}$	0	0
$d'_R$	$s'_R$	$b'_R$	$-\frac{1}{3}$	$-\frac{2}{3}$	0	0

**Table 1.3:** Overview on electroweak quantum numbers of the Standard Model fermions, their quantum numbers and their masses according to Ref. [9]. The electrical charge  $Q$  is given in units of the absolute value of the electron charge  $e$ .

transformed into each other by a unitary rotation in flavour space that is described by the Cabibbo-Kobayashi-Maskawa (CKM) matrix [12, 13].

With the abbreviation  $L$  for the set of left-handed doublets of each lepton and quark generation and  $R$  for the right handed singlets as listed in Table 1.3, the electroweak Lagrangian is given by

$$\mathcal{L}_{\text{EW}} = i\bar{L}\gamma^\mu D_\mu L + i\bar{R}\gamma^\mu D_\mu R - \frac{1}{4}W_{\mu\nu}^i W_i^{\mu\nu} - \frac{1}{4}B_{\mu\nu}B^{\mu\nu} \quad . \quad (1.6)$$

The four gauge fields  $W_\mu^i$  ( $i = 1 \dots 3$ ) and  $B_\mu$  are related to the  $3 + 1$  degrees of freedom of the  $\text{SU}(2)_L \times \text{U}(1)_Y$  group. The corresponding field strength tensors are

$$W_{\mu\nu}^i = \partial_\mu W_\nu^i - \partial_\nu W_\mu^i - g\epsilon^{ijk}W_\mu^j W_\nu^k \quad \text{and} \quad B_{\mu\nu} = \partial_\mu B_\nu - \partial_\nu B_\mu \quad . \quad (1.7)$$

The covariant derivatives that preserve local gauge invariance are

$$D_\mu = \partial_\mu + ig\frac{\sigma_i}{2}W_\mu^i + ig'YB_\mu \quad , \quad (1.8)$$

with the  $\sigma_i$  ( $i = 1 \dots 4$ ) being the Pauli matrices, which are the generators of the  $\text{SU}(2)_L$  group. The Lagrangian contains two coupling constants. The coupling constant  $g$  determines the strength of the coupling to the  $\text{SU}(2)_L$  gauge fields and the constant  $g'$  determines the coupling to the gauge field of the hypercharge. Like QCD, the electroweak theory is non-abelian, since the generators  $\sigma_i$  do not commute. Hence, the Lagrangian contains self-interaction terms of the gauge bosons of the weak isospin.

The gauge fields  $W_\mu^a$  and  $B_\mu$  cannot be directly identified with the experimentally observed  $W$  and  $Z$  boson and the photon, since the couplings described by the Lagrangian are different from those observed in experiments. Instead, the physically observable states are given by linear combinations of these fields according to

$$W_\mu^\pm = \frac{1}{\sqrt{2}}(W_\mu^1 \mp iW_\mu^2) \quad (1.9)$$

$$Z_\mu = -B_\mu \sin \theta_W + W_\mu^3 \cos \theta_W \quad (1.10)$$

$$A_\mu = B_\mu \cos \theta_W + W_\mu^3 \sin \theta_W \quad , \quad (1.11)$$

where  $W_\mu^\pm$  and  $Z_\mu$  denote the fields of the weak gauge bosons and  $A_\mu$  the photon field. The weak mixing angle  $\theta_W$  is determined by the electroweak coupling constants according to

$$\cos \theta_W = \frac{g}{\sqrt{g^2 + g'^2}} \quad . \quad (1.12)$$

It is furthermore related to the electric charge via

$$e = g' \cos \theta_W = g \sin \theta_W \quad . \quad (1.13)$$

The Lagrangian formulated in terms of these transformed fields shows that the charged  $W$  bosons couple to all left-handed fermions and right-handed anti-fermions with the same coupling strengths. Decays of the  $W$  boson are possible into fermion–anti-fermion pairs consisting of one of the components of a  $SU(2)_L$  doublet and the anti-particle of the other component<sup>3</sup>, e.g.  $W^- \rightarrow e^- \bar{\nu}_e$  or  $W^- \rightarrow \bar{u} d'$ . The photon and the  $Z$  boson both couple to fermion–anti-fermion pairs of the same type (e.g.  $Z \rightarrow e^+ e^-$ ,  $Z \rightarrow \nu_e \bar{\nu}_e$  or  $Z \rightarrow u \bar{u}$ ). The photon couples equally to the left- and right-handed states of all electrically charged particles. In contrast, the couplings to the  $Z$  boson depend on the chirality state of the fermion. Furthermore, the  $Z$  boson couples to the neutrinos, whereas the photon does not. The Lagrangian contains cubic and quartic self-interaction terms, allowing for all three- and four-boson interactions that involve a pair of charged  $W$  bosons.

## 1.2 The Higgs mechanism

So far, all Standard Model particles are required to be massless, because otherwise the local gauge invariance of the  $\mathcal{L}_{\text{SM}}$  is not preserved<sup>4</sup>. Nevertheless, experiments unambiguously revealed that the fermions and the weak gauge bosons do indeed carry a mass. Particle masses are therefore introduced to the Standard Model through an additional extension, the Higgs mechanism [14, 15, 16, 17, 18]. This mechanism exploits the principle of spontaneous symmetry breaking to generate the desired mass terms.

### 1.2.1 Spontaneous symmetry breaking

The Higgs mechanism introduces an additional complex two-component scalar field

$$\Phi = \frac{1}{\sqrt{2}} \begin{pmatrix} \phi_1^1 + i\phi_2^1 \\ \phi_1^2 + i\phi_2^2 \end{pmatrix} \quad . \quad (1.14)$$

The dynamics of the new field is described by a term

$$\mathcal{L}_{\text{Higgs}} = (D_\mu \Phi)^\dagger (D^\mu \Phi) - V(\Phi) \quad , \quad (1.15)$$

which is added to the Standard Model Lagrangian, with the covariant derivative as introduced for the electroweak interactions in Eq. (1.8). To keep the Lagrangian gauge invariant, the field  $\Phi$  is a  $SU(2)_L \times U(1)_Y$  multiplet. In contrast to the other Standard Model boson fields,  $\Phi$  is subject to an external potential, which is

$$V(\Phi) = -\mu^2 \Phi^\dagger \Phi + \lambda (\Phi^\dagger \Phi)^2 \quad . \quad (1.16)$$

If  $\lambda > 0$  and  $\mu^2 > 0$ , the potential has a continuous non-zero minimum at  $\Phi^\dagger \Phi = \frac{\mu^2}{2\lambda}$ , as illustrated in Fig. 1.1.

<sup>3</sup>Because of the CKM mixing also transitions between quark generations are possible. These are, however, suppressed by the small off-diagonal entries of the CKM matrix.

<sup>4</sup>Mass terms are only allowed for the fermions in QCD. Nevertheless, these are ruled out because they are forbidden for the same fermions in  $\mathcal{L}_{\text{EW}}$ .

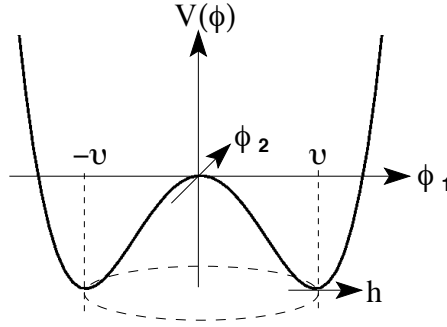


**Figure 1.1:** Two-dimensional illustration of the Higgs potential  $V(\phi) = -\mu^2\phi^2 + \lambda\phi^4$ , with complex  $\phi = \phi_1 + i\phi_2$  and parameters  $\lambda > 0$  and  $\mu^2 > 0$ . The vacuum expectation value of the field  $\phi$  is  $v = \frac{\mu^2}{2\lambda}$  (taken from Ref. [19]).

One of these minimum states is the ground state, which can be arbitrarily chosen – an act known as “spontaneous symmetry breaking”. The ground state has now less symmetry than the potential itself. A convenient choice is

$$\Phi_0 = \frac{1}{\sqrt{2}} \begin{pmatrix} 0 \\ v \end{pmatrix} , \quad (1.17)$$

with  $v \equiv \frac{\mu^2}{2\lambda}$  being the vacuum expectation value of the field  $\Phi$ . A fluctuation of this ground state can be described as

$$\Phi = \Phi_0 + \delta\Phi = \frac{1}{\sqrt{2}} \begin{pmatrix} 0 \\ v + h(x) \end{pmatrix} , \quad (1.18)$$

such that the Lagrangian close to the ground state can be expanded according to

$$\mathcal{L}_{\text{Higgs}} = \frac{1}{2} \partial_\mu h \partial^\mu h + (v+h)^2 \left( \frac{g^2}{4} W_\mu^+ W^{-\mu} + \frac{g^2}{8 \cos^2 \theta_W} Z_\mu Z^\mu \right) - \lambda v^2 h^2 - \lambda v h^3 - \frac{\lambda}{4} h^4 , \quad (1.19)$$

in the representation using the physical weak boson fields  $W_\mu^\pm$  and  $Z_\mu$  [6]. Due to the non-zero value of  $v$ , the second term contains expressions that are bilinear in the weak boson fields and are interpreted as mass terms for these fields. One finds

$$M_W = M_Z \cdot \cos \theta_W = \frac{vg}{2} \quad \text{and} \quad M_\gamma = 0 . \quad (1.20)$$

The relation between the  $W$  and  $Z$  boson masses has been confirmed in experiments. The vacuum expectation value can be estimated to be  $v \approx 246$  GeV by a comparison with the empirical value of the Fermi constant  $G_F$  [5]. This constant is the coupling constant in the Fermi model, which treats the weak interactions as point interactions and can be obtained in muon decay experiments.

### 1.2.2 Fermion masses

To describe also the fermion masses, the Lagrangian needs to be extended once more by the so-called “Yukawa”-terms

$$\mathcal{L}_{\text{Yukawa}} = -g_f (\bar{L}\Phi R + \bar{R}\Phi^\dagger L) . \quad (1.21)$$

Substituting the expansion of  $\Phi$  around its vacuum expectation value leads to terms of the form

$$-\frac{g_f}{\sqrt{2}}(v + h(x))(\bar{f}_L f_R + \bar{f}_R f_L) \quad . \quad (1.22)$$

Reading off the mass term coefficients yields the fermion masses

$$M_f = \frac{g_f v}{\sqrt{2}} \quad . \quad (1.23)$$

### 1.2.3 The Higgs boson

The field  $h$  describes a so far undetected electrically neutral  $CP$ -even spin zero particle, which couples to all massive bosons and fermions<sup>5</sup>. The coupling constants describing the strength of the Higgs boson coupling to other particles are determined by those terms in the Lagrangians  $\mathcal{L}_{\text{Higgs}}$  and  $\mathcal{L}_{\text{Yukawa}}$  (Eqs. (1.19) and (1.22)) that contain the Higgs boson field  $h$  together with the gauge boson and fermion fields. One obtains

$$g_f \propto \frac{M_f}{v} \quad (1.24)$$

for the fermions and

$$g_{VVH} \propto \frac{M_V^2}{v} \quad \text{and} \quad g_{VVHH} \propto \frac{M_V^2}{v^2} \quad (1.25)$$

for the cubic and quartic coupling constants to the gauge bosons, respectively. The couplings hence grow with the particle masses.

The third from last term in  $\mathcal{L}_{\text{Higgs}}$  as expanded in Eq. (1.19) is bilinear in the Higgs boson field  $h$  and is therefore a mass term for the Higgs boson. The Higgs boson mass is connected with the vacuum expectation value and the parameter  $\lambda$  via

$$M_H = \mu^2 = \sqrt{2\lambda v^2} \quad . \quad (1.26)$$

Since  $\lambda$  is unknown, also the mass of the Higgs boson remains undetermined from theory.

Finally, the last two terms of the Higgs Lagrangian can be interpreted as cubic and quartic self-interaction terms of the Higgs boson, which are proportional to  $\frac{M_H^2}{v}$  and  $\frac{M_H^2}{v^2}$ . Finding this newly predicted particle and establishing its predicted properties is necessary to verify the validity of the Higgs mechanism.

## 1.3 Bounds on the Higgs boson mass

Although not directly determined by the Standard Model, the Higgs boson mass is constrained by a couple of theoretical considerations. The Higgs boson contributions to elastic  $W^+W^- \rightarrow W^+W^-$  scattering guarantee a finite forward scattering amplitude, and hence the conservation of unitarity, only for Higgs boson masses up to about 1 TeV [20]. Moreover, an even tighter upper and also a lower bound comes from the  $Q^2$  dependence of the running quartic coupling constant  $\lambda(Q^2)$  [21]. The coupling increases with  $Q^2$  and diverges at a certain energy, the so-called ‘‘Landau pole’’, which grows with decreasing Higgs boson mass. For the Standard Model to be valid up to some scale  $\Lambda$  at which new physics phenomena come into play, the

<sup>5</sup>The other three degrees of freedom of the originally introduced field  $\Phi$  are absorbed in the longitudinal degrees of freedom of the weak gauge bosons and hence give them their masses.

$\lambda(Q^2)$  must be finite at least up to this scale. A  $\Lambda$  dependent Higgs boson upper mass limit is therefore needed to prevent the coupling from diverging (“triviality bound”). On the other hand,  $\lambda(Q^2)$  must also be positive up to the scale  $\Lambda$  to guarantee the stability of the vacuum. Negative contributions to the expansion of  $\lambda(Q^2)$  are generated by top quark corrections to the quartic self-coupling. To keep  $\lambda(Q^2)$  positive despite these contributions, its value  $\lambda(v^2)$  at the vacuum expectation value must exceed a  $\Lambda$  dependent lower limit, which implies also a lower limit on  $M_H$  (“vacuum stability bound”). The scale dependence of the bounds imposed by the triviality and vacuum stability arguments is shown in Fig. 1.2.

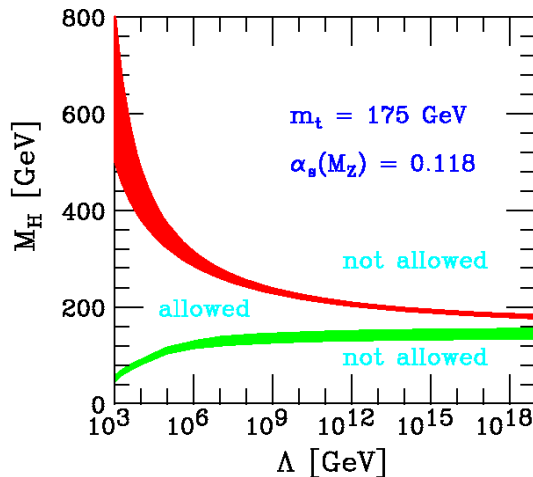


**Figure 1.2:** Lower vacuum stability bound on the Higgs boson mass and upper bound imposed by the divergence of the quartic Higgs boson coupling  $\lambda$  as a function of the validity scale  $\Lambda$  of the Standard Model for a top quark mass of  $(175 \pm 6)$  GeV and  $\alpha_s(M_Z) = (0.118 \pm 0.002)$ . The coloured bands indicate the impact of various uncertainties (taken from Refs. [20, 21]).

Two collider experiments could already put direct experimental constraints on the Higgs boson mass in the past. The  $e^+e^-$  collider LEP<sup>6</sup> at CERN<sup>7</sup> ran until the year 2000, finally reaching a centre-of-mass energy of 209 GeV. Among the searches performed at its four experiments were also searches for a Higgs boson. No Higgs boson signal could be detected, but the analyses could be used to exclude Higgs boson masses lower than 114.4 GeV at the 95% confidence level [22]. The proton–anti-proton collider Tevatron at Fermilab has just finished its final data taking phase and the data from its experiments CDF and DØ have also been analysed for Higgs boson signals. Figure 1.3 shows the most recent combined exclusion limit of the two experiments. Analysing an integrated luminosity<sup>8</sup> of  $8.6 \text{ fb}^{-1}$ , they excluded a 20 GeV wide mass region around a Higgs boson mass of 160 GeV in addition to the region already excluded by LEP.

Electroweak precision measurements also provide the possibility to constrain the Higgs boson mass indirectly. Virtual corrections from Higgs boson contributions to several physics observables depend on its mass and can thus be exploited for predictions. This can be done either with individual observables that are known with very high accuracy, e.g. the  $W$  boson mass, as shown in Fig. 1.4(a). Alternatively, a global fit to the combined electroweak precision data gives even more accurate results. The result of the current fit is shown in Fig. 1.4(b) and yields an upper bound of 161 GeV at the 95% confidence level [24].

<sup>6</sup>Short for “Large Electron–Positron collider”.

<sup>7</sup>Short for “Conseil Européen pour la Recherche Nucléaire”.

<sup>8</sup>The “integrated luminosity” is a measure for the integrated beam particle flux and is introduced in Section 2.1 of Chapter 2.

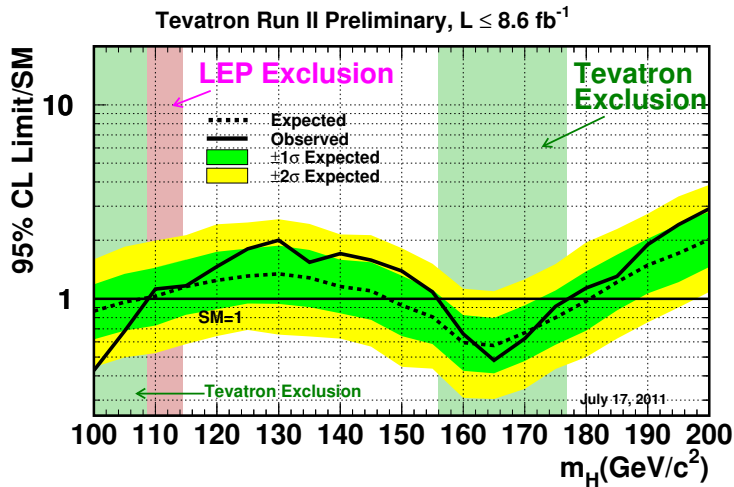


**Figure 1.3:** Combined upper limits on the Standard Model Higgs boson production cross section divided by the Standard Model expectation as a function of  $M_H$  (solid lines) obtained in a combination of results from the CDF and DØ experiments with an integrated luminosity of  $8.6 \text{ fb}^{-1}$ . The dashed line shows the median expected limit in the absence of a signal and the green and yellow bands indicate the corresponding 68% and 95% expected regions. Mass regions in which the observed limit is smaller than one, are excluded (taken from Ref. [23]).

## 1.4 Higgs boson searches at the LHC

Discovering the Higgs boson (or disproving its existence) is one of the main goals of the experiments at the Large Hadron Collider (LHC). Once the Higgs boson candidate has been found, measuring its properties is another big goal, in order to prove (or disprove) that it indeed is a Higgs boson. Higgs boson production events can be tagged by their specific particle signatures, generated by the decay products of the Higgs boson and possible accompanying particles that are produced together with the Higgs. During the last years, studies have shown that a Standard Model Higgs boson, if it exists, can be discovered within the first few years of data taking at the LHC.

### 1.4.1 Production modes and decay channels

The dominant Standard Model Higgs boson production modes at the LHC are illustrated in Fig. 1.5. The mass dependence of their cross sections is shown in Fig. 1.6(a). At the LHC, the Higgs boson is expected to be produced most abundantly in the gluon fusion mode (Fig. 1.5(a)). Though loop-induced, the process is enhanced with respect to the other production processes because of the strong coupling of the Higgs boson to the top quark and because it is a QCD process, governed by the large coupling constant  $\alpha_s$ . Furthermore, like all gluon-induced processes, the process benefits from the fact that the gluon flux is much larger than the quark flux in the low momentum fraction range that is probed at the LHC (see Fig. 2.2 in Chapter 2). Though their cross sections are at least about an order of magnitude smaller, also other production modes are of interest for a discovery of the Higgs boson because they produce additional particles, which can be exploited to identify Higgs boson production events and to reduce potential background. Weak boson fusion (Fig. 1.5(b)) is the process with the second highest rate. Since no colour exchange occurs between the incident

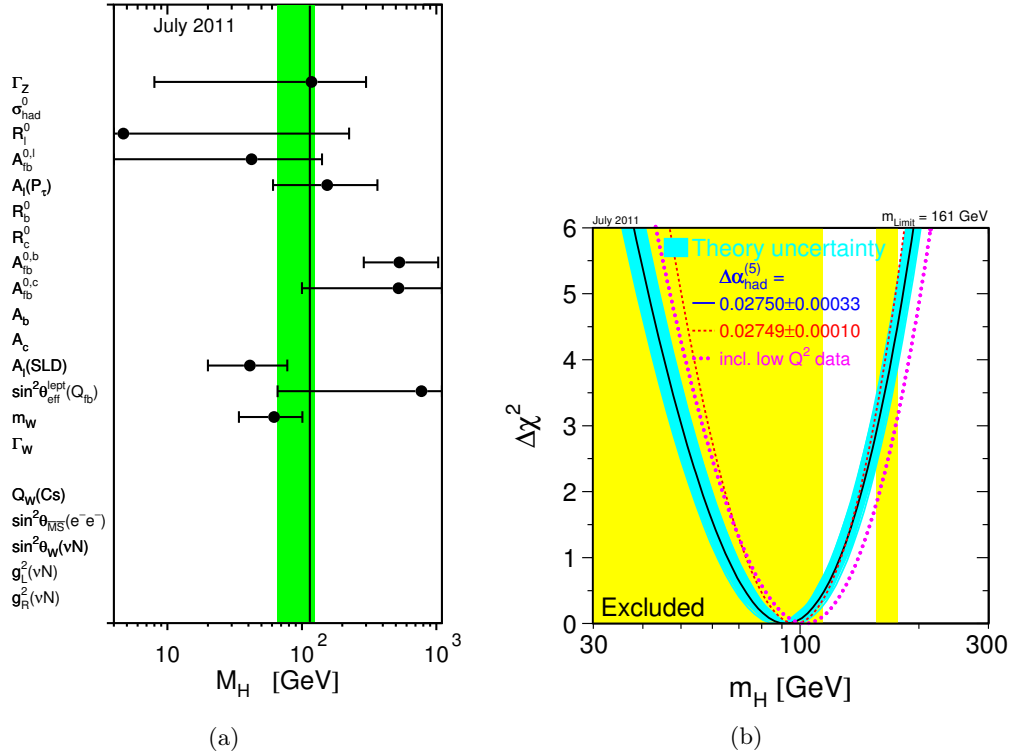


**Figure 1.4:** Higgs boson mass constraints from individual measurements of electroweak precision observables (a) and global Standard Model fit ( $\Delta\chi^2 = \chi^2 - \chi_{\text{min}}^2$ ) for different Higgs boson masses to precision electroweak observables at LEP (b). The current best fit value is  $M_H = (92_{-26}^{+34})$  GeV. Higgs boson masses above 161 GeV are excluded at the 95% confidence level, if the lower mass bound from the direct searches at LEP2 is not included in the fit. Taking this constraint into account, the upper limit rises to 185 GeV (taken from Ref. [24]).

partons, the two outgoing quarks generate a characteristic signature of two opposite-direction forward jets<sup>9</sup>. Higgs boson production in association with weak bosons or a top quark pair (Figs. 1.5(c) and 1.5(d)) are at most in the very low mass region relevant for a discovery, where Higgs boson decays are only possible into particles that are difficult to detect.

Since the Higgs boson couplings to other particles increase with their masses, the Higgs boson decays preferentially into the heaviest possible final state. At tree level<sup>10</sup>, depending on the mass of the Higgs boson, decays are possible into pairs of weak bosons or massive fermions. Decays in massless particles can occur in higher-order processes, via loops. Thus also final states of pairs of photons or gluons and  $Z\gamma$  are possible. Their contributions to the total Higgs boson decay width depend strongly on the Higgs boson mass, as shown in Fig. 1.6(a).

For small Higgs boson masses up to about 140 GeV the decay into a pair of  $b$ -quarks is dominant, but difficult to detect at a hadron collider. Therefore, Higgs boson searches need to exploit other decay channels or combinations of these. At very low Higgs boson masses, this is basically the decay into a pair of  $\tau$  leptons. In the low mass range between about 110 GeV and 130 GeV, the most promising candidate is the decay into photon pairs. The

<sup>9</sup>In HEP experiments individual partons often do not result in single hadrons, but rather in a bundle of particles emitted in a similar direction, referred to as a “jet”.

<sup>10</sup>See Section 2.2 in Chapter 2 for an overview on the calculation of cross sections in perturbation theory.

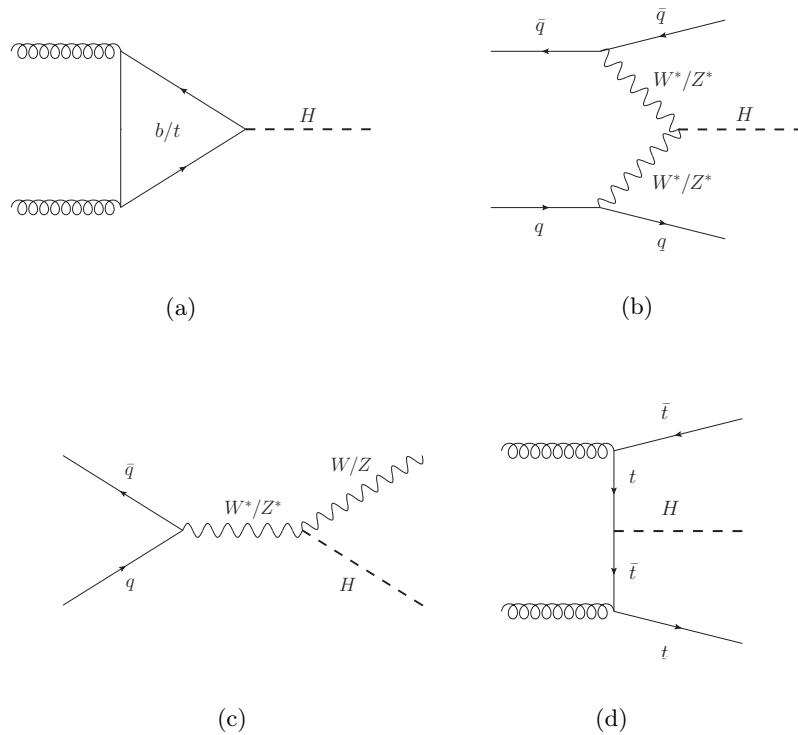


**Figure 1.5:** Feynman graphs of the four main Higgs boson production modes at the LHC: gluon fusion (a), weak boson fusion (b), radiation off weak bosons (c) and associated production with a pair of top quarks (d).

branching ratio for this decay is low but the two-photon signal is relatively easy to detect. For  $M_H > 2M_W$  the decay channel into a pair of real  $W$  bosons opens up and the Higgs boson decay width is completely dominated by the decays into pairs of  $Z$  and  $W$  bosons. Even below this threshold, there is a sizeable contribution from decays into weak boson pairs, as one of them is produced off-shell ( $WW^*$  or  $ZZ^*$ ). For Higgs boson masses above  $M_H = 2M_t$ , also the decay into a top quark pair contributes to the total width, but is difficult to detect.

The branching fractions BR are determined by the Higgs bosons partial decay widths  $\Gamma_X$  for a decay  $H \rightarrow XX$  and its total width  $\Gamma_{\text{tot}}$  according to

$$\text{BR}(H \rightarrow XX) = \frac{\Gamma_X}{\Gamma_{\text{tot}}} . \quad (1.27)$$

With increasing Higgs boson mass also the total decay width of the Higgs boson grows, with a rapid increase around the  $W^+W^-$  production threshold of almost three orders of magnitude, as shown in Fig. 1.7. For the low Higgs boson mass range, where  $\Gamma_H \ll M_H$ , the Higgs boson can be assumed to be produced on-shell. This so-called “narrow width approximation” allows the Higgs boson production and decay to be factorized in calculations.

### 1.4.2 Associated Higgs boson production with top quark pairs

Higgs boson production in association with a pair of top quarks is the production mode with the lowest production cross section considered at the LHC. Together with the Higgs boson decay into a pair of  $b$ -quarks it was, nevertheless, for some time considered the most promising candidate to discover a light Higgs boson in the very low mass region up to about 130 GeV.

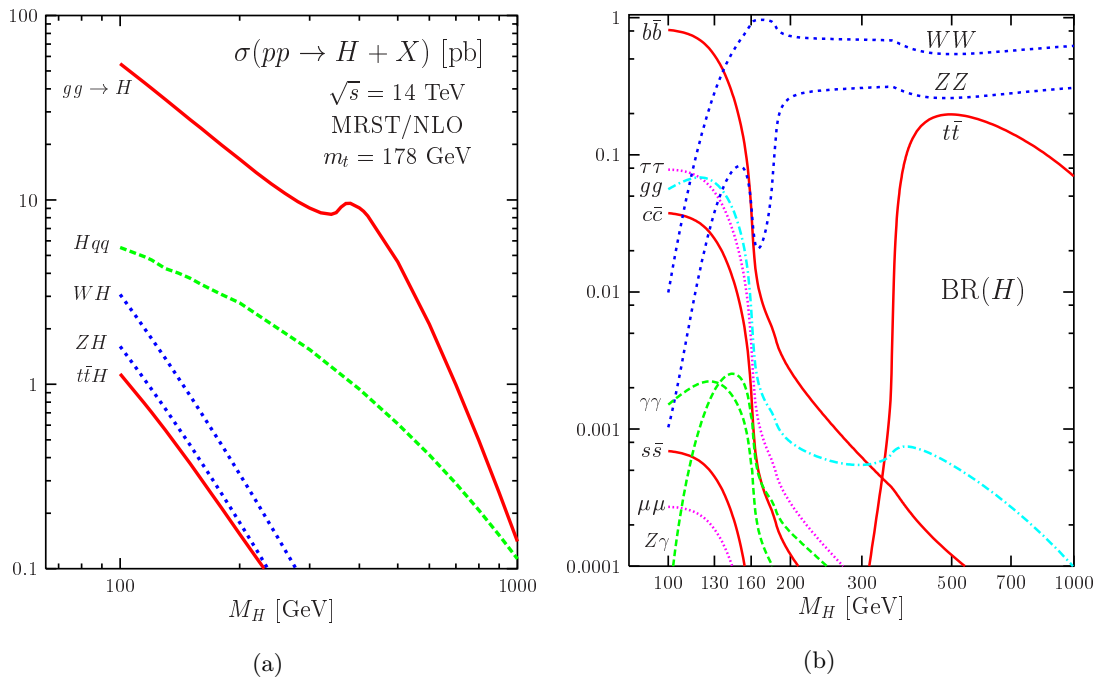


**Figure 1.6:** (a) Mass dependence of the production cross sections for the five Standard Model Higgs boson production channels at the LHC and (b) branching ratios for the different decay modes as a function of the Higgs boson mass (taken from Ref. [20]).

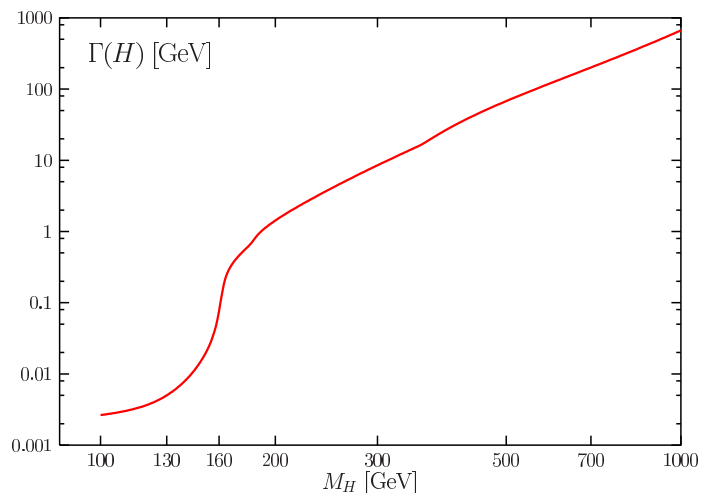


**Figure 1.7:** Total decay width of the Standard Model Higgs boson as a function of its mass (taken from Ref. [20]).

Nevertheless, studies revealed that suppressing the large non-resonant  $t\bar{t}b\bar{b}$  background is difficult and a reconstruction of the Higgs boson mass is impossible with sufficient accuracy to reach the necessary significances for a substantial contribution to the sensitivity [25, 26]. The top quark pair associated production mode is nevertheless of interest at the LHC, in particular the final states where the Higgs boson decays either into a pair of  $b$ -quarks (for Higgs boson masses up to about 135 GeV) or into a pair of  $W$  bosons (from 120 GeV upwards). Both channels can provide valuable information on the Higgs boson properties<sup>11</sup>. With two

<sup>11</sup>In addition to the decay width and coupling measurements discussed in Section 1.5,  $t\bar{t}H$  production might also allow for the discrimination between a  $CP$ -even and a  $CP$ -odd Higgs boson, as suggested in Ref. [27].

top quarks and two  $W$  bosons involved, especially  $t\bar{t}H$ ,  $H \rightarrow W^+W^-$  production generates striking signatures with many leptons and jets. The most promising of them is the decay into a pair of leptons of equal charge sign and six jets, two of them being  $b$ -quark jets. The study of the prospects to observe this final state at ATLAS is one of the main subjects of this thesis and is discussed in Chapter 6.

### 1.4.3 Discovery potential of the ATLAS experiment

Combinations of the above discussed Higgs boson production modes and decay channels lead to a variety of signatures that can be exploited for Higgs boson searches in different mass regions. All of them share the challenge of discriminating signal events from unwanted background generated by other Standard Model processes leading to similar final states. The potential to discover a significant signal excess above this background has been investigated in advance of data taking at the LHC experiments [28, 29]. Figure 1.8(a) shows the expected significance for the detection of a Higgs boson at ATLAS for a centre-of-mass energy of 14 TeV and an integrated luminosity of  $10 \text{ fb}^{-1}$ . Significances of three and larger are possible in the entire interesting mass range between the LEP exclusion threshold and 500 GeV. A discovery can be claimed at a significance level of five or larger, which is reached for  $M_H > 130 \text{ GeV}$ . A combination of the ATLAS results with the results from the CMS experiment will push the discovery threshold to somewhat smaller Higgs boson masses. For very low Higgs boson masses, however, it will be necessary to accumulate more data for a discovery. Figure 1.8(b) illustrates the integrated luminosities that are needed to reach the  $5\sigma$  discovery significance level as a function of the Higgs boson mass.

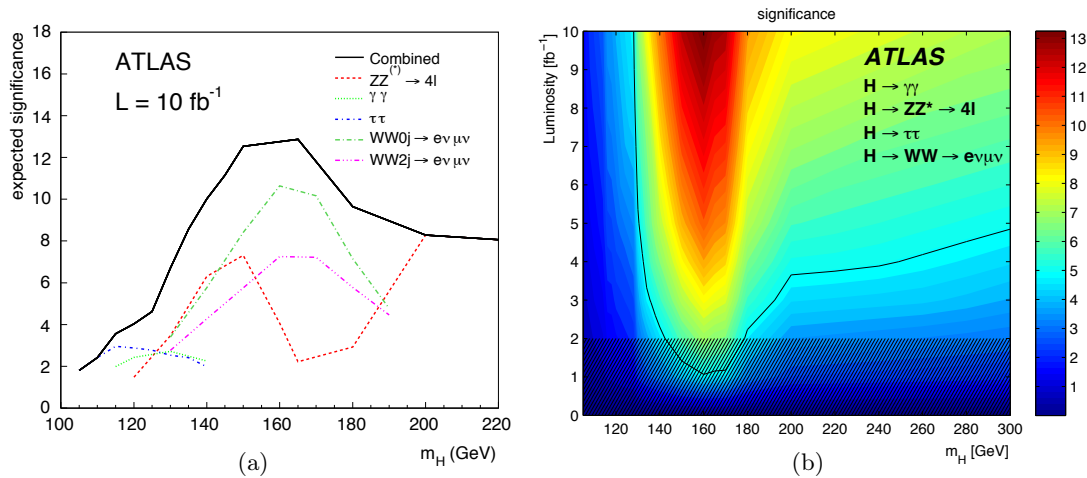


**Figure 1.8:** (a) Discovery potential of the most important Higgs boson search channels in ATLAS ( $\sqrt{s} = 14 \text{ TeV}$ ) and their combination with an integrated luminosity of  $10 \text{ fb}^{-1}$ . (b) Discovery significance contours for different masses and integrated luminosities. The black curve represents the  $5\sigma$  discovery contour (taken from Ref. [26]).

### 1.4.4 Recent exclusion limits

Since March 2010 the LHC produces proton–proton collisions at a centre-of-mass energy of 7 TeV. More than  $2 \text{ fb}^{-1}$  of data have been collected and analysed within a few months in summer 2011. So far, no evidence for Higgs boson production could be observed. Figure 1.9 shows the ATLAS and CMS exclusion limits for a Standard Model Higgs boson. Within the short period the LHC has widely extended the Tevatron exclusion range around a Higgs

boson mass of 160 GeV and can exclude almost the entire region between about 145 GeV and 450 GeV at the 95% confidence level.

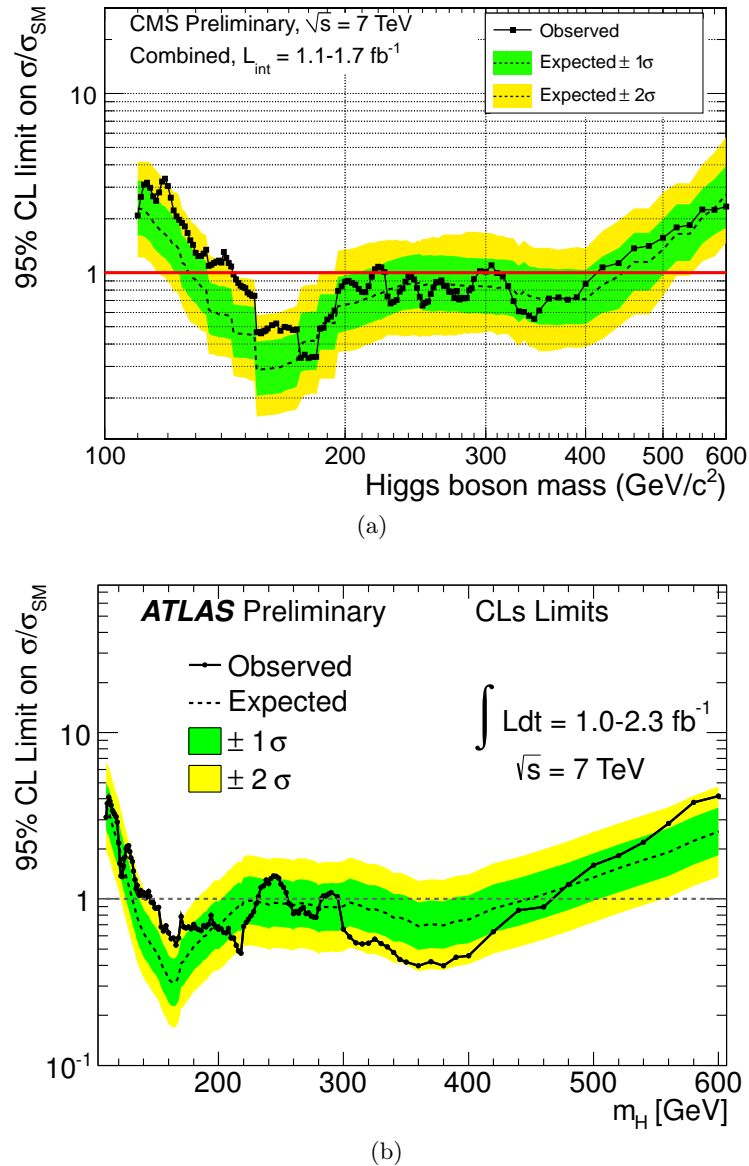


**Figure 1.9:** Combined upper limits on the Standard Model Higgs boson production cross section divided by the Standard Model expectation as a function of  $M_H$  (solid lines) as obtained by the CMS (a) and ATLAS (b) experiments, using up to  $2.3\text{fb}^{-1}$  of data. The dashed lines show the median expected limit in the absence of a signal and the green and yellow bands indicate the corresponding 68% and 95% expected regions. Mass regions in which the observed limit is smaller than one, are excluded (taken from Refs. [30] (a) and [31] (b); details on the used amount of data and the included Higgs boson production channels can be found therein).

## 1.5 Coupling measurements at the LHC

Once a Higgs boson signal has been found, it is essential to study its properties to ensure it is indeed the Higgs boson predicted by the Standard Model. Properties accessible at the LHC are its spin and CP eigenvalues [32] and, in particular, the strengths of its couplings to fermions

and weak bosons. Measurements at the LHC will allow the information of various observed and explicitly excluded Higgs boson production and decay modes to be combined to extract information on the coupling constants. Studies have been published in Refs. [33, 34], which combine all these measurements in a global maximum likelihood fit of the coupling parameters, taking into account theory and experimental uncertainties and their correlations<sup>12</sup>.

At hadron colliders Higgs boson production modes are only accessible in combination with a certain decay channel (and vice versa). Neither absolute inclusive production cross section measurements nor absolute measurements of branching ratios are possible, but only measurements of the product of both (“rates”). Also the total Higgs boson decay width is not accessible. The resolution of a Higgs boson mass measurement at the LHC is at least 1 GeV and hence too coarse for a measurement of the Higgs boson width, which is expected to be much smaller in the range of low Higgs boson masses (see Fig. 1.7). Measurements of partial widths and absolute coupling values are thus not possible at the LHC without further assumptions. What can be measured instead are ratios of partial widths. The production cross section for the production via the coupling to a particle  $X$  is proportional to the partial width  $\Gamma_X$ . In the narrow width approximation the measured rate  $\sigma \times \text{BR}$  for Higgs boson production in this channel with subsequent decay  $H \rightarrow YY$  can be expressed by the Higgs boson widths according to

$$\sigma \times \text{BR} \propto \Gamma_X \cdot \frac{\Gamma_Y}{\Gamma_{\text{tot}}} \quad . \quad (1.28)$$

Using only information on the Higgs boson decays and under the assumption that this Higgs boson is a single scalar  $CP$ -even particle, relative decay widths can be accessed in ratios of measured rates. Since the decay  $H \rightarrow W^+W^-$  is the one best accessible over the full intermediate Higgs boson mass range, it is used for the normalization.

The information on the production mode can be exploited to obtain also relative coupling strengths, if some further theoretical assumptions are made. Though these ratios do not contain sufficient information to establish the Standard Model nature of a Higgs boson, deviations from the Standard Model predictions could provide valuable hints on new physics. Figure 1.10(a) shows the expected accuracies for such measurements at the ATLAS experiment, assuming that only the known Standard Model particles couple to the Higgs boson in the expected way [33]. Successively introducing more and more constraints and theory assumptions finally allows the absolute coupling parameters to be determined [34]. Their expected accuracies, combining data from two LHC experiments are shown in Fig. 1.10(b).

Probably the most interesting among all these couplings is the Yukawa coupling to the top quark. It is the Standard Model particle with the largest mass and therefore the strength  $g_t$  of its coupling is the largest of all Higgs boson couplings, being predicted to be close to unity. For the same reason, the top quark plays also a special role in many theories beyond the Standard Model. The top quark contribution dominates the gluon fusion Higgs boson production mode. In addition, gluon fusion in combination with a subsequent Higgs boson decay in weak boson pairs is relatively easy to observe at the LHC. Therefore, the channel is responsible for the relatively high accuracies that can be reached in the above discussed measurements of  $g_t^2/g_W^2$  and  $g_t^2$ . Nevertheless, the gluon fusion process can only be exploited under the assumption that only Standard Model particles contribute to the loop in the gluon fusion process in their predicted strengths. Without these assumptions, the less easy to observe  $t\bar{t}H$  production mode is the only way to access the top Yukawa coupling. The requirement of two top quarks to be produced in association with the Higgs boson make sure that only top quarks contribute.

<sup>12</sup>A more recent study, which addresses only a 120 GeV Higgs boson, has been published in Ref. [35].

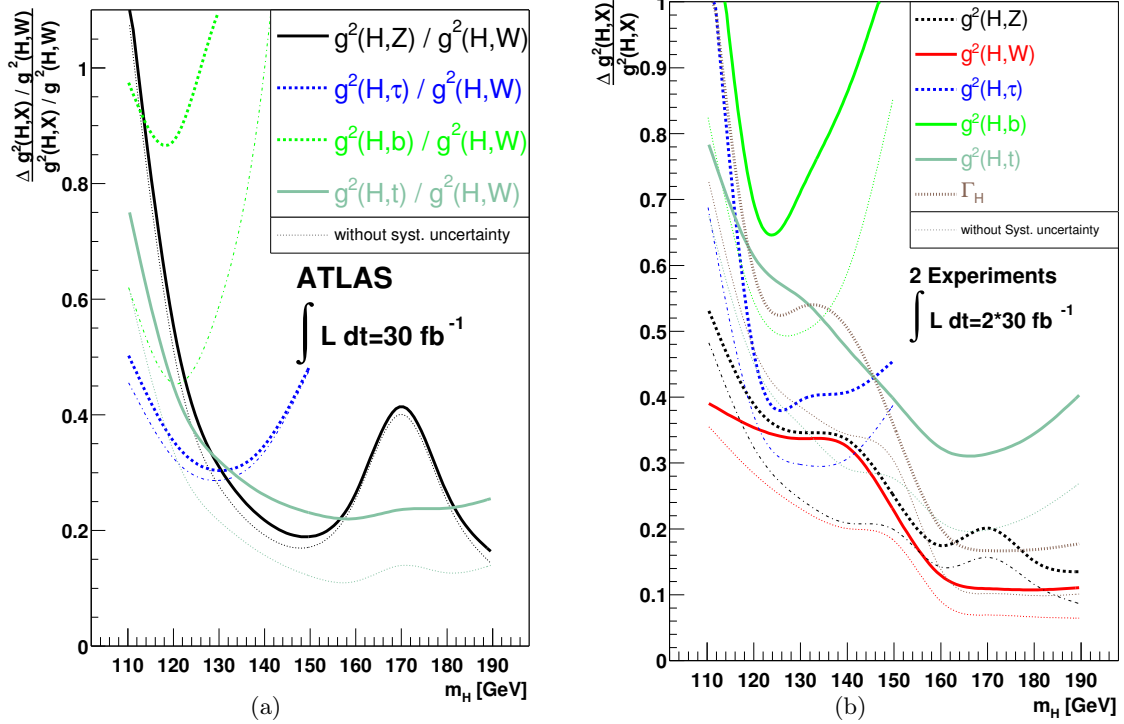


**Figure 1.10:** Expected relative accuracy for a measurement of relative Higgs boson coupling parameters at the ATLAS experiment with an integrated luminosity of  $30 \text{ fb}^{-1}$  (a) and expected relative uncertainty for a measurement of the squared coupling constants using data from two LHC experiments (b) (taken from Refs. [33] (a) and [34] (b); see these references for details on the underlying theoretical assumptions).

For the post-LHC era, plans are under way to build a linear  $e^+e^-$  collider [36, 37]. Such a machine is predestined to carry out precision measurements. Among many others, it will allow for a high-precision (almost) model independent measurement of  $g_t$ , which has to assume no more than a non-degenerate  $CP$ -even scalar Higgs boson. Such measurements are feasible, as soon as the collider runs at a centre-of-mass energy above about 800 GeV, high enough for  $t\bar{t}H$  production to occur with a sufficiently high rate [38]. Nevertheless, in its early phase, such a collider will run at lower energies, which allows only for a precision measurement of  $\text{BR}(H \rightarrow W^+W^-)$ . The results of rate measurements of  $t\bar{t}H$  production at the LHC will then still be very valuable, because they will make such a model-independent determination of the top Yukawa coupling constant possible already at this stage, if combined with the linear collider branching ratio measurements [39].

## 2 Phenomenology of hadron collider experiments

To obtain predictions from the Standard Model that can be validated in hadron collider experiments, it must be taken into account that quarks and gluons do not exist as free particles. Furthermore, cross section calculations are based on perturbative treatment and require approximations, which cause uncertainties on the obtained results. The most important techniques that aim at a realistic description of the phenomenology at hadron colliders, including Monte Carlo approaches for event generation, are briefly summarized in the following.

### 2.1 Luminosity

Events of a given type occur at a collider at a rate  $R$ , which depends on the interaction cross section  $\sigma$  for this event type, which is introduced in Section 2.2, and the “instantaneous luminosity”  $L$  delivered by the accelerator according to

$$R = \frac{dN}{dt} = \sigma \cdot L \quad . \quad (2.1)$$

$L$  is a measure for the incoming particle flux, usually given in units of  $\text{cm}^{-2}\text{s}^{-1}$ , and is determined by the operating parameters of the collider. At the LHC the beam is not operated continuously but in particle “bunches”. If two such bunches of  $n_1$  and  $n_2$  particles collide with a frequency  $f$ , the instantaneous luminosity is

$$L = f \frac{n_1 n_2}{4\pi\sigma_x\sigma_y} \quad . \quad (2.2)$$

The relation assumes head-on collisions of bunches with identical Gaussian profiles with standard deviations  $\sigma_x$  and  $\sigma_y$  in the  $x$ - and  $y$ -directions perpendicular to the beam axis. The total number of events in a given period of data taking is determined by the time integral of the rate as

$$N = \int dt R = \sigma \int dt L \equiv \sigma \cdot \mathcal{L} \quad , \quad (2.3)$$

with  $\mathcal{L}$  denoting the “integrated luminosity”. The unit of  $\mathcal{L}$  is the inverse of the unit of the cross section, which is usually given in barn ( $1 \text{ b} = 10^{-28} \text{ m}^2$ ). The goal of the LHC experiments is to collect several hundred  $\text{fb}^{-1}$ .

### 2.2 Cross sections

The cross sections are predicted by the Standard Model and can be derived from the Lagrangians introduced in Chapter 1, as summarized in Section 2.2.1. The so obtained “partonic cross sections” describe the interactions of the elementary fermions and bosons. At hadron colliders, however, the incoming beam particles are composite objects of which only individual constituents, i.e. quarks or gluons (referred to as “partons”), take part in the so-described interactions. The step from the partonic to the observable “hadronic cross sections” is described

in Section 2.2.2 (mainly following the presentation in Ref. [40]), whereas Section 2.2.3 deals with higher order calculations of cross sections.

### 2.2.1 Partonic cross sections

The differential cross sections for the transition of an incoming state of two elementary particles  $i_1$  and  $i_2$  to a final state  $f$  consisting of  $n$  other elementary particles can be expressed as

$$d\hat{\sigma}_{i_1+i_2\rightarrow f} = \frac{1}{2E_{i_1}2E_{i_2}|v_{i_1}-v_{i_2}|} |\mathcal{M}_{i_1+i_2\rightarrow f}|^2 d\Pi_n \quad . \quad (2.4)$$

The final state phase space factor  $d\Pi_n$  contains the information on the kinematics of the outgoing particles, whereas the information of the kinematics of the incoming particles is expressed by the flux factor  $\frac{1}{2E_{i_1}2E_{i_2}|v_{i_1}-v_{i_2}|}$ , with  $E_{i_1}$  and  $E_{i_2}$  being the energies of the incoming particles and  $|v_{i_1}-v_{i_2}|$  their relative velocity. The complete dynamics of the process is contained in the matrix element  $\mathcal{M}_{i_1+i_2\rightarrow f}$ . The matrix element is determined by the Lagrangian and can be expanded in a perturbation series in orders of the involved coupling constants.

The ‘‘Feynman rules’’ give a prescription how to calculate the terms contributing to this series. ‘‘Vertices’’, i.e. branching points in the Feynman diagrams describing the process, are accounted for in the calculation by vertex factors derived from interaction terms in the Lagrangian. Each vertex factor introduces one order in the involved coupling constant. Internal lines are expressed by ‘‘propagators’’, which are derived from the kinetic part of the Lagrangian. The perturbation series in which the partonic cross section is expanded consists of an infinite number of contributions and hence cannot be calculated fully, but must be truncated at some finite order. Leading order (LO) or ‘‘tree level’’ results are obtained, if only terms of the lowest possible order in the coupling constants are taken into account. The NLO contributions comprise virtual corrections, as well as real emissions of additional partons. Figure 2.1 shows some examples of the Feynman diagrams that contribute to the  $t\bar{t}H$  production cross section in leading and next-to-leading order. Real emissions lead to final states with observable extra particles that would not be produced in LO calculations. Radiations off incoming and outgoing particles are referred to as ‘‘initial state radiation’’ (ISR) and ‘‘final state radiation’’ (FSR), respectively.

The number of Feynman graphs that must be considered in higher order contributions and hence the complexity of the calculation increases rapidly with the order. Nevertheless, LO calculations normally suffer from large theoretical uncertainties. Higher order calculations are therefore essential to obtain reliable results. This affects especially the QCD contribution to the perturbation series, which converges slowly because of the large value of the running coupling constant (typically  $\alpha_s(M_Z^2) \approx 0.12$ ). Calculations up to next-to-leading order (NLO) in QCD exist for a large number of processes that are expected to play a role at the LHC. Next-to-next-to-leading (NNLO) calculations exist only for a few of them. For certain processes, also higher order electroweak contributions are of the same size as the higher order QCD corrections and must be considered in the calculation of the cross section.

The inclusive cross section  $\hat{\sigma}_{i_1+i_2\rightarrow f}$  is given as the integral of the differential cross section in Eq. (2.4), summed over all possible incoming particle colour and spin states and averaged over all outgoing particle states that lead to the considered final state. Because it occurs usually at relatively high momentum transfers  $Q^2$ , the parton process described by  $\hat{\sigma}_{i_1+i_2\rightarrow f}$  is usually referred to as the ‘‘hard scattering process’’.

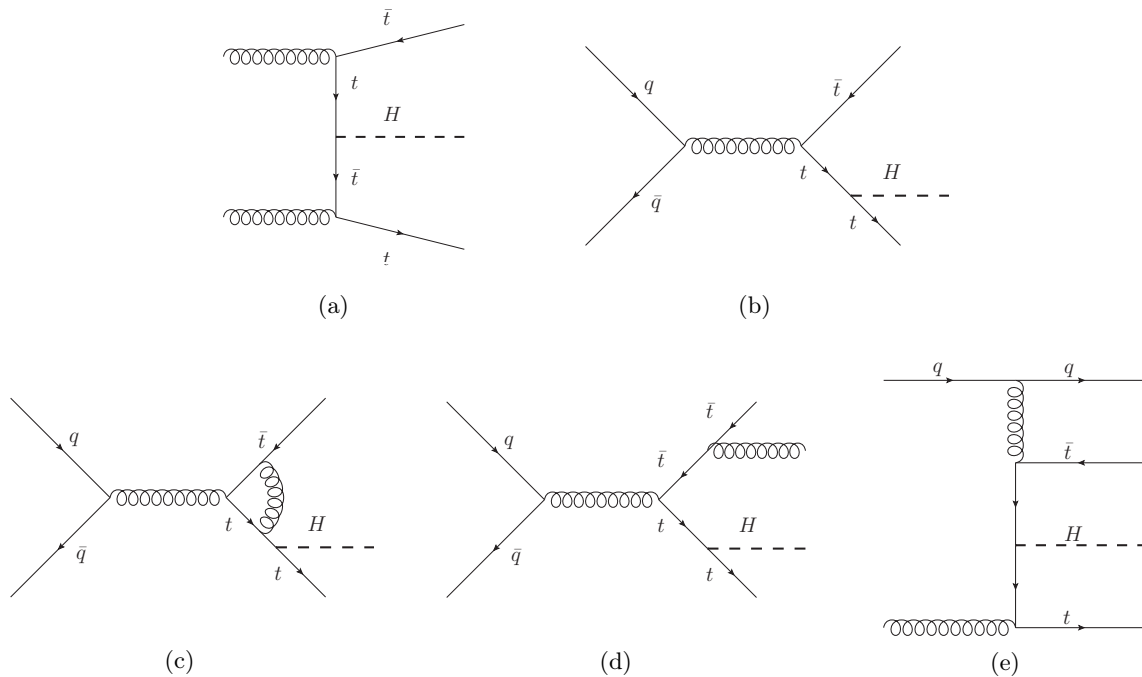


**Figure 2.1:** The two tree level Feynman diagrams contributing to  $t\bar{t}H$  production in the  $gg$  (a) and  $q\bar{q}$  (b) initial state. All other graphs show contributions to the NLO correction of the cross section: virtual corrections (c), final state radiation (d) and  $t\bar{t}H$  production in gluon splitting (e).

### 2.2.2 Hadronic cross sections

At the LHC, the initial particles  $i_1$  and  $i_2$  are constituents of compound protons  $I_1$  and  $I_2$ . Each parton carries a fraction  $x$  of the momentum of the incoming proton. The probability to extract a parton  $p$  with a certain  $x$  from a hadron  $H$  depends on the scale  $Q^2$  at which the hadron is probed and is provided by the so-called “parton distribution functions” (PDFs)  $f_{p/H}(x, Q^2)$ . These PDFs cannot be calculated theoretically, but require input from experiments. Once their  $x$  dependence is measured at one value of  $Q^2$ , they can be extrapolated to other  $Q^2$  values as solutions of the DGLAP evolution equations [41]. Figure 2.2 shows the PDFs for different kinds of partons in a proton as a function of their momentum fraction  $x$  for two values of  $Q^2$ .

Rates that are measured at the LHC experiments are determined by the cross section for a certain interaction in a proton–proton collision rather than in the parton–parton interaction. This implies the need to predict the hadronic cross section  $\sigma_{I_1+I_2\rightarrow f}$  instead of the partonic cross section. The so-called “factorization theorem” [43, 44] allows  $\sigma_{I_1+I_2\rightarrow f}$  to be expressed as a sum over all types of initial partons that can contribute to the same final state according to

$$d\sigma_{I_1+I_2\rightarrow f} = \sum_{i_1, i_2} \int_0^1 dx_1 \int_0^1 dx_2 f_{i_1/I_1}(x_1, \mu_F^2) f_{i_2/I_2}(x_2, \mu_F^2) d\hat{\sigma}_{i_1+i_2\rightarrow f}(x_1, x_2, \mu_F, \mu_R) \quad . \quad (2.5)$$

Large contributions from gluons emitted collinear with the incoming partons are absorbed in the PDFs. The “factorization scale”  $\mu_F$  is the scale that separates the long- and short-distance physics and the “renormalization scale”  $\mu_R$  is the scale for the absorption of further divergences in the partonic cross sections in the running coupling constant. With the partonic

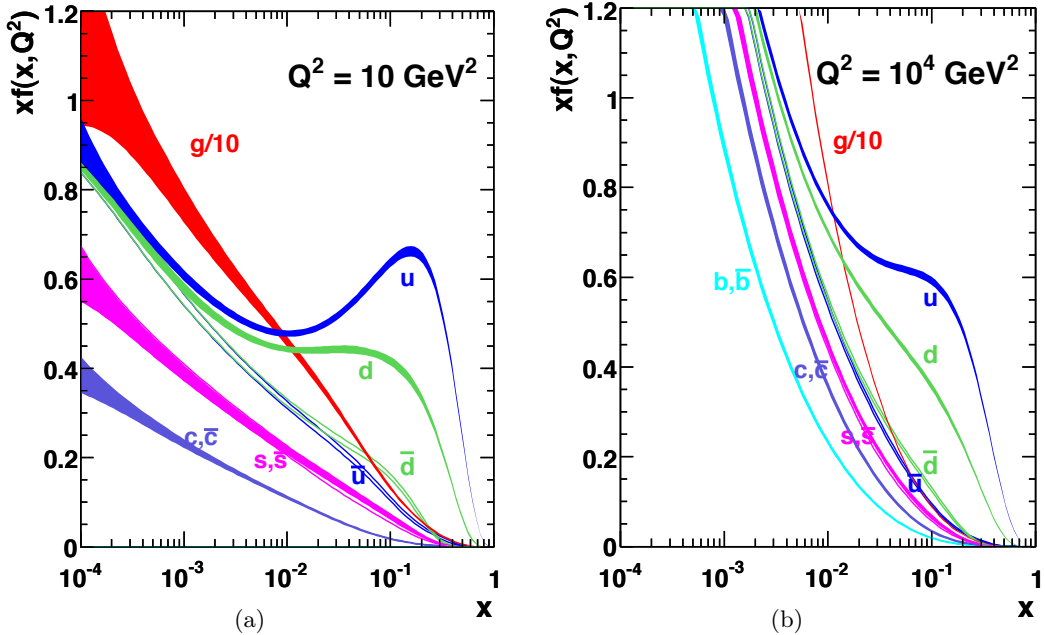


**Figure 2.2:** NLO proton PDFs (multiplied by  $x$ ) as obtained by the MSTW collaboration as a function of the parton momentum fraction  $x$  for squared momentum transfers of  $Q^2 = 10 \text{ GeV}^2$  (a) and  $Q^2 = 10^4 \text{ GeV}^2$  (b) (taken from Ref. [42]).

cross section being expanded in  $\alpha_s(\mu_R^2)$  as

$$\hat{\sigma}_{i_1+i_2 \rightarrow f} = \hat{\sigma}_{i_1+i_2 \rightarrow f}^{\text{LO}} \left( 1 + \sum_{m=1}^{\infty} \alpha_s^m(\mu_R^2) c_m^{i_1+i_2 \rightarrow f} \right), \quad (2.6)$$

formally, the cross section calculated to all orders in perturbation theory is independent from the choice of the scales  $\mu_F$  and  $\mu_R$ . The scale dependence of the coefficients  $c_m^{i_1+i_2 \rightarrow f}(\mu_F, \mu_R)$  exactly compensates the scale dependence of the PDFs and the coupling constant. If the perturbation series is truncated at some order in  $\alpha_s$  (“fixed order calculation”), a residual dependence on both scales remains, which is the smaller the more orders are included in the calculation. To avoid unnaturally large contributions reappearing in the truncated perturbation series, it is sensible to choose  $\mu_F$  and  $\mu_R$  of the order of the typical momentum scales of the hard scattering process. Often, also a common scale  $\mu_0 \equiv \mu_F = \mu_R$  is assumed.

### 2.2.3 Uncertainties in cross section calculations

The above described cross section predictions are plagued with uncertainties, caused by the perturbative treatment of the cross section determination or introduced by the use of measurements that carry an experimental uncertainty. The most important sources of uncertainties are briefly discussed in the following.

#### Scale dependence of cross section calculations

Although the dependence on the choice of the unphysical factorization and renormalization scales vanishes in the full hadronic cross section in Eq. (2.5), calculations at low orders in perturbation theory may depend strongly on the choice of these scales. This can lead to sizeable uncertainties on the cross sections, especially for processes where only LO calculations exist. Figure 2.3 shows the dependence on the relative scale  $\mu/\mu_0$  for the  $t\bar{t}H$  production cross

section for a Higgs boson mass of 120 GeV (Fig. 2.3(a)) and for  $t\bar{t}Z$  production, which is one of the main backgrounds to the  $t\bar{t}H$ ,  $H \rightarrow W^+W^-$  process studied in this thesis (Fig. 2.3(b)). The size of the uncertainties is usually estimated by scaling  $\mu_0$  up and down by a factor of two. Both figures show that this approach leads to large uncertainties if only the LO is considered. Also the effect of including one more order in  $\alpha_s$  is clearly visible, as the dependence of the NLO cross sections on  $\mu/\mu_0$  is much weaker.

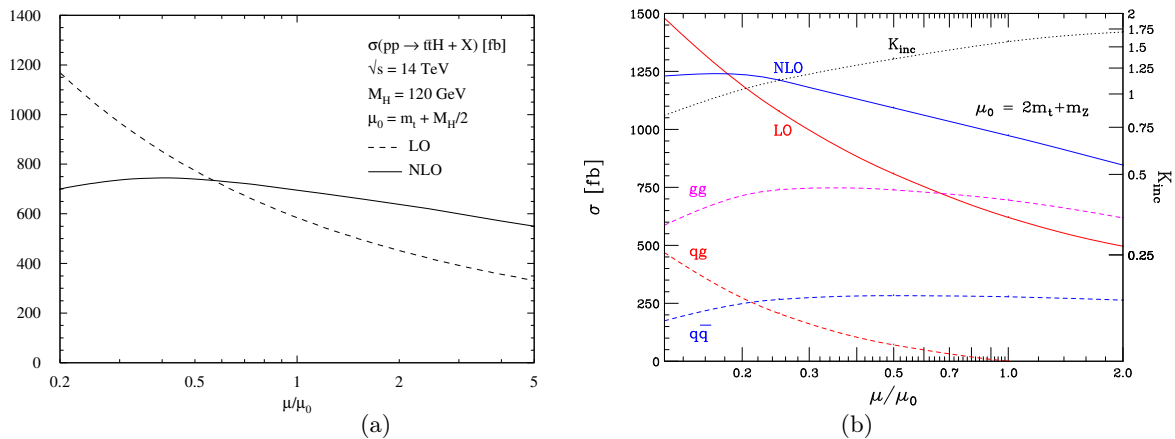


**Figure 2.3:** LO and NLO calculations of the  $t\bar{t}H$  (a) and  $t\bar{t}Z$  (b) production cross sections as a function of the factorization and renormalization scale  $\mu$  normalized to the scale  $\mu_0$  (taken from Refs. [45] (a) and [46] (b)). The scales chosen to evaluate the cross section values given in the references are  $\mu_0 = M_t + M_H/2$  and  $\mu_0 = M_t + M_Z/2$ , respectively. The Higgs boson mass in (a) is 120 GeV. The dashed lines in (b) indicate the individual  $gg$ ,  $q\bar{q}$  and  $qg$  contributions to the NLO cross section.

## PDF uncertainties

The uncertainty of the PDFs obtained from experiments also leads to uncertainties on the hadronic cross section predictions. Several PDF sets, provided by various collaborations and using different PDF fit approaches, are available. The PDFs are determined in global fits, using either a set of different fixed values of  $\alpha_s(M_Z)$  in the DGLAP evolution, such that the best suited PDFs can be chosen to match the  $\alpha_s$  value used in the calculation of the partonic cross sections. Another approach treats  $\alpha_s$  as a free parameter, thus providing the best fit  $\alpha_s$  value together with the PDFs [47]. Therefore, cross section calculations pick up some dependence on the value of  $\alpha_s$  indirectly through the  $\alpha_s$  dependence of the PDFs. This is demonstrated in Fig. 2.4, where the residual  $\alpha_s$  dependence through the PDFs is shown for the NLO cross section calculation for top quark pair production in  $\sqrt{s} = 7$  TeV proton–proton collisions, which is one of the most important backgrounds for  $t\bar{t}H$ ,  $H \rightarrow W^+W^-$ . The error bars show the individual contributions to the PDF uncertainties, coming from the uncertainties of the fit parameters and the uncertainty of the  $\alpha_s$  value (which itself is often determined in a dedicated fit). The dashed lines indicate the change in the cross section, if the central value of  $\alpha_s$  used in the fit is varied. Depending on the approach chosen for the determination of the PDFs, the  $\alpha_s$  uncertainty can either be evaluated separately, or is automatically included in the PDF uncertainties, which needs to be accounted for, when calculating combined  $\alpha_s$  and PDF uncertainties (see e.g. the treatment in Ref. [47]). Typical cross section uncertainties caused by PDF(+ $\alpha_s$ ) uncertainties are of the order of about 10%.

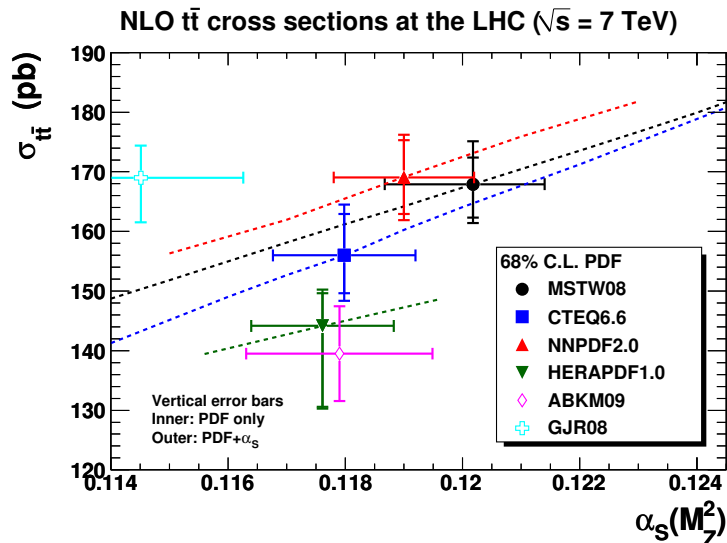


**Figure 2.4:** Cross section for  $t\bar{t}$  production in proton–proton collisions at  $\sqrt{s} = 7$  TeV obtained with the PDF sets provided by different collaborations using different central values of the strong coupling constant  $\alpha_s(M_Z)$  for the PDF determination. The dependence of the individual cross sections on the choice of the central value of  $\alpha_s(M_Z)$  is indicated by the dashed lines. The inner error bars give the uncertainties due to PDF uncertainties from the fit. The outer error bars indicate the additional uncertainty due to the uncertainty of the  $\alpha_s(M_Z)$  value used in the fit. The ABKM and GJR groups treat  $\alpha_s$  as a free parameter in the fit, therefore only combined uncertainties are given (taken from Ref. [48]).

## 2.3 Monte Carlo event generation

The analysis of Monte Carlo (MC) datasets is an important tool in particle physics experiments. Analysis strategies can be established in advance of data taking with the help of such datasets. Once data have been collected, Monte Carlo simulations are indispensable for their analysis. The generation of Monte Carlo events is done with dedicated MC generator programs. The result are “events” consisting of the four-momenta of stable particles that could be detected in an experiment, i.e. the stable particles produced in the particle collision and the decay products of unstable scattering products. Depending on the desired accuracy, these four-momenta could be directly used for predictions in so-called “parton level studies” or they can be processed further to simulate also detector effects as described in Section 3.3.6. To date, a variety of programs is available, with individual strengths and weaknesses. Monte Carlo event generation is done in several steps that are common to most of the programs but differ in the exact implementation. A description of these basic ingredients to MC event generation is given in the following, introducing also the MC programs that are used in this thesis (see also Ref. [49]).

### 2.3.1 Hard scattering

Starting point for the event generation is the hard scattering cross section, calculated according to Eq. (2.5). Specific four-momentum and spin configurations of the final state particles are then selected according to the probability for this particular final state configuration to be produced. Most available Monte Carlo generators are capable only of tree level calculations. An exception is the MC@NLO generator [50], which provides a full NLO treatment for a

limited number of processes. The NLO treatment leads to negative event weights (weight =  $-1$ ), which affect typically about 10% to 20% of all generated events. These can be considered as the finite negative interference contributions to the total cross section. In the study of MC@NLO samples, negative weight events cancel with the same amount of positively weighted events (weight =  $+1$ ). Accordingly, a larger number of events must be generated to obtain a dataset corresponding to a certain luminosity, compared with a standard LO generator producing unweighted events.

### 2.3.2 Parton shower

Additional radiation on top of the hard scattering process cannot be fully described by finite order matrix element calculations. Instead, “parton shower” algorithms are run to model parton emissions and down to the non-perturbative soft regime of hadronization. These algorithms treat the FSR as a chain of subsequent soft or collinear  $q \rightarrow qg$ ,  $g \rightarrow gg$  or  $g \rightarrow q\bar{q}$  radiation processes. These emissions take place according to the so-called,  $\alpha_s$  dependent, “Sudakov factors” [51], which give the probability for a  $1 \rightarrow 2$  branching to occur between the initial parton  $Q^2$  and a certain target  $Q^2$ . If, based on this probability, the decision is made that an emission occurs it is determined according to the probabilities and kinematics given by the so-called “Altarelli–Parisi splitting functions” [41, 52]. The successive approach is justified at least for emissions close to the soft or collinear regime, where interference contributions are small enough to be neglected. The parton shower stops at a cutoff  $Q^2$  value, which is usually chosen around 1 GeV. Algorithms that go backwards in time allow also ISR processes to be included with a similar approach, applying some constraints to ensure that the resulting state is in accordance with the partons originating from a proton. Parton showering algorithms are implemented in some of the current multi-purpose MC programs such as PYTHIA [53] and HERWIG [54]. Other LO Monte Carlo programs used in this thesis are the parton level generator MadGraph [55] and the derived generator AcerMC [56]. Like MadGraph and AcerMC, many other MC generators do not have their own parton shower modelling but their output can be interfaced to programs like PYTHIA or HERWIG for this purpose.

A correct description of ISR and FSR processes is of special importance to predict the main background contributions to  $t\bar{t}H$ ,  $H \rightarrow W^+W^-$ , since for processes like  $t\bar{t}$ ,  $t\bar{t}W$  or  $t\bar{t}Z$  production, the LO calculation does not produce sufficient final state particles to mimic the signature of the signal. Since the amount of additional particles is limited by the order in perturbation theory, the prediction of backgrounds to complex final states, such as  $t\bar{t}H$ ,  $H \rightarrow W^+W^-$ , today is still very limited.

### 2.3.3 Parton shower in higher order Monte Carlo generators

The partons described by the parton shower algorithms are usually produced at low transverse momentum  $p_T$ . If a more accurate description of extra partons with high  $p_T$  is required, dedicated generators, e.g. the generator ALPGEN [57] can be used. It generates also the physical real emissions that occur in higher orders of perturbation theory, though without performing the full higher order calculation including the virtual and collinear contributions. ALPGEN has no intrinsic parton shower algorithm, therefore the results are interfaced to HERWIG, which handles the parton shower. This requires a dedicated treatment to avoid overlap between processes described by the matrix element as well as by the parton shower. ALPGEN therefore employs the so-called “MLM matching” approach to remove overlap candidates when

running the HERWIG parton shower algorithm [58]. A jet clustering algorithm<sup>1</sup> is run on all final state partons after the parton showering and the resulting jets are matched to the hard partons from the matrix element calculation above a transverse momentum threshold, looking for a parton within a certain maximum angular distance. If all jets can be matched to one of the hard partons, the event is kept. Otherwise, extra hard jets (of the kind that should be generated by the matrix element) must have been produced by the parton shower and the event is rejected (“exclusive production mode”). In one run of the program, ALPGEN generates events with a single number of additional partons. Therefore, several datasets, each with another number of additional partons produced in exclusive mode, have to be analysed together to cover the full final state. The dataset with the largest number of additional matrix element partons is generated in the “inclusive production mode”, which means that additional jets from the parton shower are accepted to allow at least for partial coverage of the higher multiplicities.

Parton shower matching is also an issue for the MC@NLO generator, which was developed to treat matrix elements and parton showers up to NLO in combination with the HERWIG parton showering routines. The exact implementation of the matching in MC@NLO depends on the considered process.

### 2.3.4 Particle Decays

The decays of the unstable particles produced in the hard scattering process or in the parton shower are simulated in a separate step of the event generation. Most programs treat the decays with simple probabilistic approaches, based on the decay widths as calculated with the known coupling constants or from measurements in experiments. For some applications this approximation is not sufficient and it is necessary to take also the decay matrix element and spin correlations into account by the use of dedicated programs. Examples of such programs are TAUOLA [59] for the decays of  $\tau$  leptons, or PHOTOS [60] for the treatment of QED radiative corrections to different kinds of particle decays.

### 2.3.5 Hadronization

In the final step of the event generation, the partons must be transferred into colour-neutral stable final state hadrons. Hadronization processes are soft, therefore they also cannot be treated perturbatively. As for the description of the partons in the proton, phenomenological models must alternatively be used, with the parameters optimized to match the behaviour of experimental data. A common model for hadronization processes is the “string model” [61] as implemented in PYTHIA. It treats quark–anti-quark pairs as connected by a colour string, which acquires more and more potential energy as the quarks move apart. As soon as a maximum energy is reached the string breaks apart, generating another quark–anti-quark pair. Gluons are treated as kinks in the strings. Another approach are “cluster models” as employed by HERWIG. These models start from large colour-neutral parton clusters, which subsequently decay into observable hadrons. Both approaches assume a mostly independent hadronization process, which is not influenced significantly by the perturbative processes. The parameters of the models can therefore be obtained in experiments performed at lower energies and then be applied in predictions of processes at other experiments, like those at the LHC.

<sup>1</sup>Jets, i.e. the sum of all tracks belonging to the bundle and their complete energy deposit in the detector, are reconstructed in so-called “clustering” algorithms as described in Section 3.3.4 of the next chapter.

### 2.3.6 Underlying event and multiple interactions

The coloured remnants of the interacting protons are also subject to fragmentation and hadronization processes and lead to the production of additional hadrons, referred to as the “underlying event”. Furthermore, it is improbable that in a proton–proton collision only one parton per proton interacts, which gives rise to the so-called “multiple interactions”. Both processes usually occur at very low transverse momenta and can therefore not be treated perturbatively and must be described by phenomenological models based on experimental results. Routines describing the underlying event are implemented e.g. in PYTHIA or are treated by dedicated programs like JIMMY [62], which is usually used together with HERWIG. Since the current knowledge on such processes is obtained in collider experiments at lower energies than the LHC, substantial uncertainties arise from the extrapolation to the LHC operation conditions.

### 2.3.7 Pile-up

At luminosities like those at the LHC, the proton densities in the bunches will be so high, that more than one proton–proton interaction is expected per bunch-crossing. The interesting hard scattering events will therefore always be accompanied by a couple of so-called “minimum-bias” events, which mainly result from low  $p_T$  inelastic proton–proton scattering processes<sup>2</sup>. These events must be taken into account when generating MC datasets, because they produce particles that are recorded together with the products of the hard scattering event and can spoil the sought-for signatures. All non-single diffractive inelastic contributions are included in the ATLAS pile-up simulation, assuming an integrated cross section of about 65 mb as provided by PYTHIA [49]. An average of up to 23 minimum-bias events are expected per bunch crossing at the LHC when operating at the highest scheduled luminosity.

---

<sup>2</sup>This is the so-called “in-time” pile-up. In the experiment also the “out-of-time” pile-up plays a role, caused by the delayed detector response to the products of interactions in previous bunch-crossings. This is, however, not considered by the MC samples used in this thesis.



## 3 The ATLAS experiment at the LHC

The Large Hadron Collider (LHC) is the to-date largest and highest energy particle accelerator and collider, hosted at the particle physics laboratory CERN near Geneva. Hadron–hadron collisions are studied in four large experiments distributed around the LHC collider ring. The two largest of them are the ATLAS<sup>1</sup> and CMS<sup>2</sup> multi-purpose experiments, which are designed to detect so far undiscovered particles, with the search for the Higgs boson being one of the most important goals. Other searches include e.g. supersymmetry, heavy gauge bosons ( $W'$  and  $Z'$ ) or the signatures of extra dimensions. The LHCb experiment is dedicated to the study of  $b$ -hadrons and  $CP$  violation in hadron decays. The aim of the ALICE<sup>3</sup> experiment is to understand the behaviour of strongly interacting matter at extremely high temperatures and densities.

In the following, the most important aspects of the LHC and the design of the ATLAS experiment as well as the reconstruction of particles in ATLAS and the description of the detector in Monte Carlo simulations are summarized. Detailed descriptions of the layout and performance of the LHC and the ATLAS experiment have been published in Refs. [63] and [64], respectively. The object reconstruction in ATLAS is extensively discussed in Ref. [28]. The text in this chapter follows these references, unless others are given in the text.

### 3.1 Large Hadron Collider

The LHC is a two-ring superconducting hadron accelerator, installed in a 26.7 km long tunnel, 45 m to 170 m deep underground near Geneva. Proton–proton collisions are planned at a centre-of-mass energy of  $\sqrt{s} = 14$  TeV at a design luminosity of up to  $10^{34}$  cm<sup>-2</sup>s<sup>-1</sup>. The first beam was circulated in the machine in September 2008. Then, a one-year shutdown was caused by a failure of an electrical connection, which led to major damages to further parts of the accelerator. Operation was resumed in autumn 2009, when the first particle collisions occurred at 450 GeV. Since then, the centre-of-mass energy of the proton–proton collisions was raised to the 7 TeV of the current first phase of the physics research programme of the LHC, which started in March 2010. Up to now, almost  $4\text{fb}^{-1}$  of proton–proton collisions have been recorded at this centre-of-mass energy by the ATLAS and CMS experiments. The increase of the integrated luminosity recorded by the ATLAS experiment in 2011 up to now is illustrated in Fig. 3.1(a). Figure 3.1(b) shows the peak luminosities reached during the same period.

In addition to the proton programme, the LHC is also capable to collide lead ions, which is done in dedicated lead ion runs. These particularly serve the physics programme of the ALICE experiment. Therefore, the lead ion run mode is not further discussed here. In the following, the original proton-run design scenario is described, as it is the basis of the studies in this thesis. An overview of the most important operation parameters of the LHC in the proton run design scenario is given in Table 3.1.

---

<sup>1</sup>Short for “A Toroidal LHC ApparatuS”.

<sup>2</sup>Short for “Compact Muon Solenoid”.

<sup>3</sup>Sort for “A Large Ion Collider Experiment”.

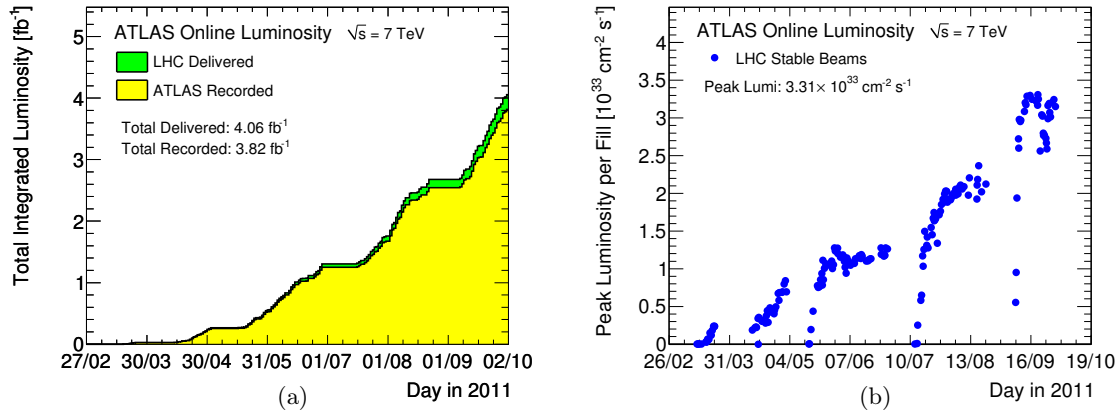


**Figure 3.1:** (a) Cumulative luminosity versus day delivered to and recorded by the ATLAS experiment during stable beams and for proton–proton collisions at 7 TeV centre-of-mass energy in 2011. (b) Maximum instantaneous luminosity versus day delivered to ATLAS during stable beam periods (taken from Ref. [65]).

Circumference	26.659 km
Centre-of-mass energy	14 TeV
Relativistic $\gamma$ factor	7461
Beam injection energy	450 GeV
Maximum design luminosity	$10^{34} \text{ cm}^{-2} \text{ s}^{-1}$
Number of turns per second	11 245
Number of bunches per beam	2808
Bunch length at collision	1.06 ns
Normalized RMS transverse emittance	$3.75 \mu\text{m}$
Bunch spacing	24.95 ns
Protons per bunch	$1.15 \cdot 10^{11}$
Beam current	0.584 A
Stored beam energy	362 MJ
Synchrotron radiation loss per turn	7 keV
Total number of magnets	9593
Number of main dipole magnets	1232
Dipole field strength	8.33 T
Dipole operating temperature	1.9 K
Magnet current	11.85 kA
Number of main quadrupole magnets	392
Number of RF cavities per beam	8
Electric field gradient in cavities	5 MV/m

**Table 3.1:** Overview of the design parameters of the LHC in the proton–proton collision mode (numbers taken from Refs. [63, 66]).

In the LHC design state, the proton-beams are circulated in 2808 “bunches” of about  $10^{11}$  protons and with roughly  $7 \mu\text{m}$  diameter, each. The spatial bunch spacing is about 7.5 cm, corresponding to a time distance of 25 ns. The high energy hadrons are kept on track by the 8.3 T magnetic field of more than 1200 superconducting dipole magnets, each about 15 m long. The magnets consist of two sets of coils and beam channels within the same mechanical structure and cryostat, thus integrating the opposite fields for the counter-rotating hadron beams in one dipole design. They are cooled down to less than 2 K by a liquid-helium cryogenic system. The beams are brought to collision at four places, where the

four experiments ATLAS, CMS, LHCb and ALICE are situated in underground caverns as illustrated in Fig. 3.2. A total of almost 400 quadrupole magnets of 5 m to 7 m length are used to focus the proton bunches before the collisions. These occur under a small angle of up to  $200 \mu\text{rad}$  to avoid long-range bunch interactions in the common beam pipe regions near the interaction points, which otherwise lead to a dilution of the beam and cause background in the detectors. The LHC is operated in “fills”, starting with the acceleration of protons in the CERN accelerator complex up to 450 GeV, where they are injected into the LHC. There they are accelerated up to their target energy of 7 TeV within about 20 minutes. The acceleration is facilitated by eight superconducting radio frequency cavities around the LHC ring, each with a field gradient of 5 MV/m. After reaching the nominal beam energy, the cavities compensate the loss of beam energy through synchrotron radiation. The intensity of the beam decreases with time and the period within which physics data are taken lasts for about 10 hours. After that, the beam is dumped on some absorber and the next fill is prepared.

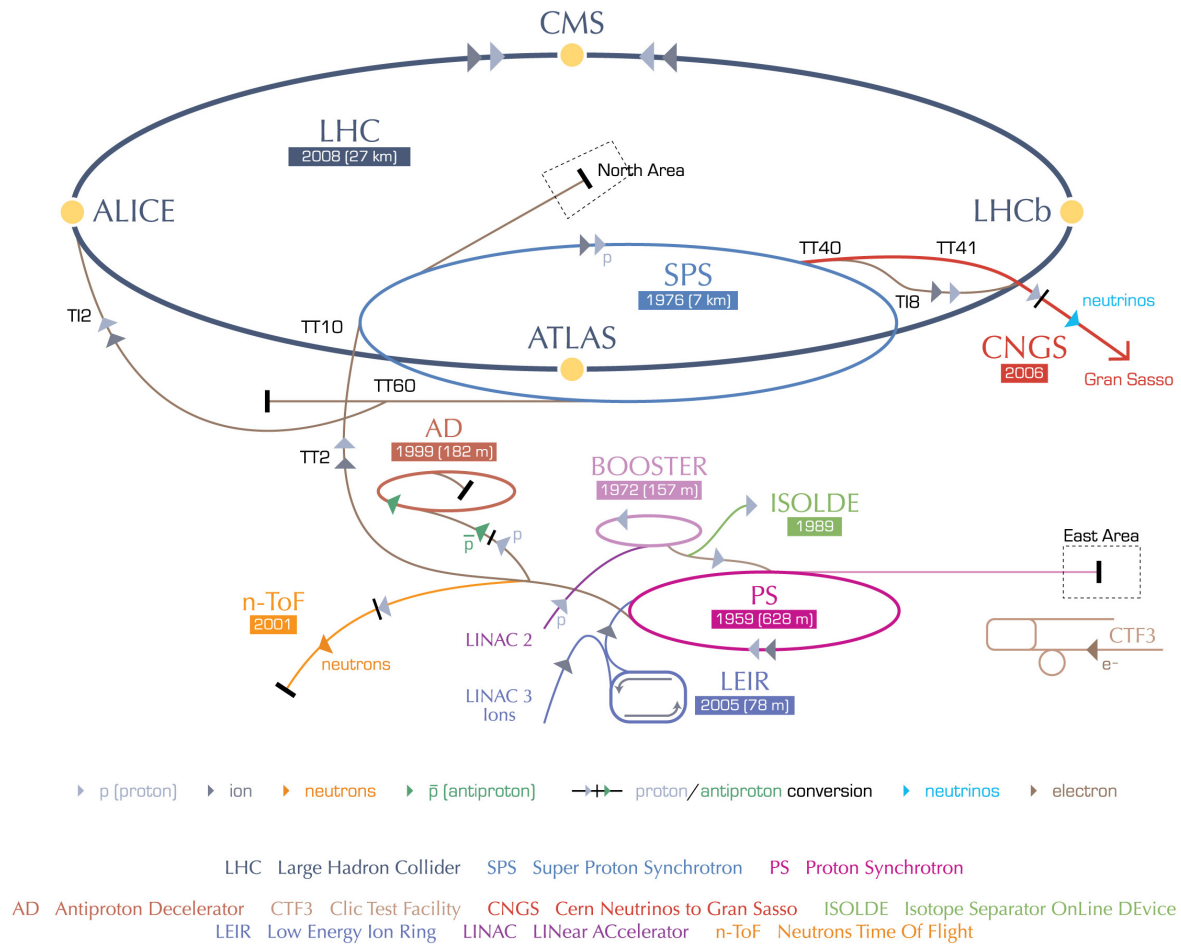


**Figure 3.2:** Schematic view of the CERN accelerator complex and the positions of the four large LHC experiments at the beam crossing points (taken from Ref. [67]).

## 3.2 The ATLAS experiment

The ATLAS experiment is one of the two multi-purpose experiments at the LHC, designed for the search for a variety of physics processes. Figure 3.3 illustrates the range of the cross

sections and the production rates for some important processes at the LHC. The experiments have to cope with a large number of more than  $5 \cdot 10^7$  inelastic scattering events per second at the design luminosity of  $10^{33} \text{ cm}^{-2} \text{ s}^{-1}$  in the first data taking phase, most of them being low- $p_T$  minimum-bias processes. The production of  $W$  and  $Z$  bosons is expected at a rate of about 100 per second. Higgs bosons are produced at rates another four to five orders of magnitude lower, depending on the Higgs boson mass. These rare events need to be filtered out of the overwhelmingly large background of uninteresting collisions. The LHC experiments are therefore required to be fast in processing the data and fast decisions are needed on whether an event is worth storing or not. At the same time, an exact and efficient reconstruction of the leptons and jets in the events of interest is needed to separate them from background processes. Finally, a largest possible coverage of the detector in the pseudorapidity  $\eta$  and full coverage in the azimuthal angle  $\phi$  are required<sup>4</sup>, to reconstruct the full event and ensure a precise reconstruction of the missing energy  $\cancel{E}_T$ .

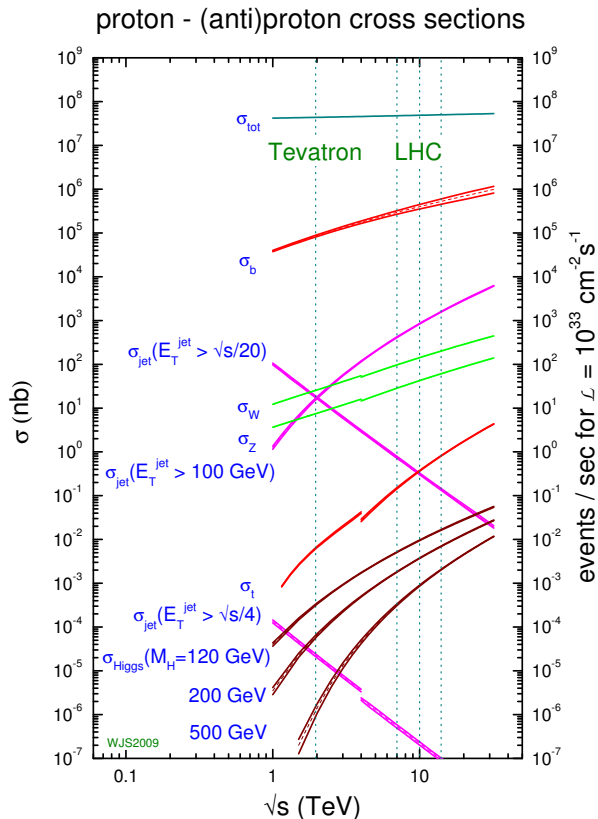


**Figure 3.3:** Cross sections (left axis) and production rates at an instantaneous luminosity  $L=10^{33} \text{ cm}^{-2} \text{ s}^{-1}$  (right axis) for some important processes in inelastic proton–anti-proton (low  $\sqrt{s}$  region) and proton–proton collisions (high  $\sqrt{s}$  region) as a function of the centre-of-mass energy  $\sqrt{s}$ . The dotted lines indicate the Tevatron proton–anti-proton collision centre-of-mass energy of 1.96 TeV and the LHC proton–proton collision energies of 7 TeV, 10 TeV and 14 TeV (taken from Ref. [48]).

To meet these requirements, the ATLAS detector is designed in the typical forward–backward symmetric onion-like setup of hermetic particle detectors, consisting of layers of

<sup>4</sup>The following coordinate definitions are used throughout this thesis: The beam direction defines the  $z$  axis. The polar angle  $\theta$  and the azimuthal angle  $\phi$  are measured with respect to this axis. The coordinate  $R$  gives the distance from the beam axis in the  $x - y$  plane perpendicular to the beam axis. The “pseudorapidity”  $\eta$  is defined as  $\eta \equiv -\ln(\tan(\theta/2))$  and the transverse momentum  $p_T$  is the projection of the momentum into the  $x - y$  plane.

tracking detectors, calorimeters and muon trackers, as displayed in Fig. 3.4. The ATLAS detector is 25 m high and 44 m long, with an overall weight of approximately 7000 t. A special design feature is its two-part magnet system: A thin superconducting solenoid surrounds the Inner Detector cavity and provides the bending power needed for momentum and charge measurements in the innermost part of the detector. The magnetic field for the muon system in the outermost detector region is generated by three large superconducting air-core toroids. The toroids, as well as most of the detector components are designed as a cylindrical “barrel” around the interaction point, complemented by two “endcaps” covering the higher  $|\eta|$ -regions. The individual detector parts are described in more detail in the following.

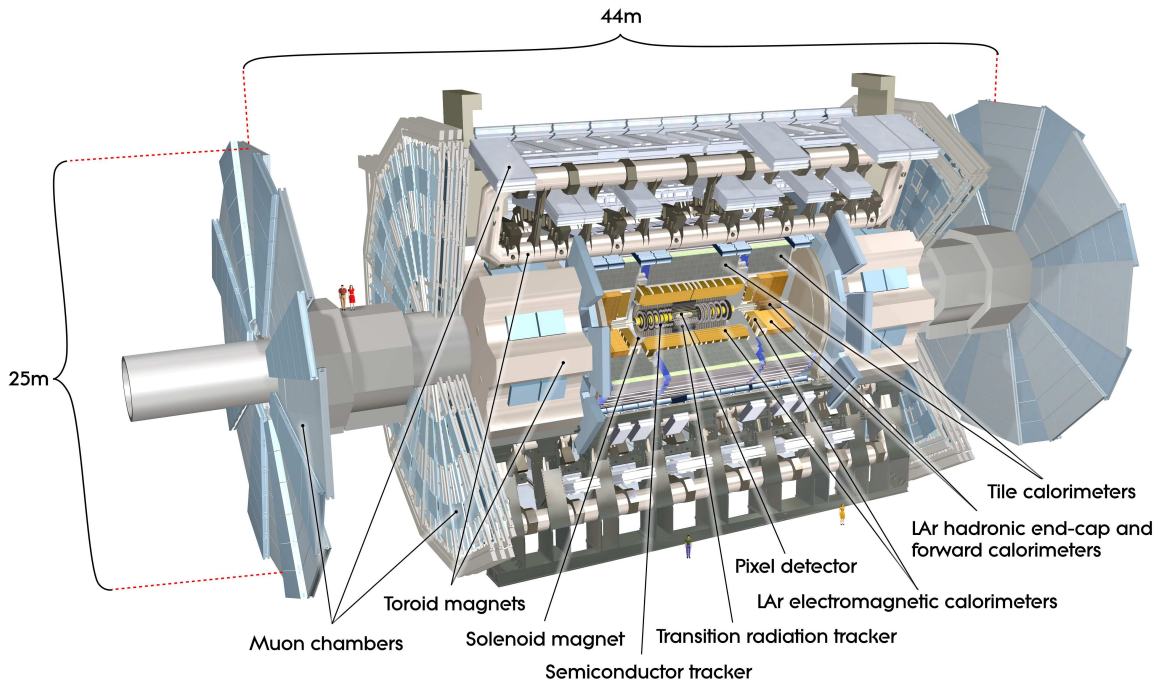


**Figure 3.4:** Cut-away view of the ATLAS detector (taken from Ref. [64]).

### 3.2.1 Inner Detector

The Inner Detector (ID) is the innermost part of the ATLAS detector, immersed in the 2 T field of the solenoid magnet. The overall ID has a diameter of 2.3 m, is 7 m long and comprises three subdetectors with decreasing spatial resolution, as illustrated in Fig. 3.5. At inner radii, silicon pixel layers and the stereo pairs of silicon microstrip sensors of the Semiconductor Tracking detector (SCT) provide high resolution measurements of track segments. At larger radii, the transition radiation tracker (TRT) consists of many layers of gaseous straw tube elements, interleaved with transition radiation material.

#### Pixel detector

To achieve the highest possible granularity, the Inner Detector component closest to the interaction point is a silicon pixel detector. As illustrated in Fig. 3.6, the pixel detector consists of a barrel region with three layers of pixel detectors arranged on concentric cylinders around the beam axis. In addition, two endcaps, each consisting of three disks perpendicular to the

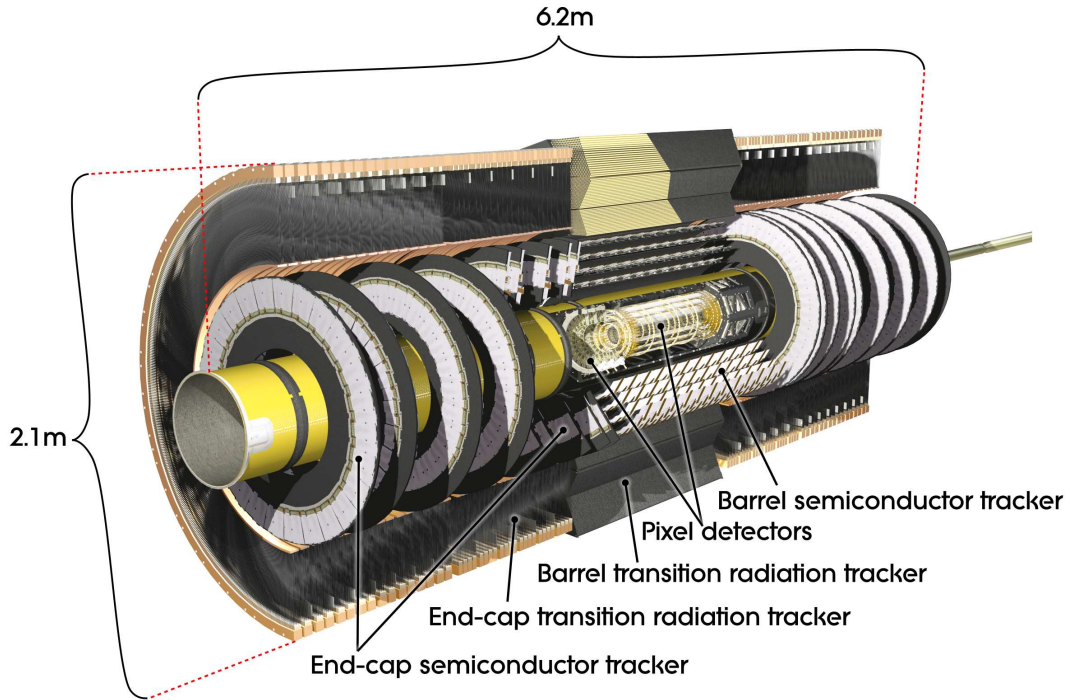


**Figure 3.5:** Cut-away view of the ATLAS Inner Detector (taken from Ref. [64]).

beam axis, cover the larger  $\eta$  region. The detector layers are arranged such, that each charged track originating from the interaction region crosses three pixel layers and hence causes three hits. The innermost barrel layer, the so-called “*b*-layer”, is installed only 50.5 mm away from the beam axis and thus as close as possible to the interaction point to guarantee optimal impact parameter resolution. The pixel detector is equipped with 1744 identical rectangular sensors with a minimum pixel size in  $R\phi \times z$  ( $R\phi \times R$  in the endcaps) of  $(50 \times 400) \mu\text{m}^2$ . The intrinsic accuracies<sup>5</sup> obtained with this design are  $(10 \times 115) \mu\text{m}$  in  $R\phi \times z$  in the barrel and in  $R\phi \times R$  in the endcaps. The third coordinate ( $R$  in the barrel and  $z$  in the endcaps) is determined by the position of the detector layer itself. The sensors are  $250 \mu\text{m}$  thick, using oxygenated  $n$ -type wafers with readout pixels on the  $n^+$ -implanted side of the detector. This guarantees good charge-collection efficiency after the type inversion caused by heavy irradiation<sup>6</sup>. The oxygenation increases the radiation tolerance to charged hadrons, thus improving the charge collection efficiency and requiring lower depletion voltages after the type inversion. To maintain an adequate noise performance, to reduce the leakage currents and to contain the annealing effects after radiation damage, the pixel detector modules are operated at temperatures below  $-10^\circ\text{C}$ . The detector is read out in pseudo-analogue read-out mode, with a total of approximately 80.4 million readout channels.

### Semi-conductor tracker

The ATLAS SCT barrel region consists of four cylindrical layers, equipped with 8448 identical rectangular single-sided  $p^+$ -in- $n^-$  silicon-strip sensors. Each endcap consists of nine disks,

<sup>5</sup>This is the precision for a measurement of a single space point. Better accuracies are achieved, if several hits are combined to form a track as explained in Section 3.3.1.

<sup>6</sup>Radiation damage in silicon detectors, as well as the phenomena of type inversion and annealing are introduced in more detail in Section 4.1.2.

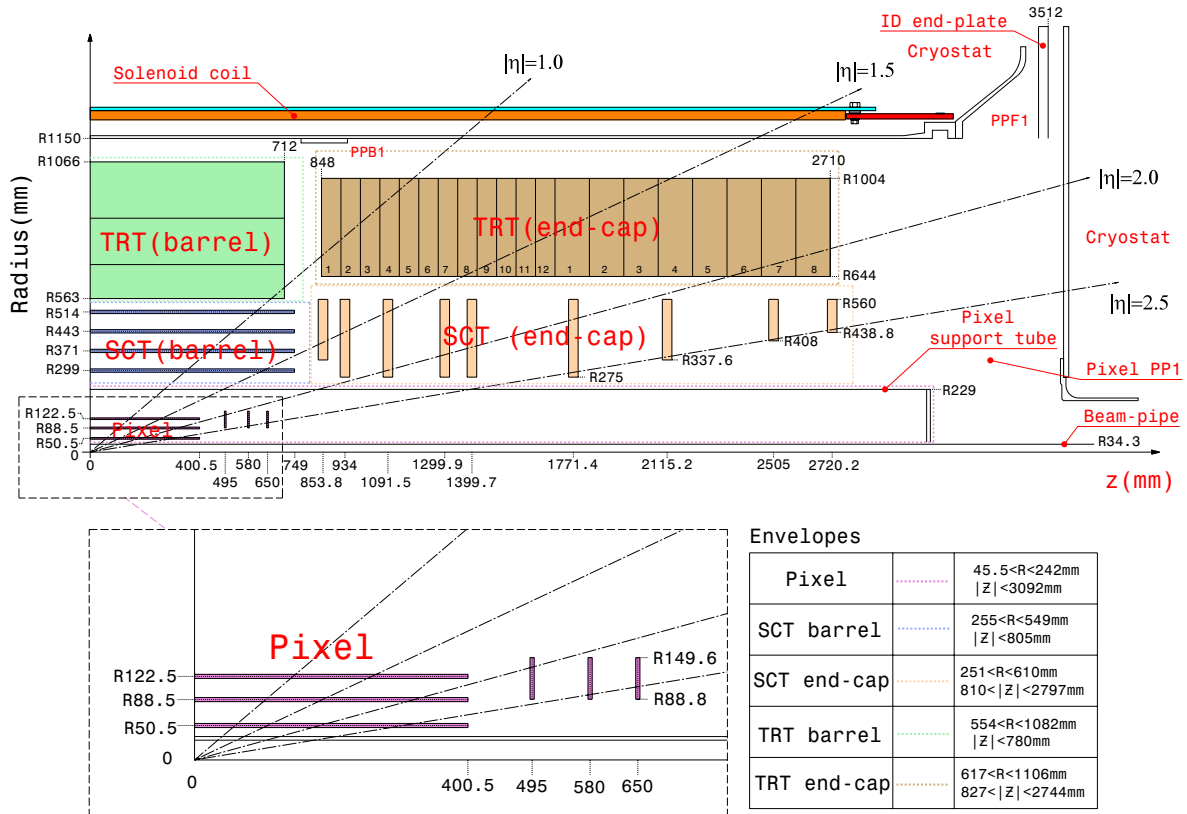


**Figure 3.6:** Plan view of a quarter-section of the ATLAS Inner Detector showing each of the major detector elements with its active dimensions and envelopes. The labels PP1, PPB1 and PPF1 indicate the patch-panels for the ID services (taken from Ref. [64]).

which are arranged such that each track crosses at least four of them. The endcap disks are built from a total of 6944 wedge-shaped sensors. The sensors in the barrel and endcaps are arranged on modules, each consisting of two or four  $285 \mu\text{m}$  thick sensors, arranged in two back-to-back layers with a  $40 \text{ mrad}$  stereo angle to measure two coordinates. In the barrel, the strips in one of the sensors are arranged parallel to the beam axis, measuring the position in  $R\phi$  and  $z$ . The strip pitch is  $80 \mu\text{m}$ . In the endcap region, the detectors have a set of strips running radially, with the distance between two strips increasing with increasing  $R$  and a mean pitch of  $80 \mu\text{m}$ , thus measuring the  $R\phi$  and  $R$  coordinates. The intrinsic accuracies per module are  $17 \mu\text{m}$  in  $R\phi$  and  $580 \mu\text{m}$  in  $z$  in the barrel and  $17 \mu\text{m}$  in  $R\phi$  and  $580 \mu\text{m}$  in  $R$ -direction in the disks. Like the pixel detector, the SCT will suffer from radiation damage and will undergo type inversion after heavy irradiation and is hence operated cold. The detector is read out in binary mode, employing a total number of about 6.3 million readout channels.

Before their installation on the disks, the individual sensors were assembled, tested and characterized in the member institutes of the ATLAS SCT collaboration, among them the University of Freiburg. Testing the electrical functionality of the Freiburg share of SCT endcap modules was part of this thesis. An overview on these tests and their results, as well as a more detailed description of the modules are given in Chapter 4.

### Transition radiation tracker

The outermost component of the ID is the transition radiation tracker, which allows for measurements of tracks up to  $|\eta| = 2$ . The TRT is built from 4 mm polyimide straw drift tubes, filled with a gas mixture of 70% Xe, 27% CO<sub>2</sub> and 3% O<sub>2</sub>. The TRT provides only  $R\phi$  information, with an intrinsic accuracy of 130  $\mu\text{m}$  per straw. Despite this low resolution compared with that of the silicon detectors, the straw hits at the outer radius enhance the pattern recognition and contribute significantly to the momentum measurement. The lower precision per point is compensated by the large number of 36 measurements on average per track and the longer measured track length. In the barrel region, the straws are parallel to the beam axis and are 144 cm long, with their wires divided into two halves approximately at  $\eta = 0$ . In the endcap region, 37 cm long straws are arranged radially in wheels. The total number of TRT readout channels is approximately 351 000.

Apart from recording tracks of charged particles, the TRT is also designed to contribute to the electron identification in the pseudorapidity range up to  $|\eta| = 2$ , covering electron energies between 0.5 GeV and 150 GeV. For this purpose, the straw tubes in the barrel are embedded in a matrix of 19  $\mu\text{m}$ -diameter polypropylene radiator fibres. In the endcaps, the straw tubes are arranged in layers and the space between successive layers is filled with layers of 15  $\mu\text{m}$  thick polypropylene radiator foils. Particles traversing the radiator material produce transition radiation of several keV, which is preferentially emitted in forward direction and has an intensity proportional to their Lorentz factor  $\gamma = E/m$ . These low energy photons are absorbed in the high- $Z$  Xe based fill gas mixture of the straw tubes and yield much larger signal amplitudes than minimum-ionizing charged particles. Because of their smaller mass, electrons start producing a significant amount of transition radiation at much smaller momenta than hadrons and can therefore be identified by the transition radiation photons they emit. The distinction between transition radiation and tracking signals is obtained on a straw-by-straw basis, using different low and high thresholds in the front-end electronics. Typically, seven to ten high-threshold hits from transition radiation are expected for electrons with energies above 2 GeV.

### Energy loss in the Inner Detector

The ID must be supplied with electronics, readout services and cooling within the detector volume, leading to a relatively massive design with an overall weight of about 4.5 t. The material distribution in the ID, expressed in terms of radiation lengths<sup>7</sup>  $X_0$  or hadronic interaction lengths  $\lambda$  is displayed in Fig. 3.7. The material in the barrel region up to  $|\eta| \approx 0.7$  represents only less than  $0.5 X_0$ . This value increases quickly up to more than  $2 X_0$  at larger pseudorapidities, with a maximum in the so-called “crack region” at  $|\eta| \approx 1.5$ . In this transition region between the barrel and the endcaps, a large fraction of the service infrastructure is located. Precise knowledge of the material distribution is important and needs to be accounted for by the tracking,  $b$ -tagging and electron identification algorithms, because it seriously influences the behaviour of particles before reaching the electromagnetic calorimeter. Many electrons lose a large fraction of their energy through bremsstrahlung and approximately 40% of all photons convert into an electron–positron pair before reaching the

<sup>7</sup>The radiation length  $X_0$  of a material is both, the mean distance over which a high-energy electron loses all but  $1/e$  of its energy by bremsstrahlung, and  $7/9$  of the mean free path to undergo conversion into an electron–positron pair by a high-energy photon [9]. The hadronic interaction length  $\lambda$  of a material is defined as the length, after which the probability for a high-energy charged hadron not to have been absorbed in an inelastic collision with a nucleus is  $1/e$ .

calorimeter. Furthermore, a significant fraction of charged pions will undergo an inelastic hadronic interaction inside the ID volume.

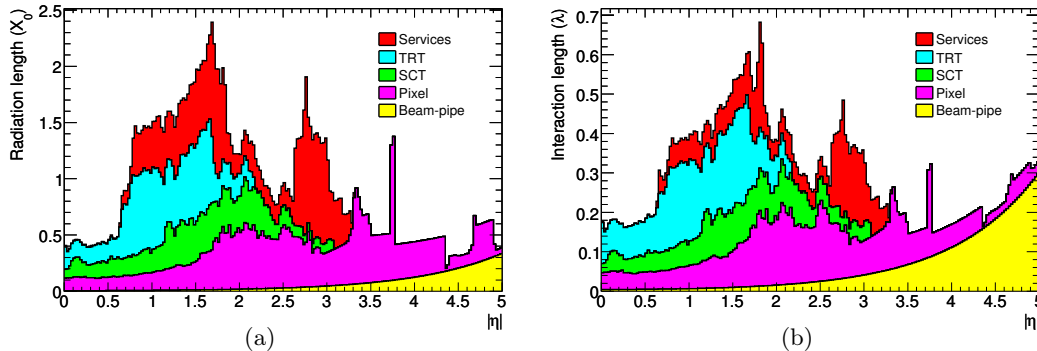


**Figure 3.7:** Material distribution expressed in units of radiation lengths  $X_0$  (a) and interaction lengths  $\lambda$  (b) at the exit of the ID envelope, including the services and thermal enclosures. The distribution is shown as a function of  $|\eta|$  and averaged over  $\phi$ . The break-downs indicate the contributions of external services and of individual subdetectors, including services in their active volume (taken from Ref. [64]).

### 3.2.2 Calorimetry

An overview on the ATLAS calorimeter system is given in Fig. 3.8. The inner part of the system is a high granularity liquid-argon (LAr) electromagnetic (EM) sampling calorimeter, consisting of a barrel and two endcap parts, which together cover the pseudorapidity range  $|\eta| < 3.2$ . The LAr calorimeter guarantees a minimum required electron and photon energy resolution<sup>8</sup> of  $\frac{\sigma_E}{E} = \frac{10\%}{\sqrt{E}} \oplus 0.7\%$ , where “ $\oplus$ ” denotes addition in quadrature and the energy is measured in GeV. The hadronic calorimeter system consists of several parts, using different technologies over the covered pseudorapidity range up to  $|\eta| = 4.9$ . The low- $|\eta|$  range up to  $|\eta| = 1.7$  is covered by a scintillator-tile calorimeter. In the endcaps, LAr technology is also used for the hadronic calorimeters. The LAr forward calorimeters at high  $|\eta|$  finally provide both, electromagnetic and hadronic energy measurements.

The fine granularity of the EM calorimeter allows for precision measurements of electrons and photons over the pseudorapidity region matched to the ID. The coarser granularity of the rest of the calorimeter is sufficient for the requirements of jet reconstruction and missing energy measurements. Calorimeters must furthermore provide good containment for electromagnetic and hadronic showers and must limit punch-through of hadrons into the muon system. The total thickness of the modules depends on their position in  $\eta$ , with a minimum depth of  $22 X_0$  in the barrel and  $24 X_0$  in the endcaps. For hadronic particles, a total of about  $9.7 \lambda$  of active material in the whole calorimeter in the barrel and  $10 \lambda$  in the endcaps guarantee a minimum energy resolution for high-energy jets of  $\frac{\sigma_E}{E} = \frac{50\%}{\sqrt{E}} \oplus 3\%$  in the barrel and endcaps and  $\frac{\sigma_E}{E} = \frac{100\%}{\sqrt{E}} \oplus 10\%$  in the forward region. The total thickness at  $|\eta| = 0$  is  $11 \lambda$ , including  $1.3 \lambda$  from the outer support.

<sup>8</sup>The resolution of an energy measurement in a calorimeter consists of a term  $\propto 1/\sqrt{E}$  describing the statistical fluctuations of the energy deposited by a particle of energy  $E$  and a constant term due to uncertainties in the calibration.

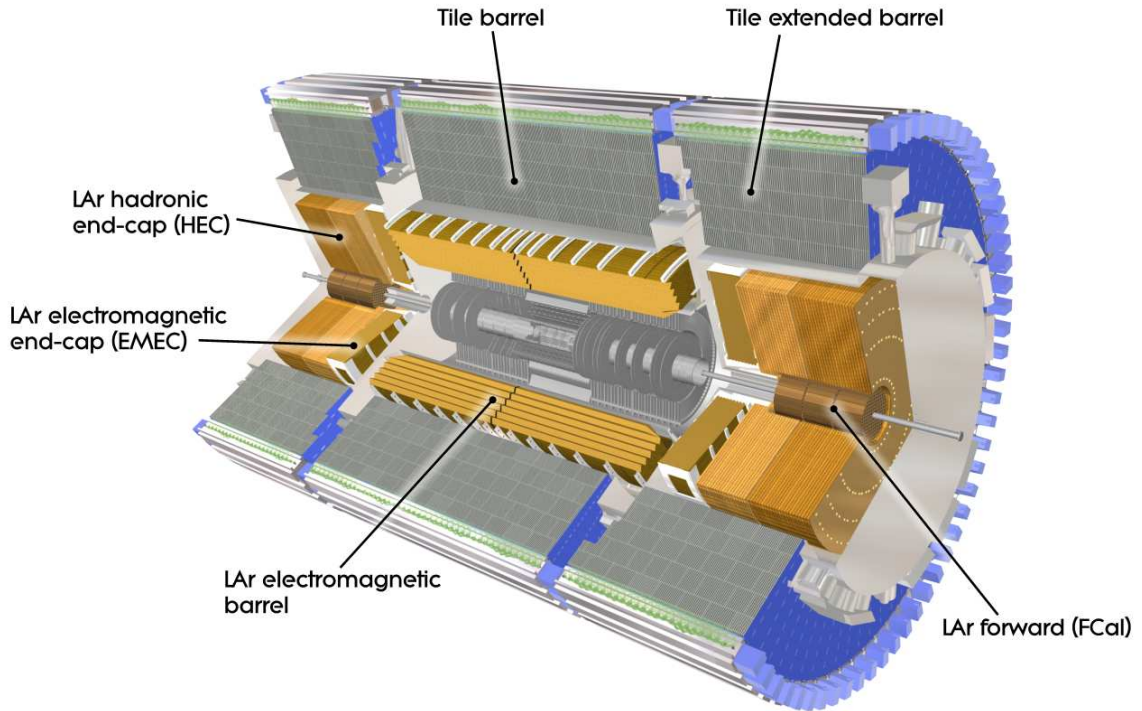
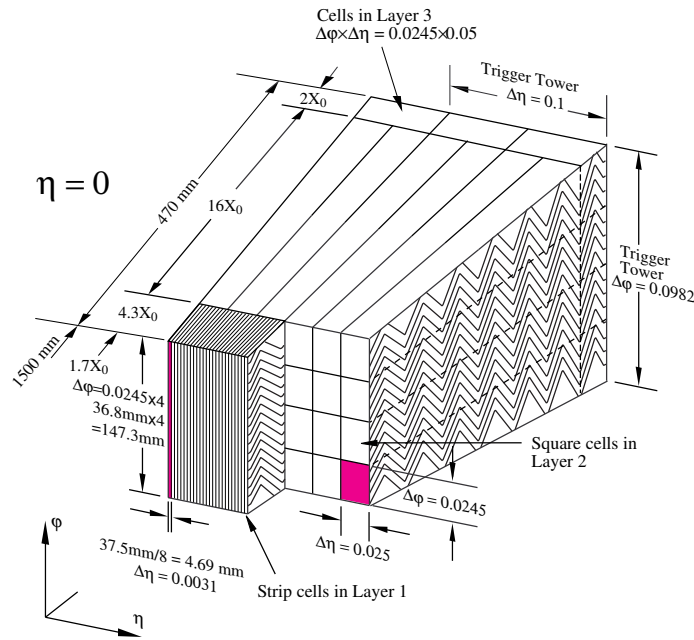


Figure 3.8: Cut-away view of the ATLAS calorimeter system (taken from Ref. [64]).

### The liquid argon electromagnetic calorimeter

The EM calorimeter is divided into a barrel part covering the range  $|\eta| < 1.475$  and two endcaps ( $1.375 < |\eta| < 3.2$ ), each housed in their own cryostat. The barrel calorimeter consists of two identical half-barrels, separated by a 4 mm gap at  $z = 0$ . Both half-barrels are divided into 16 modules, each covering a sector of  $22.5^\circ$  in  $\phi$ . The endcap calorimeters are mechanically divided into two coaxial wheels with the outer one covering the region  $1.375 < |\eta| < 2.5$  and the inner one the pseudorapidity range  $2.5 < |\eta| < 3.2$ . The EM calorimeter is a lead-LAr detector with lead absorber plates and accordion-shaped kapton electrodes, providing complete  $\phi$ -symmetry without azimuthal cracks. Over the region devoted to precision physics up to  $|\eta| = 2.5$ , the EM calorimeter is segmented in three sections in longitudinal direction. Due to its fine granularity in  $\eta$ , the first layer is referred to as the “ $\eta$ -strip layer”. It allows for a precision measurement of the structure of electromagnetic showers, enabling the separation of single photons and even close photon pairs produced in  $\pi^0$  decays. The “middle” layer has a depth of at least  $16 X_0$  and a coarser granularity and contains the main energy deposit of an EM shower. The “back” layer consists of cells with twice coarser granularity to correct for EM energy leakage into the hadronic calorimeter. A sketch of a barrel module with the individual cell dimensions is shown in Fig. 3.9.

To correct energy losses in the dead material in front of the calorimeters, the region of  $|\eta| < 1.8$  is covered by an additional separate 5 mm to 11 mm deep thin liquid-argon layer of coarser granularity in front of the active electromagnetic calorimeter and inside the barrel cryostat, the so-called “presampler”.



**Figure 3.9:** Sketch of a LAr EM calorimeter barrel module, where the different layers are visible with the ganging of the accordion-shaped electrodes in  $\phi$ . The granularity in  $\eta$  and  $\phi$  of the cells of each of the three layers and of the trigger towers is also shown (taken from Ref. [64]).

### Hadronic calorimeters

The hadronic calorimetry in the range  $|\eta| < 1.7$  is provided by a scintillator-tile sampling calorimeter (the “TileCal”), placed directly outside the EM calorimeter envelope. It consists of a large barrel, covering the region  $|\eta| < 1$  and two smaller extended barrel cylinders in the range  $0.8 < |\eta| < 1$  on either side of the central barrel. Stacks of steel plates are used as the absorber and 3 mm thick polystyrene scintillator tiles serve as the active material. The two sides of the scintillating tiles are read out into two separate photomultiplier tubes by wavelength shifting fibres. The tile calorimeter extends from an inner radius of 2.28 m to an outer radius of 4.25 m. It is segmented in depth in three layers, approximately  $1.5 \lambda$ ,  $4.1 \lambda$  and  $1.8 \lambda$  deep in the barrel and  $1.5 \lambda$ ,  $2.6 \lambda$  and  $3.3 \lambda$  in the extended barrel. The total thickness of the TileCal is  $9.7 \lambda$  at  $\eta = 0$ .

The hadronic calorimetry is extended to larger pseudorapidities up to  $|\eta| = 4.9$  by the LAr Hadronic Endcap Calorimeter (HEC) and the Forward Calorimeter (FCal). The HEC is the inner wheel part of the EM endcap calorimeter described above. It consists of two independent wheels per endcap, each divided into two segments in depth, for a total of four layers per endcap. The wheels are built from 25 mm to 50 mm thick parallel copper plates, interleaved with 8.5 mm LAr gaps. The FCal consists of three modules in each endcap. The first, made of copper, is optimized for electromagnetic measurements, whereas the other two, made of tungsten, are better suited to measure the energy of hadronic particles. Again, liquid argon serves as the sensitive medium. The total depth of the forward calorimeter is approximately ten interaction lengths.

### 3.2.3 Muon spectrometer

The outermost part of the ATLAS detector is the muon spectrometer, built to detect charged particles traversing the calorimeters and to measure their momentum in the pseudorapidity range up to  $|\eta| = 2.7$ . Except for some rare punch-throughs, muons are the only kind of charged particles that do not lose their complete energy in the calorimeter and can be detected in the muon system. This unique characteristic can be exploited for a clean muon identification and reconstruction. The muon spectrometer allows muons to be reconstructed on a stand-alone basis, i.e. without ID information. The system is designed to provide a stand-alone transverse momentum resolution of approximately 10% for 1 TeV tracks and good momentum resolution and charge identification up to muon momenta around 3 TeV. Since many of the interesting processes at the LHC contain high energy leptons, the almost unambiguous signature of the muons in the muon system can also be used to “trigger” on, i.e. for a fast online decision, if the event is of interest and should be recorded or not. The muon system consists therefore not only of precision tracking chambers, but also of fast detectors with smaller resolution, dedicated to the triggering of muons with a timing resolution faster than 4 ns.

The layout of the muon spectrometer is shown in Fig. 3.10. The toroid magnets bend the muon tracks in the  $R - z$  plane. A large barrel toroid generates field strengths up to 2.5 T in the range  $|\eta| < 1.4$ . Within  $1.6 < |\eta| < 2.7$ , muon tracks are deflected by two smaller endcap magnets of up to 3.5 T strength, inserted into both ends of the barrel toroid. Magnetic deflection between these pseudorapidity ranges is provided by a combination of the barrel and endcap fields. The total toroid system is 25.3 m long, with inner and outer diameters of 9.4 m and 20.1 m, respectively. The chambers in the barrel are arranged in three layers at radii of approximately 5 m, 7.5 m and 10 m around the beam axis. In the transition and endcap regions, muon chambers in the form of large wheels are installed perpendicularly to the  $z$ -axis at distances of about  $|z| = 7.4$  m, 10.8 m, 14 m and 21.5 m from the interaction point. The coverage with muon chambers is intercepted by a gap for the services to the solenoid magnet in the centre of the detector ( $|\eta| \approx 0$ ). Additional gaps in the acceptance are caused by the detector support structure at the bottom of the detector. The muon reconstruction efficiency and momentum resolution are significantly reduced in these gap regions.

Monitored Drift Tubes (MDTs) allow for precision measurements of the muon track coordinates in the  $R - z$  plane up to  $|\eta| = 2.7$ . They consist of three to eight layers of pressurized drift tubes of approximately 3 cm diameter, operated with an 93:7 Ar:CO<sub>2</sub> gas mixture at 3 bar pressure. The average resolution is 80  $\mu\text{m}$  per tube, or about 35  $\mu\text{m}$  per chamber. The innermost MDT plane in the barrel wheels ( $2 < |\eta| < 2.7$ ) is replaced by Cathode Strip Chambers (CSCs) with higher granularity, i.e. multi-wire proportional chambers with cathodes segmented into strips. Their resolution is 40  $\mu\text{m}$  in the bending plane and about 5 mm in the transverse plane. To preserve the high track parameter resolution of the muon system, the locations of MDT wires and CSC strips must be known with an accuracy better than 30  $\mu\text{m}$ . This is guaranteed by a combination of precision mechanical assembly techniques and optical alignment systems.

The trigger system covers the pseudorapidity range up to  $|\eta| = 2.4$ . The barrel region is equipped with Resistive Plate Chambers (RPCs) and the endcaps are equipped with Thin Gap Chambers (TGCs). The trigger chambers do not only provide fast trigger information, but contribute also to the precision track measurement, providing an additional coordinate in the direction perpendicular to the plane determined by the MDTs and CSCs.

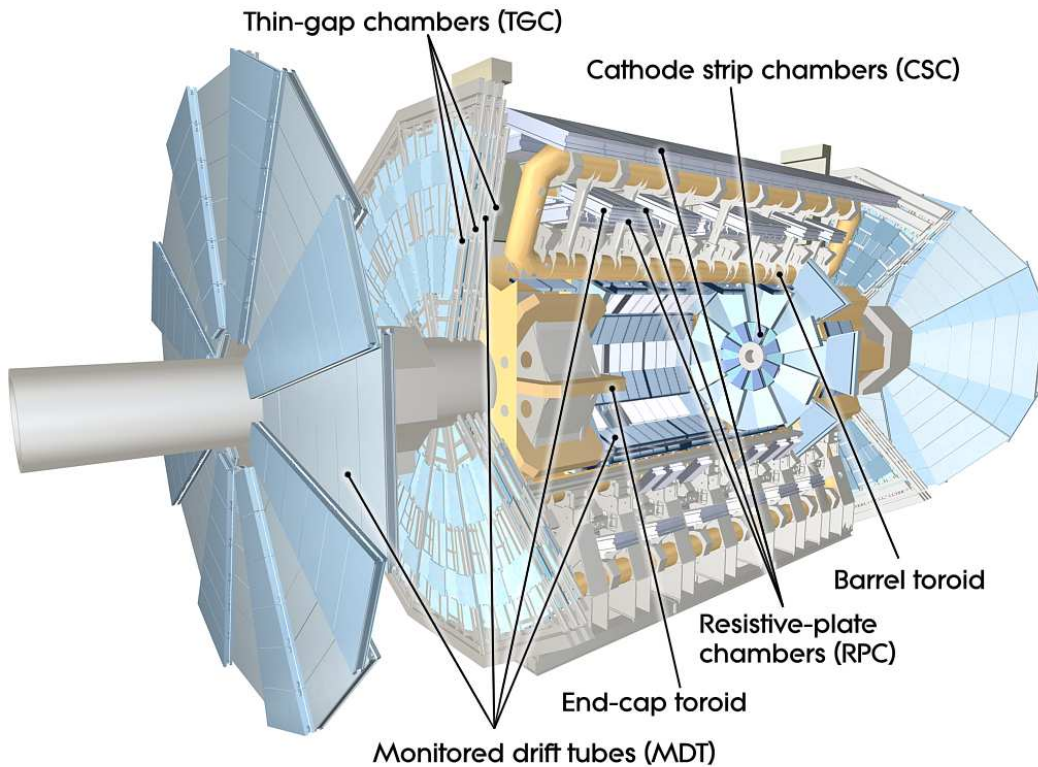


Figure 3.10: Cut-away view of the ATLAS muon system (taken from Ref. [64]).

### 3.2.4 Forward detectors

Three smaller detector systems cover the ATLAS forward region close to the beamline. LUCID<sup>9</sup> detects inelastic proton–proton scattering at a distance in  $z$ -direction of  $\pm 17$  m from the interaction point, thus providing online-monitoring of the relative luminosity. Also the ALFA<sup>10</sup> detector at  $z = \pm 240$  m is dedicated to luminosity measurements. It consists of scintillating fibre trackers placed inside Roman pots only 1 mm away from the beam. Finally, the Zero-Degree Calorimeter (ZDC) is installed at  $z = \pm 140$  m to measure the centrality of heavy-ion collisions. It consists of layers of alternating quartz rods and tungsten plates to detect neutral particles at pseudorapidities up to  $|\eta| = 8.2$ .

### 3.2.5 Trigger system and data flow

With the high event rates at the LHC it will be impossible to record the data from every bunch crossing for the offline-analyses. The ATLAS experiment is therefore equipped with a three-stage trigger system to decide if an event is of interest and should be recorded or not. This system consists of the fast online “Level-1” (L1) selection stage and an offline High Level Trigger (HLT), consisting of the “Level-2” (L2) and Event Filter (EF) stages. The scheduled proton–proton interaction rate at the maximum design luminosity of  $10^{34} \text{ cm}^{-2}\text{s}^{-1}$  is approximately 1 GHz, which requires an overall rejection factor of  $5 \cdot 10^6$  against minimum-bias processes to reduce the data rate to the processable limit of about 200 Hz. Since trigger

<sup>9</sup>Short for “Luminosity measurement using Cerenkov Integrating Detector”.

<sup>10</sup>Short for “Absolute Luminosity For ATLAS”.

decisions must be made every 25 ns, the system is required to be fast. A schematic view of the trigger system and data flow in ATLAS is given in Fig. 3.11.

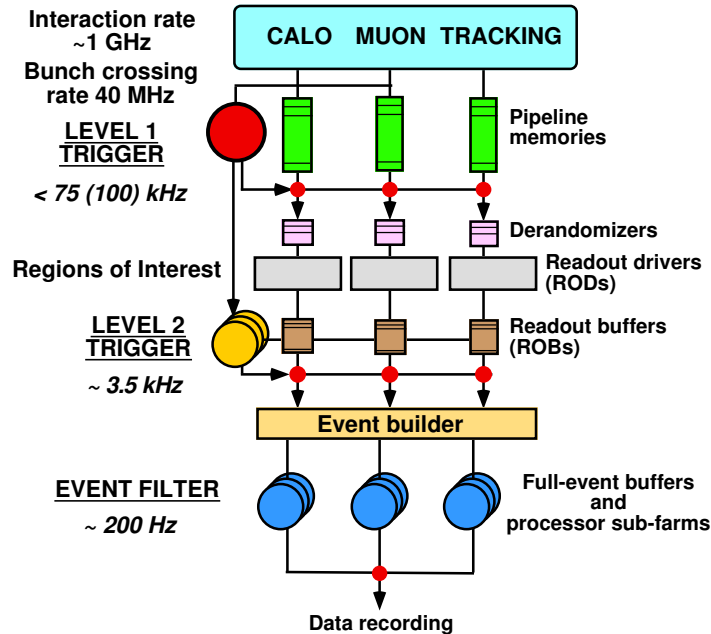


**Figure 3.11:** Schematic view of the ATLAS trigger system and data flow (taken from Ref. [68], with numbers updated from Ref. [64]).

The L1 trigger searches for signatures from high- $p_T$  muons, electrons and photons, jets and  $\tau$ -leptons decaying into hadrons. It also selects events with large missing transverse energy  $\cancel{E}_T$  and a large total transverse energy. These particles and energies are reconstructed on the basis of reduced-granularity information from a subset of detectors, among them the RPCs and TPCs of the muon system and all calorimeter subsystems. Inner Detector measurements are not used at this stage. A trigger signal is issued, if candidates of the above mentioned objects are found, passing certain  $p_T$  or energy thresholds. The information on the reconstructed objects is then passed to the HLT. To keep the L1 trigger as fast as possible, it is implemented on custom-made electronics. The L1 decision must reach the front-end electronics within  $2.5 \mu\text{s}$  after the bunch-crossing to which it is associated. Until then, the data are time-stamped and buffered in pipeline-memories on detector-specific readout electronics. The maximum L1 rate that the detector readout systems can handle is 75 kHz (upgradeable to 100 kHz).

The HLT is almost entirely based on commercially available computers and networking hardware. At both stages, the algorithms use the full granularity and precision of calorimeter and muon chamber data, as well as the measurements in the Inner Detector to refine the trigger selections. To keep the L2 trigger fast, it is seeded by so-called “regions of interest” (RoIs), in which the L1 trigger has identified possible trigger objects. The L2 trigger reduces the event rate to less than 3.5 kHz, with an average event processing time of approximately 40 ms. The Event Filter uses offline analyses of the full events to reduce the event rate to about 200 Hz, which can be recorded for subsequent offline analysis. The average event processing time is about four seconds.

The intermediate buffering and the distribution of the data is handled by the Data Acquisition system (DAQ). It receives and buffers the data from the detectors at the L1 trigger rate. Data requested by the L2 trigger are then transmitted to the HLT trigger stage. Event build-

ing is performed for the events passing the L2 trigger and the events are passed to the Event Filter. The events selected by the EF are written to permanent event storage in the CERN computer centre. Another copy of these raw data is stored in one of the ten ATLAS Tier-1 grid centres outside CERN to prevent data loss. The raw data are later processed by higher level event reconstruction algorithms and provided in different formats optimized for fast and efficient user-specific analyses. In addition to controlling the distribution of the data, the DAQ system provides the configuration, control and monitoring of the ATLAS detector during data taking. In contrast, the detector hardware, including the gas systems, power-supply voltages, etc., is separately controlled by the so-called “Detector Control System” (DCS).

### 3.3 Event reconstruction and ATLAS detector simulation

The basis for physics analyses of ATLAS data is the reconstruction and identification of physics objects from the detector information, i.e. from the electronic signals provided by the read-out electronics. This includes the reconstruction of tracks and “vertices”, i.e. the common origin of certain sets of tracks, from Inner Detector information. The reconstruction of jets, photons, electrons and  $\tau$ -leptons is based on tracking information combined with the energy deposits measured in the calorimeters. Electrons and photons generate similar shower shapes in the calorimeter and are therefore reconstructed by common software tools. Tracking information is furthermore used in the classification of jets according to their origin either from heavy quarks or from light quarks and gluons. Muons are reconstructed, combining track measurements in the ID and the muon system. Finally, the balance of the transverse momenta and energy deposits is exploited to reconstruct the missing  $p_T$ -sum and the missing energy. This allows the transverse momentum of all invisible particles in the event to be determined, i.e. neutrinos and stable, uncharged new physics particles<sup>11</sup>.

The offline analyses of ATLAS data and the reconstruction of physics objects from the detector signals as well as the generation of Monte Carlo datasets are performed with a dedicated software framework called “Athena” [69]. Athena is written in C++, using the C++ based CERN data analysis framework ROOT [70], and steered by scripts in Python. The framework is written and maintained by the ATLAS collaboration and issued in different releases. If not otherwise stated, the studies in this thesis are performed with Athena release 12. The basic aspects of the physics object reconstruction as available in Athena 12 and the detector simulation are summarized from Ref. [28] in the following<sup>12</sup>.

#### 3.3.1 Track reconstruction and vertexing

Track reconstruction from Inner Detector information is performed in three steps. In the first, space-points are built from the hits in the silicon detectors and the timing information from the TRT. In the second step, prompt tracks are searched for with different algorithms. The default track finding algorithm in ATLAS looks for track candidates, using the high-precision silicon detector information close to the interaction region. These candidates are fitted, and fake tracks are rejected by quality cuts, e.g. on the number of associated clusters and the number of silicon layers without hit information. The selected tracks are then extended to the TRT and refitted, using the full information of all three detectors. A complementary track-finding strategy, called “back-tracking”, starts from unused track segments in the TRT.

<sup>11</sup>In hadron collider experiments, the momentum fractions of the colliding partons are unknown. Therefore, the longitudinal momentum of possible invisible products of the hard scattering process cannot be directly measured, but only their transverse momenta and energies.

<sup>12</sup>Missing energy and  $\tau$  leptons are of no importance within this thesis and are therefore not addressed.

These are extended into the SCT and pixel detectors to improve the tracking efficiency for secondary tracks from conversions or decays of long-lived particles. The final stage is the post-processing stage, in which primary vertices, i.e. the positions of the original hard scattering processes, are reconstructed and algorithms for the reconstruction of photon conversions and secondary vertices are run.

The reconstructed tracks are parameterized by five quantities, the so-called ‘‘helix parameters’’, defined at the point of a track closest to some reference point, typically the origin of the coordinate system. These give the distance  $z_0$  and  $d_0$  in beam direction and in the transverse plane and the corresponding azimuthal angle  $\phi$  and the cotangent of the polar angle,  $\cot\theta$ . Furthermore, the inverse transverse momentum  $q/p_T$  is given, multiplied with the a charge sign associated to the track. These parameters define the transverse and longitudinal impact parameters  $IP_T$  and  $IP_L$ , which are used in the definition of track quality criteria applied in this thesis, according to

$$IP_T = d_0^{\text{PV}} \quad \text{and} \quad IP_L = |z_0^{\text{PV}} - z_{\text{PV}}| \cdot \sin\theta^{\text{PV}} \quad , \quad (3.1)$$

with the reference point now being the position of the primary vertex (PV), requiring extrapolation of the track to this point to obtain the parameters  $d_0^{\text{PV}}$ ,  $z_0^{\text{PV}}$  and  $\theta^{\text{PV}}$ . The position of the PV in  $z$ -direction is  $z_{\text{PV}}$ . The resolution of the helix parameters depends strongly on the amount of multiple scattering a charged particle is subject to and hence on the amount of traversed detector material. The resolution of parameter  $X$  can be parameterized as a function of the transverse momentum  $p_T$  of the track as

$$\sigma_X(p_T) = \sigma_X(\infty) \left(1 \oplus \frac{p_X}{p_T}\right) \quad , \quad (3.2)$$

where  $\sigma_X(\infty)$  is the asymptotic resolution expected at infinite momentum. The constant  $p_X$  represents the value of  $p_T$  for which the intrinsic and multiple-scattering terms in the equation are equal for the considered parameter  $X$ . Table 3.2 lists the  $\sigma_X(\infty)$  and  $p_X$  values for two pseudorapidity regions, one with small and one with large amount of detector material.

Parameter	$0.25 <  \eta  < 0.5$		$1.5 <  \eta  < 1.75$	
	$\sigma_X(\infty)$	$p_X$ [GeV]	$\sigma_X(\infty)$	$p_X$ [GeV]
Inverse transverse momentum $1/p_T$	$0.34 \text{ TeV}^{-1}$	44	$0.41 \text{ TeV}^{-1}$	80
Azimuthal angle $\phi$	$70 \mu\text{rad}$	39	$92 \mu\text{rad}$	49
Polar angle $\cot\theta$	$0.7 \cdot 10^{-3}$	5.0	$1.2 \cdot 10^{-3}$	10
Transverse impact parameter $IP_T$	$10 \mu\text{m}$	14	$12 \mu\text{m}$	20
Longitudinal impact parameter $IP_L$	$91 \mu\text{m}$	2.3	$71 \mu\text{m}$	3.7

**Table 3.2:** Expected track parameter resolutions (RMS) at infinite transverse momentum,  $\sigma_X(\infty)$ , and transverse momentum,  $p_X$ , at which the multiple-scattering contribution equals that from the detector resolution (see Eq. (3.2)). The momentum and angular resolutions are shown for muons, whereas the impact parameter resolutions are shown for pions. The values are given for two pseudorapidity regions, one in the barrel Inner Detector where the amount of material is close to its minimum and one in the endcap where the amount of material is close to its maximum (taken from Ref. [71]).

The nominal beam spot size at the LHC is  $\sigma_{xy} = 15 \mu\text{m}$  and  $\sigma_z = 5.6 \text{ cm}$ . Therefore, the determination of the PV position in  $z$  direction is of special importance, whereas in the transverse plane the vertex position is determined by the beam line. The reconstruction of primary vertices is performed in two steps of vertex finding and vertex fitting. In the primary vertex finding step, the reconstructed tracks are associated to a vertex candidate.

The position of the PV is determined in the vertex fitting step. Furthermore, the parameters of the associated tracks are recalculated, using the constraint from the PV position. Three different strategies for primary vertex finding are implemented in Athena, based either on a separate vertex finding step or employing a combined “finding through fitting” approach. Also, several strategies for vertex fitting are available in the ATLAS reconstruction software. All of them are based on the minimization of a  $\chi^2$ -function with respect to the position of the vertex and the parameters of the incident tracks at this position. They differ in the methods chosen to minimize the  $\chi^2$  and to reweight the tracks during the iterative process.

The efficiency to find the primary vertex depends on the number of associated tracks. In the case of  $t\bar{t}$  events, the PV can be reconstructed and identified as the hard interaction vertex with an efficiency of 99% efficiency in the presence of low-luminosity pile-up. The resolution of the primary vertex position is around  $12\ \mu$  in  $x$ - and  $y$ -direction and  $50\ \mu\text{m}$  in  $z$ -direction. In higher-luminosity scenarios, the presence of additional minimum-bias vertices affects the choice of the primary vertex a wrong vertex can be picked up as the primary vertex in up to several per cent of all the cases, depending on the event topology.

Besides primary vertices, also secondary vertices are important for the reconstruction of physics processes. They play a key role in the identification of photon conversions and long-lived particles, in particular in  $b$ -tagging algorithms. Secondary vertices of  $K_s^0$  decays can be reconstructed up to a radius of 400 mm. Conversions can be identified by reconstructing pairs of tracks or tagging single electrons in the TRT with 80% efficiency up to a radius of 800 mm.

### 3.3.2 Muon reconstruction

A variety of strategies exist in ATLAS for the identification and reconstruction of muons. “Standalone muons” are obtained by finding tracks in the muon spectrometer and then extrapolating these to the beam line. “Combined muon” algorithms match the standalone muons to Inner Detector tracks and then combine the measurements from the two systems. “Tagged muons” are found by extrapolating ID tracks to the spectrometer detectors. Standalone algorithms cover a slightly larger pseudorapidity range out to  $|\eta| = 2.7$  than the combined and tagged muon algorithms, which are limited to the ID pseudorapidity range up to  $|\eta| = 2.5$ . Nevertheless, the coverage of the muon system has gaps near  $|\eta| = 0$  and  $|\eta| = 1.2$ . Muons with transverse momenta of only a few GeV do not cross to the outermost detector layers and are hence difficult to detect. Muons produced in the calorimeter or e.g. from pion and  $K$ -meson decays late in the detector are likely to be found by the standalone algorithms and constitute background for most physics analyses, which is significantly reduced when using combined or tagged muons. Furthermore, the combination of measurements from both systems enhances also the  $p_T$  resolution.

The standalone algorithms start from track segments found in each of the three muon stations and combine these to form tracks. The extrapolation to the beamline accounts for multiple scattering and energy loss in the calorimeter. Depending on the algorithm, energy losses are either only assigned based on the material crossed in the calorimeter or makes use of the calorimeter energy measurements. The combined muon reconstruction algorithms pair muon spectrometer tracks with ID tracks, based on a  $\chi^2$  quantifying the compatibility between the outer and inner track segments. The combined track is then determined either by a statistical combination of the inner and outer track measurements or by a partial refit, starting from the inner track and adding the measurements from the outer track. In contrast, the tagging algorithms propagate all ID tracks above some momentum threshold out to the muon spectrometer station and search for nearby track segments. This is done either by

defining a  $\chi^2$  quantifying the difference between any nearby track segment and its prediction from the extrapolated track or using an artificial neural network to define a discriminant. The ID track is the associated to a muon, if it is sufficiently close to the predicted track position. The match to the muon spectrometer is only used to identify muon candidates, but no combined tracks are fitted, such that the muon momentum is determined by the ID measurement only. Typical reconstruction efficiencies obtained for muons from  $W$  boson decays in  $t\bar{t}$  events are up to 94% with the combined muon algorithms. The efficiency is lower in the case of low- $p_T$  muons or muons with transverse momenta above about 1 TeV, which are more likely to radiate a substantial fraction of their energy. The typical fake rate in  $t\bar{t}$  events is few per thousand events for a muon  $p_T$  larger than 20 GeV.

### 3.3.3 Electrons and photons

To reconstruct electrons and photons, EM calorimeter clusters are searched for with a “sliding window” algorithm. The algorithm builds rectangular calorimeter cell clusters of a fixed size and positions them such, that the energy contained in the cluster is maximized. The employed cluster sizes depend on the calorimeter region and the type of particle to be searched for. Electron clusters are larger than photon clusters due to the bend in the magnetic field in the Inner Detector and due to their larger interaction probability before reaching the calorimeter. For each of the electron candidate clusters above a minimum energy of about 2 GeV, the reconstruction tries to find a matching ID track within a  $|\Delta\eta \times \Delta\phi|$  window of  $0.05 \times 0.10$  and a cluster energy to track momentum ratio  $E/p$  smaller than ten. For this purpose, bremsstrahlung losses in front of the calorimeter are corrected by dedicated tracking algorithms and tracks associated to  $\gamma \rightarrow e^+e^-$  conversions are rejected. If a matching track is found, an electron candidate is created. Otherwise, the candidate is classified as a photon. Approximately 93% of all true isolated electrons with  $p_T > 20$  GeV and within  $|\eta| < 2.5$  are selected as electron candidates. A second algorithm, seeded by good-quality ID tracks, is optimized for low-energy electrons. If a relatively isolated deposition of energy in the EM calorimeters is found to match a track, this cluster is regarded as an electron candidate, too. After the classification, energy calibration corrections are applied to the electron and photon candidates.

The calibrated clusters are the subject to more refined identification algorithms that are optimized for the separation of electrons or photons from hadronic background. Three levels of electron quality are defined in ATLAS, referred to as the “loose”, “medium” and “tight” selection criteria, with increasing background rejection at the cost of decreasing signal selection efficiency. All three are based on a set of cuts that have been optimized in up to seven bins in  $\eta$  and up to six bins in  $p_T$ . The photon selection corresponds to the tight electron selection, excluding tracking requirements. The criteria for the three electron selections are:

- The “**loose**” electron identification applies cuts on the energy leakage into the hadronic calorimeters and on the lateral shower shape and shower width, derived only from information from the middle layer of the EM calorimeter. The “loose” set of cuts provides a very high electron selection efficiency, but a relatively low background rejection. Hence, it is e.g. suited for analyses of rare processes with distinct signatures that are not subject to large backgrounds.
- The “**medium**” cuts in addition use the information on the energy deposits in the strips in the first layer of the EM calorimeter and on the quality of the reconstructed track. The cuts on the strip layer information are optimized to separate single photons or electron clusters from photon pairs produced in the decay of neutral  $\pi$  mesons. The latter often

cause a specific energy-deposit pattern with two maxima, which can be resolved in the strip layer, studying a window  $|\Delta\eta \times \Delta\phi| = 0.125 \times 0.2$  around the cell with the highest  $E_T$ . The variables used to reject such clusters with multiple maxima are the difference between the energy associated with the second maximum and the energy reconstructed in the strip with the minimal value in between the first and second maximum, the second largest energy deposit, normalized to the cluster energy and the total with of the shower in the strip layer. Furthermore, the shower width for three strips around the strip with the maximum deposit and the fraction of energy outside a core of three central strips but within seven strips are taken into account. The considered tracking variables include the number of hits in the pixels detector, the number of silicon hits (pixel and SCT) and the transverse impact parameter. The medium cuts increase the jet rejection by a factor of three to four with respect to the loose cuts, while reducing the identification efficiency by about 10%.

- The “**tight**” selection finally, in addition to the “medium” requirements, applies a cut on the number of hits in the innermost layer of the pixel detector to reject electrons from conversions. Cuts on the number of hits in the TRT and on the ratio of high threshold hits to the number of hits in the TRT improve the rejection of the charged hadron background. Finally, tighter track matching criteria are applied through cuts on the difference between the cluster and the extrapolated track positions in  $\eta$  and  $\phi$  and on the ratio of the cluster energy to the track momentum.

These selection criteria are optimized for the rejection of non-electron background. Another source of background for analyses of final states with “isolated” electrons from  $W$  or  $Z$  boson decays are real electrons produced in the decays of heavy quarks. A strategy for the effective suppression of this background, resulting in a dedicated “isolation” tool, was developed in the course of this thesis and is described in detail in Chapter 5.

### 3.3.4 Jet finding and calibration

Jet finding algorithms are applied to reconstruct the four-momenta of partons produced in particle-collisions from their hadronization products. These can be either Monte Carlo generator level partons or particles or, in the case of a real measurement, the reconstructed detector objects with four-momentum representation. The most commonly used jet finder implementations in ATLAS are a seeded fixed cone finder and a sequential  $k_T$  algorithm implementation:

- The iterative seeded fixed-cone jet finder first orders all input in decreasing size of the transverse momentum  $p_T$ . If the object with the highest  $p_T$  is above a seed threshold of 1 GeV, all objects within a given cone<sup>13</sup> of either  $\Delta R = 0.4$  or  $\Delta R = 0.7$  are combined with this seed. The direction of the so-obtained combined object is determined and used as the centre of a new cone for the next iteration of adding or removing objects and readjusting the cone axis. This is repeated, until the direction is stable and the outcome is considered a jet candidate. All objects incorporated in this jet candidate are removed from the list and the algorithm starts again, forming the next jet candidate.
- The  $k_T$  algorithm compares the squared transverse momenta  $d_i = (p_T^2)_i$  of all objects from the input object list with the squared relative transverse momentum of all object

<sup>13</sup>The cone size is defined by  $\Delta R \equiv \sqrt{\Delta\eta^2 + \Delta\phi^2}$  = separation in the  $\eta - \phi$  plane.

pairs  $i, j$  defined by

$$d_{ij} = \min((p_{\text{T}}^2)_i, (p_{\text{T}}^2)_j) \cdot \frac{\Delta R_{ij}^2}{R^2} \quad \text{with} \quad \Delta R_{ij}^2 = (\Delta\phi_{ij})^2 + (\Delta\eta_{ij})^2 \quad . \quad (3.3)$$

The parameter  $R$  is a free distance parameter, controlling the size of the jets ( $R = 0.4$  and  $R = 0.6$  are available in ATLAS). If the minimum of all  $d_{ij}$  and  $d_i$  is a  $d_{ij}$ , a new combined object is built from the pair that replaces the individual objects  $i$  and  $j$  in the list. Otherwise, the object  $i$  is considered to be a jet and is removed from the list. This is repeated until no more objects are on the list.

The most important detectors for jet reconstruction in ATLAS are the calorimeters. For the jet finding, first the cell signals need to be combined in four-momenta, which can be used as input to the above described jet finding algorithms. Two concepts are available in ATLAS for this purpose: Either calorimeter signal towers are built from the energy deposits in individual cells, projecting them onto a fixed grid in  $\eta$  and  $\phi$  with a bin size of  $\Delta\eta \times \Delta\phi = 0.1 \times 0.1$ . Each cell contributes a fraction of its energy deposit, corresponding to the overlap of the projection of the cell with the tower. Alternatively, topological cell clusters are built, trying to reconstruct the energy blobs produced by individual particles in the calorimeter. For this purpose, seed cells with a signal-to-noise ratio above a certain threshold are chosen and combined with neighbouring cells if their signal-to-background ratios exceed other, lower, threshold values. Both types of clusters initially use the basic electromagnetic energy scale cell signals and can already be used for jet reconstruction. In addition, they can be calibrated to a local hadronic energy scale. For this purpose, the cell signals are corrected by weights depending on the cell position and the size of the energy deposit. Further corrections are applied for the energy loss in front of the calorimeter and for energy missed by the clustering procedure.

Jet reconstruction in ATLAS is possible, starting from a minimum jet  $p_{\text{T}}$  of about 7 GeV. The choice of the optimal cone size depends on the needs of the analysis. Larger cone jets have the advantage of a more precise energy resolution. Smaller cone sizes, on the other hand, do not pick up as much contamination from neighbouring objects in the case of final states with many objects involved. Due to leakage of electromagnetic energy into the hadronic calorimeter, rare calorimeter showers induced by non-minimum-ionizing muons and the similarity of jets and hadronically decaying  $\tau$  leptons, there are ambiguities in the collections of jets and leptons. Objects appearing in several different collections must therefore be identified and the decision must be made, which of the two should be kept for an analysis and which should be removed from the collection in question. Different analyses require different purities of the different collections, therefore this decision is usually made depending on the needs of individual analyses (see Section 6.4.1 of Chapter 6 for the case of the  $t\bar{t}H$ ,  $H \rightarrow W^+W^-$  analysis).

### 3.3.5 $b$ -tagging

Jets containing  $b$ -quarks can be distinguished from jets that contain only lighter quarks or gluons, because they differ in some characteristic properties. The  $b$ -hadrons retain a large fraction, typically 70% of the original  $b$ -quark momentum and their mass is typically larger than 5 GeV. In consequence, the products from  $b$ -hadron decays tend to have a large transverse momentum with respect to the jet axis and they can be separated due to their large decay opening angle. Finally, they have a relatively long lifetime ( $\approx 1.5$  ps), resulting in typical flight path lengths in the transverse plane of a few millimetres. Their secondary vertices

can therefore be identified, either by exploiting the relatively large impact parameters of the individual tracks or by reconstructing the decay vertex.

Finally, possible semi-leptonic decays of  $b$ -hadrons can be exploited, using the leptons to tag the jet, as is done by dedicated “soft lepton tagging” algorithms. Several different  $b$ -tagging algorithms exist in ATLAS. Most of them are based on a likelihood ratio approach or a neural network, combining several variables related to the properties of  $b$ -quark jets described above. Also simpler and more robust tagging algorithms are available, as well as taggers combining the separation power of several likelihood based tagging approaches, combining e.g. impact parameter and vertexing information.

### 3.3.6 Detector simulation

To obtain reasonable predictions for experimental data analyses from Monte Carlo samples, the events generated according to the procedure described in Section 2.3 need to be modified such that they account also for detector effects. Three different approaches, a full detector simulation, the parameterization based ATLFAST-II simulation and the very fast ATLFAST simulation (providing decreasing accuracy in the detector description), are available in ATLAS. The more accurate a description is, the more time consuming is the generation. Analyses requiring the study of large datasets are therefore preferentially performed on ATLFAST or ATLFAST-II samples, whereas detailed studies of e.g. shower shapes are only possible with the full detector simulation.

#### Full detector simulation

The full detector simulation uses an exact description of the material distribution in the ATLAS detector to simulate the full detector response, i.e. the signals provided by the front-end electronics of the individual detector components [72]. The passage of the particles through the matter and the simulation of the detector response are performed by the dedicated GEANT4 program [73]. The output is then passed through the full object reconstruction chain, as it is applied to the data taken in the experiment. The full simulation therefore allows for detailed studies e.g. of calorimeter shower shapes and reconstruction or identification efficiencies. The drawback is the time consumed by the full simulation of an event, which depends on its complexity and the number of involved particles, but typically takes several minutes per event. To take possible imperfect alignment and calibration procedures into account and to include also a possible imperfect knowledge of the material distribution in the detector, the Monte Carlo datasets studied in this thesis were produced with a so-called “distorted” detector geometry [49]. Misalignments were introduced for the ID and additional material was added in the ID and in front of the calorimeters. In addition, distorted magnetic field configurations were used, where the symmetry axis of the field did not coincide with the beam axis.

#### ATLFAST

The least exact, but fastest, approach to include detector effects in Monte Carlo simulations is used by the ATLFAST package [74]. Instead of a simulation of the full detector response, ATLFAST provides the four momenta of physics particles, thus including detector effects as well as inaccuracies of the reconstruction algorithms in one step. For this purpose, the four-momenta provided by the Monte Carlo generator are subject to smearing according to  $\eta$  and  $p_T$  dependent parameterizations of the experimental resolutions expected for the individual particle types. Furthermore, particles are removed randomly according to their expected

reconstruction efficiencies. The approach is very fast, allowing for the generation of large amounts of Monte Carlo events. On the other hand, these samples are only suited for very sketchy estimations of signal and background yields in physics analyses. The reconstructions and resolutions can vary depending on the event type, which is not accounted for by dedicated parameterizations. Furthermore, measured quantities like e.g. variables describing the detailed shape of an electromagnetic shower are not defined. Detailed studies, as e.g. the electron isolation studies in Chapter 5 are impossible.

### **ATLFAST-II**

A compromise between the accuracy of the full detector simulation and the speed of ATLFAST, is provided by the ATLFAST-II package [75], available in Athena version 14 and higher. ATLFAST-II is based on a full simulation of the ID and muon system, but replaces the calorimeter simulation by a detailed parameterization of the individual shower parameters [76]. In the approach followed by ATLFAST-II, only the longitudinal properties of the individual showers are simulated including fluctuations and correlations, whereas the lateral properties are described by average values. The parameterizations are obtained from fully simulated datasets of single photons and charged pions and employ a fine binning in the particle energies and pseudorapidity to allow for an accurate description of the material distribution in the detector. Since the shower development depends strongly on the origin of the shower, also a binning in the longitudinal shower depth is included. As in the full simulation, the output of ATLFAST-II can be passed through the full ATLAS object reconstruction chain, thus resulting in the same output format as the full simulation. The calorimeter simulation is the most time consuming part of the full detector simulation and the replacement by the parameterized shower shapes typically reduces the necessary computing time per event by a factor of 10 to 20.

## 4 Electrical tests of ATLAS SCT endcap modules

Part of the work for this thesis was the responsibility for the electrical characterization of a number of ATLAS Semiconductor Tracking detector (SCT) endcap modules that were assembled at the University of Freiburg. The SCT consists of four cylindrical barrel layers equipped with 2112 silicon modules in total and two sets of nine disks in the endcaps, each comprising 988 modules, corresponding to  $63\text{ m}^2$  of silicon microstrip sensors. The assembly and testing of the 1976 endcap modules plus a number of spares was distributed over 14 institutes in Europe and Australia. Among them was the University of Freiburg, which contributed about 200 “Inner” modules. Details on the module and sensor layouts, the testing procedure and a summary of the results were published in 2007 by the ATLAS SCT collaboration in Refs. [77] and [78], which the following chapter is partly based on. Section 4.1 describes the layout of the SCT endcap modules and disks. An overview on the testing system is given in Section 4.2 and the electrical characterization of the sensors and readout electronics are dealt with in Section 4.3. The test results are discussed and summarized in the final Sections 4.4 and 4.5.

### 4.1 The SCT endcap modules

The design of the ATLAS Inner Detector is described in Section 3.2.1 and Fig. 3.6 therein. It was developed to match a variety of requirements imposed by the needs of the planned physics analyses and running conditions of the LHC [79]. These demand the semiconductor tracker to reconstruct isolated leptons with a transverse momentum of  $p_T > 5\text{ GeV}$  with at least 95% efficiency out to  $|\eta| \leq 2.5$ . Furthermore, transverse momenta up to  $p_T = 500\text{ GeV}$  must be measured with a precision better than 30%. Tracking back to the vertex  $z$ -coordinate must be possible with better than 1 mm accuracy and a two track resolution of better than  $200\text{ }\mu\text{m}$  at 30 cm radius must be achieved. The SCT material amount must not exceed  $0.2 X_0$  in total.

These specifications are met by a design consisting of a four-layer barrel region, which on its own covers the  $\eta$ -range up to roughly  $|\eta| = 1$  and two endcaps, each built up from nine disks extending the range up to  $|\eta| = 2.5$ . Each of the endcap disks consists of one, two or three rings equipped with modules of four different types. All modules belonging to a particular ring type are identical. The first disk and the last three are not fully equipped with modules, omitting part of the active silicon sensor material closest to the beam axis, which is not needed to cover the required  $\eta$ -range with a sufficient number of detector layers. A photograph of a fully equipped endcap disk is shown in Fig. 4.1. The outer and inner rings are mounted on the side of the disk towards the interaction point, whereas the modules of the middle ring are mounted on the side away from the interaction point (with the exception of the outermost disk, which is rotated about the vertical axis to maximise the coverage in  $\eta$ ) [80]. To ensure an overlap of the active area of neighbouring modules in  $R\phi$ , they are staggered in  $z$  by 1.5 mm about the mean  $z$  of the ring.

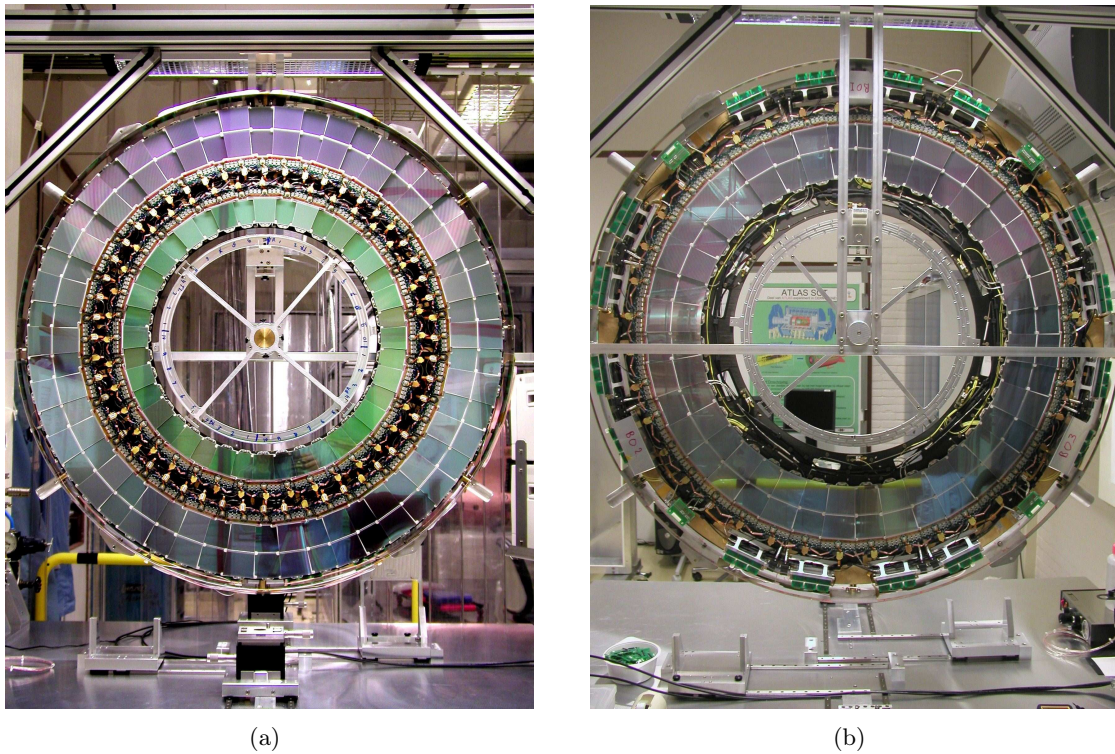


**Figure 4.1:** One of the endcap disks with modules mounted: front side (towards the interaction point) of disk, with Inner and Outer modules (a) and rear side (away from the interaction point) of disk, with Middle modules (b) (taken from Ref. [64]).

#### 4.1.1 Module layout

Depending on their position on the disk, the modules differ in their geometry, referred to as “Inner”, “Middle” and “Outer” modules. Figure 4.2 shows photographs of these module types. To cover the geometry of a ring, the shape of the modules is trapezoidal, resulting in a variable strip pitch of the sensors. Each module consists of two planes of silicon sensors glued back-to-back around a central spine. The length of the active material for the outer and middle rings is 120 mm, whereas that of the inner ring is 55 mm. In the case of Outer and Middle modules, each side contains two daisy chained sensors to achieve the required active length. A fourth type, mounted on the ninth disk instead of a regular Middle is referred to as the “Short middle” and consists only of the upper sensor. The two planes of sensors include a stereo angle of 40 mrad to give the required position resolutions of  $16 \mu\text{m}$  in  $R\phi$  and  $500 \mu\text{m}$  in  $R$ , with the strips on the front-side sensor pointing in radial direction.

The design of the modules and the individual components they consist of is illustrated in Fig. 4.3. Each of the sides of the SCT endcap module has 768 sensor channels that are connected to six chips for the signal readout. The chips are placed on a support, the “hybrid”, which provides the electrical interface between the module and the disk services and is described in more detail in Section 4.1.3. The hybrid and sensors are attached to the so-called “spine” a  $500 \mu\text{m}$  thick support structure made from thermalised pyrolytic graphite (TPG), with aluminium nitride (AlN) ceramic side-wings, shown in Fig. 4.4(a). For electrical insulation and mechanical protection, the TPG is coated with a  $10 \mu\text{m}$  thick layer of Parylene-C. AlN reinforcements protect the soft TPG part at the cooling contacts. An aluminiumoxide ( $\text{Al}_2\text{O}_3$ ) spacer is attached to the AlN wing at the hybrid end to match the thickness of the



**Figure 4.2:** Three types of modules assembled on the ATLAS SCT endcaps, showing the layout of the five different wedge-geometries of the endcap sensors (taken from Ref. [64]). Each module consists of two back-to-back sensor layers, rotated with respect to each other by  $40\text{ mrad}$ . From left to right: Outer module, Middle module and Inner module. The readout electronics are mounted on hybrids at the ends of the modules.

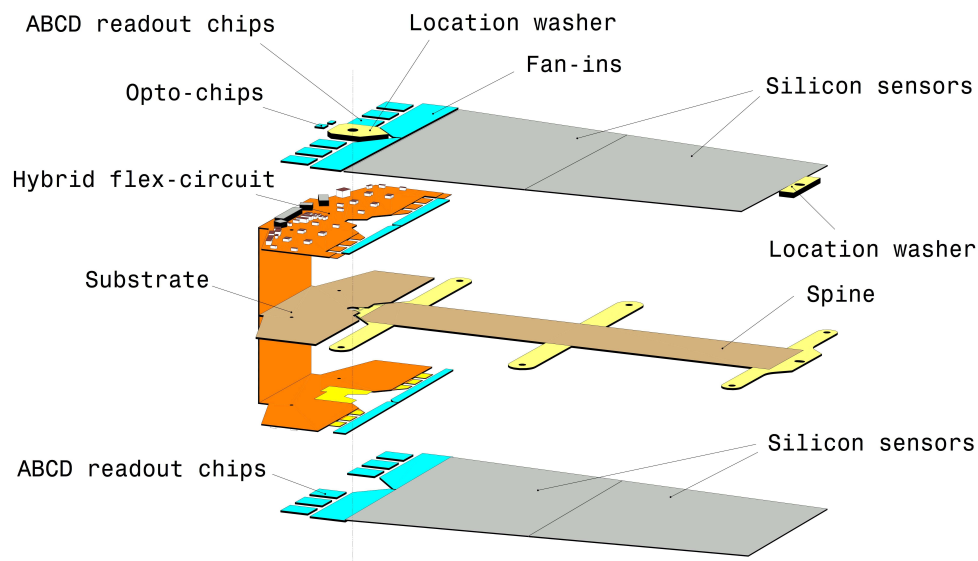


**Figure 4.3:** Exploded view of an SCT endcap module showing its different components (taken from Ref. [64]).

spine to the hybrid. The sensor bias high voltage is supplied by the hybrid at a pad in an extension of the hybrid. This pad contacts a metal trace on one of the AlN cross pieces of the spine, onto which the sensors are glued with a conductive epoxy.

Besides its supporting and electrical function, the TPG backbone of the spine provides a thermal path between the sensors and cooling contacts at each end. The heat production rises with the radiation damage and after the expected radiation dose from ten years of ATLAS operation, the sensors will produce up to  $2\text{ W}$ . This heat needs to be transported from the

sensors to the module mounting and cooling blocks at each end, which are held at around  $-15^\circ\text{C}$ . Outer and middle modules are supported and cooled by their contact with two cooling blocks. The main block is shared between the hybrid and the spine, whereas the far block cools only the spine. Inner modules are cooled only by the main block and the far block is only used for mechanical support.

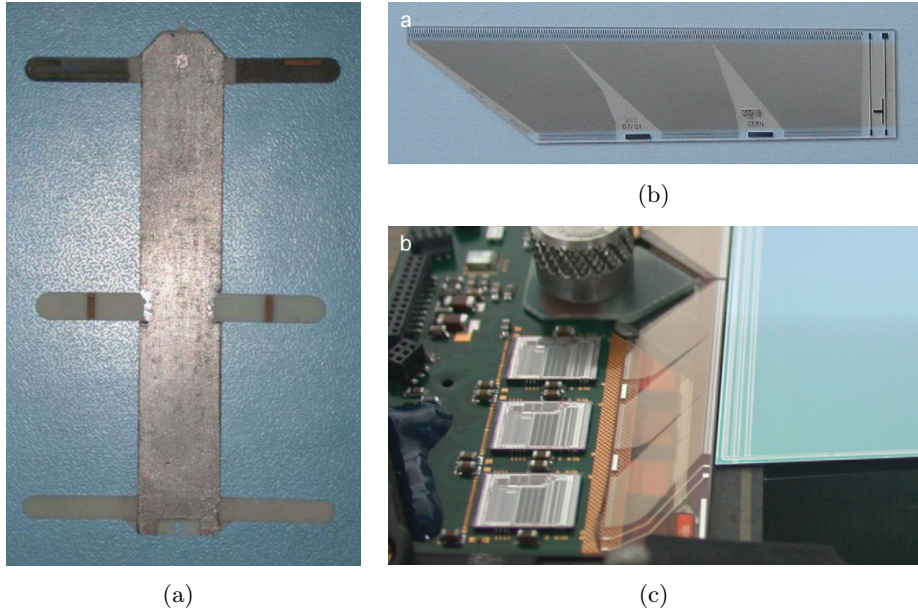


**Figure 4.4:** Photographs of the ATLAS SCT endcap module spine (a) and fan-in (b). Figure (c) shows the fan-in glued to the hybrid and the spine spacers (taken from Ref. [77]).

The separation of the readout chips on the hybrid, together with the different pitch of the various sensor types and the stereo angle between the two sensor planes prevents the direct and automatic wire bonding of the sensors to the chips. Instead, pitch adaptors, referred to as “fan-ins”, as shown in Figs. 4.4(b) and 4.4(c) are used, which provide electrical connection of every channel, adapting the different pad pitch and configuration. They also contribute to the mechanical support between the hybrid and the sensors and maintain an effective barrier to heat flow between these parts. The fan-ins are made of high density metal tracks deposited on top of an isolating glass substrate. A passivation layer with openings at the pads for the wire bonding covers the tracks for both mechanical and chemical protection.

Finally, two aluminium precision location washers are attached to the hybrid and the far end of the spine to fix the module on the disk. The plastic base of the main location washer on the hybrid furthermore provides the thermal isolation between the hybrid and sensor.

#### 4.1.2 Sensors

The ATLAS silicon microstrip sensors are fabricated using  $p^+$  implanted strips of about  $20\ \mu\text{m}$  width in a  $285\ \mu\text{m}$  thick high resistivity ( $> 4\ \text{k}\Omega/\text{cm}$ )  $n^-$  substrate<sup>1</sup>. The sensors are operated with a biased  $n^+$  backplane and the metal strips kept on ground potential. The sensors were manufactured by two different suppliers, Hamamatsu [81] and CiS [82]. The Hamamatsu supply covers all the 8448 barrel sensors installed, and 82.8% of the 6944 installed endcap

<sup>1</sup>The index “ $\pm$ ” refers to the dopant concentration of the substrates: Strongly  $n^-$  and  $p^-$  type doped materials (typically about one acceptor/donator per  $10^4$  atoms) are denoted by  $n^+$  and  $p^+$ . No superscript refers to a normal doping concentration of about  $1 : 10^7$ . The index “ $-$ ” denotes a small residual dopant concentration.

sensors. The remaining 1196 installed endcap sensors were supplied by CiS. There are five different types of forward silicon sensors. They all have 768 readout strips plus two edge strips and a wedge-like geometry with inter-strip angles of  $207\ \mu\text{rad}$  (Inners and Middles) and  $161.5\ \mu\text{rad}$  (Outer modules). The strip pitch varies between  $56.9\ \mu\text{m}$  and  $94.2\ \mu\text{m}$ , depending on the sensor type and position on the sensor, always allowing for a  $1000\ \mu\text{m}$  distance from the sensitive area to the physical cut edge. The “guard region”, designed to guarantee a controlled voltage drop between the bias potential and the strips and hence to prevent breakdowns, was optimized by each manufacturer according to their processing. The implanted strips were required to have a resistance smaller than  $200\ \text{k}\Omega/\text{cm}$  and to be capacitively coupled with greater than  $20\ \text{pF}/\text{cm}$  to aluminium readout strips ( $< 15\ \Omega/\text{cm}$ ) matching the implant dimensions. The implants are biased by resistors of  $1.25\ \text{M}\Omega$ . Microscopic photographs of corners of a Hamamatsu and a CiS sensor are shown in Fig. 4.5, showing the strip, bond pad and guard ring structures of the two sensor types.

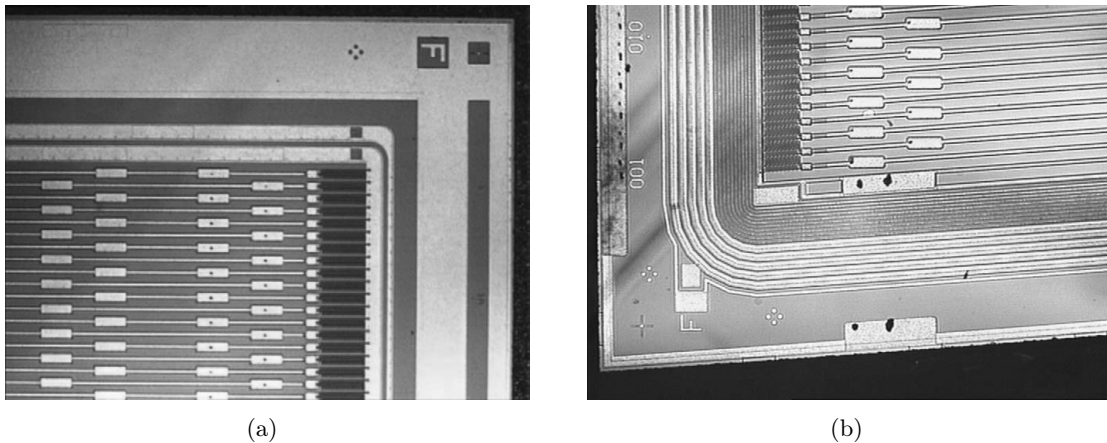


**Figure 4.5:** (a) Microscopic photograph of a corner of an SCT barrel silicon microstrip sensor supplied by Hamamatsu, showing the guard structure, a selection of fiducial alignment marks, the bias ring, the polysilicon bias resistors and the metallisation above the implant strips, including wirebonding pads. (b) Microscopic view of a corner of a CiS endcap silicon microstrip sensor, showing the angled strips, the multi-guard structure and the implanted bias resistors (both taken from Ref. [78]).

Figure 4.6 illustrates the different layouts of the guard region, the bias resistors and arrangement of the bond pads of the two detector types. The implant strip width of the Hamamatsu sensors is  $16\ \mu\text{m}$ , and the metal readout strip is  $22\ \mu\text{m}$  wide. Thus the metal overlaps the implant each side by  $3\ \mu\text{m}$ , forming a field-plate structure. Such structures force the strip implants on a finite potential and thus serve avoid field peaks, which trap charges and cause charging on the detector surface. This design was chosen because it delays the onset of strip micro-discharge after irradiation [83]. It was subsequently established that it also protects against strip micro-discharge when the bias voltage is ramped in a very dry environment [84]. For the CiS sensors, the implant strip width is  $20\ \mu\text{m}$  and the aluminium readout strip width is  $16\ \mu\text{m}$ . Thus, the strip metal is  $4\ \mu\text{m}$  narrower than the strip implant, which was a design originally proposed by the collaboration because of its low interstrip capacitance. This choice has resulted in some difficulties, identified only at a late stage in the project, with micro-discharge in CiS sensors at low relative humidity, causing humidity dependent breakdown effects, which are also related to the storage history of the sensors [84]. The problem is ascribed to high fields at the edge of the strip implants induced by surface charges when the voltage is ramped in a dry atmosphere. The dry breakdown problem is cured after type-inversion following irradiation, when the  $p$ - $n$  junction moves to the backplane as described in

the next section. For the later high-voltage running of the SCT it is therefore not an issue, as has been verified by measurements of irradiated CiS sensors. Nevertheless, it influences the behaviour in the tests performed during construction as discussed below.

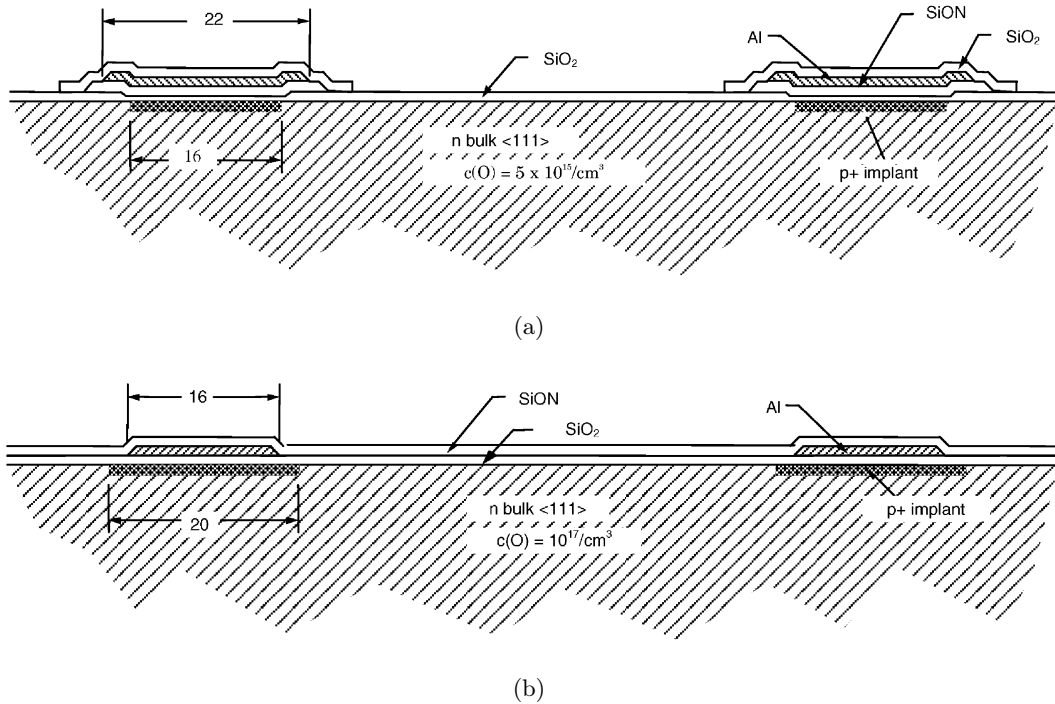


**Figure 4.6:** Comparison of the strip layouts for sensors from Hamamatsu (a) and CiS (b) (taken from Ref. [84]). The aluminium strips of the Hamamatsu sensors are insulated from the implants by silicon nitride and silicon oxide layers, and the strips and front sensor surface are passivated by a layer of silicon oxide. Layers of silicon oxide and silicon nitride insulate and passivate the strips and front CiS sensor surface. In contrast to the Hamamatsu sensors, in CiS sensors the implant strip (checked area) is wider than the Al readout strip (hatched).

### Type inversion and annealing

The expected integrated radiation dose<sup>2</sup> of  $2.14 \cdot 10^{14} \text{ n}_{\text{eq}}/\text{cm}^2$ , including a 50% safety factor on top of the anticipated dose, has severe consequences for the sensors (as for all other active module components and for the thermal design of the system). The irradiation causes substrate damages leading to additional lattice impurities, with more acceptors than donators being generated. Hence, the effective doping concentration  $N_{\text{eff}}$  in the substrate of  $p^+$ -in- $n^-$  sensors initially drops with dose. After about  $2 \cdot 10^{13} \text{ n}_{\text{eq}}/\text{cm}^2$  the material effectively inverts space-charge from being  $n$ -type and acts as if it is increasingly  $p$ -doped with dose (“type inversion”) [85, 86]. The time dependence of these changes strongly depends on the irradiation history and the operating temperature of the sensors.

The behaviour of the effective doping concentration  $N_{\text{eff}}$  determines the depletion voltage  $V_{\text{dep}}$ . As the doping concentration changes, the required depletion voltage  $V_{\text{dep}}$  of the irradiated high-resistivity silicon microstrip sensors, and hence their required operating voltage for high efficiency, varies with time long after exposure to radiation, as illustrated in Fig. 4.7.

<sup>2</sup>The dose is normalized using the non-ionizing energy loss (NIEL) cross sections to the expected damage of 1 MeV neutrons [79].

The voltage required for the depletion of the sensor first drops to a minimum at the point of type inversion. After that, it starts rising again in a way depending on the temperature and irradiation history without a change of the polarity, with the depletion of the sensor now starting from its back plane.

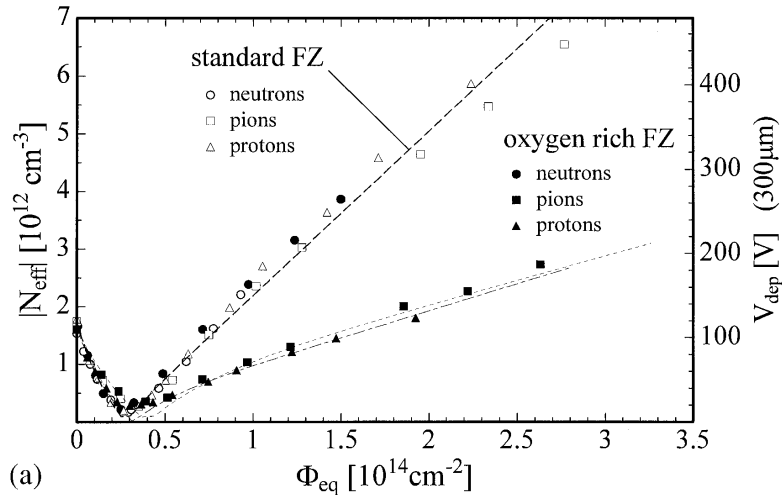


**Figure 4.7:** Dependence of the effective dopant concentration  $N_{\text{eff}}$  and the depletion voltage  $V_{\text{dep}}$  for a  $300 \mu\text{m}$  thick sensor on the accumulated 1 MeV neutron equivalent fluence for standard and oxygen enriched FZ silicon irradiated with neutrons, protons and pions (taken from Ref. [86]). The type inversion occurs at an integrated fluence of about  $2 \cdot 10^{13} \text{ n}_{\text{eq}}/\text{cm}^2$ , where the curve reaches its minimum.

The doping concentration changes with time even after irradiation. Two adversed time dependent annealing effects act on top of a stable damage contribution. A shorter-scale “beneficial annealing” occurs because of impurities drifting back to their original lattice sites, which reduces the number of impurities. In contrast, the longer term “reverse annealing” effect is caused by cluster defects in the substrate, which tend to increase with time and cause the space charge to become more negative. Both effects are accelerated by high temperatures. Figure 4.8 illustrates the time dependence and the composition of the change of the effective doping concentration caused by the radiation damage out of three contributions at a given operating temperature. The time dependence of both annealing contributions is determined by the temperature. To retain a good performance and to slow down the increase in the required  $V_{\text{dep}}$  after type inversion as much as possible, the reverse annealing of the sensors must be limited to benefit as much as possible from the positive beneficial annealing effect. There is a shallow optimum between both at an average operating temperature on the sensors of  $-7^\circ\text{C}$  that effectively freezes out the reverse annealing at least during data taking. Realistic maintenance scenarios [79] require to allow for  $V_{\text{dep}}$  values of up to 300 V and corresponding operating voltages of up to 350 V. A number of features in the sensor design ensure this high voltage operation to cope with the substrate effective doping changes following heavy irradiation. The requirement of cold operation of the sensors, given the 7 W module power dissipation after irradiation, leads to the need for coolant temperatures of down to  $-25^\circ\text{C}$ . This in turn requires the dew-point in the detector environment to be well below this value, leading to the need to flush the SCT with nitrogen or very dry air, which needs to be reflected in the testing of the modules discussed below.

The increase of the depletion voltage with rising integrated fluence  $\Phi_{\text{eq}}$  after the type inversion can be reduced by the use of oxygen-enriched silicon, as illustrated in Fig. 4.7. The

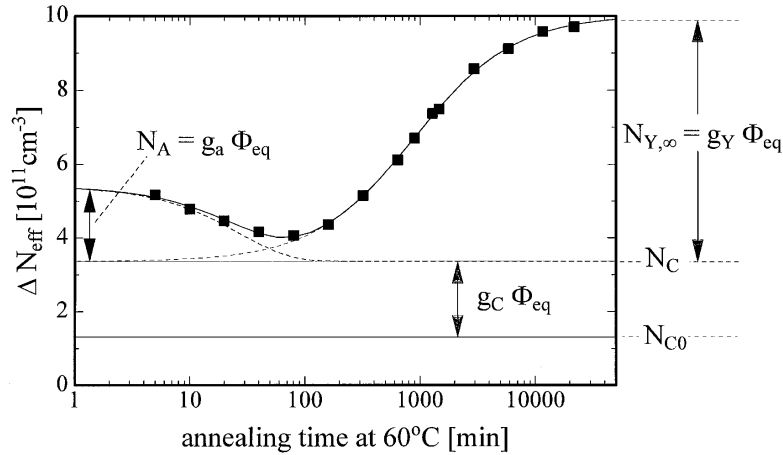


**Figure 4.8:** Annealing behaviour of the radiation induced change in the effective doping concentration  $\Delta N_{\text{eff}}$  at  $60^\circ\text{C}$  (taken from Ref. [85]). The dashed lines indicate the composition from three different contributions: a stable damage contribution  $N_C$ , a short-term beneficial annealing contribution  $N_A$  and a longer term reverse annealing component  $N_Y$  (see Ref. [85] for more details).

wafers for the CiS Inner module sensors, which are exposed to the highest fluences, were therefore enriched with an oxygen concentration of  $\approx 10^{17}\text{ cm}^{-3}$  in order to increase radiation hardness for this innermost type of sensor [86].

### 4.1.3 Hybrids

The endcap electronics hybrid provides the electrical interface between the module and the disk services. All necessary assembly steps to build the hybrids were developed at Freiburg University and then transferred to industrial partners. Freiburg was furthermore responsible for the control of the industrial production and for testing a large fraction of the hybrids before being forwarded to the module assembly sites.

The basic design of the hybrid is six layers of kapton wrapped around a carbon core. As illustrated in Fig. 4.9, it carries twelve application-specific integrated circuit chips (ASICs), six on each side of the hybrid. These ABCD3TAs<sup>3</sup> [87] do the preamplifying, digitization and intermediate buffering of the signal. They have been designed to meet the specifications of radiation resistance up to 10 mrad and speed in order to efficiently identify the beam crossings. Furthermore, low noise, low power and the capability of keeping the data in on-detector buffers during the first level trigger latency time are required. Therefore, the chips were fabricated using the radiation hard DMILL<sup>4</sup> technology [88] and implement a binary readout architecture in a single chip. Binary readout offers advantages in terms of requiring lower data transmission bandwidth compared with other readout modes, less stringent requirements on the quality of the data links and simpler off-detector electronics. On the other hand, special care was taken in the design and grounding of the system to avoid problems due to external electromagnetic interference. In addition, the proper threshold setting and channel-to-channel matching is crucial for a binary system, as it is impossible to distinguish between large noise fluctuations and genuine signal after the discriminator.

The ABCD3TA chip has 128 channels and comprises front-end circuitry (employing a bipolar transistor at the input stage), discriminators, binary pipeline, derandomising buffer, data

<sup>3</sup>Short for “ATLAS Binary Chips DMILL”, version 3 with trim DACs, revised version.

<sup>4</sup>Short for “Durci Mixte sur Isolant Logico-Linéaire”.

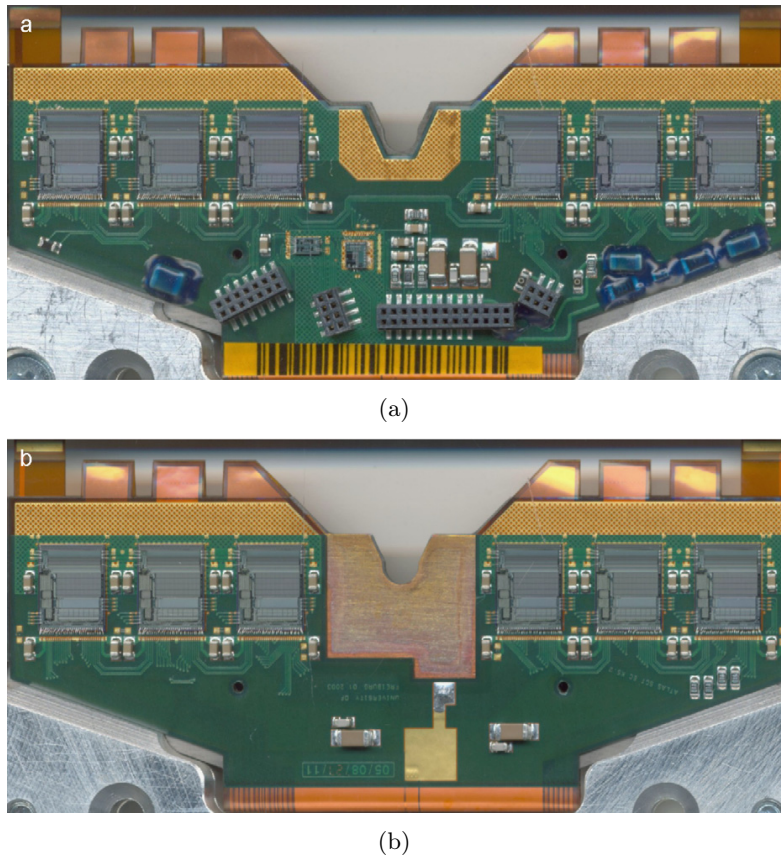


**Figure 4.9:** Photographs of the front (a) and back (b) sides of an endcap module hybrid (taken from Ref. [77]). An overview of the chips and connectors on the hybrid is given in Fig. 4.10.

compression and readout control logic as well as internal calibration circuitry. The 25 ns peaking time is short enough to keep the double peak resolution below 50 ns, ensuring that less than 1% of the data will be lost at the highest occupancies. To compensate the expected drop of the DC current gain after irradiation, a 5-bit digital-to-analogue converter (DAC) has been implemented in the chip to adjust the collector current of the input stage and optimize the noise performance. In addition, the bias current of the following stages is also controlled by another 5-bit DAC. The preamplifier-shaper stage is followed by a discriminator with a common threshold for all the channels that is controlled by an 8-bit DAC. To maintain the channel-to-channel variation of the threshold below 4%, especially after irradiation, the ADCD3TA implements an individual threshold correction in each channel with a 4-bit DAC with four selectable ranges. Data from the discriminator output are latched in the input register every 25 ns, either in edge sensing or level mode, and clocked into a 132-cell pipeline that matches the first level trigger latency time. Upon reception of a trigger, the data are transferred from the pipeline to the second level buffer, which is capable to store eight events. The data are then compressed by the data compression logic and read out via a token ring, allowing for the readout of the six chips in a hybrid side through a single data link. The data flow and the distribution of the clock and commands on the hybrid are illustrated in Fig. 4.11.

The ABCD3TAs can be configured to three different operation modes: master, end and slave. The default configuration is realized by connecting the appropriate bond pads on the ASICs to the digital ground potential. In addition, these settings can be changed through control commands. The six chips on each side form a chain with the master and the end chip

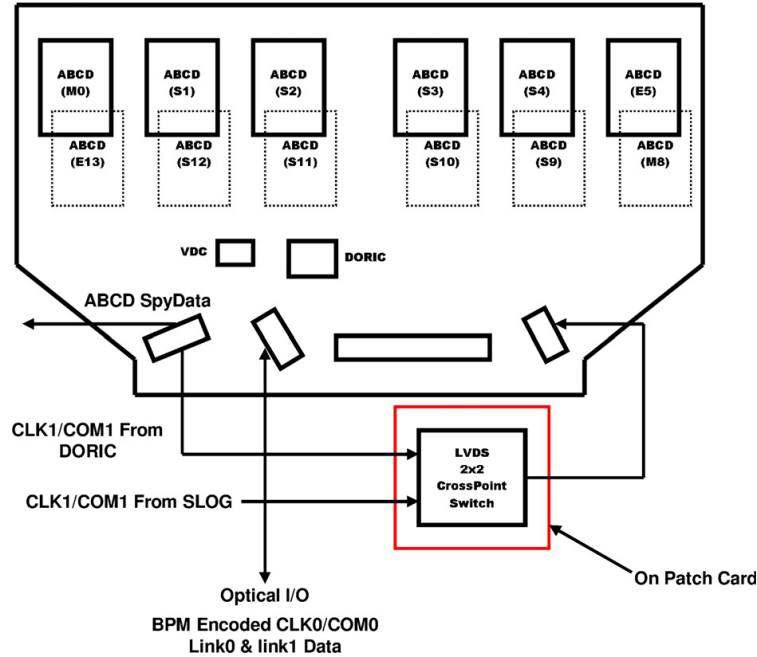


Figure 4.10: Distribution of the chips and connectors on the endcap module hybrid.

at the ends of the chain. Each chain is read out serially using the aforementioned token based scheme. Single chip failure can therefore cause the loss of all data from the following chips. To avoid this, a bypass scheme is implemented in the hybrid to cope with single chip failures without losing the data of the remaining chips. The only limitation is that the failing chips must not be immediate neighbours.

Given the large data rates expected, a system based on optical fibres is used for the data transmission off the detector and for the distribution of the timing, trigger and control (TTC) signals, because of its low mass and the absence of electromagnetic interference [90, 91]. Also the clock and commands are provided to the hybrid via optical fibres. Two additional ASICs are attached to the front side of the hybrid for optical communication. The DORIC4A<sup>5</sup> provides the TTC signals and the VDC<sup>6</sup> handles the data transmission off the module [91].

All chips on the hybrid are provided with analogue and digital supply voltages and the sensors are connected via the hybrid to the HV power supplies to bias the sensors. Power supply currents and DC levels are carried by power tapes connecting the hybrid to the periphery of the disk. As for the grounding, the modules' power return is shorted to the cooling tubes at the module mounting point. The connection is made by an additional small kapton finger with a copper trace, soldered to each module end of the power tape. A direct contact of the carbon substrate to the cooling system removes the heat dissipated from the readout chips.

The equivalent noise charge of the ABCD3TA readout chip has a temperature dependence of six electrons per °C before irradiation and 24 electrons per °C after irradiation [92]. This temperature dependence is not negligible compared with the design noise level of around  $1500 e^- \text{ ENC}$ <sup>7</sup>, which requires to keep the readout chips reasonably cool.

<sup>5</sup>Short for “Digital Opto-Receiver Integrated Circuit”.

<sup>6</sup>Short for “VCSEL Driver Chip”, with VCSEL being “Vertical Cavity Surface Emitting Laser”.

<sup>7</sup>Short for “Equivalent Noise Charge”:  $1 \text{ fC} \approx 6300 e^- \text{ ENC}$ , with the electron charge being  $1.6 \cdot 10^{-19} \text{ C}$ .

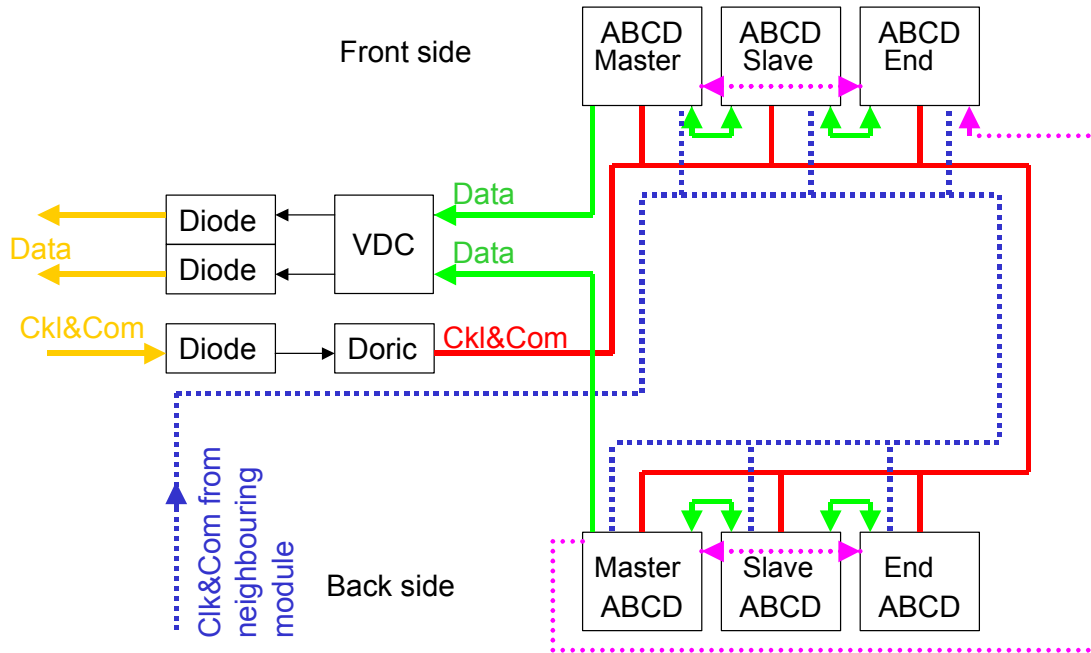


**Figure 4.11:** Illustration of the data flow and clock and command signal distribution on the ATLAS SCT endcap hybrids. Only one instead of four slave ABCD3TAs are displayed per side (taken from Ref. [89]).

## 4.2 Testing system

All electrical tests of the fully assembled module were performed with the module placed inside a light-tight aluminium test box as shown in Fig. 4.12 where it was supported at the two cooling blocks of the spine. The test box provided nitrogen flow and cooling through a channel connected to an adjustable liquid coolant system. The module temperature is monitored using a thermistor on the hybrid. Up to four modules in their test boxes could be placed inside a controlled environment and tested simultaneously at the Freiburg institute. Except for the  $I - V$  curve measurements, all tests were performed with the sensor biased at 150 V and in cool ( $\approx 10^\circ\text{C}$ ) and dry conditions.

The electrical functionality tests were performed with a system based on VME<sup>8</sup> modules. It can read out up to six modules using the optical ASICs electrically, while also testing the functionality of the module redundancy links, as illustrated in the schematic view in Fig. 4.13. The system consists of the following VME modules:

- The **CLOAC (CLOCK And Control)** [93] generates a clock, fast trigger and reset commands for the SCT modules in the absence of the TTC system as provided by the experiment.
- The **SLOG (SLOW command Generator)** [94] generates slow commands for the control and configuration of the SCT front-end chips. It fans out clock and fast commands from an external source (the CLOAC). Alternatively an internal clock may be selected, allowing the SLOG to generate clock and commands in stand-alone mode. When the SLOG runs in stand-alone mode, the CLOAC is not used in the set-up.

<sup>8</sup>Short for the “Versa Module Eurocard”-bus system.



**Figure 4.12:** Photograph of an Outer endcap module supported by its transport frame inside its aluminium test box (taken from Ref. [77]). The dry air and coolant inlets are visible, as well as the patch card and the kapton cables.

- The **AERO (ATLAS Endcap Read-Out)** [95] card provides an electrical interface for up to six endcap modules. Data communication to and from the modules is via their onboard optical ASICs. The AERO encodes the module clock and command signals onto a single bi-phase mark carrier signal for transmission to the DORIC4A. The two module data links are transmitted back to the AERO via the VDC and then routed to the MuSTARD. Configuration of the channel allows the module to be read out using either the primary (optical) or the redundant data routes.
- The **MuSTARD (Multichannel Semiconductor Tracker ABCD Readout Device)** [96] card receives, stores and decodes data from multiple SCT modules. Up to twelve data streams (six modules) can be read out from one MuSTARD card.
- The **SCTHV** [97] card is a prototype high voltage supply, providing the sensor bias voltage for up to four SCT modules.
- The **SCTLV** [98] card is a custom designed low voltage power supply for the readout electronics of two SCT modules.

Single AERO channels are interfaced to a module through a module patch card, visible in the lower right of the test box in Fig. 4.12. The connections to the AERO card are made via two standard ethernet cables, allowing for separation of the primary and redundant data routes onto the individual balanced cables. Using screened twisted pair cables and differential signals results in a system with low electromagnetic interference and good immunity to external noise.

The AERO card provides three readout modes for testing a module or hybrid, as follows:

- **Primary mode:** the module is configured and read out via the opto chips.
- **VDC bypass test mode:** the module is configured via the DORIC4A outputs and the module data is read out via the Master ABCD3TAs. This scheme is used to bypass

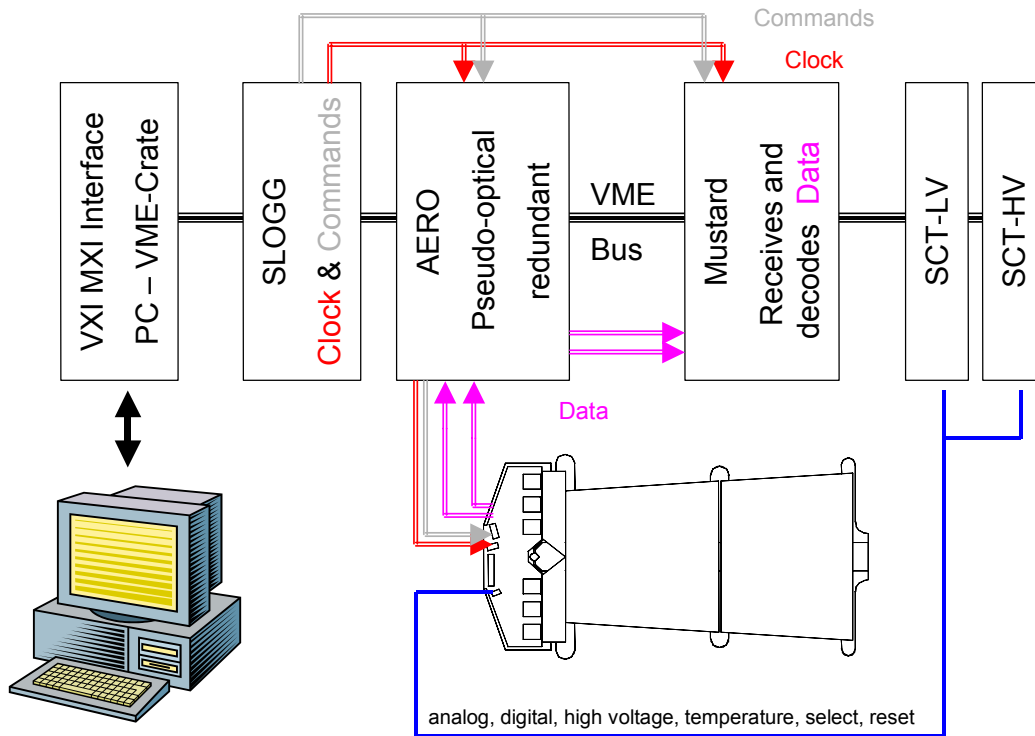


Figure 4.13: Schematic view of the ATLAS SCT endcap module testing system (taken from Ref. [89]).

the the VDC for data transmission from the module while retaining the DORIC4A for module configuration.

- **Redundancy mode:** the module is configured via the redundant clock and commands provided from the SLOG and the module data is read out via the Master ABCD3TAs.

The SCTDAQ [99] software package has been developed for testing both the bare hybrids and the modules using the VME units described above. SCTDAQ consists of a C++ dynamically linked library and a set of ROOT macros that analyse the raw data obtained in each test and store the results in a database.

Each module and its components were tracked through their history in the SCT production database. Thus, details of tests, component trees, movements between sites and overall status of modules were made available to the whole collaboration [100]. The architecture for the ATLAS-SCT database is based on the client-server model, with a main Oracle (kernel 9i) application server at the University of Geneva. Access is granted from client machines communicating over the network, either by dedicated programs to monitor particular aspects of the production, through specialised applications for massive data upload or with the help of a WWW portal.

### 4.3 ATLAS SCT endcap module testing

The LHC operating conditions demand challenging electrical performance specifications for the SCT modules. The limitations, defined in Ref. [101], mainly concern the accepted noise occupancy level, the tracking efficiency, the timing and the power consumption. Before shipping to the institutes responsible for the assembly of the SCT endcap disks, the modules were

therefore subject to thorough testing during construction in the institutes they were built. The responsibility for the execution and documentation of the electrical functionality tests on the Freiburg share of Inner modules was part of this thesis. The tests and the specifications to be met are therefore described in more detail in the following.

The characterization was performed according to a sequence defined by the ATLAS SCT collaboration in Ref. [102], including

- **Visual inspection** to identify damaged sensor edges, bonds, spines etc.
- **Thermal cycling:** to verify their temperature adaptability, the modules were cycled ten times between  $-35^{\circ}\text{C}$  and  $+35^{\circ}\text{C}$  with ramp up and down times not smaller than 30 min and soak times of also 30 min at each temperature.
- A full **metrology survey** to ensure the mechanical parameters of the modules to be within the specifications.
- Monitoring of  **$I - V$  curves** at various stages of the assembly and testing procedure.
- A **long-term test** with electrical readout to monitor the electrical performance over an 18 period and to confirm each module's long term electrical and leakage current stability at low temperature.
- A **full electrical characterization** to test all the analogue and digital features of the module.

The test results were used to place the modules into four categories according to their quality, as

- **Good:** passed all acceptance tests.
- **Pass:** failed one test, but still within the pass tolerance.
- **Hold/Rework:** outside the pass tolerance but may be usable if reworked.
- **Fail:** too bad to use, but stored safely.

Some electrical defects during the characterization could be cured directly at the assembly sites, e.g. by refreshing broken wire bond connections or the replacement of individual ASICs. After rework, the modules were again subject to a full electrical characterization.

### 4.3.1 $I - V$ curves

To examine the  $I - V$  characteristic of the sensors assembled on the modules, the high voltage was ramped up in steps of 10 V at a rate of 10 V/s and the leakage current was measured after 10 s settling time. During this procedure, the low voltage was not powered and the module was kept at  $20^{\circ}\text{C}$  or the currents were normalized to this temperature as described in Ref. [102]. The measurements were done in a dry nitrogen atmosphere with a relative humidity of only a few per cent. The leakage currents were required not to exceed  $5\ \mu\text{A}$  in the case of Hamamatsu and  $10\ \mu\text{A}$  in the case of CiS sensors and the modules were required to operate at bias voltages up to 500 V. Furthermore, the stability of the leakage current with respect to previous measurements was monitored.  $I - V$  scans were performed on the fully assembled modules before and after the thermal cycling and after the long-term test procedure. Further  $I - V$  curve scans were performed with modules showing breakdowns. The leakage current

stability was also monitored in the long-term test, where the current at a bias voltage of 150 V was observed over 18 h under cold and dry conditions, with the low voltage supply powered. The main reasons for current excesses were mechanical stress induced by the sensor gluing, charge trapping on the surface or conductive debris as small as a few tens of micrometres.

Some typical  $I - V$  curve of Hamamatsu and CiS sensors when measured directly after finishing the assembly are shown in Figs. 4.14(a) and 4.14(b), respectively. The leakage currents of the Hamamatsu sensors typically are one order of magnitude below those of the CiS sensors. A small number of Hamamatsu sensors showed some strip micro-discharge above 350 V and 500 V bias voltage in their initial non-irradiated state, but this does not affect the operation of the modules within ATLAS, initially biased at 150 V bias. The  $I - V$  characteristics of the Hamamatsu sensors are similar when biased in a dry or humid atmosphere. In contrast, CiS sensors often show temperature and humidity dependent breakdowns even at relatively low bias voltages when tested in a dry atmosphere, for the reasons explained in Section 4.1.2. Since this behaviour is expected to alter, as soon as the type inversion has occurred and the sensors are depleted from the backplane, CiS sensors were accepted x if they could at least be operated at the initial ATLAS bias voltage of 150 V.

### **$I - V$ training**

A large fraction of those CiS sensors that exhibit very early breakdowns could be recovered in a dedicated training procedure. In this procedure, the bias voltage was ramped up in steps of 10 V until the leakage current exceeded  $10 \mu\text{A}$  in a dry nitrogen atmosphere<sup>9</sup>. Then, the voltage was kept and the leakage current was monitored. If the sensor is trainable, the leakage current decreased with time. As soon as it undercut the  $10 \mu\text{A}$ , the bias voltage was raised again and the procedure was repeated until the required bias voltage was reached. In contrast, the leakage current of un-trainable modules rises with time. The training process is illustrated in Fig. 4.15, which shows the leakage current as a function of the bias voltage and the time during a training sequence for a trainable, an untrainable and a module without pathological findings, for comparison. After the training procedure, the successfully trained modules exhibit no longer the early breakdown behaviour as before training. The effect of the  $I - V$  training is also visible in the comparison of Figs. 4.14(b) and 4.14(c), where the breakdown behaviour of almost all displayed sensors is much less severe in the later  $I - V$  curve test. Nevertheless, after mounting on the disk, the behaviour of some candidates worsens again slightly, as illustrated in Fig. 4.14(d).

### **4.3.2 Digital functionality tests**

A couple of digital tests were executed to identify chip or hybrid malfunction. These included tests of the redundancy links, the chip by-pass functionality and the 128-cell pipeline circuit, as described in the following. According to the ATLAS quality assurance procedure defined in Ref. [102], these tests were performed in the following steps:

- The “**power and hard reset test**” was performed to verify that the clock, command and hard reset signals are received correctly, that the chips can be configured and that the current consumption is reasonable. The module was clocked and the power switched on. It had to be verified manually that each data link responded with half the frequency of the clock signal and that the clock signal stops after configuration of the chips. The

<sup>9</sup>Other institutes applied a less time consuming procedure, involving changing humidity conditions, as explained e.g. in Ref. [84].

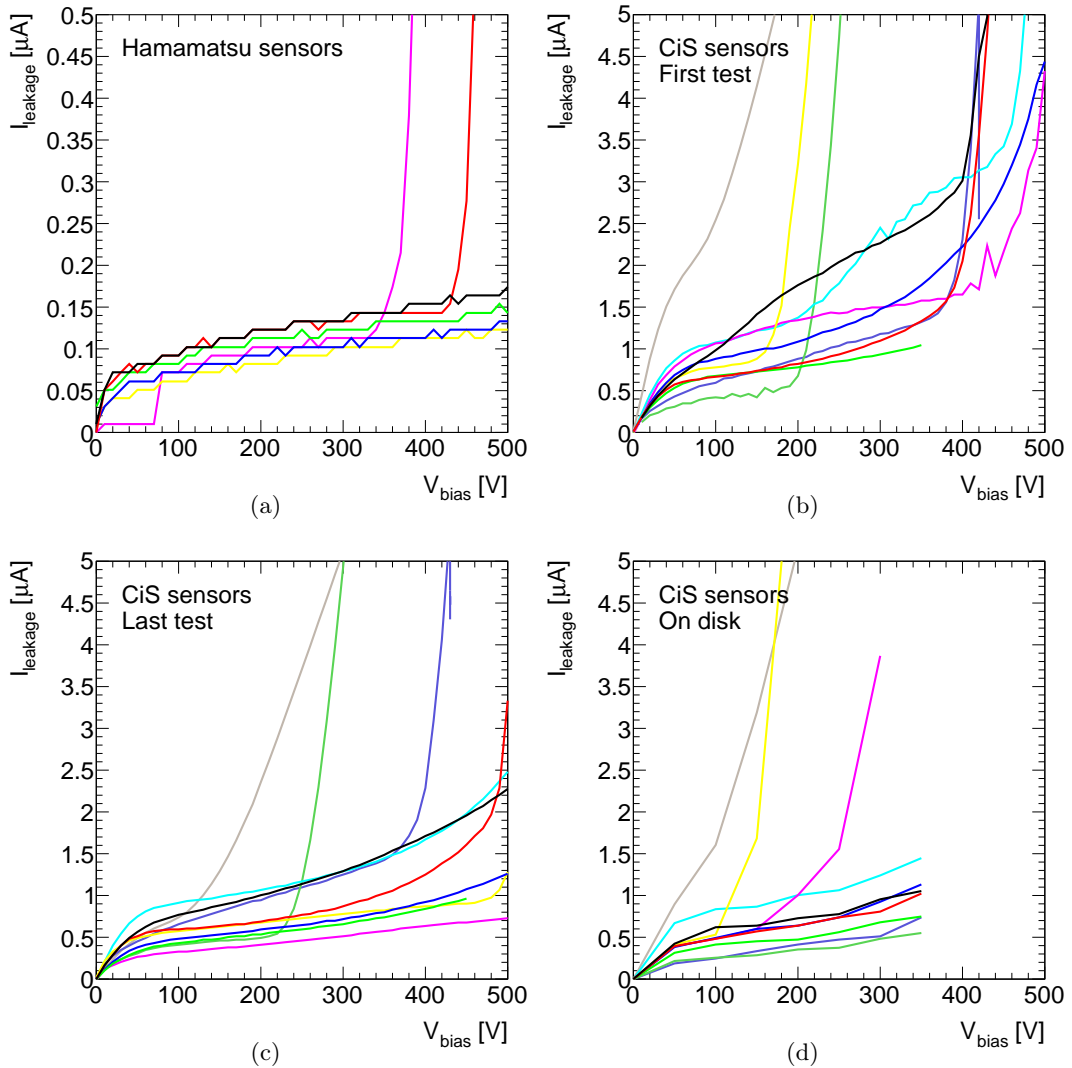


**Figure 4.14:** Leakage currents as a function of the bias voltage for some of the ATLAS SCT endcap Inner modules assembled in Freiburg. The figures show the  $I - V$  curves of modules equipped with Hamamatsu (a) and CiS (b, c, d) sensors. It should be noted that the leakage current range in (a) is a factor of ten smaller than that in (b, c, d). In the latter three, three different  $I - V$  measurements are shown for the same set of modules: (b) first measurement directly after assembly, (c) last scan performed in Freiburg and (d) after assembly on the disks, measured at 35% relative humidity (data displayed in (d) from Ref. [103]).

analogue and digital currents were then recorded. Finally, a hard reset was issued to bring back the clock/2 signal. The test had to be passed without error.

- The “**redundancy test**” identified faulty command reception or addressing errors. The chips were configured to return the contents of the mask register and a burst of triggers was issued for each of the primary and redundant clock and command options. Prior to each event, a different bit pattern is loaded in the mask register such that consecutive events are not the same. In a comparison of the received data with the expectation it was verified that both, the primary and redundant clock and command signals were received correctly and that the top address bit of each chip changed as the clock and command source was varied, as specified in the module design. The test must be passed

without error for the module to be accepted.

- The “**pipeline efficiency test**” was performed to test the efficiency of the pipelines and to identify dead pipeline cells or channels. A soft reset command was sent to reset the pipeline, followed by a pulse input register command and a trigger signal a certain number of clock periods later. In this way, a known pattern was injected into a given location in the pipeline. By varying the distance between the soft reset and the pulse input register commands it could be verified that each of the eleven blocks within the pipeline was free of defects. Zero occupancy for a particular number of clock periods between the soft reset and pulse input register commands would indicate a dead cell in the corresponding block. Zero occupancy for all values would indicate a dead channel. Modules with a large number of dead pipeline cells or dead channels were rejected.
- The functionality of the extra data and token passing links to bypass defective chips was the readout chain is verified in the “**bypass test**”. For this purpose a trigger burst was recorded with the module programmed to each of a number of different configurations, sufficient to exercise all data and token passing links between the chips. In each case, the chips were configured to return the contents of the mask register such that the expected data were accurately known. The test was repeated across a range of digital supply voltages  $V_{dd}$  to determine the minimum value of the digital supply voltage needed for each of the data and token passing links to work. Modules were rejected, if links were found that did not work at the designated supply voltage and could not be identified as being due to a missing wire bond (and be subsequently repaired).

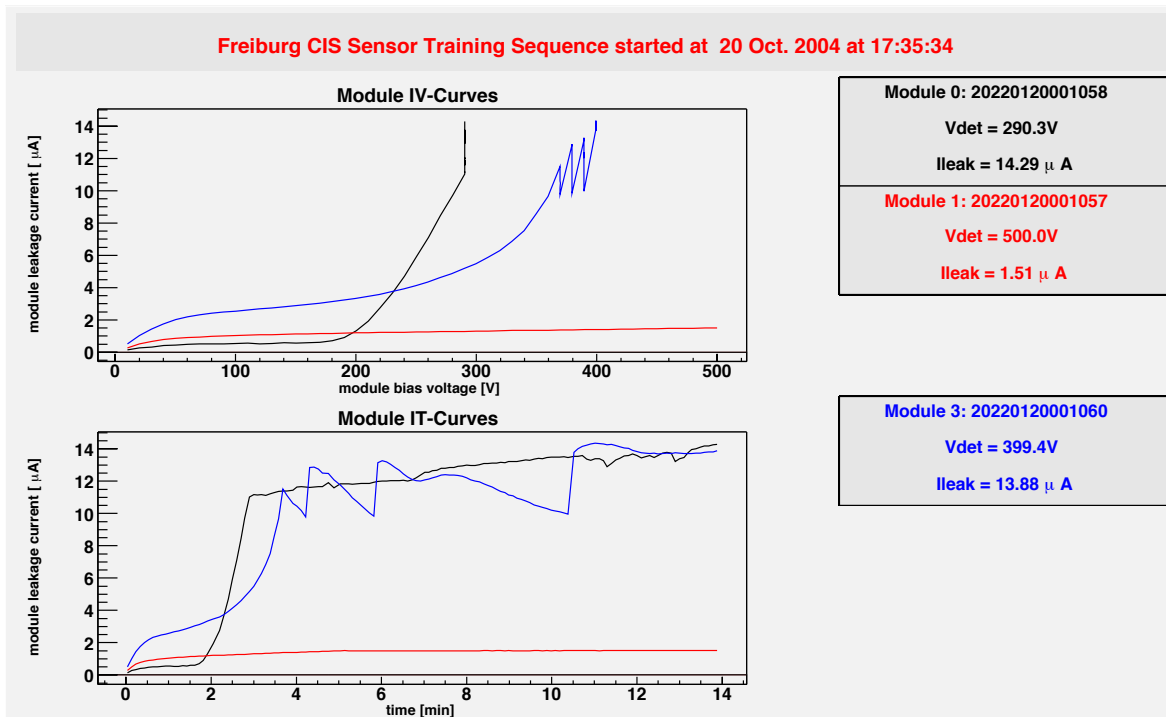


**Figure 4.15:**  $I - V$  training curves of ATLAS SCT end cap modules. The upper curves show the leakage current as a function of the bias voltage for three Freiburg Inner CiS modules, one of them trainable (blue curve), one un-trainable (black curve) and a module without pathological findings for comparison (red curve). The leakage current is given as a function of the time in the lower curves.

### 4.3.3 Analogue functionality tests

In order to simulate the passage of a charged particle through the detector, a calibration signal was generated by an internal calibration circuit of the ABCD3TA chips to inject charge of adjustable amplitude in the preamplifier of each channel. Voltages between 0 and 160 mV could be applied, corresponding to input charges between 0 and 16 fC.

#### Gain and noise in binary readout mode

Since the module is operated in binary readout mode, analogue properties like gain and noise cannot be measured directly. Instead, they are determined in so-called “threshold scans”. For this purpose, a given charge is injected several times for different settings of the discriminator threshold. Due to the noise, a certain fraction of pulses passes this threshold and triggers a signal even if the injected charge itself is too low. The lower the threshold is set, the more pulses pass until the curve reaches a saturation level. The fraction of passed pulses as a function of the threshold is the so-called “S-curve”, which can be interpreted as illustrated in Fig. 4.16. The response of an ideal detector is a step function, letting all pulses pass uniformly amplified and with 100% efficiency until the threshold equals the input charge and the efficiency drops to zero (Fig. 4.16(a)). A real detector is subject to noise (see Fig. 4.16(b)), which causes some pulses to be amplified such that some of them trigger a signal even at thresholds higher than the pulses itself. On the other hand, other pulses are attenuated and fail to pass a low threshold. The S-curve shown in Fig. 4.16(c) is therefore a convolution of the response of an ideal detector with the Gaussian noise distribution.

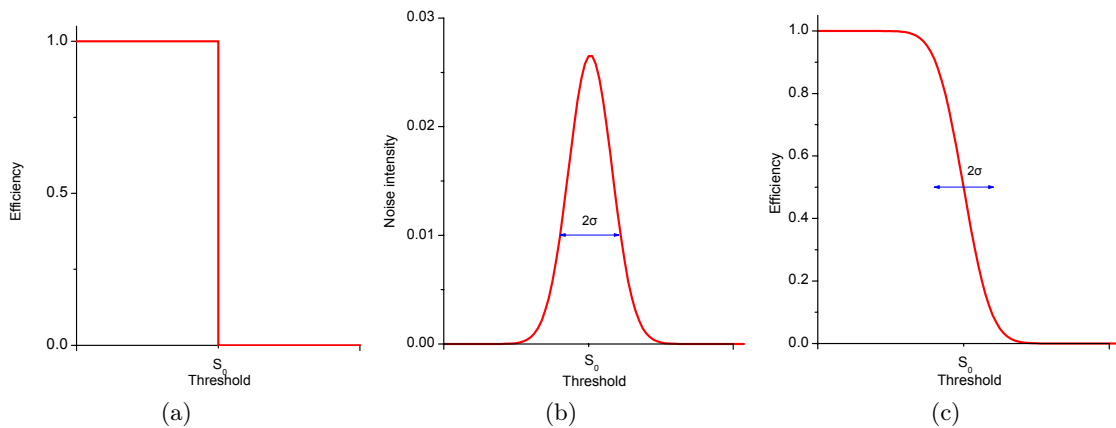


**Figure 4.16:** Illustration of the use of threshold scans to determine analogue properties in a binary system (taken from Ref. [89]): (a) Response of an ideal detector if the threshold is varied for a fixed input charge. (b) Input noise distribution of a real detector. (c) The S-curve is the convolution of both and can be used to determine properties like gain and noise.

To determine the gain and noise, this occupancy is fitted with a complementary error function. The output voltage corresponding to the threshold giving an occupancy of 50% with respect to the saturation is referred to as the “*vt50* parameter”. It is given by the mean value of the fit function. The output noise corresponds to its width. The input noise can be obtained as the ratio of the output noise over the measured gain. The so-obtained noise is given in units of  $e^-$  ENC and gives the noise generated by the sensor and front-end electronics. In contrast to that, “noise occupancies” are measured in a dedicated scan and give the rate of noise-induced fluctuations that pass the threshold and generate a signal, as discussed below. Finally, the position of the *vt50* value differs from channel to channel. This displacement is

referred to as the “offset”.

In the analogue functionality tests gain, electronic noise and offset are determined in repeated threshold scans, performed for different values of the injected charge, e.g. in ten steps ranging from 0.5 to 8 fC. The  $vt50$  value, given as a function of the injected charge, yields the so called “response curve”, as indicated in Fig. 4.17. The slope of the response curve determines the gain as a function of the equivalent test charge.

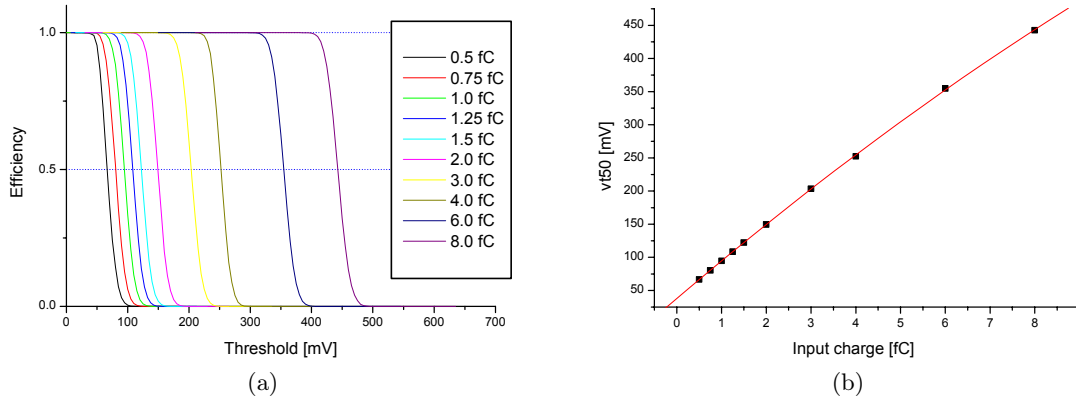


**Figure 4.17:** S-curves for ten different input charges (a) and corresponding response curve (b), showing the  $vt50$  value as a function of the injected charge equivalent (taken from Ref. [89]).

### Time-walk

An implication of the binary readout is that pulses generated by different charge deposits reach the threshold voltage with different time delay, as illustrated in Fig. 4.18. This time variation is referred to as “time-walk”. When operated in ATLAS, every hit has to be associated to a specific bunch crossing to ensure a correct track reconstruction, therefore the time-walk may not be too large. The fraction of output signals shifted to the wrong beam crossing is required to be less than 1%. Given a peaking time of 25 ns, this requires a time-walk of less than 16 ns.

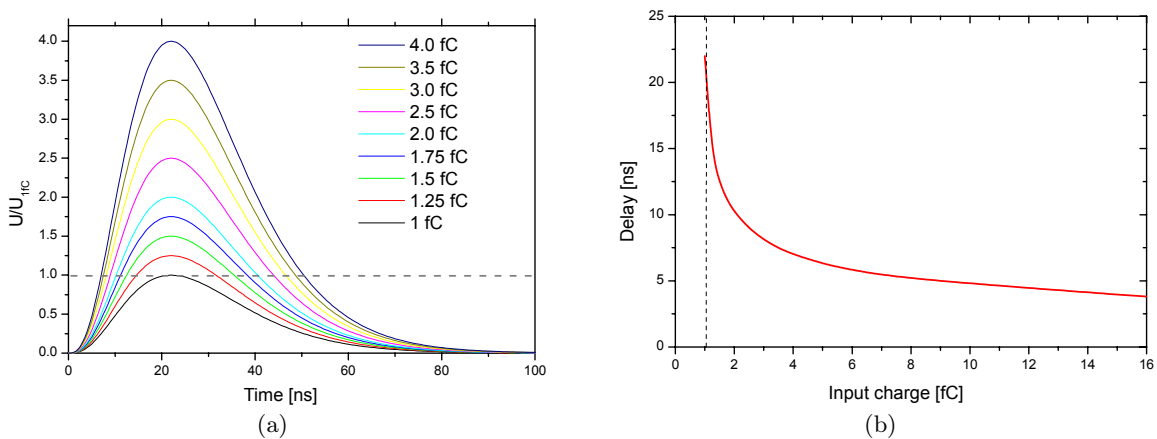


**Figure 4.18:** Illustration of the time-walk in a digital readout system (taken from Ref. [89]): (a) Pulse shapes for different input charges: the larger the charge is, the smaller is the delay until the threshold at 1 fC is reached. (b) Time-walk as a function of the injected charge.

Since the threshold cannot be set for each individual channel but only for a complete chip, it is crucial to keep the channel-by-channel threshold non-uniformity and hence the gain and

offset spread as small as possible. To minimize the impact of the offset spread on the noise occupancy, the ABCD3TA allows the discriminator offset to be adjusted, using a digital-to-analogue converter (the “trim DAC”). This “trimming” can be done with four selectable ranges (common for each chip), corresponding to 4 mV, 8 mV, 12 mV and 16 mV. Within each range, the offset can be adjusted individually for each channel. The trimming is important to achieve the desired maximum initial 4% threshold spread due to the poor matching of the DMILL transistors and, in particular, due to the increase of the offset spread with radiation dose.

### The ATLAS SCT endcap module test sequence

In the ATLAS quality assurance procedure in Ref. [102] the sequence of the analogue functionality tests was defined as follows:

- A **strobe delay scan** was performed to determine the correct strobe delay setting on a chip-to-chip basis, corresponding to the delay between the calibration signal and the clock to be used during the remaining analogue tests.
- **Three point gain:** Threshold scans were taken for three injected charges to facilitate a quick measurement of gain, noise and the discriminator offset. Pathological channels were categorized as “faulty” if the defect resulted in the channel having a reduced but non-zero detection efficiency in ATLAS or as “lost” if the defect would result in the channel having zero efficiency. A list of the affected channels was stored in the database.
- **Trim range scan:** For each of the four possible trim range settings, a series of threshold scans was performed for a subset of the sixteen trim DAC settings, with 1 fC injected charge. The trim DAC setting was displayed as a function of the  $vt50$  value and a straight line was fitted for each channel to characterize the trim DAC response and to determine the trim DAC slope. The number of trimmable channels and the spread of the trimmed thresholds were also recorded. The optimized trim DAC settings and a list of channels to be masked were produced for use in the subsequent tests. Modules with more than 1% channels that could not be trimmed in the smallest trim range were rejected and stored for potential rework, as were those where a particular trim range had a slope other than that expected.
- The **response curves** were determined on the trimmed module with threshold scans for a series of ten input charges between 0.5 fC and 8 fC, from which the gain, noise and offset were determined for each channel. The parameters from the fit were stored and the categorization of pathological channels was repeated as for the three point gain.
- In the **noise occupancy scan** a high statistics threshold scan was performed on the trimmed module at the nominal ATLAS trigger rate of 100 kHz without any injected charge to determine the noise occupancy of each channel as a function of the threshold. Also, the analogue and digital currents were recorded as a function of the threshold. Channels with high noise occupancy were added to the list of masked channels.
- **Time-walk scan:** A dedicated scan of the strobe delay was performed in edge-mode with the threshold set to 1 fC, varying the input charge from 1.25 to 10 fC. The efficiency curve obtained that way is 100% only during a 25 ns interval whose width was used to calibrate the strobe delay DAC. In each case, a complementary error function was fitted to the falling edge of the efficiency vs. strobe delay curve to determine the strobe delay value at which the efficiency has dropped to 50%. The time-walk was computed as the difference between delays obtained such for a 1.25 fC and for a 10 fC injected pulse.

The full sequence of all digital and analogue tests (the “characterization sequence”) was only performed once for each module. In the long-term test, in which the modules were clocked and configured during 18h with the sensors biased at 150 V, only a minimal performance test was carried out every 2 h. This “confirmation sequence” consisted of a redundancy and bypass functionality test, as well as a three point gain and trim range scan to determine the gain, noise and dead channels and to check the configurability of the ASICs. Between two confirmation sequences, the bias voltage, chip currents, hybrid temperature, leakage current and noise occupancy were recorded every 15 min. The monitoring of the currents served to identify modules with a power consumption exceeding the specifications of a maximum of 7 W for the hybrid, and 2.6 W for the sensors (1.6 W for short modules). A typical result of a long-term test performed on four Inner modules built in Freiburg is shown in Fig. 4.19.

Figures 4.20 and 4.21 show some typical monitoring distributions produced by the three point gain and response curve routines. The result of the channel-by-channel determination of the  $vt50$ , gain, offset and input noise of an un-trimmed Inner module, observed at an input charge of 2 fC, are shown in Fig. 4.20(a). The effect of trimming on the threshold uniformity is evident by comparison with Fig. 4.20(b), where the same parameters are shown for the same module after application of the trimming procedure. Figure 4.21 displays the input charge dependence of the characteristic parameters ( $vt50$ , gain, output and input noise) for the same module, as averaged over the 128 channels of one ASIC.

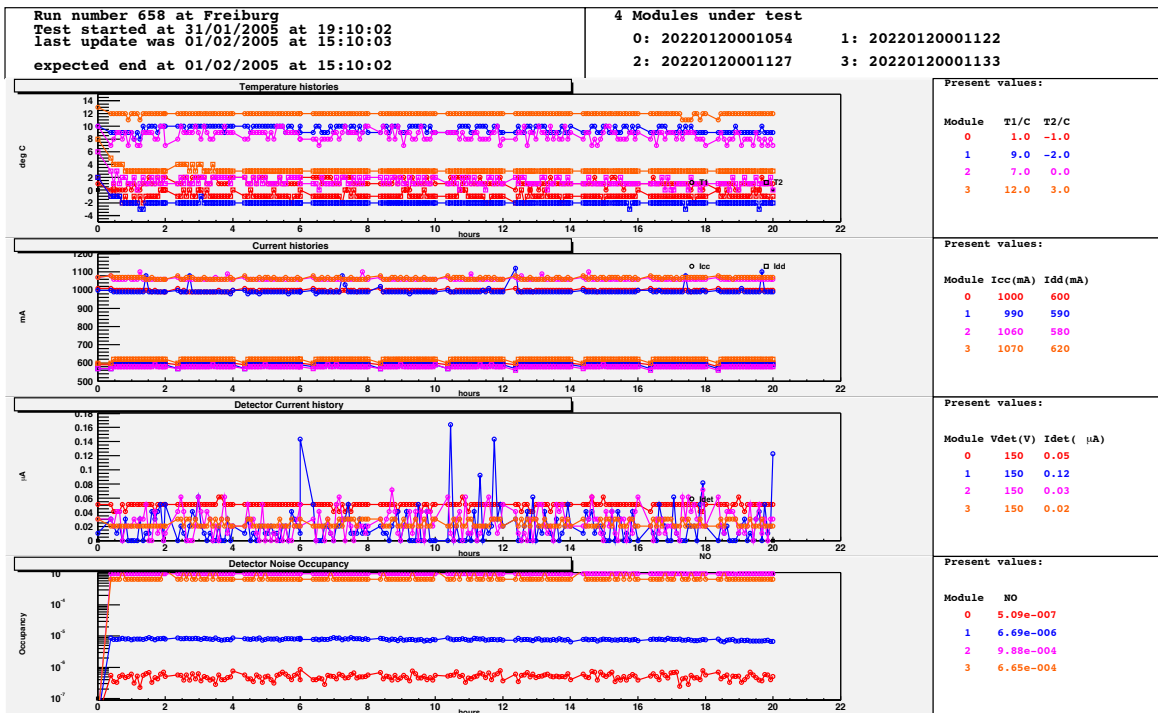
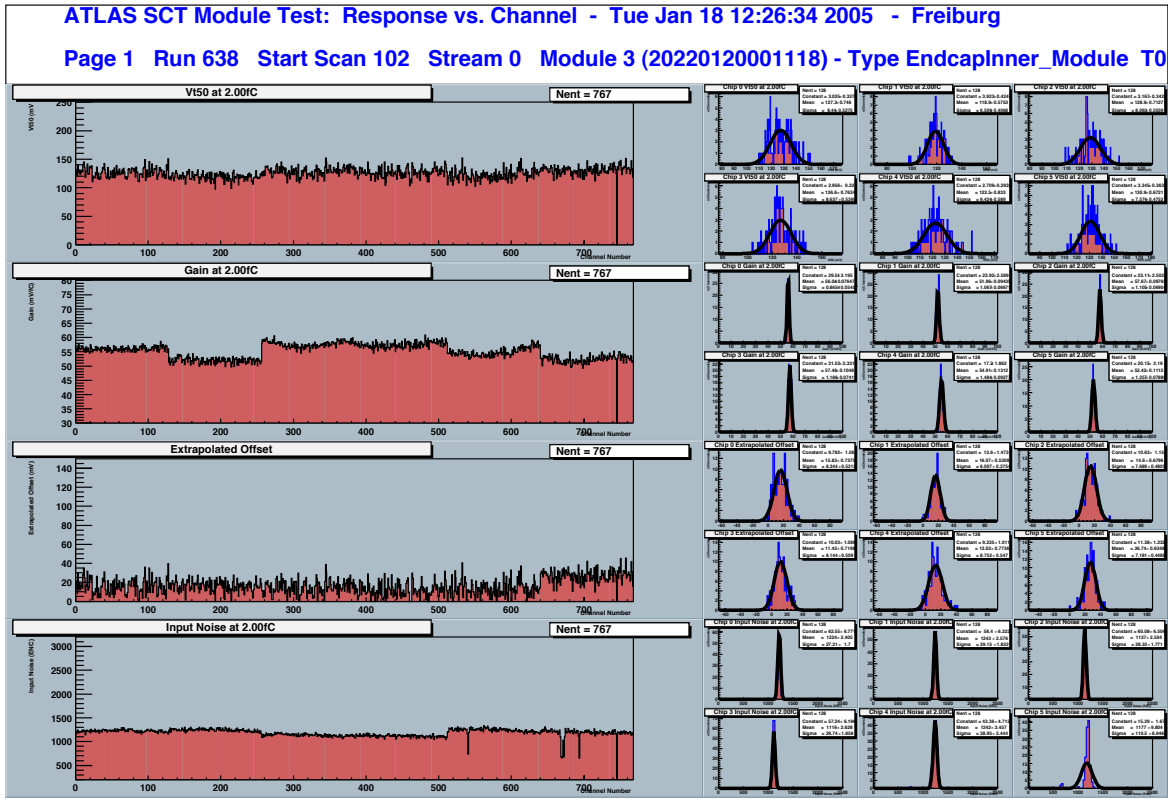
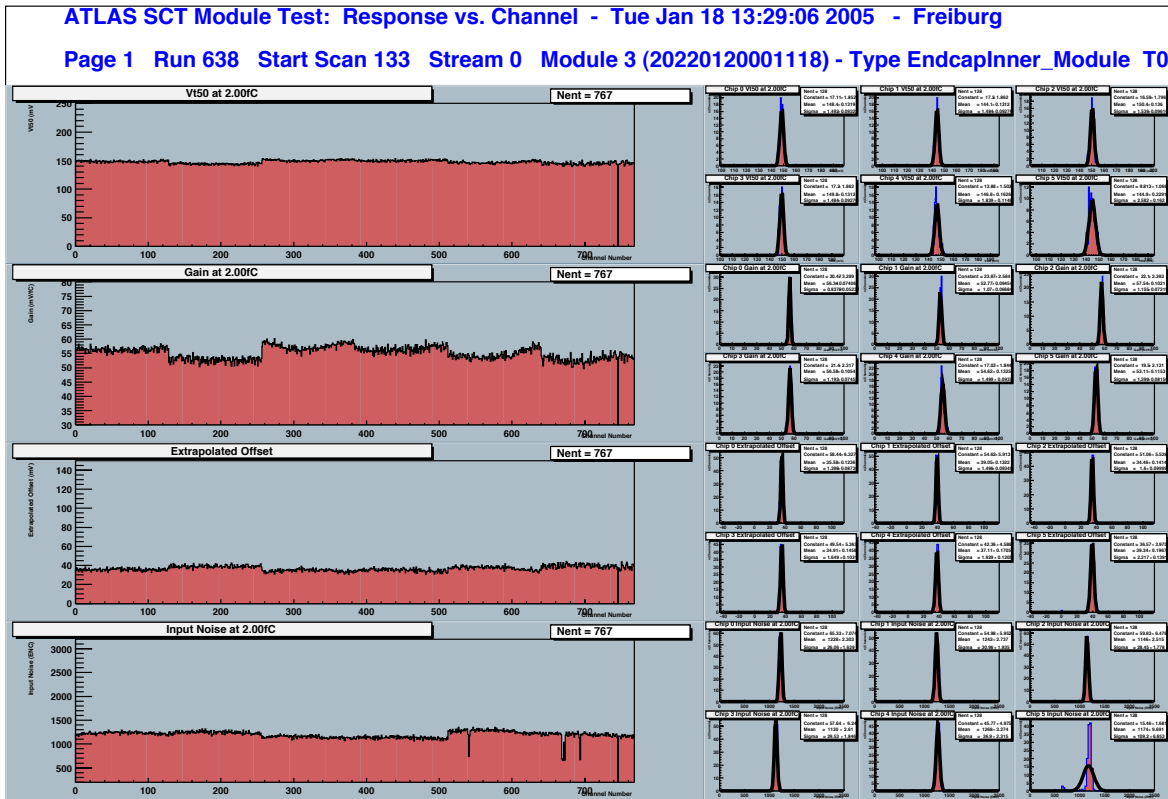


**Figure 4.19:** Long-term test results for four Inner modules tested in Freiburg, showing from top to bottom: the hybrid temperature, the analogue and digital currents  $I_{CC}$  and  $I_{DD}$ , the sensor leakage current  $I_{det}$  and the noise occupancy (measured every 15 min) as a function of time. Every two hours the monitoring of these parameters stopped to run a confirmation sequence.



(a)



(b)

**Figure 4.20:** A typical set of results obtained with the response curve procedure before (a) and after (b) trimming for one data stream, corresponding to six chips (768 channels) on the front side of one of the Freiburg Inner modules. From top to the bottom the  $vt50$  value, the gain, the offset and the input noise are shown for each channel on the left hand side. On the right, the chip-by-chip distributions of the corresponding parameters are shown.

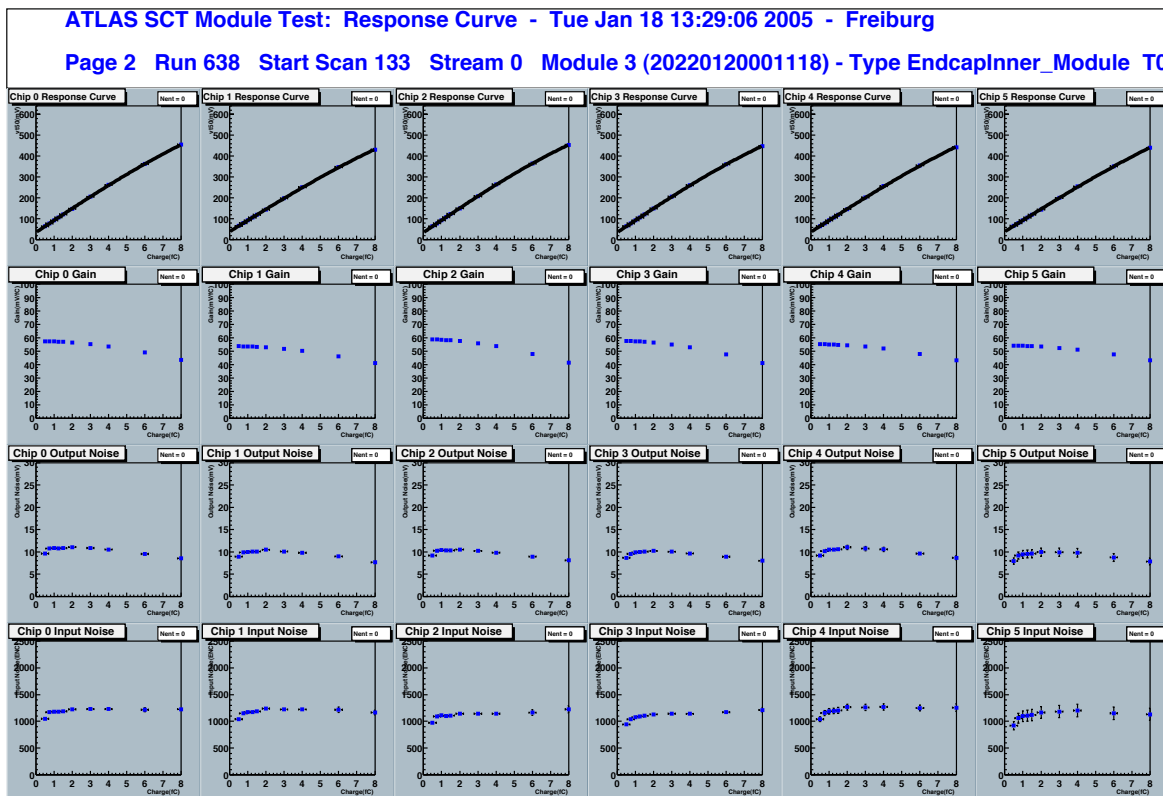


**Figure 4.21:** Response curves (i.e. charge dependence of the  $v_{t50}$  distributions shown on the right hand side of Fig. 4.20(b)) for the six chips on the front side of the same module as in Fig. 4.20 after trimming (upper row). The corresponding ten point gain curves are shown in the second row. The remaining two rows show the output noise [mV] and the input noise [ $e^-$  ENC] as a function of the calibration charge. All values are averaged over the 128 channels on one ABCD3TA.

The tracking performance of a particle detector depends on the intrinsic precision and efficiency of the detector elements. To meet the above mentioned requirements on the tracking performance, at least 99% of all channels must be working. To ensure this, the accepted number of bad readout channels was therefore specified fewer than 16 for each module. Furthermore, no more than eight consecutive bad channels were accepted. Bad channels comprise both, channels that are completely lost (e.g. because they are dead, stuck, noisy, untrimmable or unbonded) and channels that are at least partly functional (faulty) (e.g. partly bonded, inefficient or high/low gain or offset channels). Most pathological channels were identified in the three point gain or response curve scans. Figure 4.20 displays two typical defects leading to lost channels. The empty channel on the right gives no response at all and is hence classified “dead”. Another group of channels exhibits a reduced noise level of only about  $600 e^- \text{ ENC}$ , corresponding to the noise level expected for the bare hybrid, indicating missing or damaged wire bonds. Two effects connected with high noise are illustrated in Figs. 4.22 and 4.23. The former shows the effect of a short circuit of a small number of sensor strips, which results in increased noise, accompanied by a low  $vt50$  value and zero gain. The latter shows a “noise bump” as observed sometimes in the input noise distributions of modules equipped with CiS sensors. The cause are probably surface charge phenomena connected to the pathological behaviour of CiS sensors when biased in dry conditions. Tests in other institutes showed that these noise bumps can be cured if the module is exposed to ionized air for a couple of hours [104].

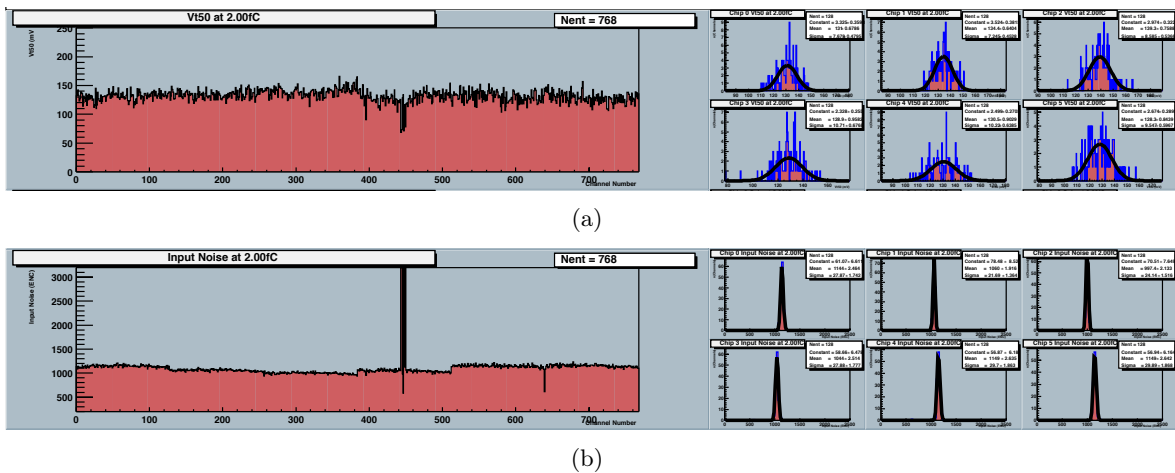


**Figure 4.22:** Monitoring results of  $vt50$  (a) and the input noise for a short circuit detected on an Inner module assembled in Freiburg (three point gain scan before trimming). The corresponding gain distribution is empty for the affected channels.

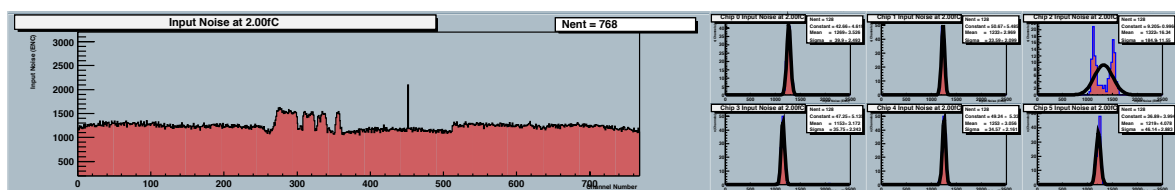


**Figure 4.23:** Input noise vs. channel number for a Freiburg Inner module with “noise bumps” (three point gain scan before trimming).

The total effective noise of the modules is the result of the combination of the front-end electronics noise, the gain spread and the offset spread. The former is the equivalent noise charge for the front-end system including the silicon strip detector, as determined in the three point gain and response curve tests. It is specified to be less than  $1500 e^-$  ENC before irradiation and  $1800 e^-$  ENC after the specified dose of  $2.14 \cdot 10^{14} n_{eq}/cm^2$ . The other two factors affect the channel-to-channel threshold matching, which, in turn, influences the final noise occupancy. The noise hit occupancy needs to be significantly lower than the real hit occupancy to ensure that it does not affect the data transmission rate, the pattern recognition and the track reconstruction. The foreseen limit of a noise occupancy below  $5 \cdot 10^{-4}$  per strip requires the discrimination level in the front-end electronics to be set to 3.3 times the equivalent noise charge. To achieve this condition with an operating threshold of 1 fC, the total equivalent noise charge should never be greater than  $1900 e^-$  ENC, including the electronics noise as well as the offset and gain spread in the chips. If the noise is higher, the operating threshold could be increased provided that it does not compromise the efficiency. A typical result of a noise occupancy measurement in a threshold scan without injecting a calibration pulse is displayed in Fig. 4.24.

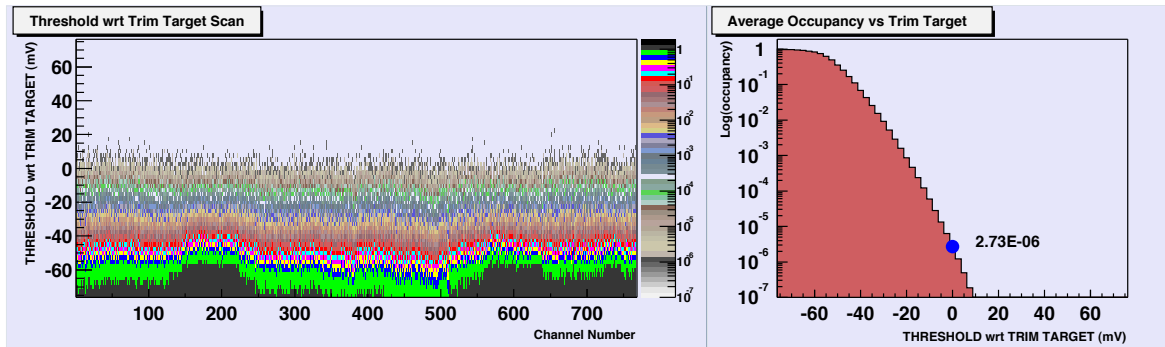


**Figure 4.24:** Noise occupancy measured in a threshold scan without injecting a calibration charge. Occupancy for one data stream per channel as a function of the threshold (a) and average occupancy for the stream as a function of the threshold (b) (taken from Ref. [105]). The threshold is expressed with respect to the 1 fC point (0 mV) as determined during the trimming procedure.

## 4.4 Results

After testing in Freiburg, the modules were shipped to the institutes in Amsterdam and Liverpool, where they were mounted on the two endcaps. Some data on the performance of the Freiburg modules after assembly on the disk are presented in the following in Section 4.4.1. After finalizing the module production and assembly on the disks, the details of the complete module production were gathered and published in Ref. [77]. These results are summarized in Section 4.4.2.

### 4.4.1 Performance after assembly on the disk

The first Freiburg Inner modules to be assembled on disk were a set of CiS modules, destined for disks 5c and 6c in Endcap C<sup>10</sup>. Figure 4.25 shows the distributions of the number of bad

<sup>10</sup>The numbering of the disks is as follows: Endcap A (assembled in Amsterdam) consists of the disks 1a to 9a (from the barrel to the outer end of the endcap), Endcap C consists of the disks 1c to 9c. The Barrel is referred to as “B”. Only five disks (2 to 6) per endcap are equipped with Inner modules, 40 per disk.

channels per module for the Freiburg Inners on two of the disks mounted in endcap C. Both disks are fully equipped with CiS Inners, which in general have more pathological channels than modules built from Hamamatsu sensors usually do. The Freiburg share of 71 modules on these two disks shows an average 6.4 bad channels.

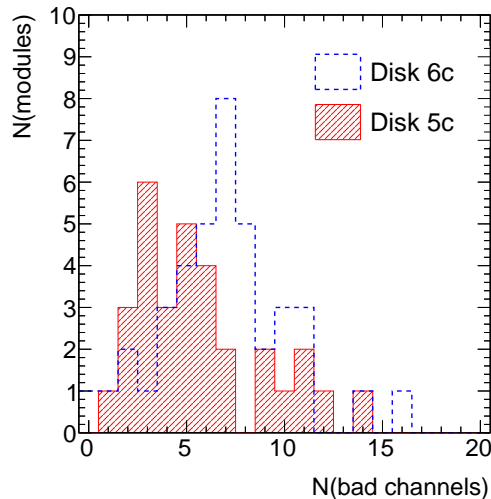


**Figure 4.25:** Number of faulty channels on the Freiburg Inner modules mounted on two of the disks of Endcap C (displayed data from test measurements on the disk [103]). The inner ring of both disks is fully equipped with CiS sensors. The average number of defective channels are 5.7 on disk 5c (31 modules from Freiburg) and 6.9 on disk 6c (40 modules).

Figure 4.26 shows the average gain (Fig. 4.26(a)), noise (Fig. 4.26(b)), offset (Fig. 4.26(c)) and the number of defective channels (Fig. 4.26(d)) of all modules mounted on disk 6c, which is fully equipped with CiS Inner modules from the Freiburg production. The position of the Inner modules can clearly be identified in the noise distribution, which spreads around  $1060 e^-$  ENC for the Inners but is much larger for the long Middle and Outer modules.

#### 4.4.2 Summary of the results from tests during construction

A total of 2380 endcap modules were assembled by the ATLAS SCT collaboration and their main performance parameters measured and compared with the nominal values in order to ascertain the usability of each module. Mechanical and electrical properties were the main issues checked during the production process. Figure 4.27 shows the leakage current distributions at bias voltages of 150 V (Fig. 4.27(a)) and 350 V (Fig. 4.27(a)) of all the modules, regardless of the strip length. Only about 1.4% of the modules failed the  $I - V$  test irreversibly and had to be rejected.

A fraction of 3.9% of all endcap modules failed the electrical tests. Figure 4.28 shows both the noise occupancy (Fig. 4.28(a)) and the electronics noise (Fig. 4.28(b)) as measured in the electric tests of the modules. The noise occupancy is well below the upper limit of  $5 \cdot 10^{-4}$  in the specifications. The noise distribution is composed of three different components, corresponding to the three different sensor geometries.

Figure 4.29 shows the number of bad channels. On average, after module assembly, one finds about three more dead channels than were found when measuring the bare hybrid. This excess contains both the sensor defects and the channels lost during the assembly process.

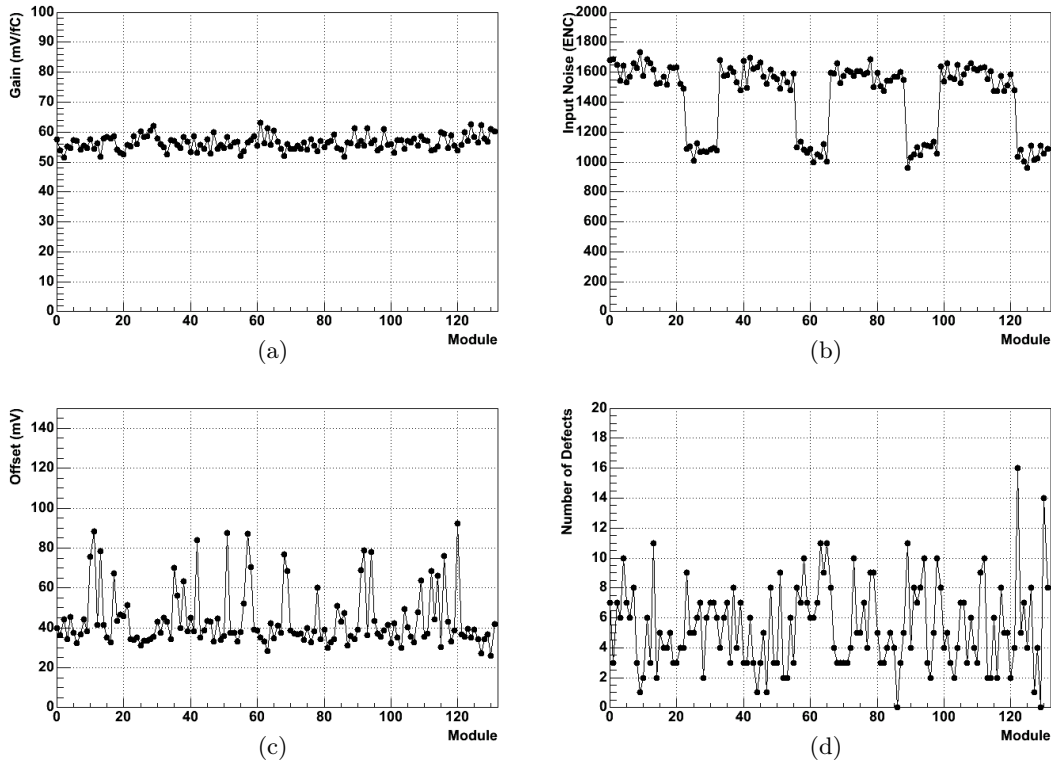


**Figure 4.26:** Average (per module) gain (a), noise (b), offset (c) and number of bad channels (d) of the modules on disk 6c, as obtained in tests at the endcap assembly site in Liverpool. The Inner modules on this disk were supplied by the Freiburg group. Their position in the distributions can be identified by the characteristically low noise level (all taken from [106, 103]).

Overall, only 7% of the production modules were rejected, including those exhibiting defects in the visual inspection and modules failing to meet the mechanical specifications.

## 4.5 Summary

Between spring 2004 and autumn of 2005, 190 SCT endcap Inner modules were assembled in Freiburg. The responsibility for the validation of their electrical functionality within the specifications imposed by the ATLAS SCT collaboration was part of this thesis. Except for some problems with the breakdown and noise behaviour of some modules equipped by the supplier CiS, most of the modules were well within the specifications and could be delivered in time to the endcap assembly sites at NIKHEF (Amsterdam) and the University of Liverpool. Except for the mentioned problems with the CiS sensors, the failure causes for those few fully assembled modules that were finally rejected were damages due to scratches or corrosion. In September 2008, the ATLAS detector was fully assembled in its underground cavern and ready for the first beam. By now, the data taking has started very successfully and the SCT detector has proved its functionality in full operation, contributing to a variety of first physics results.

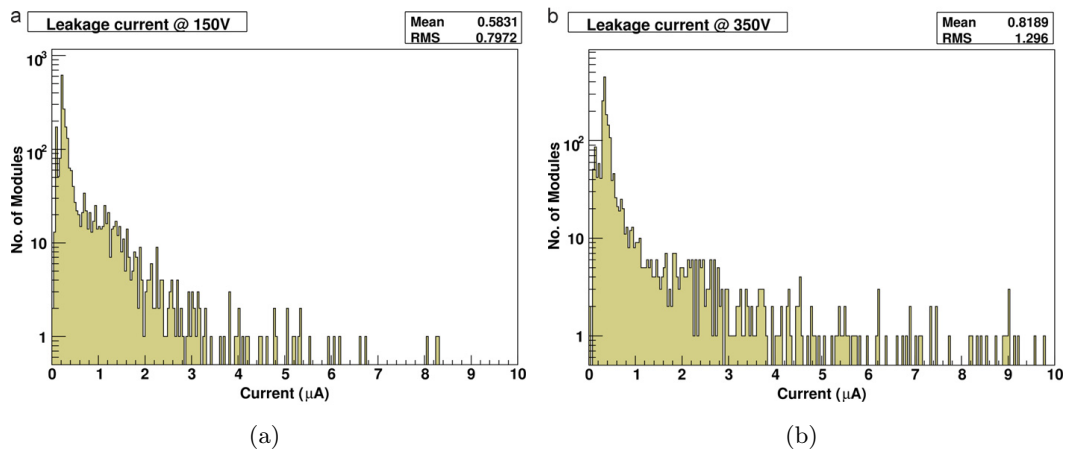


**Figure 4.27:** Leakage current in mA for all ATLAS SCT endcap modules biased with 150 V (a) and 350 V (b) (taken from Ref. [77]).

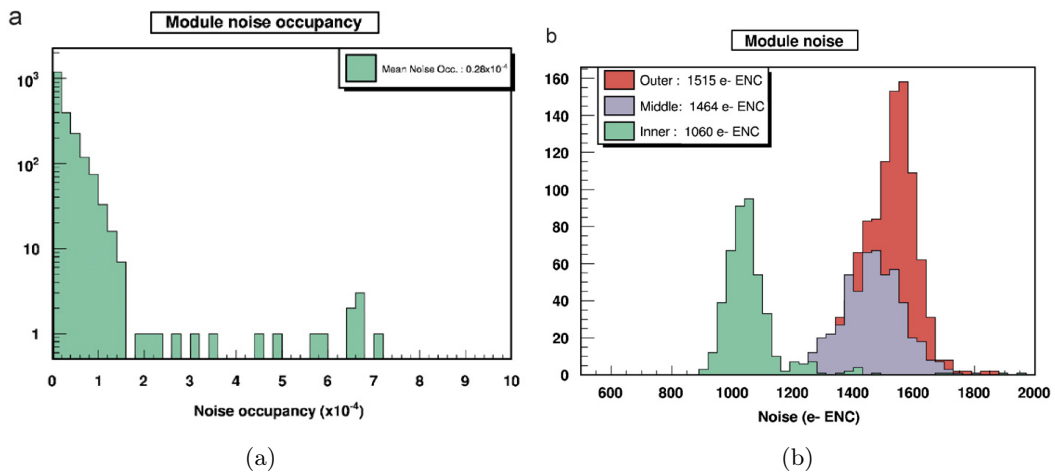


**Figure 4.28:** Average noise occupancy per module at 1fC threshold (a) and average electronic noise (b) for all ATLAS SCT endcap modules (taken from Ref. [77]).

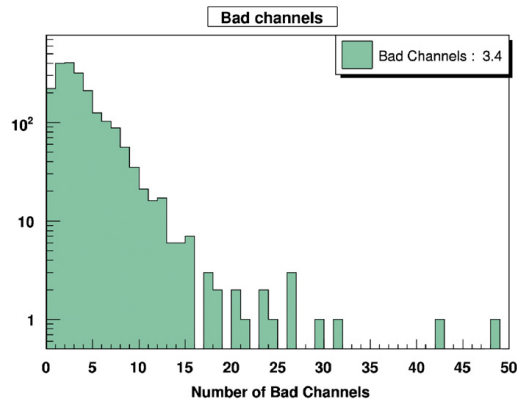


**Figure 4.29:** Distribution of the number of bad channels for all ATLAS SCT endcap modules (taken from Ref. [77]).

# 5 Projective likelihood estimator for electron isolation

Many physics analyses in ATLAS are based on final states with isolated leptons from decays of  $W$  or  $Z$  bosons. These channels usually have the advantage of smaller background expectation compared with channels with hadronic final states. Nevertheless, they may also suffer from jet background processes, either from jets that are by mistake reconstructed as lepton candidates, or from real leptons from semi-leptonic heavy quark decays that mimic the isolated leptons of the signal. Though these leptons mostly have low transverse momenta and are identified less efficiently than isolated leptons, they can have a big impact as long as the background cross section is large enough compared with that of the signal. For the channel studied in this thesis, high rejection of lepton background from heavy quark decays is required to suppress a large contamination from semi-leptonic  $t\bar{t}$  events<sup>1</sup>.

Therefore, the `IsolationLikelihood`, was established in the course of this thesis (see also Refs. [107, 108]), which is a dedicated projective likelihood estimator tool for the separation of isolated from non-isolated electron background. The tool, which meant to be used in addition to the standard electron identification criteria, was made available in the Athena software. Furthermore, the results of this study for electrons are also transferred to muons to take advantage of the large background rejections provided by the likelihood tool for both lepton flavours in the Higgs analysis described in Chapter 6.

## 5.1 Monte Carlo samples

Lacking experimental data, Monte Carlo datasets are employed to study the features of signal and background electrons. As a source of clean isolated electrons from gauge boson decays,  $Z \rightarrow e^+e^-$  events are used. Background electrons from the decays of heavy quarks are obtained from a sample of  $t\bar{t}$  events, filtered for a pair of leptons with equal electric charge on generator level to provide a sufficiently large sample of background events for the  $t\bar{t}H$  study<sup>2</sup>. The same sample was furthermore used to study signal electrons from  $W$  boson decays in an environment with larger jet activity. For the study of the influence of pile-up on the electron isolation, a sample of  $Z \rightarrow e^+e^-$  events, overlaid with minimum-bias events is used. The sample assumes an average of 2.3 minimum-bias events per event, corresponding to a luminosity of  $10^{33} \text{ cm}^{-2}\text{s}^{-1}$ . An overview of the samples and their sizes is given in Table 5.1.

Samples of “signal electrons” are obtained from these datasets by demanding a generated electron from a  $Z$  or  $W$  boson decay to be found within a cone of opening angle  $\Delta R = 0.1$  around the electron candidate. “Background electrons” are selected, if a generated electron that can be traced back to the semi-leptonic decay of a  $b$ - or  $c$ -hadron is found in the cone. Only

---

<sup>1</sup>The term “semi-leptonic”  $t\bar{t}$  events in the following refers to top quark pair production events, where one of the two  $W$  bosons decays into a charged lepton and a neutrino, whereas the other decays into a pair of quarks. Events with two leptonic/hadronic  $W$  boson decays are accordingly referred to as “fully leptonic” and “hadronic”  $t\bar{t}$  events.

<sup>2</sup>A description of the filter and the sample is given in Section 6.3.2.

Process	Generator	# events	Remark
$Z \rightarrow e^+e^-$	PYTHIA 6.3	12700	
$Z \rightarrow e^+e^-$	PYTHIA 6.3	2750	Pile-up ( $L = 10^{33} \text{ cm}^{-2}\text{s}^{-1}$ )
$t\bar{t}$	MC@NLO	475450	Same charge lepton filter

**Table 5.1:** Overview of the Monte Carlo samples used for the electron isolation study.

candidates that pass the ATLAS standard electron selection cuts as described in Section 3.3.3 are taken into account. Unless otherwise stated, this study is based on the “medium” electron definition.

The samples are sub-divided into four bins in the transverse momentum  $p_T$  of the electron candidates in the range  $15 \text{ GeV} < p_T < 75 \text{ GeV}$  in the barrel and endcap regions of the detector, each<sup>3</sup>. Only electrons within this transverse momentum range and inside the pseudorapidity range  $0 < |\eta| < 1.37$  (“barrel”) or  $1.52 < |\eta| < 2.47$  (“endcap”) are considered in the analysis<sup>4</sup>. Table 5.2 lists the ranges of the bins in  $p_T$  and  $\eta$  and the available number of signal and background electrons in the studied Monte Carlo samples per bin.

Bin	$ \eta $	$p_T$ [GeV]	$N_S$			$N_B$
			$Z \rightarrow e^+e^-$	$Z \rightarrow e^+e^-$ pile-up	$t\bar{t}$	$t\bar{t}$
1	0 - 1.37	15 - 19	593	141	9287	45124
2	0 - 1.37	19 - 27	1639	319	22622	52785
3	0 - 1.37	27 - 43	4637	1008	38512	40413
4	0 - 1.37	43 - 75	3117	657	45861	16967
5	1.52 - 2.47	15 - 19	333	83	3773	13526
6	1.52 - 2.47	19 - 27	1033	230	8171	14949
7	1.52 - 2.47	27 - 43	3030	650	13613	11196
8	1.52 - 2.47	43 - 75	1924	443	15054	4407

**Table 5.2:** Division of the samples into bins of the transverse momentum  $p_T$  and the pseudorapidity  $\eta$  and numbers of generated signal and background electrons. The signal electron numbers of electrons generated in  $W$  or  $Z$  boson decays are given for all three samples listed in Table 5.1. Background electrons from the decay of  $b$ - or  $c$ -hadrons are only selected from the  $t\bar{t}$  dataset.

Tables 5.3 and 5.4 summarize the signal selection efficiencies and background rejections of the standard electron reconstruction and identification cuts in the bins, defined according to

$$\epsilon_{\text{ID}} \equiv \frac{\# \text{ reconstructed} + \text{identified signal electrons}}{\# \text{ generated signal electrons}} \quad (5.1)$$

and

$$R_{\text{ID}} \equiv \frac{\# \text{ generated background electrons}}{\# \text{ reconstructed} + \text{identified background electrons}} \quad (5.2)$$

<sup>3</sup>Depending on the context,  $p_T$  and  $\eta$  refer either to the generated quantities  $p_T^{\text{gen}}$  and  $\eta^{\text{gen}}$  or to their reconstructed values  $p_T^{\text{rec}}$  and  $\eta^{\text{rec}}$ . In the following it will be indicated which of the two applies.

<sup>4</sup>The contribution of non-isolated leptons and light jets that are mistaken for electrons is very high below 15 GeV and therefore leptons with smaller transverse momenta will not be considered in most analyses. Semi-leptonic heavy quark decays resulting in leptons with higher transverse momenta are rare and hence usually do not significantly contribute to the background. The crack region between the barrel and endcaps of the calorimeter ( $1.37 < |\eta| < 1.52$ ) is not considered because of the poor electron reconstruction and identification efficiency in this region and the region beyond  $|\eta| = 2.47$  is not covered by the ATLAS tracking detectors.

The electron identification cuts already remove a sizeable amount of background candidates, resulting in background rejections ranging from about 3.5 to 27, depending on the tightness of the identification requirements and the kinematic region.

Bin	$\epsilon_{\text{ID}}$				
	“loose”	$Z \rightarrow e^+e^-$		$Z \rightarrow e^+e^-$ pile-up	$t\bar{t}$
		“medium”	“tight”	“medium”	“medium”
1	0.892±0.013	0.69±0.02	0.54±0.02	0.65±0.04	0.685±0.005
2	0.905±0.007	0.743±0.011	0.598±0.012	0.70±0.03	0.736±0.003
3	0.932±0.004	0.799±0.006	0.643±0.007	0.788±0.013	0.783±0.002
4	0.933±0.004	0.821±0.007	0.668±0.008	0.846±0.014	0.812±0.002
5	0.772±0.023	0.53±0.03	0.46±0.03	0.47±0.05	0.473±0.008
6	0.779±0.013	0.53±0.02	0.48±0.02	0.53±0.03	0.538±0.006
7	0.796±0.007	0.607±0.009	0.568±0.009	0.58±0.02	0.583±0.004
8	0.797±0.009	0.629±0.011	0.590±0.011	0.59±0.02	0.620±0.004

**Table 5.3:** Signal efficiencies for the “loose”, “medium” and “tight” electron identification cuts applied on signal electrons in the  $Z \rightarrow e^+e^-$  dataset and for “medium” cuts on signal electrons in the  $Z \rightarrow e^+e^-$  dataset overlaid with minimum-bias events and the  $t\bar{t}$  dataset. Signal electrons need to be matched to the decay of a  $Z$  boson.

Bin	$R_{\text{ID}}$		
	“loose”	“medium”	“tight”
1	3.70±0.03	6.22±0.07	7.89±0.10
2	3.59±0.03	6.43±0.07	7.98±0.09
3	3.48±0.03	7.47±0.10	9.17±0.13
4	3.49±0.04	10.6±0.3	12.8±0.3
5	6.85±0.14	13.4±0.4	15.2±0.5
6	7.3±0.2	14.4±0.4	16.5±0.5
7	7.3±0.2	16.5±0.6	18.9±0.8
8	7.3±0.3	24±2	27±2

**Table 5.4:** Background electron rejections for the “loose”, “medium” and “tight” electron identification cuts. Background electrons are required to be produced in the decay of a  $b$ - or  $c$ -hadron and are selected from the  $t\bar{t}$  sample.

The  $p_{\text{T}}$  and  $\eta$  distributions of the generated signal electrons in  $Z \rightarrow e^+e^-$  and background electrons in  $t\bar{t}$ , passing the “medium” electron cuts are displayed in Fig. 5.1, together with the boundaries of the bins. In the following, these are used as standard signal and background samples, if not indicated otherwise. The bin sizes are chosen such that a sufficiently large number of background electrons is kept per bin to ensure proper training of the likelihood tool. Especially in the larger bins, this still causes sizeable differences between the shapes of the signal and background distributions, which needs to be taken into account when interpreting the results that will be presented in the following. Figure 5.2 shows the  $p_{\text{T}}$ -resolutions and correlations between  $p_{\text{T}}^{\text{gen}}$  and  $p_{\text{T}}^{\text{rec}}$ . Whereas the  $p_{\text{T}}$  of the signal electrons tends to be underestimated, the tail on the right hand side of the distribution for background electrons shows that the energy deposition of the heavy quark jet leads to an overestimation of the transverse momentum in this case.

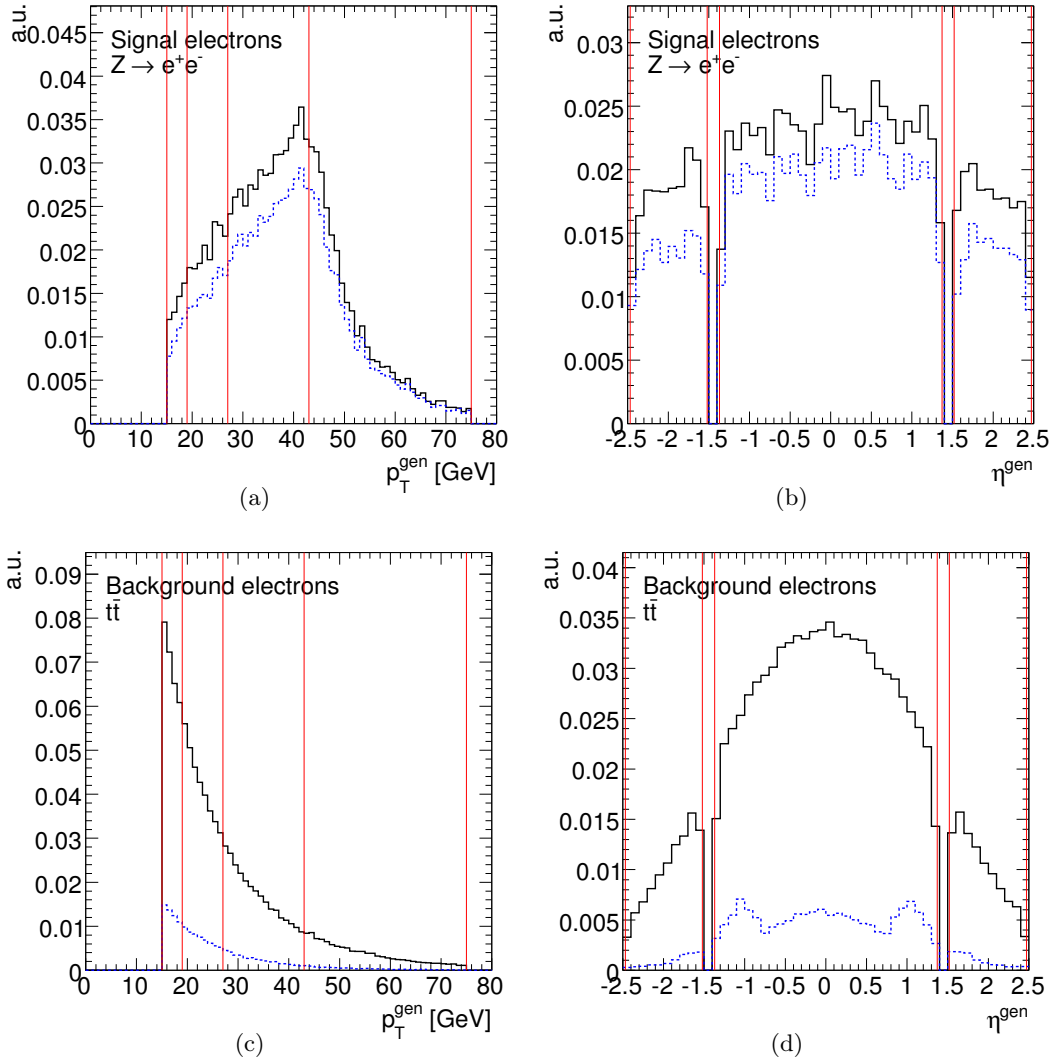


**Figure 5.1:** Distributions of the  $p_T^{\text{gen}}$  (a, c) and  $\eta^{\text{gen}}$  (b, d) of the generated electrons (solid line) and for electrons reconstructed as “medium” electron clusters (dashed line). The distributions are shown separately for signal (a, b) and background (c, d) electrons. The red lines indicate the boundaries of the kinematic bins in which the samples are divided for the study.

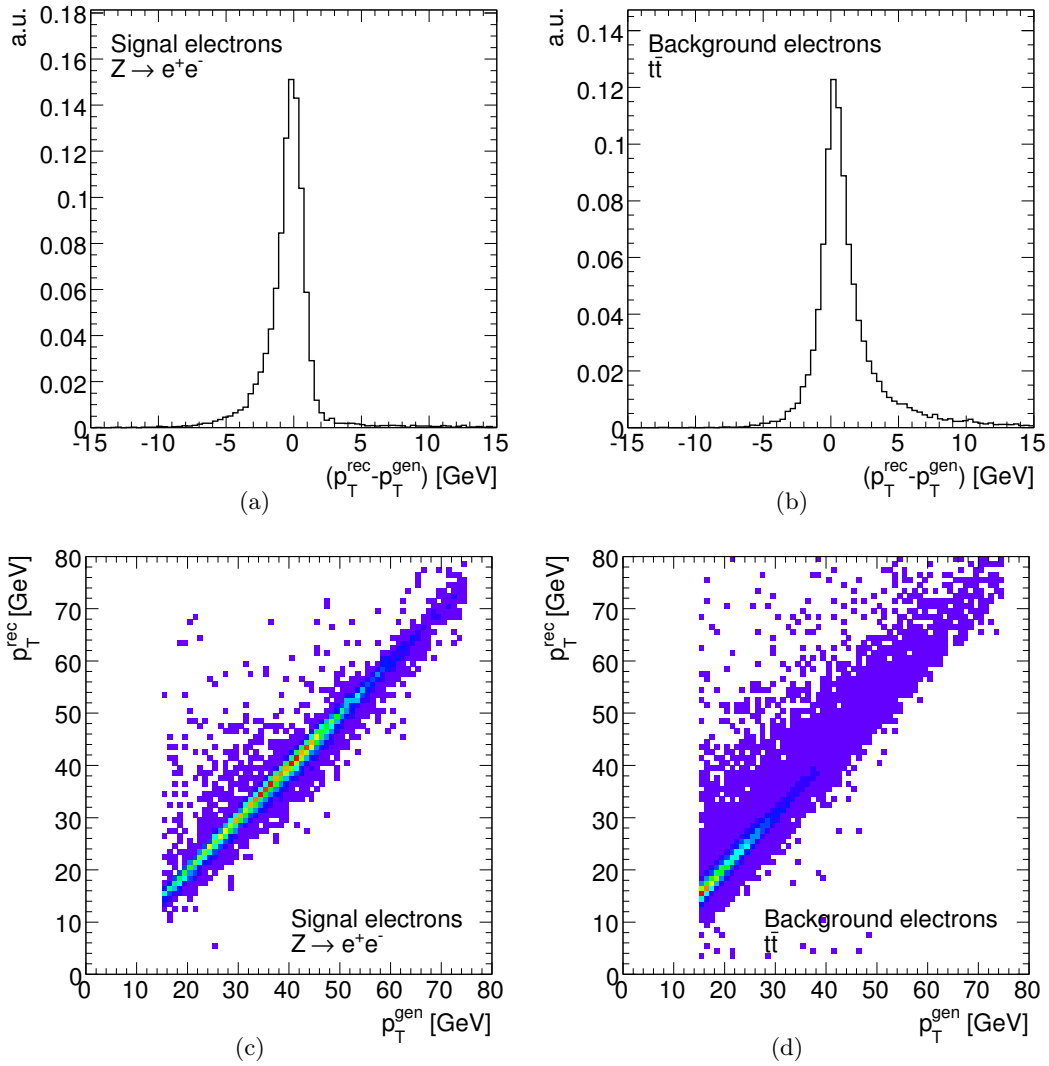


**Figure 5.2:** Transverse momentum resolution of signal electron candidates in  $Z \rightarrow e^+e^-$  (a) and background electrons in  $t\bar{t}$  events (b) and correlations between the reconstructed and generated transverse momenta in the two samples (c, d).

## 5.2 Discriminating variables

The shapes of the signal and background distributions differ in some variables based on information from measurements in the calorimeter and the Inner Detector. These differences can be exploited to distinguish signal from background electrons. A large number of variables was studied for their separation power in the course of this thesis. Those found to be the most powerful ones, are discussed in the following.

Calorimeter information can be used to check for additional energy deposition close to the electron cluster. In the case of background electrons a lot of extra calorimeter activity is expected to be caused by additional particles from the heavy quark jet<sup>5</sup>. The strongest discriminating variables are (see Fig. 5.3 for examples of their signal and background distributions):

- The transverse energies  $E_T^{\text{cone}}(0.2)$  and  $E_T^{\text{cone}}(0.4)$  deposited in the electromagnetic and hadronic calorimeter cells in cones of  $\Delta R = 0.2$  and  $\Delta R = 0.4$  around the electron cluster (Figs. 5.3(a) and 5.3(b)). The electron  $E_T$ -contribution is removed by subtracting the energy deposited in  $5 \times 14$  calorimeter cells in  $\eta \times \phi$ -direction.
- The transverse energy  $E_T^{\text{cone}}(0.4 - 0.2)$  deposited in a hollow cone of  $0.2 < \Delta R < 0.4$  around the electron cluster (Fig. 5.3(c)).

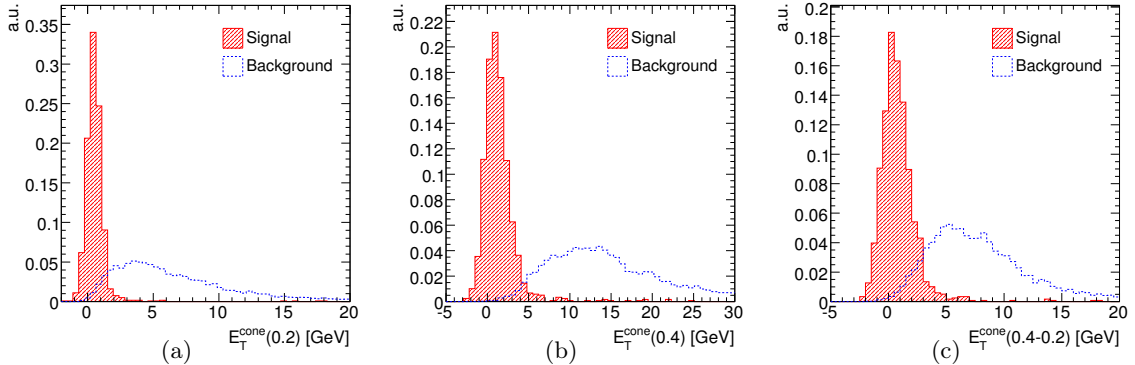


**Figure 5.3:** Comparison of the signal and background distributions of the calorimeter based isolation variables  $E_T^{\text{cone}}(0.2)$  (a),  $E_T^{\text{cone}}(0.4)$  (b) and  $E_T^{\text{cone}}(0.4 - 0.2)$  (c). The bin  $19 \text{ GeV} < p_T < 27 \text{ GeV}$  and  $0 < |\eta| < 1.37$  is shown as an example and all distributions are normalized to unity, including the overflows.

Information on additional tracks in the vicinity of electron candidates can also be used to reject background candidates. The number of tracks, as well as their transverse momenta, summed up with suitably chosen weights, are candidates for powerful discriminating variables. To guarantee optimal performance, tracks originating from photon conversions and pile-up need to be rejected, whereas as many tracks belonging to the jet as possible should be taken into account. The tracks are therefore selected according to the relatively loose “standard quality cuts” defined for the tracking studies in Ref. [71]<sup>6</sup>, but with two exceptions: A stronger

<sup>5</sup>Also the shape of the shower itself and its track match quantities (as they are also used for the ID cuts) can be exploited to distinguish between signal and background candidates. The discrimination power of these variables is nevertheless small compared with the strongest isolation variables considered in this study. A list of some of the candidates that were investigated is given in Appendix A.1.

<sup>6</sup>These require at least seven hits in the silicon detector and a minimum track  $p_T$  of 1 GeV. In addition, the impact parameters are required to fulfil  $|IP_T| < 2 \text{ mm}$  and  $|IP_L| < 10 \text{ mm}$ .

cut on the longitudinal impact parameter ( $IP_L < 2$  mm) is applied to reject pile-up tracks, with the impact parameters defined as in Eq. (3.1) in Section 3.3.1. Furthermore, the minimum  $p_T$  is lowered to 0.5 GeV to exploit the information of as many tracks as possible.

The impact parameter of the track associated to the electron itself can also be used to reject background candidates from heavy quark decays. Due to the long lifetimes of  $b$ - and  $c$ -hadrons, the transverse impact parameter significances of their daughter leptons tend to be larger than those of leptons from  $W$  or  $Z$  boson decays.

The most powerful isolation variables based on tracking information are (see Fig. 5.4 for examples of their signal and background distributions):

- $\Sigma p_T^{\text{trk}}(0.2)$  and  $\Sigma p_T^{\text{trk}}(0.4)$ : the sum of the  $p_T$  of all additional tracks measured in cones of  $\Delta R < 0.2$  and  $0.4$  around the electron cluster (Figs. 5.4(a) and 5.4(b)).
- $\Sigma p_T^{2\text{trk}}(0.2)$  and  $\Sigma p_T^{2\text{trk}}(0.4)$ : the sum of the  $p_T^2$  of all additional tracks (Figs. 5.4(c) and 5.4(d)).
- $\Sigma(p_T^{\text{trk}}/\Delta R)(0.2)$  and  $\Sigma(p_T^{\text{trk}}/\Delta R)(0.4)$ : the  $p_T$ -sum, weighted with the distance between the track and the cluster (Figs. 5.4(e) and 5.4(f)).
- The maximum transverse momenta  $p_T^{\text{max trk}}(0.2)$  and  $p_T^{\text{max trk}}(0.4)$  of the additional tracks in cones of  $\Delta R < 0.2$  and  $0.4$  around the electron cluster (Figs. 5.4(g) and 5.4(h)).
- The transverse impact parameter significance  $|IP_T|/\Delta IP_T$  of the electron track (Figure 5.4(i)).

A combination of information from both systems helps to increase the overall performance. The advantage of the calorimeter lies in its equal sensitivity to charged and neutral particles. The tracking detectors, on the other hand, are capable only to detect charged particles but allow their tracks to be traced back to their original vertex. This can be exploited to reject tracks from vertices other than the vertex of the interaction of interest, which makes the tracking information less sensitive to pile-up effects than the calorimeter information (see the first part of Appendix A.2 for a discussion of pile-up conditions).

### Electron isolation in environments with high jet activity

$Z \rightarrow e^+e^-$  events are a source of isolated signal electrons in very clean conditions, since only few jets are produced in addition to the electron pair. Compared with these, signal electrons in final states with higher jet multiplicities, e.g. the electrons from  $W$  boson decays in semi-leptonic  $t\bar{t}$  events, are less easy to isolate. Leakage of energy depositions or tracks belonging to the jets into the vicinity of the electrons cause the distributions of the discriminating variables to look more background-like. This is demonstrated in Fig. 5.5, which shows comparisons of the signal distributions of some of the discriminating variables in  $Z \rightarrow e^+e^-$  and  $t\bar{t}$ . The distributions differ especially in the tails of the variables calculated in cones of opening angle  $\Delta R = 0.4$ , which are much larger in the case of  $t\bar{t}$ . This leads to rapid loss in signal efficiency already in the region where a cut provides only a small background rejection. This effect needs to be taken into account when selecting a suited set of discriminating variables as input for the likelihood tool.

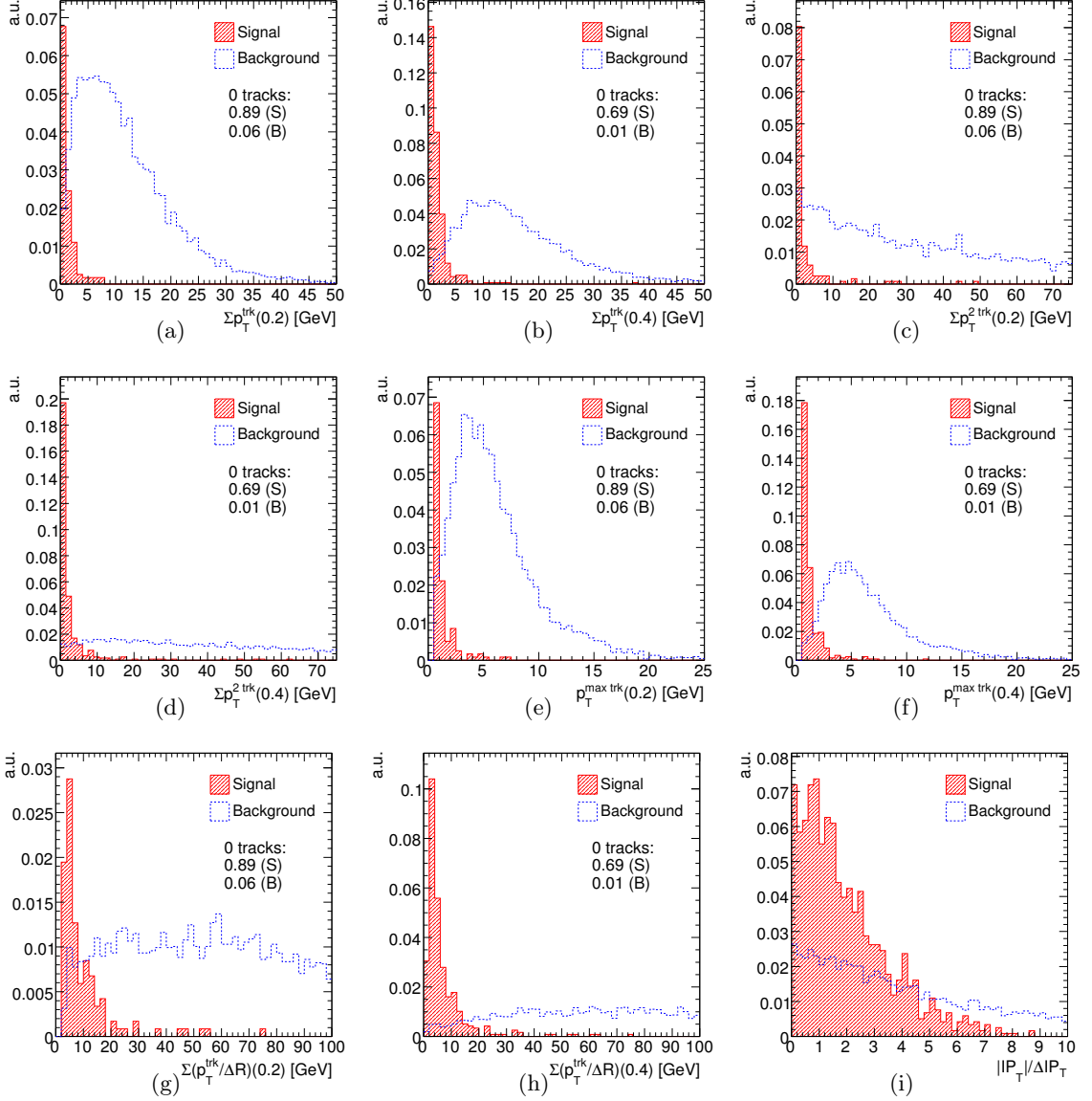


**Figure 5.4:** Comparison of the signal and background distributions of the tracking based isolation variables  $\Sigma p_T^{\text{trk}}(0.2)$  and  $\Sigma p_T^{\text{trk}}(0.4)$  (a, b),  $\Sigma p_T^2(0.2)$  and  $\Sigma p_T^2(0.4)$  (c, d),  $\Sigma(p_T^{\text{trk}}/\Delta R)(0.2)$  and  $\Sigma(p_T^{\text{trk}}/\Delta R)(0.4)$  (e, f),  $p_T^{\text{max trk}}(0.2)$  and  $p_T^{\text{max trk}}(0.4)$  (g, h) and  $|IP_T|/\Delta IP_T$  (i). The distributions contain only candidates for which at least one track was found. The numbers give the fraction of candidates where no additional tracks are found in the respective cones. The bin  $19 \text{ GeV} < p_T < 27 \text{ GeV}$  and  $0 < |\eta| < 1.37$  is shown as an example and all distributions are normalized to unity, including the overflows.

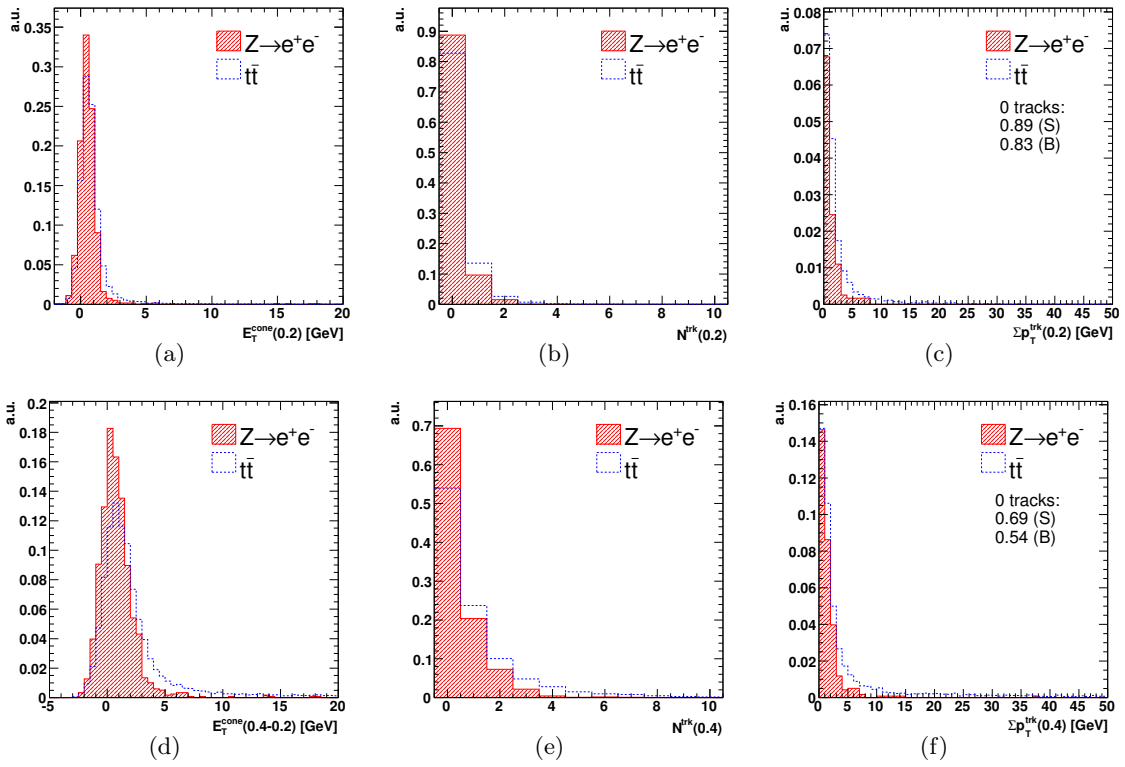


**Figure 5.5:** Comparison of the distributions of  $E_T^{\text{cone}}$ ,  $N^{\text{trk}}$  and  $\Sigma p_T^{\text{trk}}$  in cones of  $\Delta R = 0.2$  (a, b, c) and 0.4 (d, e, f) for signal electrons in  $Z \rightarrow e^+e^-$  and  $t\bar{t}$ . The bin  $19 \text{ GeV} < p_T < 27 \text{ GeV}$  and  $0 < |\eta| < 1.37$  is shown as an example and all distributions are normalized to unity.

### 5.3 The projective likelihood estimator

The projective likelihood estimator combines the separation power of a set  $x$  of discriminating variables in one single variable  $r$ , defined according to

$$r \equiv \ln \frac{P_S(x)}{P_B(x)} \approx \sum_v \ln \frac{P_S^v(x_v)}{P_B^v(x_v)} \quad . \quad (5.3)$$

Here,  $P_S(x)$  and  $P_B(x)$  are the probabilities for an electron to be signal or background, if the variable set  $x$  has been measured. The individual probabilities for the variable  $v$  to take a given value  $x_v$  are given as  $P_S^v(x_v)$  and  $P_B^v(x_v)$ , respectively, in the case of a signal and background electron. The approximation by the individual probabilities holds only in the case of weakly correlated input variables. Otherwise, the correlations are neglected, which may lead to a degradation of the separation power with respect to the optimal performance. Better results are expected from other multivariate methods in this case, such as e.g. multidimensional likelihood estimators or neural networks, which fully exploit the correlations. Such methods, however, require a sufficiently large sample of training events. The available number of Monte Carlo events to date is too small for a proper training of such advanced methods, especially in the higher  $p_T$  regions in the background. Therefore, the projective likelihood approach is chosen here, although there are considerable correlations among some of the discriminating variables discussed above (see Appendix A.3). In addition, the `IsolationLikelihood` is meant to be used for a variety of different analyses as part of Athena. To avoid the necessity of analysis dependent training, the chosen method needs therefore to be sufficiently robust still to provide reasonable results in the case of changes in the distributions of the discriminating variables, e.g. due to changes in the event reconstruction or different event topologies.

The probabilities  $P_S^v$  and  $P_B^v$  are obtained from probability density functions (PDFs)  $p_S^v$  and  $p_B^v$  that need to be estimated either from Monte Carlo samples or, once data are available, from conveniently defined data samples. For the time being, Monte Carlo samples are used to determine the PDFs. In order to reduce the unwanted contributions of the event kinematics to the separation power of the likelihood tool, the distributions are determined separately in the bins of  $p_T^{\text{rec}}$  and  $\eta^{\text{rec}}$  defined in Table 5.2.

The signal and background PDFs are estimated from the distributions of the input variables, using a kernel density estimator (KDE). In short, the idea of the KDE is to produce a continuous estimate from a finite dataset consisting of  $n$  events by adding up a set of suitably chosen Gaussian distributions for each event instead of simple histogramming. The technique is non-parametric, so no assumptions have to be made on the underlying model. It is therefore superior to parametric methods like e.g. fits if, as in the case of this analysis, there is no knowledge about this model. Following Ref. [109], the method used in this thesis is derived from the procedure described in Ref. [110], modified such that it can be directly applied to the histogrammed distributions of the input variables. The result is again a histogram with the same number of bins as the original one, such that the likelihoods  $P_S^v$  and  $P_B^v$  are given by the content of the respective bin of these histograms. This avoids the necessity to evaluate a continuous function for each candidate to be tested. If the binning is chosen sufficiently small, the signal and background distributions can be determined precisely enough to ensure no significant deviation from the values obtained with the un-binned approach. The estimation of the true PDFs  $p^v(x)$  is performed in two steps, using the histogrammed distribution  $\hat{p}_0^v$  as a starting point. The histogram  $\hat{p}_0^v$  is assumed to be normalized to unity and consists of  $N_{\text{bins}}$  bins with entry  $\hat{p}_0^v(x_i)$  in the  $i$ -th bin.

In the first step,  $p^v(x)$  is estimated using a “fixed” kernel estimator  $\hat{p}_1^v$  with entries  $\hat{p}_1^v(x_i)$ .

These are calculated according to

$$\hat{p}_1^v(x_i) = \sum_{j=1}^{N_{\text{bins}}} \hat{p}_0^v(x_j) \cdot \frac{1}{h} K\left(\frac{x_i - x_j}{h}\right) \quad , \quad (5.4)$$

with a Gaussian kernel

$$K(x) = \frac{1}{\sqrt{2\pi}} \exp\left(-\frac{1}{2}x^2\right) \quad . \quad (5.5)$$

The distribution  $K$  is sampled by a histogram with  $N_{\text{bins}}$  bins in the histogrammed approach, with  $x_i - x_j$  being the distance of the bin centres of the  $i$ -th and  $j$ -th bin. The width of  $K$  is given by the “smoothing parameter”  $h$ . In the fixed case,  $h$  depends only on the width  $\sigma$  of the distribution to be smoothed according to

$$h = \left(\frac{4}{3}\right)^{1/5} \sigma n^{-1/5} \quad , \quad (5.6)$$

with  $\sigma$  estimated by the RMS of the original histogram  $\hat{p}_0$ . This choice of  $h$  minimizes the mean integrated squared error of the estimator  $\hat{p}_0^v(x_i)$ , if the data follow a Gaussian distribution and for a large number of events (see Ref. [110]). To ensure reasonable results, the input variables are therefore transformed such that the shapes resemble a Gaussian distribution as much as possible. In general, a logarithmic transformation of the form

$$y = \ln(x + c_1) + c_2 \quad (5.7)$$

is a sensible choice, with the constant  $c_1$  adjusted such that it shifts the bulk of the original distribution to positive values<sup>7</sup>. Candidates with no additional tracks in their vicinity are excluded from the transformation in the case of the tracking based variables. The value of the isolation variable is then fixed to zero. The constant  $c_2$  is introduced for the tracking variables, to shift the transformed part of the distributions back to positive values to keep both parts separated<sup>8</sup>.

The fixed kernel estimator provides reasonable results in regions where the histogram is strongly populated. In order to get a sensible estimate of the distributions also in the tails, a second iteration, using an “adaptive” kernel estimate, is applied to the outcome  $\hat{p}_1^v(x_i)$  of the first one, according to

$$\hat{p}^v(x_i) = \sum_{j=1}^{N_{\text{bins}}} \hat{p}_1^v(x_j) \cdot \frac{1}{h_j} K\left(\frac{x_i - x_j}{h_j}\right) \quad . \quad (5.8)$$

The smoothing parameter  $h_j$  is in this step chosen individually for each bin as

$$h_j = \frac{h}{\sqrt{n\hat{p}_1^v(x_j)}} \quad , \quad (5.9)$$

thus being the larger the fewer events effectively contribute to the content of the respective bin. This choice ensures that the second iteration affects mainly those bins with small entries, whereas no further smoothing is applied to highly populated regions. The resulting estimators  $\hat{p}^v(x_i)$  for the PDFs  $p^v(x)$  for some of the discriminating variables in one example  $p_T$  and  $\eta$ -bin are shown in Fig. 5.6, together with their raw distributions  $\hat{p}_0^v(x_i)$ .

<sup>7</sup>Possible remaining (small) negative tails are mapped onto a single value close to 0.

<sup>8</sup>Table A.1 in Appendix A.4 gives an overview on all considered isolation variables and the applied transformations.

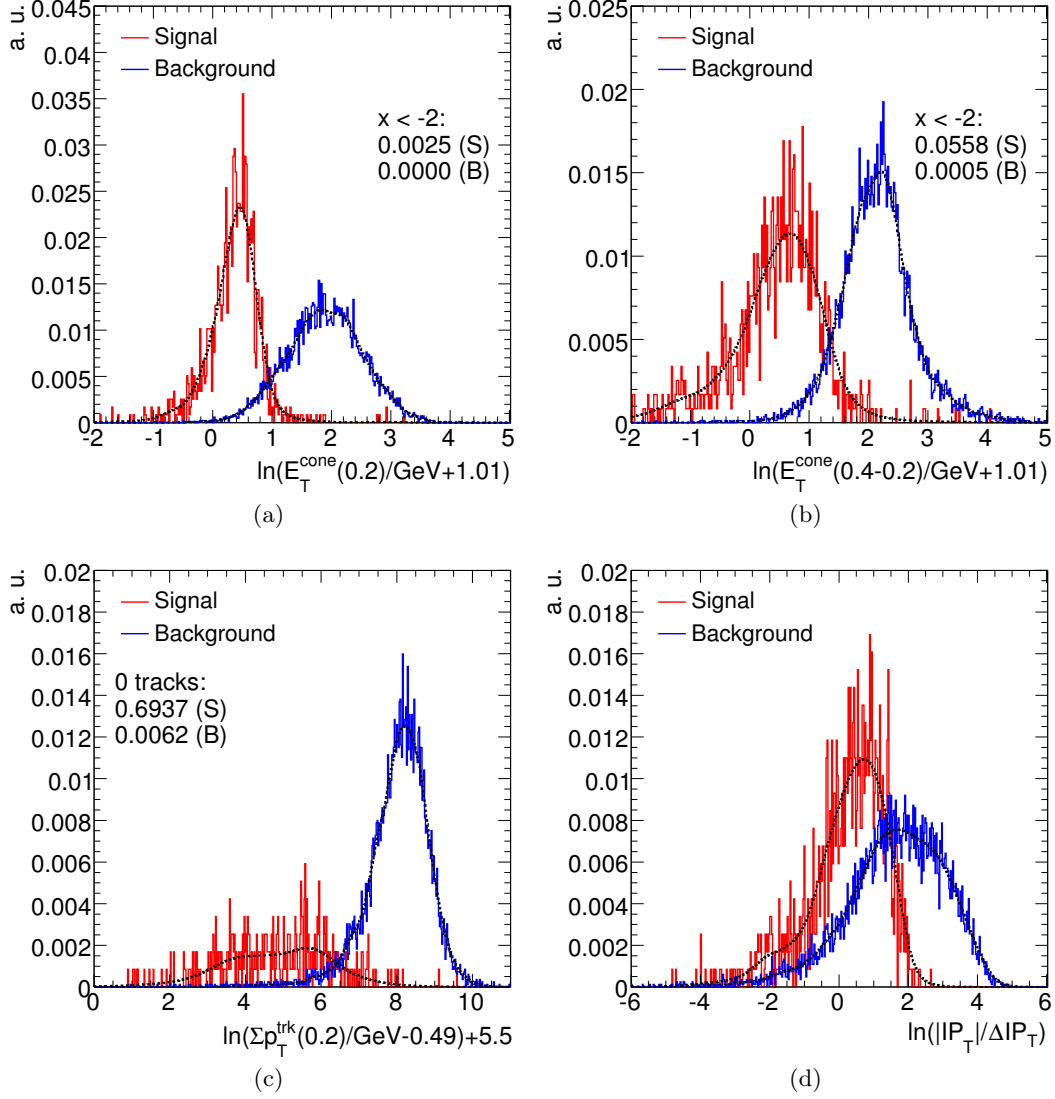


**Figure 5.6:** Raw transformed signal and background distributions and PDF estimates for the four variables  $E_T^{\text{cone}}(0.2)$  (a),  $E_T^{\text{cone}}(0.4-0.2)$  (b),  $\Sigma p_T^{\text{trk}}(0.4)$  (c) and  $|IP_T|/\Delta IP_T$  (d) for  $19 \text{ GeV} < p_T < 27 \text{ GeV}$  and  $0 < |\eta| < 1.37$ . The bins gathering the underflow (e.g. the 0-tracks bin in the case of  $\Sigma p_T^{\text{trk}}(0.4)$ ), which are not affected by the smoothing procedure, are not displayed but their content is given by the numbers in the figures.

To classify the electron candidates in a test sample, the likelihood output value  $r$  is calculated according to Eq. (5.3), looking up the individual likelihood values  $P_S^v$  and  $P_B^v$  in the respective bins of the histograms that are obtained with the above described procedure.

## 5.4 Variable selection and separation power of the likelihood output

To study the separation power of individual input variables and their impact on the performance in combination with other variables, the  $r$  distributions are calculated for various sets of input parameters. To compare the outcome, “performance curves” are studied, which show the background rejection  $R_r$  as a function of the signal efficiency  $\epsilon_r$  corresponding to the same cut on  $r$ . The efficiency and rejection are defined as

$$\epsilon_r \equiv \frac{\# \text{ identified signal electrons, passing the cut on } r}{\# \text{ identified signal electrons}} \quad (5.10)$$

and

$$R_r \equiv \frac{\# \text{ identified background electrons}}{\# \text{ identified background electrons, passing the cut on } r} \quad (5.11)$$

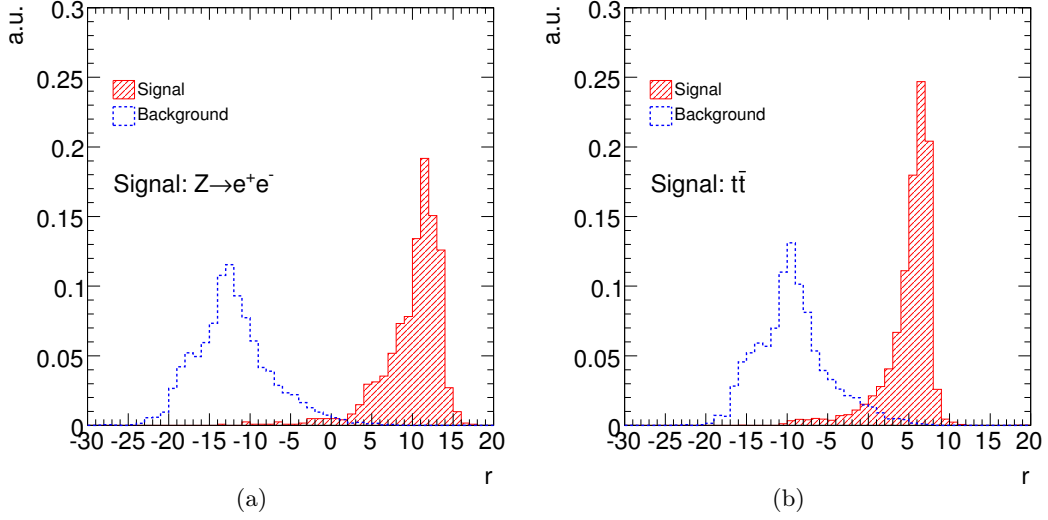
To find the optimal choice of input variables, the performance curves are calculated and compared for different input variable sets. A detailed comparison of the input variables introduced in Section 5.2 is given in Appendix A.5. The comparison is done in bins of  $p_T$  and  $\eta$  and in the following, only the bin  $19 \text{ GeV} < p_T < 27 \text{ GeV}$  and  $0 < |\eta| < 1.37$  is shown as an example<sup>9</sup>.

The best performing set of input variables found for most physics processes is the combination of  $E_T^{\text{cone}}(0.2)$ ,  $E_T^{\text{cone}}(0.4 - 0.2)$ ,  $\Sigma p_T^{\text{trk}}(0.4)$  and  $|IP_T|/\Delta IP_T$ , referred to as “default” selection of variables in the following. In the case of physics analyses in environments with high jet multiplicities, the use of isolation variables calculated in cones of  $\Delta R = 0.4$  degrades the performance of the likelihood noticeably, especially if high signal efficiencies are desired. For this case, another selection is defined in addition (referred to as “highJetMulti”), consisting of  $E_T^{\text{cone}}(0.2)$ ,  $\Sigma p_T^{\text{trk}}(0.2)$  and  $|IP_T|/\Delta IP_T$ . Examples of the resulting signal and background likelihood output distributions for the two variable sets are shown in Fig. 5.7.

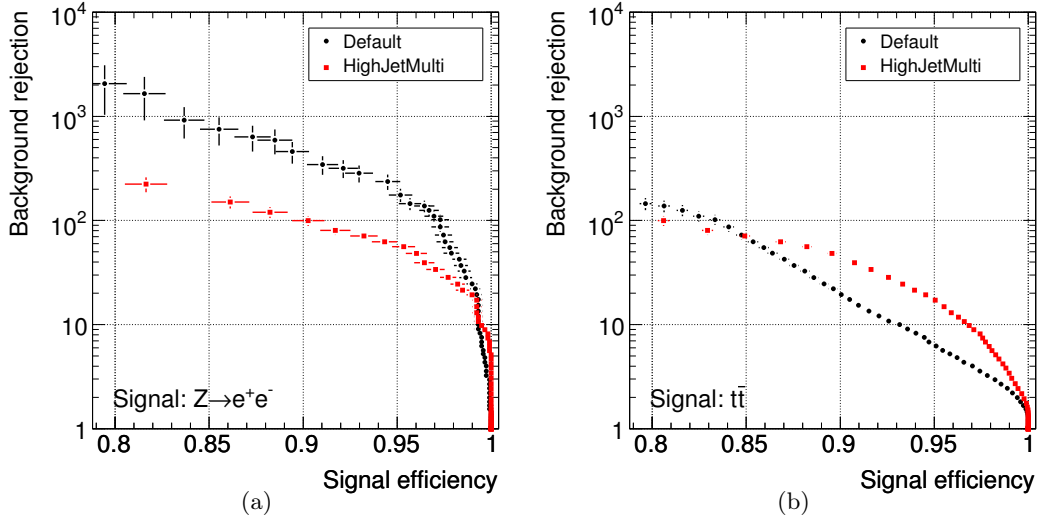
The “default” set of variables is also used to calculate the default output provided by the `IsolationLikelihood` tool as implemented in the official ATLAS reconstruction software. Nevertheless, depending on the needs an analysis, the user may want to choose his own set of variables. The Athena tool is therefore designed such that it can be configured individually and support is provided for all variables listed above.

Figure 5.8 shows a comparison of the performance for the “default” and “highJetMulti” configuration of the tool on signal test samples of  $Z \rightarrow e^+e^-$  (Fig. 5.8(a)) and  $t\bar{t}$  (Fig. 5.8(b)). Depending on the kinematic bin, background rejection factors of the order of 20 to 500 can be reached at 95% signal efficiency for isolated signal electrons from  $Z \rightarrow e^+e^-$  events in the “default” configuration. Rejection factors up to 1000 are possible, if  $\epsilon_r$  is decreased to 90%. The rejection that is reached by the “highJetMulti” selection is in general considerably lower than for the “default” selection if electrons from the  $Z \rightarrow e^+e^-$  dataset are considered. Especially at low  $p_T$  and in the endcaps the rejections at a given efficiency differ by a factor up to ten. Rejection factors of the order 10 to 100 can be reached at 95% signal efficiency

<sup>9</sup>To ensure unbiased tests of the performance, the testing sample should be independent from the sample the PDFs are trained with. Nevertheless, because of the small number of available background events, subdividing the available events in two subsets of reasonable size is impossible in some bins. Tests in bins that contain a sufficiently large number of events reveal no visible deviations in the performance curves obtained with independent and identical test and training samples. No quantitative results are obtained from studies of the performance curves in the following. Therefore, identical testing and training samples are used, assuming that the conclusions drawn are not affected by a possible small bias in the bins that could not be tested.



**Figure 5.7:** Distribution of the output value  $r$  in the signal and background for the “default” (a) and “highJetMulti” (b) variable selections. Signal electrons from  $Z \rightarrow e^+e^-$  events are used in (a), whereas in (b) the signal electrons are selected from the  $t\bar{t}$  dataset. The bin  $19 \text{ GeV} < p_T < 27 \text{ GeV}$  and  $0 < |\eta| < 1.37$  is shown as an example and all distributions are normalized to unity.



**Figure 5.8:** Comparison of the background rejection as a function of the signal efficiency for the “default” and “highJetMulti” configurations of the likelihood in the bin  $19 \text{ GeV} < p_T < 27 \text{ GeV}$  and  $0 < |\eta| < 1.37$ . The curves are obtained with signal electrons from a sample of  $Z \rightarrow e^+e^-$  (a) and  $t\bar{t}$  (b) events.

for signal electrons in the  $t\bar{t}$  dataset with the “default” configuration, and another factor of 2 to 4 can be gained in the rejection, if  $\epsilon_r$  is decreased to 90%. In the high efficiency range, the differences between the corresponding background rejection factors obtainable with the two configurations are large, with the rejections that are attained at given  $\epsilon_r$  differing by factors of up to 10. These differences increase with rising  $p_T$  and are stronger in the barrel than in the endcaps. At high  $\epsilon_r$  the dedicated “highJetMulti” selection provides far better separation power, providing up to a factor of about five more rejection of background. At signal efficiencies  $\epsilon_r$  below about 80-90% the “default” selection is again superior.

### Performance of individual variables

Figure 5.9 shows the individual separation power of the four input variables that enter the “default” configuration of the likelihood (Fig. 5.9(a)) tool and their influence on the combined performance. To test the latter, the performance curve of the likelihood calculated from each possible set of three input variables is compared with that of the full configuration in Fig. 5.9(b). The input variable providing the best overall separation in the “default” selection is  $\Sigma p_{\text{T}}^{\text{trk}}(0.4)$ . Nevertheless, in the end caps the contribution from  $E_{\text{T}}^{\text{cone}}(0.4 - 0.2)$  is almost equal, especially in the low- $p_{\text{T}}$  bins. Accordingly, if  $E_{\text{T}}^{\text{cone}}(0.4 - 0.2)$ , which has only small impact in the barrel bins, is dropped, the degradation in the endcaps is as large as if  $\Sigma p_{\text{T}}^{\text{trk}}(0.4)$  is omitted. Furthermore,  $E_{\text{T}}^{\text{cone}}(0.4 - 0.2)$  is stronger in the endcaps than  $E_{\text{T}}^{\text{cone}}(0.2)$ , whereas  $E_{\text{T}}^{\text{cone}}(0.2)$  is superior in the barrel. Despite the sizeable correlations between  $\Sigma p_{\text{T}}^{\text{trk}}(0.4)$  and the calorimeter isolation variables, the combination of four variables provides an increase of the order of 5 to 10 at a given efficiency for electrons reconstructed in the barrel (less in the endcaps), compared with the simple cut on the best performing single isolation variable.

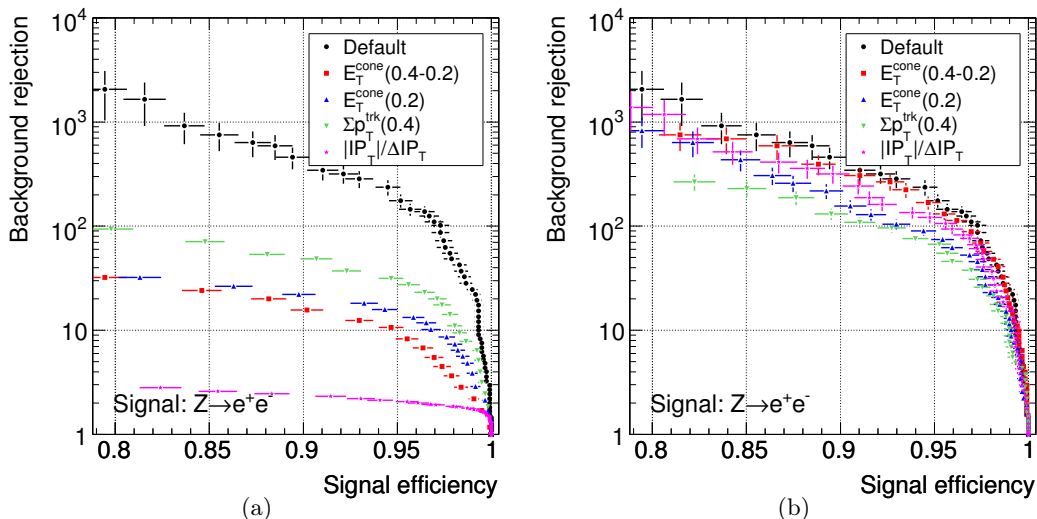


**Figure 5.9:** Background rejection as a function of the signal selection efficiency of the individual input variables of the “default” configuration (a) and if the variable indicated in the legend is omitted from the full set of input variables (b) in the bin  $19 \text{ GeV} < p_{\text{T}} < 27 \text{ GeV}$  and  $0 < |\eta| < 1.37$ .

Since for some applications it might be more suited to base the electron isolation either only on calorimeter or on track isolation variables, the performance curves for these cases are calculated as well. They are displayed in Fig. 5.10. Except for the two low- $p_{\text{T}}$  bins in the barrel, where the performance of the track variables is slightly better, the calorimeter variables provide the best separation power.

### $p_{\text{T}}$ - and $\eta$ dependence of the signal and background separation

To study the performance of the likelihood separator in different signal samples and to compare different kinematic bins, the separation power of the electron reconstruction and identification needs to be taken into account (see Tables 5.3 and 5.4). Hence, the total efficiencies and rejections are displayed in the following, defined according to

$$\epsilon_{\text{tot}} \equiv \epsilon_{\text{ID}} \cdot \epsilon_r \quad (5.12)$$

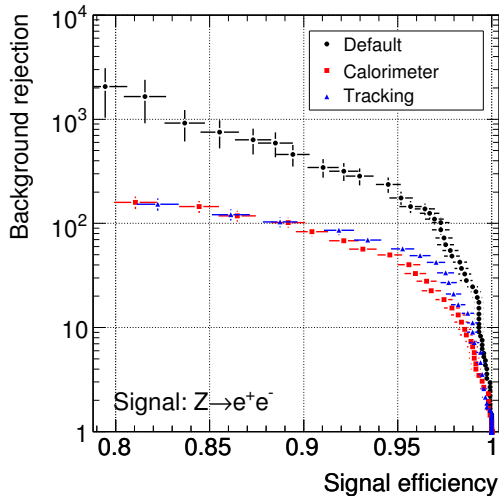


**Figure 5.10:** Comparison of the background rejection as a function of the signal selection efficiency obtained with either tracking based variables  $\Sigma p_{\text{T}}^{\text{trk}}$  (0.4) and  $|IP_{\text{T}}|/\Delta IP_{\text{T}}$  or the calorimeter based input variables  $E_{\text{T}}^{\text{cone}}$  (0.2) and  $E_{\text{T}}^{\text{cone}}$  (0.4 – 0.2) in the “default” variable selection are used (19 GeV  $< p_{\text{T}} < 27$  GeV and  $0 < |\eta| < 1.37$ ).

and

$$R_{\text{tot}} \equiv R_{\text{ID}} \cdot R_r \quad . \quad (5.13)$$

This definition requires to display the performance curves in bins of  $p_{\text{T}}^{\text{gen}}$  and  $\eta^{\text{gen}}$ .

Figures 5.11 and 5.12 show the total performance curves for “medium” signal electrons in  $Z \rightarrow e^+e^-$  and  $t\bar{t}$ . The  $\eta$  and  $p_{\text{T}}$  dependence of the background rejections that can be gained at a given efficiency is given in addition<sup>10</sup>. Background rejections of the order of  $10^3$  can easily be reached without much loss in signal efficiency compared with the efficiency of the electron ID itself. In total, the signal efficiencies lie in this case between 50% and 80% for the “default” selection almost over the full kinematic range, basically due to the low  $\epsilon_{\text{ID}}$ . If needed, also rejection factors up to  $10^4$  are possible almost over the full range, if a decrease of the signal efficiency by up to about 20% with respect to that attainable for a rejection factor of  $10^3$  can be accepted. Depending on the desired signal efficiency and on the kinematic region, the `IsolationLikelihood` tool can provide up to a factor of  $10^3$  more rejection than the “medium” electron ID (see Figs. A.8 and A.9 in Appendix A.6). The total efficiency at given  $R_{\text{tot}}$  is lower by about 20% in the endcaps with respect to the corresponding bin in the barrel, again mainly due to the deviations in the reconstruction and identification efficiencies. In active environments, such as  $t\bar{t}$  production, the total performance is degraded by about an order of magnitude, if obtained with the “highJetMulti” configuration of the likelihood. Total rejection factors up to  $5 \cdot 10^3$  should be realistic here on average, at still reasonable signal selection efficiencies.

Figures 5.13 and 5.14 show the background rejection that can be achieved for given signal efficiency for testing samples of electrons in the  $Z \rightarrow e^+e^-$  dataset passing the “loose” and

<sup>10</sup>Due to the large spread in the electron identification efficiencies it is difficult to find a reasonable efficiency range to show the  $p_{\text{T}}$  dependence over the full studied transverse momentum range. For barrel and endcaps together, this is impossible. So, the curves are displayed for different efficiency values. Actual physics analyses will for the same reason not aim at a constant signal selection efficiency over the full kinematic range, which is in general not aimed at by the ATLAS electron selection strategies.

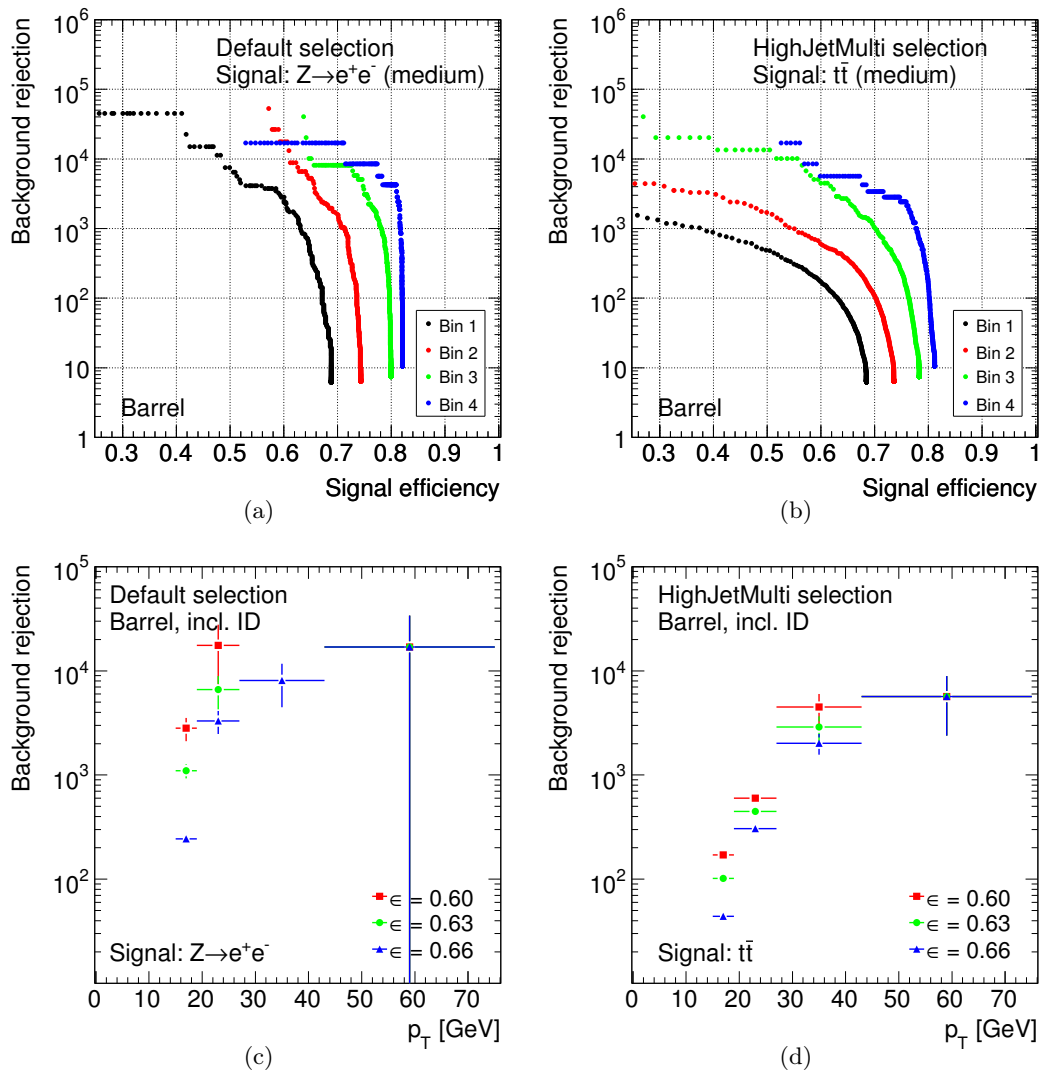


**Figure 5.11:** Overall performance of the likelihood tool on signal electrons from the  $Z \rightarrow e^+e^-$  (a, c) and  $t\bar{t}$  (b, d) datasets (barrel region of the ATLAS detector). Background electrons are selected from the  $t\bar{t}$  sample in all scans. The “default” variable set is used for signal electrons from  $Z \rightarrow e^+e^-$ , whereas the likelihood is trained with the “highJetMulti” variable set for signal electrons from  $t\bar{t}$ . The curves in (a) and (b) are given in bins of  $p_T^{\text{gen}}$  and  $\eta^{\text{gen}}$ . The corresponding  $p_T$  dependence of the background rejections at given signal selection efficiencies is shown in (c) and (d). The curves include the electron ID signal selection efficiencies and background rejections as listed in Tables 5.3 and 5.4. The corresponding curves obtained without taking these efficiencies into account are added in Appendix A.6 (Fig. A.8). For the definition of the bins, see Table 5.2. Error bars are not displayed in (a) and (b) for the sake of clarity.

“tight” selection. The likelihood output values are still determined from the PDFs obtained from samples of “medium” electrons, as implemented in Athena. Studies show that the performance cannot be enhanced significantly by the use of training samples of “loose” or “tight” electrons, respectively (see Appendix A.7).

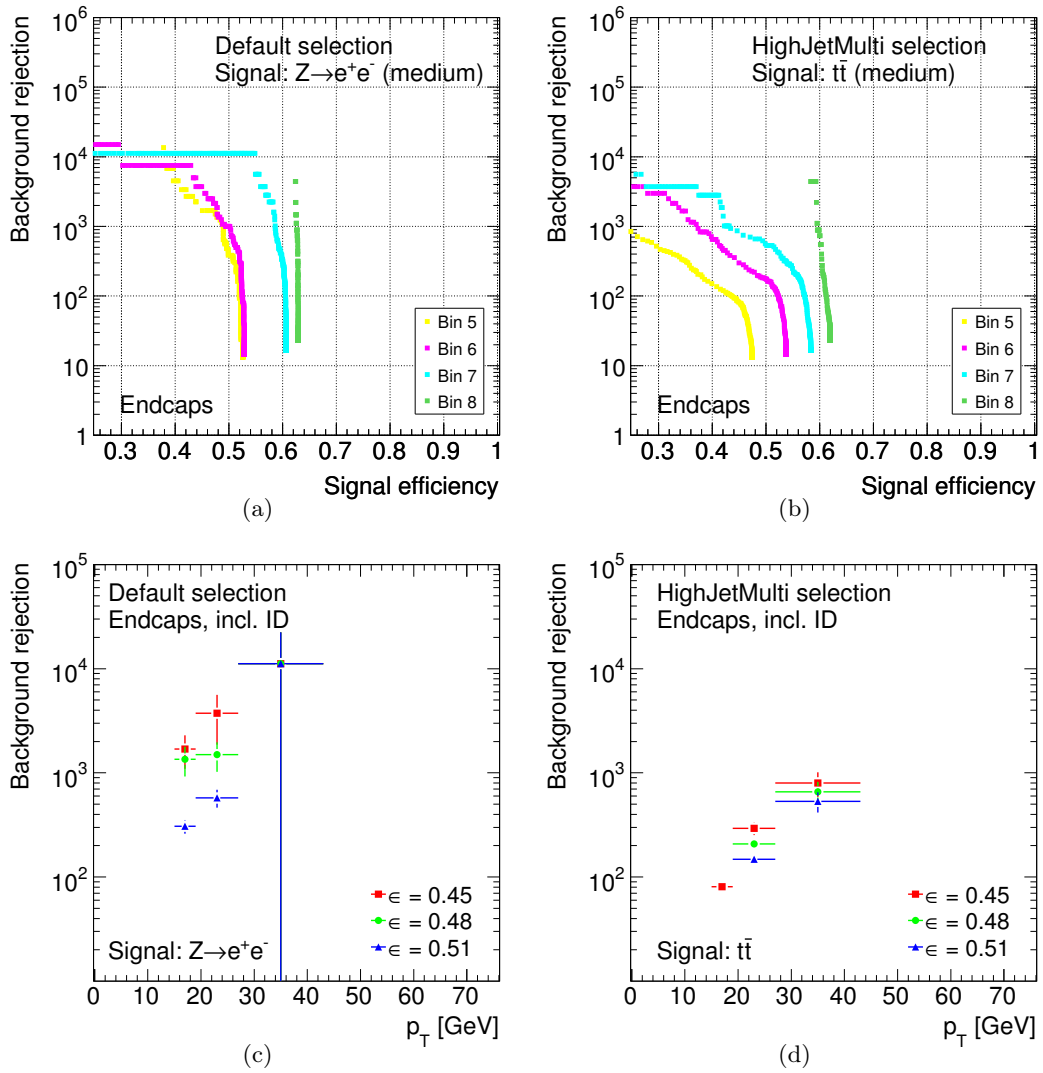


**Figure 5.12:** The same as in Fig. 5.11, but for the endcap regions of the ATLAS detector. See Fig. A.9 for the corresponding curves without the ID efficiencies.

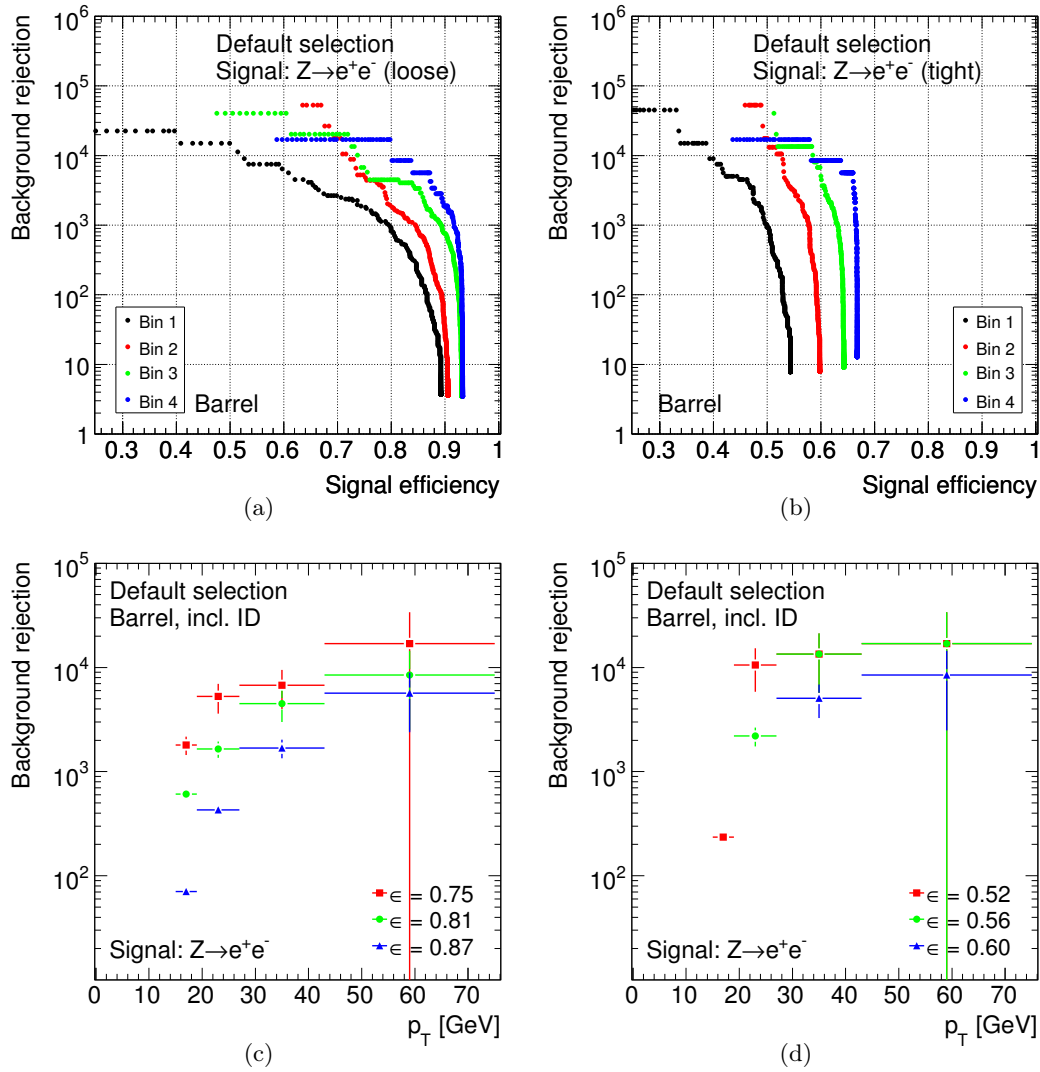


**Figure 5.13:** Overall performance of the likelihood tool on “loose” (a, c) and “tight” signal electrons (b, d) from the  $Z \rightarrow e^+e^-$  dataset (barrel region of the ATLAS detector). Background electrons are selected from the  $t\bar{t}$  sample. The curves in (a) and (b) are given in bins of  $p_T^{\text{gen}}$  and  $\eta^{\text{gen}}$ . The corresponding  $p_T$  dependence of the background rejections at given signal selection efficiencies is shown in (c) and (d). The curves include the electron ID signal selection efficiencies and background rejections as listed in Tables 5.3 and 5.4. The corresponding curves obtained without taking these efficiencies into account are added in Appendix A.6 (Fig. A.10). For the definition of the bins, see Table 5.2. Error bars are not displayed in (a) and (b) for the sake of clarity.

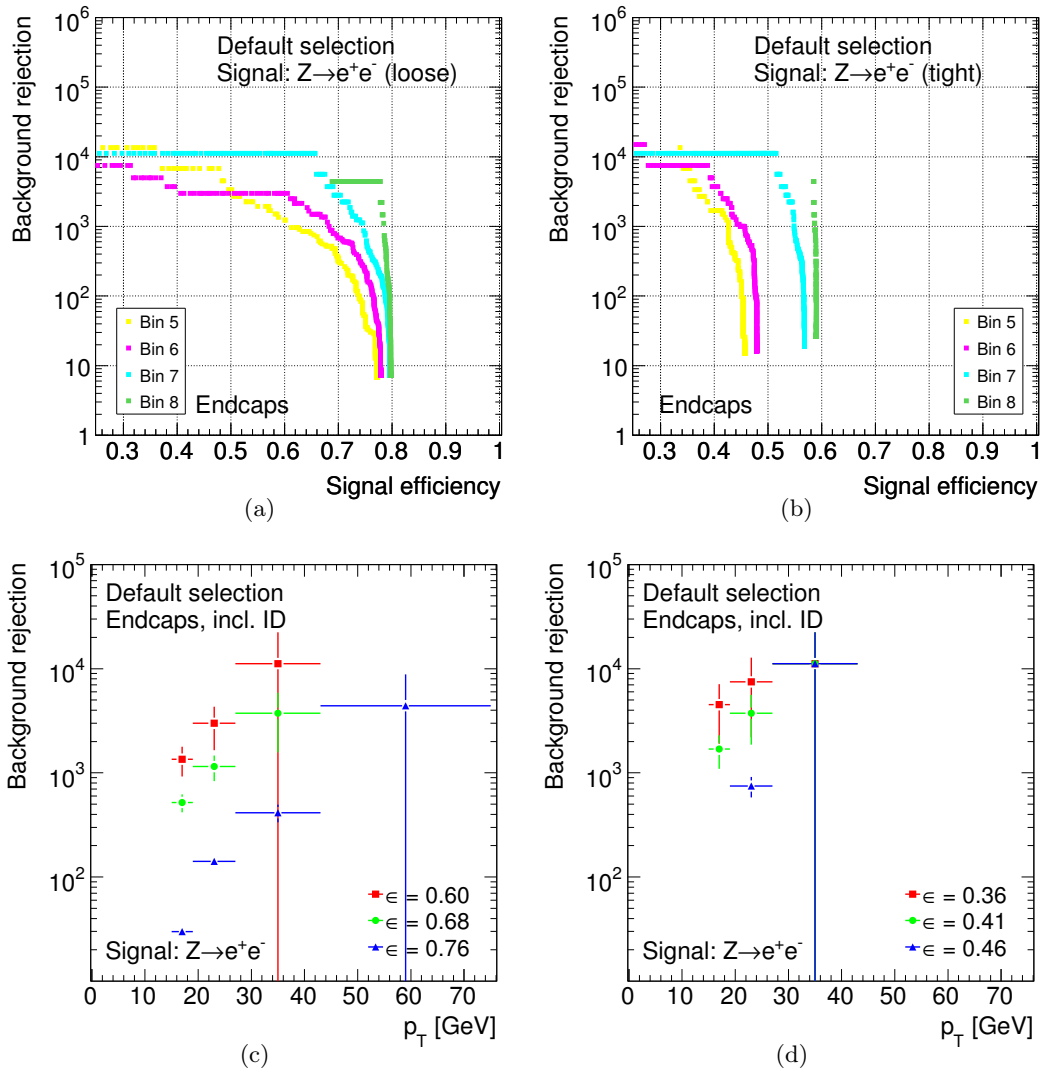


**Figure 5.14:** The same as in Fig. 5.13, but for the endcap regions of the ATLAS detector. See Fig. A.11 for the corresponding curves without the ID efficiencies.

## 5.5 Summary and outlook

A set of variables has been defined that provides separation of isolated signal electrons and background electrons produced in the decays of heavy quarks. Their separation power is combined in a projective likelihood estimator that has been implemented in the official ATLAS reconstruction software. On clean signals, such as  $Z \rightarrow e^+e^-$ , total background rejection rates of about  $10^3$  can be reached at signal efficiencies not far below those of the electron ID itself for “medium” electron candidates. Rejections of up to  $10^4$  can be achieved at still reasonable total signal selection efficiencies. In view of the application of the tool on the  $t\bar{t}H$ ,  $H \rightarrow W^+W^-$  analysis in Chapter 6, signal electrons in high-occupancy events are of special interest. In such environments the total performance is degraded by about an order of magnitude and discriminating variables calculated in large cones around the electron candidates lose their separation power. The selection of the input variables is therefore optimized, using smaller cone sizes. Rejection factors of up to about  $5 \cdot 10^3$  on average are then realistic in  $t\bar{t}$  events. Pile-up effects might degrade the separation power in a similar way, but could not be studied in detail due to the lack of a suited background sample (a first glance on pile-up conditions is given in Appendix A.2). Especially the tracking based variables can at least partly be cleaned from pile-up contributions by suitably chosen track requirements. This needs to be considered by future data driven studies.

So far, the study refers only to background electrons from heavy quark decays. It has been extended in later Athena releases to provide further rejection also against “fake” electrons from other sources than real electrons and is now applied also to a photon signal [111].

Although the projective likelihood estimator is expected to provide good signal and background separation even in the case of non-optimal estimation of the PDFs, it is affected by uncertainties in the description of the distributions of the input variables as long as these are obtained from Monte Carlo datasets. Further improvement of the separation power is therefore expected, if the input PDFs are obtained from signal and background samples of experimental data as soon as these are available. Effects like pile-up will then be automatically correctly described. Furthermore, a more accurate description of the discriminating variables and the large numbers of events that are to be expected will allow advantage to be taken of the correlations among the variables by the use of more advanced multivariate analysis tools, which is also expected to increase the discrimination power.

Finding strategies to define sufficiently clean signal and background samples will therefore be the next important step to improve the performance of the `IsolationLikelihood`, which is, however, out of the scope of this thesis. Whereas the selection of clean  $Z \rightarrow e^+e^-$  samples will be easily possible due to the reconstruction of the  $Z$  boson mass peak, the selection of electrons from heavy quark decays will be more challenging. A candidate are semi-leptonic  $t\bar{t}$  events that contain two leptons of equal charge. Such events can be selected by the requirement of one jet passing tight  $b$ -tagging criteria, a  $W$  boson, reconstructed from a light jet pair, a top quark candidate (either leptonic or hadronic) and  $\cancel{E}_T$ , as proposed in Ref. [112]. A study of this approach should be considered by future analyses.



# 6 Prospects for the search for $t\bar{t}H, H \rightarrow W^+W^-$ at the ATLAS experiment

## 6.1 Introduction

Once a Higgs boson has been discovered, Higgs boson production in association with a top quark pair will play an important role in measuring the top quark Yukawa coupling. The main part of this thesis is dedicated to a Monte Carlo study of the feasibility of an observation of the Higgs boson in the  $t\bar{t}H, H \rightarrow W^+W^-$  channel. The starting point of the analysis is work done in collaboration with the Marseille/Beijing group for a study of the signal and background conditions in this channel. The results were published in Ref. [108]. Compared with that study, the analysis presented in the following aims at a more efficient suppression of irreducible backgrounds, using tighter signal selection criteria. This increases the signal-to-background ratio and hence reduces the sensitivity of the result to uncertainties on the background determination. The  $t\bar{t}$  background is studied in more detail and an upper limit on the expectation of the  $W$ +jet contribution to the background is determined, which was neglected as a potential source of background so far.

Top quark pair production is the most important background to a  $t\bar{t}H, H \rightarrow W^+W^-$  signal. Its cross section is more than  $10^3$  times larger than that of the signal, so the process needs to be suppressed very effectively. After the decays of the top quarks, the final state of the signal process consists of four  $W$  bosons and two  $b$ -quarks. The impact of the  $t\bar{t}$  background depends on which final state is selected, i.e. how many out of the four  $W$  bosons are required to decay leptonically. Table 6.1 gives an overview of all possible final states and their respective branching ratios.

Final state		Branching ratio
$WW WW b\bar{b} \rightarrow qq' qq' qq' qq' b\bar{b}$	“Fully hadronic”	0.2088
$WW WW b\bar{b} \rightarrow qq' qq' qq' \ell^\pm \nu b\bar{b}$	“One lepton”	0.2634
$WW WW b\bar{b} \rightarrow qq' qq' \ell \nu \ell \nu b\bar{b}$	“Two leptons”	0.1246
$WW WW b\bar{b} \rightarrow qq' qq' \ell^\pm \nu \ell^\pm \nu b\bar{b}$	“Like-sign leptons”	0.0415
$WW WW b\bar{b} \rightarrow qq' \ell \nu \ell \nu \ell \nu b\bar{b}$	“Three leptons”	0.0262
$WW WW b\bar{b} \rightarrow \ell \nu \ell \nu \ell \nu \ell \nu b\bar{b}$	“Fully leptonic”	0.0021

**Table 6.1:** Classification of the possible final states of the  $t\bar{t}H, H \rightarrow W^+W^-$  process and the number of leptonically and hadronically decaying  $W$  bosons and the corresponding branching ratios. “Leptons” corresponds to electrons and muons. Final states with  $\tau$  leptons are not included, therefore the contributions listed in the table add up to only about 67%.

The fully hadronic final state is difficult to trigger on and it is affected most by an overwhelmingly large background from QCD jet production. This background is also relevant in the case of the final state with only one leptonically decaying  $W$  boson. In addition,  $W$ +jet

production has to be considered as a serious background component for the latter. A significant observation of the signal is therefore difficult in both final states. The four lepton final state on the other hand has a very clean signature, but its cross section is too small to provide a reasonable expected number of signal events after application of event selection criteria. The two and three lepton final states are both good candidates for an observation of a signal. The signal signature of the three lepton final state comprises in addition a pair of light jets with an invariant mass close to  $M_W$ , two  $b$ -jets and a sizeable amount of missing transverse energy due to the neutrinos from the three leptonic  $W$  boson decays.

In this thesis only the most promising final state with two leptons of equal charge (“like-sign” leptons), four light jets and two  $b$ -jets is covered. In this final state, the product of the production cross section and the branching ratio is still higher than in the three lepton case, whereas the restriction to like-sign leptons helps to reduce the fully leptonic  $t\bar{t}$  background ( $t\bar{t} \rightarrow b\ell\nu b\ell\nu$ ) significantly, at the cost of two thirds of the signal events. The remaining  $t\bar{t}$  background mainly consists of semi-leptonically decaying  $t\bar{t}$  events ( $t\bar{t} \rightarrow bjj b\ell\nu$ ), where the second lepton originates from a semi-leptonic decay of a heavy quark, as indicated in Fig. 6.1. To suppress these events, a powerful lepton isolation, i.e. a separation of isolated leptons, originating mainly from  $W$  and  $Z$  boson decays, from non-isolated leptons produced in the decays of heavy quarks, as established in Chapter 5, is mandatory.

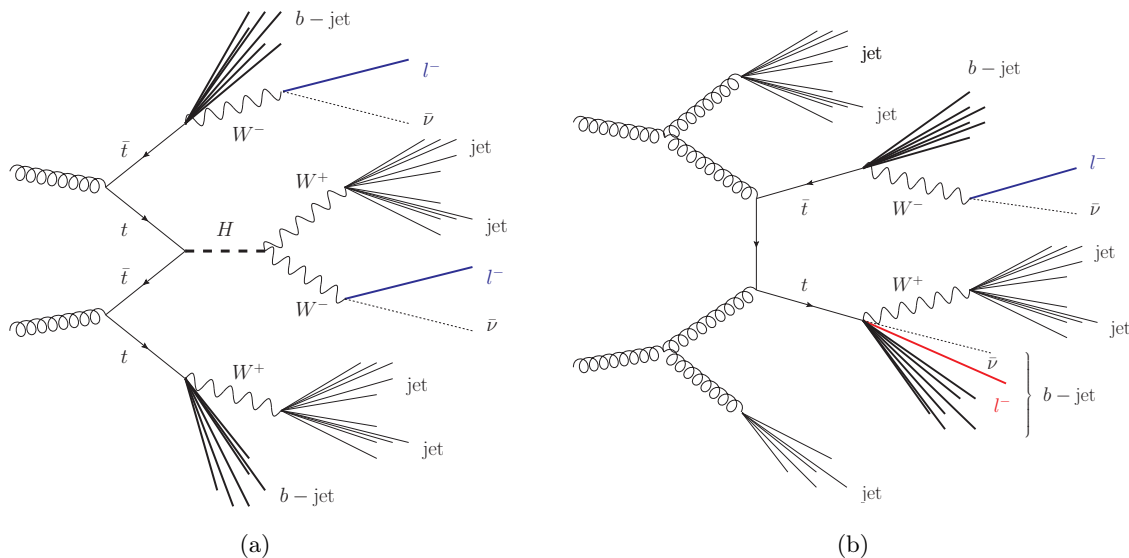


**Figure 6.1:** Illustration of the processes resulting in the like-sign lepton and six jets signature of the  $t\bar{t}H, H \rightarrow W^+W^-$  signal (a) and the background from semi-leptonic  $t\bar{t}$  events with semi-leptonically decaying heavy quarks (b). The different origins of the two leptons are indicated by the colours, as either from  $W$  boson (blue) or heavy quark decays (red).

The study presented in this chapter is based on Monte Carlo signal and background samples that were produced with the ATLAS full detector simulation as introduced in Section 3.3.6 (for details on the Monte Carlo simulation and detector description see also Ref. [49]). A proton–proton centre-of-mass energy of 14 TeV is assumed and predictions are made for an integrated luminosity of  $30 \text{ fb}^{-1}$ . The signal and background sample generation are described in Sections 6.2 and 6.3 of this chapter. The event selection strategy is outlined in Section 6.4 and predictions for the accepted cross sections are made for the signal and the irreducible<sup>1</sup>

<sup>1</sup>In the context of this thesis, “irreducible” refers to all backgrounds which, like the signal, contain pairs of

backgrounds. The statistical uncertainties on the reducible  $t\bar{t}$  and  $W$ +jet backgrounds are large because of the limited size of the available Monte Carlo datasets. More sophisticated approaches need therefore to be followed to estimate the contributions of these backgrounds with better precision. These are discussed in Sections 6.5 and 6.6. The results of the latter three sections are combined in Section 6.7, where the total background expectation is determined and discovery significances are discussed. These numbers serve as the basis for the pile-up studies addressed in Section 6.8 and the estimation of systematic uncertainties in Section 6.9. The results are discussed in Section 6.10 of this chapter and an outlook is given on possibilities to further enhance the significance in this channel. Finally, a comparison to previous studies of the channel is given in Section 6.11 and the impact of the results obtained in this thesis on measurements of the top Yukawa coupling constant is discussed in Section 6.12.

---

isolated like-sign leptons from  $W/Z$  boson decays, independently of the number of top quarks and  $W$  bosons that are actually produced. In contrast, all backgrounds containing at least one lepton candidate that is not produced in a weak boson decay are classified “reducible”.

## 6.2 Generation of Monte Carlo samples for the $t\bar{t}H$ , $H \rightarrow W^+W^-$ signal

The cross section for Standard Model Higgs boson production in association with a top quark pair has been calculated up to next-to-leading order in QCD in Refs. [45, 113, 114, 115, 116, 117]. For the normalization of the results obtained in this thesis, the  $t\bar{t}H$  cross sections are used as provided by the Higgs boson production cross section calculation program HQQ [118, 119]<sup>2</sup> at a renormalization and factorization scale of  $\mu_R = \mu_F = \mu_0 = M_t + M_H/2$  and using the CTEQ6M [120] PDF set. Details on the parameter settings used for the calculation of the Higgs boson production cross sections are given in Ref. [119]. The LO and NLO cross sections and the  $H \rightarrow WW^{(*)}$  decay branching ratio as provided by the program HDECAY [121, 119] are shown in Figs. 6.2(a) and 6.2(b) a function of the Higgs boson mass<sup>3</sup>. Since the decreasing production cross section is compensated by the rising branching ratio into a pair of  $W$  bosons up to  $M_H = 2M_W$ ,  $\sigma \times \text{BR}$  reaches a maximum of about 200 fb at leading and 250 fb at next-to-leading order, as illustrated in Fig. 6.2(c). Including the decays of the two  $W$  bosons into two like-sign leptons and four jets, the maximum cross section decreases to less than 10 fb. This corresponds to 300 candidate events produced at the LHC, assuming an integrated luminosity of  $30 \text{ fb}^{-1}$ .

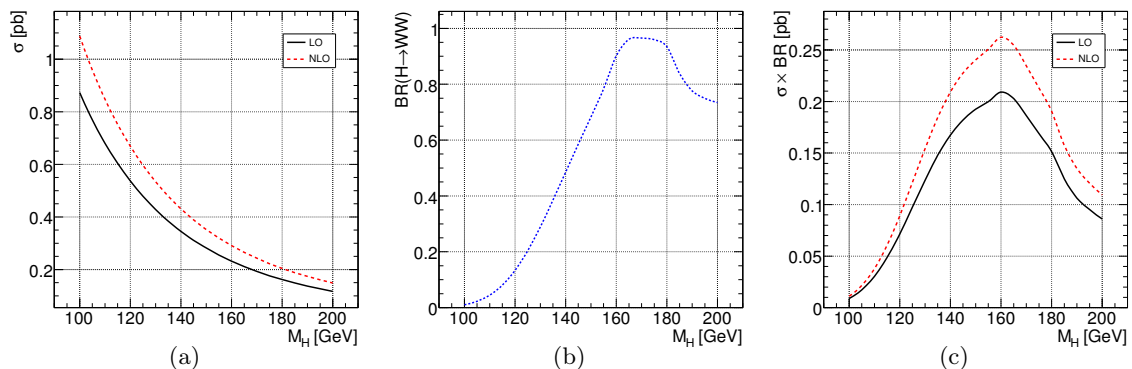


**Figure 6.2:** (a) Leading and next-to-leading order cross sections for  $t\bar{t}H$  production at the LHC at a proton–proton collision energy of 14 TeV and (b) branching ratio for the decay  $H \rightarrow WW^{(*)}$  as a function of the Higgs boson mass and (c) product of both. The  $t\bar{t}H$  cross section values and branching ratios  $\text{BR}(H \rightarrow W^+W^-)$  are taken from Refs. [119, 122, 121] (see also Table 6.2).

The samples used for the analysis of the mentioned signal final state were generated for the interesting Higgs boson mass range between 120 GeV and 200 GeV in steps of 10 GeV, using the leading order generator PYTHIA. A pair of samples was generated for each mass point, one with both  $W^+$  and the other with both  $W^-$  forced to decay leptonically ( $W^\pm \rightarrow \ell^\pm \nu$ ,  $\ell = e/\mu$ ) to generate the desired lepton signatures with a positively or negatively charged lepton pair. The remaining two  $W$  bosons are forced to decay hadronically. Final states with  $\tau$  leptons were not considered for the signal event generation, although leptonic  $\tau$  decays contribute to the selected final state<sup>4</sup>. The generated events were filtered for a lepton pair

<sup>2</sup>Recently, recommendations for the  $t\bar{t}H$  cross section normalization have been published in Ref. [47], which was, however, too late to be considered in this thesis. Only NLO cross sections are given in this reference, using a more recent PDF set, leading to up to 3% larger values compared with the NLO values used in this thesis.

<sup>3</sup>In the following, the index “(\*)” to indicate the off-shell  $W$  boson is no longer carried along for simplicity, although it still applies for Higgs boson masses smaller than  $2M_H$ .

<sup>4</sup>For most of the backgrounds the  $\tau$  contributions were generated, or otherwise conservatively estimated from

( $e$ ,  $\mu$  of either source) with  $p_T > 5$  GeV and  $|\eta| < 2.7$  before being passed through the full ATLAS detector simulation. In addition, a pair of samples, overlaid with an average of 2.3 minimum-bias collisions per event, corresponding to a luminosity of  $10^{33}$  cm $^{-2}$ s $^{-1}$ , was generated for  $M_H = 160$  GeV, to study the impact of pile-up. The most important parameters of the signal samples used for this thesis are summarized in Table 6.2, including the cross sections and branching ratios employed to normalize the results. Since reliable NLO cross section calculations are lacking for most of the backgrounds, the LO calculations are used to normalize the signal cross sections in a consistent way.

$M_H$ [GeV]	$\sigma_{\text{tot}}$ [fb]	$\text{BR}(H \rightarrow W^+W^-)$	$\epsilon_{\text{filter}}$	$\sigma_{\text{in}}$ [fb]	$N_{\text{MC}}$	$L$ [fb $^{-1}$ ] standard	$N_{\text{MC}}$	$L$ [fb $^{-1}$ ] pile-up
120 (+)	537	0.133	0.928	1.377	8.5k	12346	–	–
130 (+)	428	0.289	0.935	2.402	7.0k	5828	–	–
140 (+)	345	0.485	0.940	3.267	9.5k	5785	–	–
150 (+)	282	0.683	0.944	3.777	8.0k	4236	–	–
160 (+)	232	0.902	0.945	4.108	8.8k	4260	7.3k	3530
170 (+)	193	0.965	0.948	3.667	8.7k	4745	–	–
180 (+)	162	0.935	0.945	2.973	6.0k	4003	–	–
190 (+)	137	0.776	0.947	2.091	10k	9565	–	–
200 (+)	117	0.735	0.949	1.695	7.5k	8850	–	–
120 (–)	537	0.133	0.929	1.378	8.5k	12337	–	–
130 (–)	428	0.289	0.938	2.410	7.0k	5809	–	–
140 (–)	345	0.485	0.939	3.264	9.5k	5790	–	–
150 (–)	282	0.683	0.936	3.745	8.0k	4272	–	–
160 (–)	232	0.902	0.946	4.112	8.8k	4256	7.3k	3526
170 (–)	193	0.965	0.947	3.664	8.7k	4749	–	–
180 (–)	162	0.935	0.952	2.995	6.0k	3973	–	–
190 (–)	137	0.776	0.949	2.096	10k	9542	–	–
200 (–)	117	0.735	0.949	1.695	7.5k	8850	–	–

**Table 6.2:** Summary of the signal Monte Carlo datasets used for the study of the two lepton final state in  $t\bar{t}H$ ,  $H \rightarrow W^+W^-$ . The datasets were generated with PYTHIA 6.4 and for a proton–proton centre-of-mass energy of 14 TeV. The samples denoted with a “(+)/(–)” contain the final state with a pair of positively/negatively charged leptons, respectively. The columns denoted  $\sigma_{\text{tot}}$  and  $\text{BR}(H \rightarrow W^+W^-)$  give the respective total inclusive leading order cross sections and branching fractions for the decays  $H \rightarrow WW^{(*)}$ , taken from Refs. [122, 121, 119]. The product of these two, together with the  $W$  boson decay branching ratios and the efficiency  $\epsilon_{\text{filter}}$  of the generator level filter gives the actual input cross sections  $\sigma_{\text{in}} = \sigma_{\text{tot}} \cdot \text{BR}(H \rightarrow W^+W^-) \cdot \text{BR}(WWWW \rightarrow \ell^\pm \ell^\pm jjjj) \cdot \epsilon_{\text{filter}}$ , where  $\ell = e, \mu$ .  $L$  denotes the effective integrated luminosity the available number of Monte Carlo events  $N_{\text{MC}}$  per sample corresponds to, according to  $L = N_{\text{MC}}/\sigma_{\text{in}}$ . The columns entitled “pile-up” contain the number of events and corresponding integrated luminosities of the samples overlaid with an average of 2.3 minimum-bias events, when applicable.

---

the  $\tau \rightarrow e/\mu$  decay branching ratios.

### 6.3 Monte Carlo samples for background studies

Despite its unique signal signature, the search for the Higgs boson in the  $t\bar{t}H$ ,  $H \rightarrow W^+W^-$  channel is affected by a number of background processes, which need to be kept under control. The cross sections of various potential backgrounds are listed in Table 6.3. Their relevance is discussed in Section 6.3.1, and the details of the Monte Carlo event generation for the most important ones are given in Sections 6.3.2 to 6.3.5.

Process	Reference	Comment	Order in pert. theory	$\sigma$ [nb]
$t\bar{t}$	Ref. [49]		NLO	0.794
			NLO + NLL	0.833
$t\bar{t}t\bar{t}$	AcerMC [56]	$\mu_0 = \hat{s}$	LO	$2.9 \cdot 10^{-6}$
$t\bar{t}Z$	Ref. [46]		LO	$0.808 \cdot 10^{-3}$
$t\bar{t}W$	ALPGEN [57]		NLO	$1.09 \cdot 10^{-3}$
			LO	$0.651 \cdot 10^{-3}$
$t\bar{t}WW$	MadGraph [55]	$\mu_0 = \hat{s}$	LO	$5.2 \cdot 10^{-6}$
Single top production	Ref. [49]	t-channel	LO	0.251
			NLO	0.246
			LO	0.007
			NLO	0.011
			LO	0.058
			NLO	0.066
$W \rightarrow \ell^\pm \nu$	Ref. [49]		LO	16.8
			NLO	20.7
			NNLO	20.5
$Z \rightarrow \ell^+ \ell^-$	Ref. [49]	$m_{\ell^+ \ell^-} > 60$ GeV	LO	1.66
			NLO	2.02
			NNLO	2.03
$WW$	Ref. [49]	$M_{W^{(*)}} > 20$ GeV, $p_T^W > 10$ GeV	LO	0.072
			NLO	0.112
$WZ$	Ref. [49]	$M_{W^{(*)}/Z^{(*)}} > 20$ GeV, $p_T^{W/Z} > 10$ GeV	LO	0.032
			NLO	0.056
$ZZ$	Ref. [49]	$M_{Z^{(*)}} > 12$ GeV	LO	0.0165
			NLO	0.0221
Total inelastic $pp$	Ref. [49]			$79 \cdot 10^6$
Non-single diffractive	Ref. [49]			$65 \cdot 10^6$
Di-jet	Ref. [49]	$p_T^{\text{jet}} > 25$ GeV	LO	$367 \cdot 10^3$
			NLO	$477 \cdot 10^3$

**Table 6.3:** Production cross sections for potential background processes for proton–proton collisions at a centre-of-mass energy of 14 TeV. The order to which the perturbative calculation is done is labelled “LO”, “NLO”, “NNLO”. “NLL” indicates that next-to-leading logarithm contributions from higher orders in  $\alpha_s$  are included to improve the calculation. The cross section values given in this table are taken from the references given in the “Reference” column. These are not necessarily the inclusive cross sections the results are normalized to in the following (see the text in this section for details). The relevant backgrounds and the choice of the normalization are discussed in Sections 6.3.2 to 6.3.5 and summarized in Table 6.4. If generator level cuts are applied for the calculation of the cross sections, this is mentioned in the column denoted “Comment”. This column also gives the choice of the factorization and renormalization scale  $\mu_0$  in the case of highly scale dependent cross section values.

### 6.3.1 Backgrounds for $t\bar{t}H$ , $H \rightarrow W^+W^-$ production

The most important candidates for background processes are those which, like the signal itself, contain top quarks. Among those,  $t\bar{t}$ ,  $t\bar{t}W$  and  $t\bar{t}Z$  are produced with sufficiently large cross sections to contribute significantly. Top quark pair production, due to the missing weak bosons, must be considered as a reducible background. The other two are irreducible. Further irreducible background candidates are  $t\bar{t}t\bar{t}$  and  $t\bar{t}WW$  production. Production of  $t\bar{t}t\bar{t}$  events is considered in the following, but turns out to provide only a minor background contribution compared with  $t\bar{t}W$  and  $t\bar{t}Z$  production. The cross section for non-resonant production of  $t\bar{t}WW$  is of the same order of magnitude as that for  $t\bar{t}t\bar{t}$ . At the same time, the selection efficiency for  $t\bar{t}t\bar{t}$  events is much higher than that for  $t\bar{t}WW$  (as long as, like in this analysis, no dedicated  $t\bar{t}t\bar{t}$  vetoes are applied), because of the higher jet multiplicity and the existence of four real  $b$ -jets in the case of the former. Therefore, the  $t\bar{t}WW$  contribution to the background is expected to be even smaller than that of  $t\bar{t}t\bar{t}$ . Another argument against a significant  $t\bar{t}WW$  background is its low production cross section compared with the signal, whereas the selection efficiency of events produced in non-resonant  $t\bar{t}WW$  processes is comparable to that of the signal. Consequently, the  $t\bar{t}WW$  background is not considered in this analysis. A further potential source of background containing top quarks is single top production. The total production cross section for this process is smaller than that for top quark pair production, because it only occurs via the electroweak interaction. The selection efficiency for single top production events is expected to be considerably lower than for  $t\bar{t}$  events because of the lack of a second lepton and  $b$ -jet. Therefore, this background is also considered negligible and not studied either.

Associated production of weak bosons, either singly or in pairs ( $WZ$ ,  $WW$ ,  $ZZ$ ,  $W$ ,  $Z$ ), and jets occur with a large cross section compared with that of the signal at the LHC. Given the lepton fake rate and the  $b$ -jet mistag rate are sufficiently high and the exclusive cross sections for the final states with many additional jets are large, these processes might also contribute to the reducible background. The cross sections for weak boson pair production are smaller than the cross section for top quark pair production. Because of the missing  $b$ -jets, the selection efficiency is furthermore expected to be well below that for  $t\bar{t}$  events. The weak boson pair production is therefore neglected here. With the cross section for single  $W$  boson production being about ten times that for  $Z$  boson production in the leptonic decay channels,  $W$ +jet production must be considered the most serious among the weak boson backgrounds. Hence, it is studied in more detail in the following (but shown to be negligible).

Finally, jet production from QCD processes, notably processes with  $b$ -jets, could be a source of reducible background. Nevertheless, these are not studied here, as lepton identification and isolation requirements are assumed to suppress the QCD background to a negligible level.

A description of the Monte Carlo samples used is given in the following sections. Their most important characteristics and respective cross sections can be found in Table 6.4.

Process	Generator	$(\sigma \times \text{BR})_{\text{tot}}$ [fb]	$\epsilon_{\text{MLM}}$	$\epsilon_{\text{filter}}$	$\sigma_{\text{in}}$ [fb]	$N_{\text{MC}}$	$L$ [fb $^{-1}$ ]	$N_{\text{MC}}$	$L$ [fb $^{-1}$ ]	Reference
$\sqrt{s} = 14 \text{ TeV}$										
$t\bar{t}$ no all-hadronic	MC@NLO 3.1	833000	–	0.543	452319	437k	0.97	72k	0.17	Ref. [123]
$t\bar{t}$ all-hadronic	MC@NLO 3.1	833000	–	0.457	380681	67k	0.18	–	–	Ref. [123]
$t\bar{t}$ filtered	MC@NLO 3.1	833000	–	0.0384	31983	352k	11	–	–	Ref. [123]
$t\bar{t}Z$	AcerMC 3.4	120	–	0.790	94.8	20k	208	–	–	AcerMC [124]
$t\bar{t}W$	AcerMC 3.4	205	–	0.540	110.7	20k	178	–	–	AcerMC [124]
$t\bar{t}W+0p$ (ex.)	ALPGEN 2.06	180	0.47	0.414	25.3	15k	591	10k	389	ALPGEN [57]
$t\bar{t}W+1p$ (ex.)	ALPGEN 2.06	187	0.27	0.410	20.7	15k	722	10k	481	ALPGEN [57]
$t\bar{t}W+2p$ (in.)	ALPGEN 2.06	233	0.33	0.442	34.0	15k	440	10k	262	ALPGEN [57]
$gg \rightarrow t\bar{t}t$	AcerMC 3.4	2.2	–	0.655	1.44	11k	7634	–	–	AcerMC [124]
$qq \rightarrow t\bar{t}t$	AcerMC 3.4	0.48	–	0.651	0.31	7k	23194	–	–	AcerMC [124]
$W \rightarrow e\nu+4p$ (ex.)	ALPGEN	273000	0.252	0.780	53661	29k	0.54	–	–	Ref. [125]
$W \rightarrow e\nu+5p$ (in.)	ALPGEN	91000	0.264	0.929	22318	4k	0.17	–	–	Ref. [125]
$W \rightarrow \mu\nu+4p$ (ex.)	ALPGEN	273000	0.229	0.576	36010	19k	0.54	–	–	Ref. [125]
$W \rightarrow \mu\nu+5p$ (in.)	ALPGEN	91000	0.264	0.840	20180	4k	0.17	–	–	Ref. [125]
$Wb\bar{b}+3p$ (in.)	ALPGEN	6020	–	–	2770	3k	1.08	–	–	Ref. [125]
$\sqrt{s} = 10 \text{ TeV}$										
$W \rightarrow e\nu+2p$ (ex.)	ALPGEN 2.13	2499000	0.271	–	676000	–	–	2M	2.77	Ref. [126]
$W \rightarrow e\nu+3p$ (ex.)	ALPGEN 2.13	1099400	0.185	–	203300	–	–	585k	2.88	Ref. [126]
$W \rightarrow e\nu+4p$ (ex.)	ALPGEN 2.13	431300	0.130	–	56100	59k	1.05	152k	2.71	Ref. [126]
$W \rightarrow e\nu+5p$ (in.)	ALPGEN 2.13	141500	0.117	–	16600	17k	1.05	45k	2.68	Ref. [126]
$W \rightarrow \mu\nu+2p$ (ex.)	ALPGEN 2.13	2498600	0.273	–	682300	–	–	2M	2.75	Ref. [126]
$W \rightarrow \mu\nu+3p$ (ex.)	ALPGEN 2.13	1099700	0.184	–	202000	–	–	563k	2.79	Ref. [126]
$W \rightarrow \mu\nu+4p$ (ex.)	ALPGEN 2.13	431500	0.129	–	55500	59k	1.06	153k	2.76	Ref. [126]
$W \rightarrow \mu\nu+5p$ (in.)	ALPGEN 2.13	141500	0.115	–	16300	17k	1.07	45k	2.73	Ref. [126]
$Wb\bar{b}+0p$ (ex.)	ALPGEN 2.13	6820	0.75	–	5130	16k	3.02	–	–	Ref. [126]
$Wb\bar{b}+1p$ (ex.)	ALPGEN 2.13	11520	0.44	–	5010	15k	3.09	–	–	Ref. [126]
$Wb\bar{b}+2p$ (ex.)	ALPGEN 2.13	10400	0.28	–	2890	9k	3.10	–	–	Ref. [126]
$Wb\bar{b}+3p$ (in.)	ALPGEN 2.13	5950	0.27	–	1610	5k	3.11	–	–	Ref. [126]
						full simulation		ATLFAST-II		

**Table 6.4:** Overview of the Monte Carlo datasets used for the study of the background processes to the two like-sign lepton final state of  $t\bar{t}H$ ,  $H \rightarrow W^+W^-$ . The ALPGEN datasets are generated separately for each number of additional partons “ $N_p$ ”. The cross section  $(\sigma \times \text{BR})_{\text{tot}}$  is the cross section used for the normalization of the results, as provided by the generator, with branching ratios of decays forced in the generation included. An exception in the normalization is made for the  $t\bar{t}$  datasets, for which the cross section is normalized to the NLO value from the reference given in the “Reference” column, instead of the MC@NLO generator value of 774 pb. For the ALPGEN datasets the cross sections before MLM matching are given in this column. These must be scaled with the MLM matching efficiencies  $\epsilon_{\text{MLM}}$ . If a generator level filter is applied on the datasets, the corresponding filter efficiency is given as  $\epsilon_{\text{filter}}$ . The accepted cross sections for each background process is scaled to the “input cross section”  $\sigma_{\text{in}} = (\sigma \times \text{BR})_{\text{tot}} \cdot \epsilon_{\text{MLM}} \cdot \epsilon_{\text{filter}}$ . All numbers are obtained from the reference in the last column of the table. The available number of Monte Carlo events is given in the “ $N_{\text{MC}}$ ” columns. For MC@NLO datasets the effective numbers of events are given, added with their respective weights.  $L = N_{\text{MC}}/\sigma_{\text{in}}$  denotes the effective integrated luminosity of the samples.

### 6.3.2 Top quark pair production

The  $t\bar{t}H$ ,  $H \rightarrow W^+W^-$  channel is plagued by the large  $t\bar{t}$  background, which is produced with a cross section that is about a thousand times larger than that of the signal. In leading order,  $gg$  as well as  $q\bar{q}$  scattering contribute to  $t\bar{t}$  production at the LHC, as shown in the Feynman graphs in Fig. 6.3. Due to the gluon flux being much higher than that of the anti-quarks, the former is the dominant one of the two processes.

Top quark pair production events were generated with the MC@NLO generator, interfaced to HERWIG to simulate the fragmentation and hadronization. The underlying event was modelled with JIMMY. Since MC@NLO is a NLO generator, the production of one of the additional partons is treated in the matrix element calculation. Hence, both, the inclusive cross section and also the jet spectra, are described in next-to-leading order. Accordingly, the NLO cross section value of  $(833 \pm 100)$  pb, including NLL resummation of soft effects, from Refs. [123, 127] is used to normalize the  $t\bar{t}$  cross section, although LO normalization is applied to the signal and the remaining backgrounds.

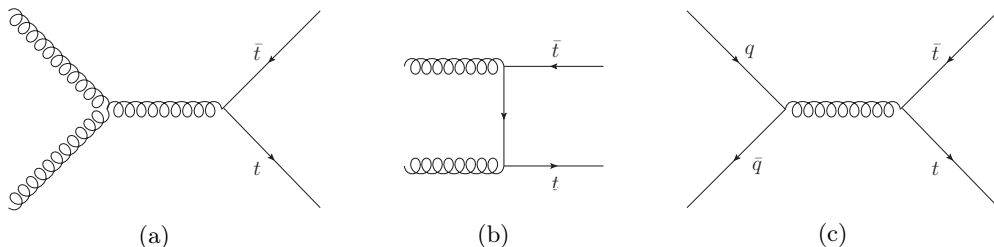


**Figure 6.3:** Leading order Feynman diagrams for top quark pair production.

Three  $t\bar{t}$  samples, differing in the selection of the events at generator level, are used in the following: For the first two samples, the process is split into two sub-samples produced with complementary generator level filters. The filter for the first sample accepts only the final states with at least one leptonic  $W$  boson decay (including the decay into a  $\tau$  lepton), the second one selects the fully hadronic decay mode. The filter efficiencies are calculated according to the  $W \rightarrow \ell\nu$  branching ratio of 10.8% per flavour. These samples are referred to as the “no all-hadronic” and “all-hadronic”  $t\bar{t}$  datasets in the following. With roughly one million events in total, the samples is not large enough for a reliable background estimation for a low cross section process like  $t\bar{t}H$ ,  $H \rightarrow W^+W^-$ . A large fraction of the  $t\bar{t}$  events surviving the like-sign lepton requirement is expected to contain leptons from semi-leptonic heavy quark decays. A large dedicated  $t\bar{t}$  dataset was therefore produced in addition, with a filter for pairs of like-sign leptons ( $e$  or  $\mu$  within  $p_T > 13$  GeV and  $|\eta| < 2.6$ ) on generator level. This sample is referred to as the “pre-filtered”  $t\bar{t}$  dataset in the following. With a resulting filter efficiency about an order of magnitude smaller than that of the “no all-hadronic” sample, this filter provides a large increase in the effective number of Monte Carlo events available after the basic event selection requirements. Nevertheless, effects caused by charge sign mismeasurement or by lepton candidates falsely reconstructed from other sources than real leptons are underestimated and need to be estimated separately (see Section 6.5)<sup>5</sup>.

<sup>5</sup>In the course of the activities for the publication of Ref. [108], the production of the filtered dataset had to be done with the Athena code that was already in the official release at that time. The best suited code was actually not written for the selection of like-sign leptons. At least, it be configured such that it selected events containing pairs of like-sign leptons fulfilling  $p_T > 13$  GeV and  $|\eta| < 2.6$ , but with a small

In order to avoid double counting with the  $t\bar{t}t\bar{t}$  sample described later,  $t\bar{t}t\bar{t}$  events found in the  $t\bar{t}$  datasets are excluded from the analysis by a generator level filter. In contrast, the  $t\bar{t}b\bar{b}$  production events are kept in the sample, because dedicated  $t\bar{t}b\bar{b}$  samples are available, but contain too little events to provide reasonable results. Production of  $t\bar{t}b\bar{b}$  events occurs with a cross section of about 10 pb. For pile-up studies a smaller sample of “no all-hadronic”  $t\bar{t}$  events is available, overlaid with an average of 2.3 minimum-bias collisions per event.

Events produced with MC@NLO are generated with a weight, which is either +1 or -1 (see Section 2.3.1 of Chapter 2). These weights have to be taken into account in calculations based on studies of such a sample, in particular, if only small numbers of events are selected. The treatment of the MC@NLO weights in this thesis is described in Appendix B.2.

### 6.3.3 Associated production of weak bosons with a top quark pair

Production of weak bosons in association with a top quark pair and additional jets is the most important source of irreducible background for  $t\bar{t}H$ ,  $H \rightarrow W^+W^-$  in the final state with two leptons. Since  $t\bar{t}W$  and  $t\bar{t}Z$  both contain fewer jets than the signal, a correct description of additional jets is crucial for a reliable estimation of these backgrounds.

Samples of  $t\bar{t}Z$  and  $t\bar{t}W$  were produced with the leading order AcerMC event generator, with the parton showering done with PYTHIA. Only the final states with leptonic weak boson decays  $Z \rightarrow \ell^+\ell^-$  and  $W \rightarrow \ell^\pm\nu$  ( $\ell = e, \nu, \tau$ ) were generated. Events with at least two leptons ( $e$  or  $\mu$ ) of either charge were selected by a generator level filter, requiring a minimum transverse momentum of 10 GeV and  $|\eta| < 2.7$  for both leptons.

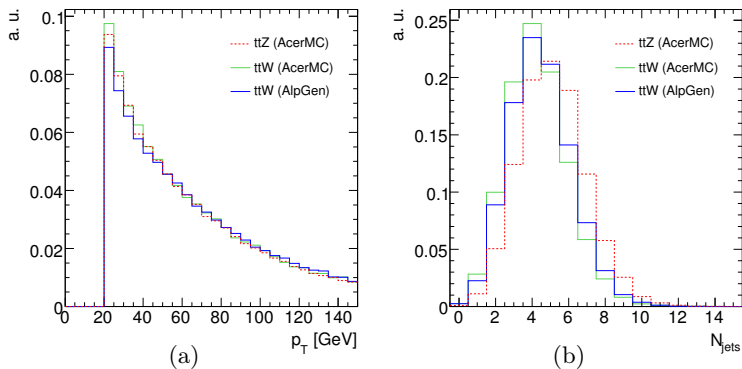
In the case of  $t\bar{t}W$ , a set of samples with up to two extra partons was generated with ALPGEN in addition. Samples of  $t\bar{t}W+0p$ ,  $t\bar{t}W+1p$ , and  $t\bar{t}W+2p$  (“Np” applies to the number of extra partons treated in the matrix element calculation as introduced in Section 2.3.3 of Chapter 2) were produced separately, the latter in inclusive production mode. Fragmentation and hadronization were simulated with HERWIG, and JIMMY was used to model the underlying event. Only the process with leptonic  $W$  boson decays was generated, including the decay  $W \rightarrow \tau\nu$ . In addition, a generator level filter was run on the sample, requiring two leptons ( $e$  or  $\mu$ ) fulfilling  $p_T > 10$  GeV and  $|\eta| < 2.7$ . To study the influence of pile-up on the  $t\bar{t}W$  background, smaller  $t\bar{t}W$  samples overlaid with 2.3 minimum-bias events on average were produced.

Figure 6.4 shows a comparison of the  $p_T$  distributions and multiplicities of parton level jets fulfilling the acceptance cuts  $p_T > 20$  GeV and  $|\eta| < 2.5$  in the  $t\bar{t}Z$  and the two  $t\bar{t}W$  samples. ALPGEN produces a slightly harder  $p_T$  spectrum and also a higher jet multiplicity. Correspondingly, the fraction of events with six or more parton level jets inside the acceptance region rises from 22% (AcerMC) to 26% (ALPGEN). In the case of  $t\bar{t}Z$ , the jet multiplicities are significantly higher than in both  $t\bar{t}W$  samples, with 40% of all events of the AcerMC sample containing six or more jets. The large difference is explained by the fact that, as shown in Fig. 6.5,  $t\bar{t}Z$  events can be produced at leading order in  $gg$  as well as in  $q\bar{q}$  initial states, whereas only  $q\bar{q}$  graphs contribute to the LO  $t\bar{t}W$  calculation. Graphs with gluons in

---

reservation affecting events that contain three or more leptons: In fully leptonic  $t\bar{t}$  events, leptons other than those from the  $W$  boson decays were not always considered to search for like-sign leptons. They were only taken into account, if the leptons from the  $W$  boson decays did not both fulfil  $p_T > 30$  GeV and  $|\eta| < 1.3$  or  $1.7 < |\eta| < 2$  in the case of electrons and  $p_T > 15$  GeV and  $|\eta| < 1.05$  or  $1.45 < |\eta| < 1.8$  in the case of muons. Unlike stated in the publication, these extra requirements do not significantly contribute to the underestimation of the  $t\bar{t}$  background to the two lepton  $t\bar{t}H$ ,  $H \rightarrow W^+W^-$  final state, as shown in Appendix B.1.

the initial state contribute only, if at least one additional parton is generated. Nevertheless, gluons in the initial state enhance the probability for initial state radiation and hence the jet multiplicity in the event. The ALPGEN sample is therefore used in the following to estimate the  $t\bar{t}W$  background, whereas  $t\bar{t}Z$  is considered to be described with sufficient accuracy by AcerMC. Although being suppressed by the higher order in  $\alpha_s$ , the  $gg$  and  $q\bar{q}$  graphs also contribute significantly to the inclusive  $t\bar{t}W$  cross section<sup>6</sup>. This is due to the comparably high gluon flux, which compensates part of the loss in the partonic cross section compared with the leading order graphs.



**Figure 6.4:** Distribution of the parton level jet  $p_T$  (a) and multiplicity (b) in AcerMC samples of  $t\bar{t}Z$  and  $t\bar{t}W$  events and the ALPGEN sample of  $t\bar{t}W$  events with up to two additional partons. Jets are required to have a minimum transverse momentum of 20 GeV and to fulfil  $|\eta| < 2.5$ . All distributions are normalized to unity.

An inclusive NLO cross section calculation exists for  $t\bar{t}Z$ , which yields a total NLO cross section of 1.09 pb with a combined scale and PDF uncertainty of  $\pm 15\%$  [46]. The corresponding LO result is 0.81 pb, with  $\pm(25 - 35)\%$  scale uncertainty [46]. Taking into account the  $Z \rightarrow \ell^+\ell^-$ , ( $\ell = e + \mu + \tau$ ) branching ratio of 0.101, the NLO value, however, is smaller than the LO  $t\bar{t}Z$ ,  $Z \rightarrow \ell^+\ell^-$  cross section of 120 fb provided by AcerMC<sup>7</sup>. Furthermore, the spectra (and hence the crucial phase space region with many jets) are described only at LO by the generator. No NLO calculation exists for the inclusive  $t\bar{t}W$  cross section. To ensure a conservative and consistent estimation of the background, the cross section values and spectra provided by the respective generator were therefore used for all  $t\bar{t}W$  and  $t\bar{t}Z$  samples.

### 6.3.4 $t\bar{t}t\bar{t}$ production

AcerMC was used to generate samples of  $t\bar{t}t\bar{t}$  events produced in the  $gg$  and  $q\bar{q}$  initial states (see Fig. 6.6 for examples of Feynman diagrams for both processes), with the top quark decays and parton showering modelled by PYTHIA. All decays of the top quarks were generated, but the sample was filtered for two leptons ( $e$  or  $\mu$ ) with  $p_T > 5$  GeV and  $|\eta| < 2.7$  afterwards. As for  $t\bar{t}Z$  and  $t\bar{t}W$  production, the cross sections for the two  $t\bar{t}t\bar{t}$  production processes are taken at leading order from the generator<sup>8</sup>.

<sup>6</sup>The importance of the  $gg$  contribution has also been discussed in Ref. [128], where after all event selection cuts two thirds of all  $t\bar{t}W$  events were of the  $gg$  type. The  $gg$  contribution was not studied there.

<sup>7</sup>These differences are the consequence of the different choice of factorization and renormalization scales used in Ref. [46] and the default AcerMC settings. The AcerMC value is in agreement with the scale dependence of the LO cross section given in Ref. [46].

<sup>8</sup>The cross section varies strongly with the choice of the factorization and renormalization scale. The AcerMC default of  $\mu_0 = \hat{s}$  was used here, leading to a relatively low value of the inclusive cross section.

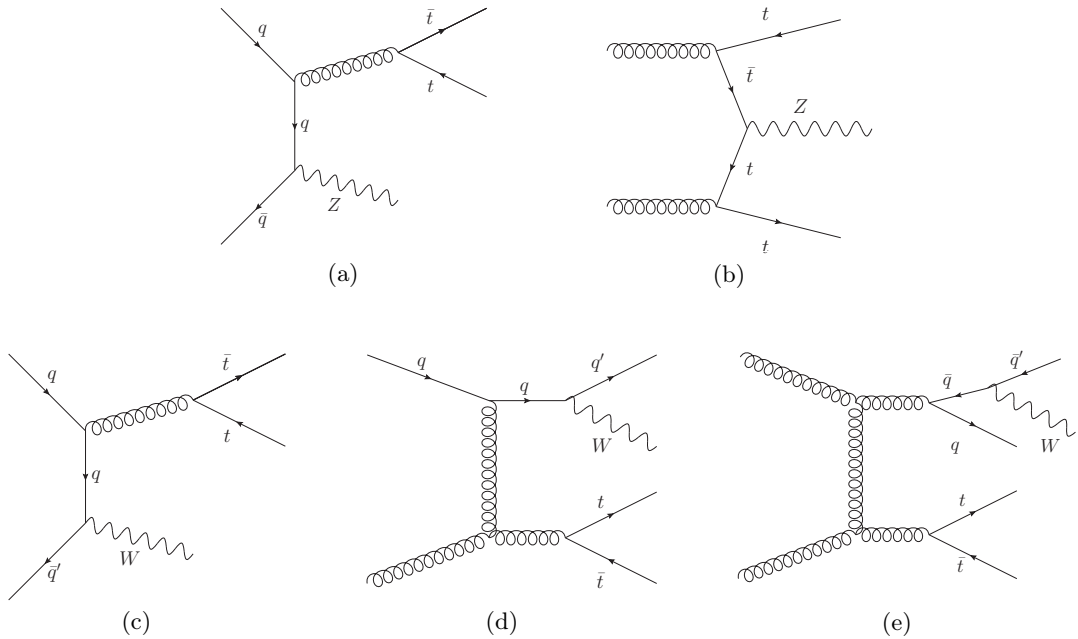


**Figure 6.5:** Feynman diagrams for the associated  $t\bar{t}Z$  production without additional partons in the  $q\bar{q}$  (a) and  $gg$  initial state (b). The production of  $t\bar{t}W$  events without additional partons is only possible in the  $q\bar{q}$  initial state (c). The  $qq$  initial state requires at least one (d), and the  $gg$  initial state at least two (e) extra partons to be produced.

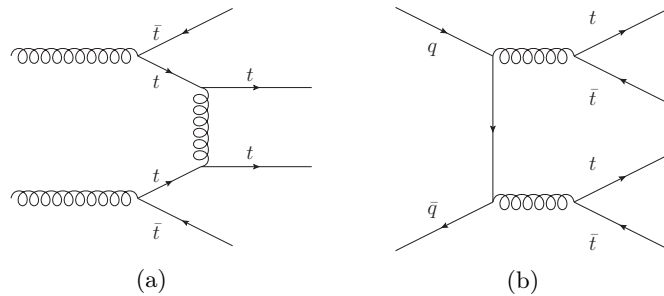


**Figure 6.6:** Examples of Feynman diagrams contributing to the AcerMC cross section calculation of  $gg \rightarrow t\bar{t}t\bar{t}$  (a) and  $q\bar{q} \rightarrow t\bar{t}t\bar{t}$  (b).

### 6.3.5 $W$ boson production in association with jets

$W$ +jet production, including the especially relevant  $Wb\bar{b}$  production process, does not provide top quarks. Nevertheless, it could be a non-negligible source of background, because of its large inclusive production cross section of about 20 nb for the  $W \rightarrow \ell\nu$  channel. The prerequisites for a sizeable background contribution from this process are a sufficiently large lepton misidentification rate (to obtain a second lepton from a jet) and a high enough probability for the production of many additional jets, to generate the signal event topology with six jets. The large rejection factors needed to suppress the  $W$ +jet background to a level well below the accepted signal cross section requires the study of very large Monte Carlo samples.

The largest available  $W$ +jet Monte Carlo dataset produced with a generator suited for the high jet multiplicity final states, is a set of ALPGEN (+HERWIG and JIMMY) samples,

run through the fast ATLAS detector simulation ATLFast-II, as described in Section 3.3.6. Since ATLFast-II was not yet implemented in Athena 12, the ATLAS reconstruction software release mainly used for this analysis, the  $W$ +jet background is studied in Athena 14, which provides support for ATLFast-II. Smaller release 14 datasets are passed through the full detector simulation for validation. The events were produced separately for the decays of the  $W$  bosons to  $e$  and  $\mu$  and for each number of up to five<sup>9</sup> additional partons included in the matrix element calculation. The five parton datasets were produced in inclusive mode. No further generator level filter was applied. The  $\tau$  contribution is conservatively estimated in the analysis by scaling the  $e$  and  $\mu$  results with the  $\tau \rightarrow \mu$  lepton branching ratios. Since the contribution from the datasets with low numbers of additional partons is expected to be negligible, only the datasets with two to five additional matrix element partons are considered for the analysis.

Events containing heavy quarks are treated separately in ALPGEN. Therefore, dedicated samples were produced for  $Wb\bar{b}$ , ( $W \rightarrow \ell\nu$ ,  $\ell = e, \mu, \tau$ ) plus up to three additional partons. In the case of  $Wb\bar{b}$ , only datasets passed through the full detector simulation are available. An overlap occurs with the light jet datasets, which contain  $b$ -quark pairs produced via the gluon splitting process. This was shown to be negligible in Ref. [126], if the generator level filter cuts in the  $Wb\bar{b}$  samples are chosen in correspondence to the matching cuts used for the MLM matching: non-collinear  $b\bar{b}$  pairs from gluon splitting processes that are produced at sufficiently high  $p_T$  are rejected by the MLM matching requirements in the light jet samples. To prevent double counting of the remaining candidates in the  $Wb\bar{b}$  datasets, only events containing  $b$ -quarks with a minimum transverse momentum of 20 GeV and  $\Delta R(b\bar{b}) > 0.7$  were allowed to pass the filter.

The release 14  $W$ +jet samples were produced for studies for the early LHC runs, and hence assume a centre-of-mass energy of 10 TeV, which needs to be corrected to  $\sqrt{s} = 14$  TeV. In the present analysis, scale factors are applied to the inclusive cross sections for each dataset for this purpose (see Section 6.6.3). Small  $W$ +jet datasets produced for a centre-of-mass energy of 14 TeV are also available, which are run through the full detector simulation and reconstructed in Athena 12. They are used to validate the release 14 datasets. The events of these datasets were required to contain at least three cone-0.4 parton-level jets with transverse momenta larger than 30 GeV at the generator level.

The tree-level cross sections provided by the generator are used to normalize the results obtained from the individual datasets. This is done despite the existence of inclusive calculations up to NNLO, because these calculations describe only the phase space regions with a low number of additional jets correctly, whereas they are not expected to provide an accurate description of the high multiplicity final states relevant for this analysis.

---

<sup>9</sup>To date, five additional partons is the maximum number dedicated generators can integrate over. Further partons are only produced by gluon splitting in the evolution of the parton shower. Consequently, the phase space region with six and more high  $p_T$  jets, which is the region relevant for the  $t\bar{t}H$ ,  $H \rightarrow W^+W^-$  analysis, is expected to be described only with large uncertainties even by dedicated generators like ALPGEN.

## 6.4 Event selection

Effective suppression of large background contributions is essential to achieve the signal-to-background ratios needed for an observation of the Higgs boson in the  $t\bar{t}H, H \rightarrow W^+W^-$  channel. In order to suppress the large  $t\bar{t}$  background, lepton isolation is crucial. The likelihood tool described in Chapter 5 has been developed for this purpose. Three event selection approaches are compared in the following that differ from each other only in the treatment of the lepton isolation. The analyses are derived from the “basic” analysis published in Ref. [108]. Some modifications, mainly concerning the jet selection criteria, are made, though, to improve the background rejection. A short comparison is given in Appendix B.3.

To demonstrate the gain in  $t\bar{t}$  suppression due to the likelihood, the lepton isolation cuts used in the baseline analysis of Ref. [108] are adopted for a reference analysis. Two additional analyses, referred to as “likelihood loose” and “likelihood tight”, making use of the likelihood tool for electrons and muons, are compared for their  $t\bar{t}$  rejection. Both provide the same accepted signal cross sections as the “reference” analysis, but differ in the choice of the minimum  $p_T$  required for the muons.

The jet and lepton selection criteria for the three analyses are discussed in Section 6.4.1 of this chapter. Section 6.4.2 outlines the event selection strategy, which is based on the selected physics objects. Signal datasets for nine Higgs boson masses in the range between 120 GeV and 200 GeV are analysed. The Higgs boson mass is not exploited in the event selection, so the analysis strategy and the resulting background expectations are identical for all mass points. In the following, results are given only for the  $M_H = 160$  GeV dataset, if not indicated otherwise.

### 6.4.1 Jet and lepton selection

#### Jets

The analysis requires six jets that are reconstructed with the cone tower clustering algorithm. A cone size of  $\Delta R = 0.4$  is used to ensure the reconstruction of individual jets despite the high activity in the final state. A minimum transverse momentum of 20 GeV is required for all jets. This reduces the influence of pile-up (see Section 6.8) and rejects jets from QCD radiation, which are mainly produced with relatively low transverse momentum. Furthermore, only jets inside the Inner Detector acceptance ( $|\eta| < 2.5$ ) are considered.

#### Leptons

Electron candidates are required to be reconstructed and identified with the high- $p_T$  electron reconstruction algorithm “egammaRec”. They need to pass at least the “medium” electron definition requirements as described in Section 3.3.3 of Chapter 3. This definition is the optimal compromise between rejection of jets and signal electron selection efficiency. Muon candidates must be reconstructed and identified in the muon spectrometer with the “Staco” combined muon algorithm [129]. Electrons and muons have to fulfil the kinematic requirements of  $p_T > 15$  GeV and  $|\eta| < 2.5$ , to be inside the acceptance regions of the trigger and the Inner Detector. The contribution by  $\tau$  leptons is not considered for the analysis, but electrons and muons from leptonic  $\tau$ -decays are accepted if they pass the lepton selection requirements<sup>10</sup>.

<sup>10</sup>This concerns only the backgrounds, since  $\tau$  lepton final states were not generated in the case of the signal, as described in Section 6.2.

### Lepton isolation

Lepton isolation is crucial for the effective suppression of the semi-leptonic  $t\bar{t}$  background, which is the main reducible background after application of the same-sign lepton requirement. The discrimination power of the isolation variables introduced in Chapter 5 is either exploited in a series of cuts in the case of the “reference” analysis, or combined by the `IsolationLikelihood` for the other two analyses as follows:

- **“Reference”**: The transverse energy deposited in the calorimeter in a cone of opening angle  $\Delta R = 0.2$  around the lepton ( $E_T^{\text{cone}}(0.2)$ ) is required to be less than 10 GeV for both electrons and muons<sup>11</sup>. In addition, the transverse momentum of any additional track inside a cone of  $\Delta R = 0.2$  around the lepton candidate ( $p_T^{\text{max trk}}(0.2)$ ) must not exceed 2 GeV. Finally, the muon  $p_T$  is required to be larger than 20 GeV, as it was done in Ref. [108] (see Appendix B.3 for details).
- **“Likelihood loose”**: Alternatively, the `IsolationLikelihood` output value  $r$  is used to reject background leptons. The likelihood is used in the “highJetMulti” configuration as described in Chapter 5. Muons are treated in the same way as the electrons, with the measurement of the Inner Detector track segment used for determination of  $|IP_T|/\Delta IP_T$ . The extra requirement of  $p_T > 20$  GeV for muons is kept to demonstrate the gain in background rejection through the use of the likelihood instead of a set of cuts on individual isolation variables.
- **“Likelihood tight”**: An even better background rejection than with the “likelihood loose” selection can be obtained, if the muons in the range  $15 \text{ GeV} < p_T < 20 \text{ GeV}$  are kept, as done in the “likelihood tight” selection. Instead, the cut on  $r$  is tightened for all muon candidates, such that the total event selection efficiency is the same as in the two other analyses.

The distributions of all considered isolation variables are displayed in Fig. 6.7. Figure 6.8 shows the background rejections for leptons from heavy quark decays that can be achieved with the likelihood as a function of the signal selection efficiency. For comparison with the cut based lepton selection, the working points of the lepton isolation requirements of the “reference” analysis are shown in addition. Compared to these, the likelihood improves the rejection in the non-isolated lepton background by a factor larger than four for electrons and five for muons, at equal lepton selection efficiency. The selection efficiencies for isolated leptons in the  $t\bar{t}H$  dataset after the lepton selection requirements applied in the different analyses and the corresponding background rejection factors in the  $t\bar{t}$  dataset are summarized in Table 6.5.

<sup>11</sup>The lepton  $E_T$ -contribution is removed by subtracting the energy deposited in  $5 \times 14$  calorimeter cells in  $\eta \times \phi$ -direction for electrons and all cells within a cone of  $\Delta R = 0.05$  for muons.

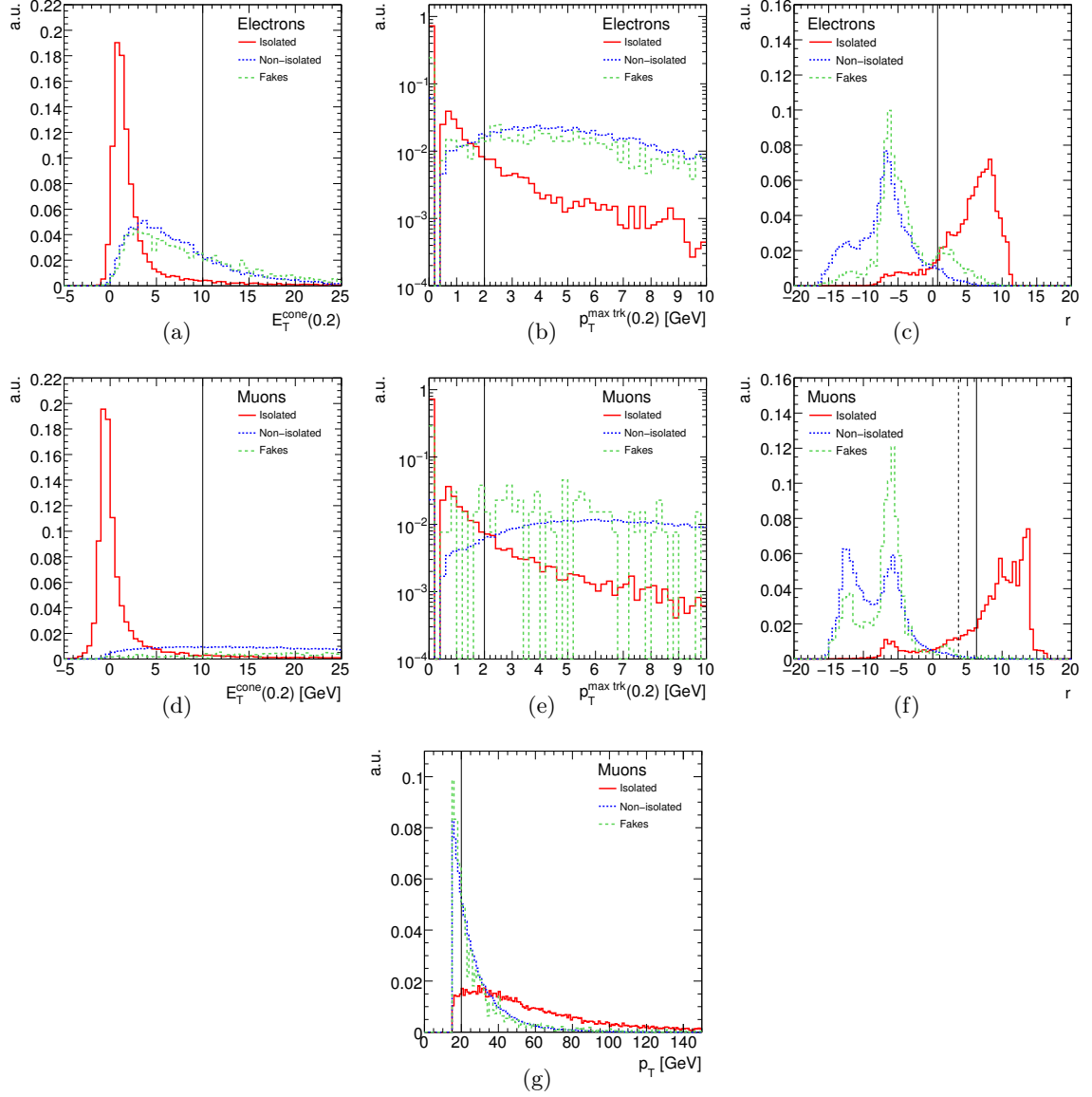


**Figure 6.7:** Lepton isolation variables for the three analyses:  $E_T^{\text{cone}}(0.2)$ ,  $p_T^{\text{max trk}}(0.2)$  and the likelihood output  $r$  for electrons (a, b, c) and muons (d, e, f) and the muon transverse momentum (g). The distributions are shown for leptons from  $W$  and heavy quark decays (“isolated” / “non-isolated”) as well as for lepton candidates that are caused by other sources than real leptons (“fakes”). All distributions are normalized to unity, including possible over- or underflows. The lines indicate the cut values. In the case of the muon likelihood, the dashed line corresponds to the cut for the “likelihood loose” analysis. The prominent double peak structure in the background distributions for the muon likelihood is an artefact caused by the transformation of the  $|IP_T|/\Delta IP_T$  variable. This feature is much weaker for the electrons, where the impact parameter distribution is diluted by bremsstrahlung processes. All distributions are shown for lepton candidates that satisfy the reconstruction and identification criteria, as well as the acceptance cuts on  $p_T > 15$  GeV and  $|\eta| < 2.5$ . No isolation cuts on the leptons or kinematic event selection cuts are applied.

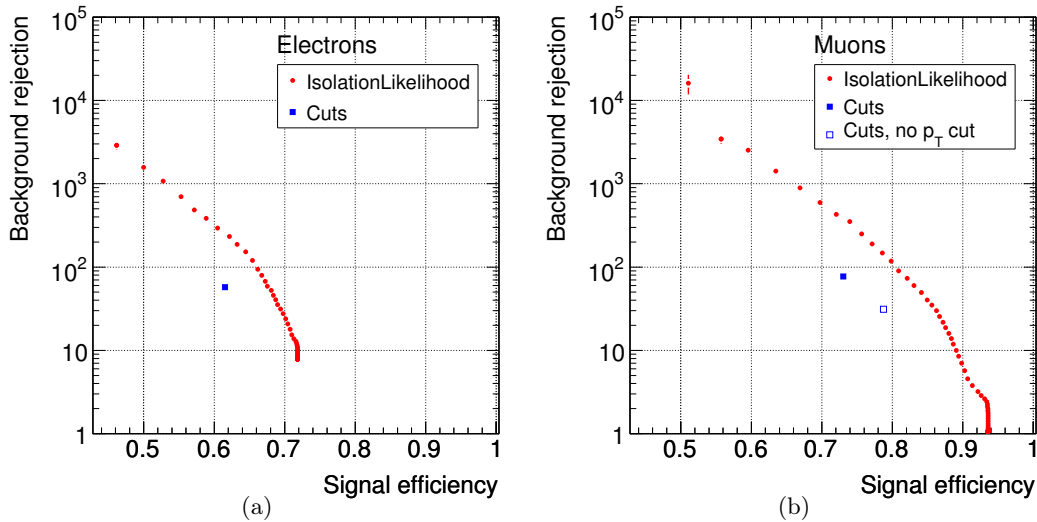


**Figure 6.8:** Background rejection for electrons (a) and muons (b) from heavy quark decays in the filtered  $t\bar{t}$  sample as a function of the selection efficiency for signal electrons in the  $t\bar{t}H$ ,  $H \rightarrow W^+W^-$  datasets that can be achieved by the use of the isolation likelihood. Reconstruction and identification efficiencies are included for both lepton types. The boxes mark the working points of the isolation cuts used by the “reference” analysis. Only lepton candidates are considered that satisfy the reconstruction and identification criteria, as well as the acceptance cuts on  $p_T > 15$  GeV and  $|\eta| < 2.5$ . No isolation cuts on the leptons or kinematic event selection cuts are applied.

### Elimination of ambiguities between electron and jet definitions

Electrons usually are also reconstructed as jet candidates, as discussed in Section 3.3.4. To resolve these ambiguities for the  $t\bar{t}H$ ,  $H \rightarrow W^+W^-$  analysis, where the signal is expected to contain well isolated leptons as well as leptons from semi-leptonic heavy quark decays, a compromise needs to be found between good rejection of jet candidates caused by isolated electrons and a sufficient efficiency for the identification of real jets containing electrons. A suited choice is to look for the closest reconstructed jet candidate in the vicinity of a reconstructed electron candidate fulfilling the lepton identification requirements and the analysis dependent isolation criteria described above. Figure 6.9(a) shows the resulting distribution for the angular distance  $\Delta R^{e-\text{jet}}$  between the electron cluster and the jet candidate. Both, the electron and the jet, are kept for the analysis if the distance  $\Delta R^{e-\text{jet}}$  is larger than 0.1. In the case of a smaller  $\Delta R^{e-\text{jet}}$ , the cluster energy ratio  $E_e/E_{\text{jet}}$  is used to decide whether to keep the jet or the lepton, as can be seen in Fig. 6.9(b). For large fractions of electromagnetic energy the probability is high that the candidate is actually an isolated electron. Hence the electron is kept and the jet rejected, if  $E_e/E_{\text{jet}} > 0.65$ , whereas the jet is kept and the electron rejected in the case of a lower  $E_e/E_{\text{jet}}$ .

### Angular separation of leptons and jets

Leptons from semi-leptonic heavy quark decays are expected to be found close to a jet. After defining leptons and jets, this characteristic can be used to further reject background leptons by demanding a minimum angular distance  $\Delta R_{\text{min}}^{\text{jet}}$  between the lepton and the closest jet. In the case of electrons, all jets in the jet collection ( $p_T > 10$  GeV) are considered for determining the closest jet candidate. As for the electron/jet definition described above, the  $\eta$  and  $\phi$  coordinates of the electron cluster are used to calculate the distance. In the case of

	Efficiency (isolated)		Rejection (non-isolated)	
	Signal, $M_H = 160$ GeV		$t\bar{t}$ (filtered)	
	Electrons	Muons	Electrons	Muons
Reconstruction	$0.907 \pm 0.002$	$0.936 \pm 0.002$	$1.260 \pm 0.001$	$1.067 \pm 0.001$
+ ID	$0.718 \pm 0.004$	–	$7.86 \pm 0.04$	–
+ $E_T^{\text{cone}}(0.2) > 10$ GeV	$0.669 \pm 0.004$	$0.837 \pm 0.003$	$10.75 \pm 0.04$	$6.09 \pm 0.03$
+ $p_T^{\text{max trk}}(0.2) > 2$ GeV	$0.615 \pm 0.004$	$0.788 \pm 0.003$	$57.5 \pm 0.9$	$31.1 \pm 0.4$
+ $p_T > 20$ GeV ( $\mu$ )	–	$0.731 \pm 0.004$	–	$77.4 \pm 1.4$
+ Likelihood loose	$0.626 \pm 0.004$	$0.790 \pm 0.003$	$179 \pm 5$	$140 \pm 3$
+ $p_T > 20$ GeV ( $\mu$ )	–	$0.737 \pm 0.004$	–	$292 \pm 10$
+ Likelihood tight	$0.626 \pm 0.004$	$0.718 \pm 0.004$	$179 \pm 5$	$510 \pm 24$

**Table 6.5:** Identification and selection efficiencies for leptons from  $W$  boson decays in the signal sample at  $M_H = 160$  GeV and corresponding background rejection factors for leptons from semi-leptonic heavy quark decays in the filtered  $t\bar{t}$  sample. The efficiencies and rejections are calculated according to Eqs. 5.10 and 5.11 in Chapter 5 with respect to all generated leptons passing  $p_T > 15$  GeV and  $|\eta| < 2.5$ . No event selection criteria are applied. It should be noted that the working points chosen for the likelihood analyses do not correspond to a signal selection efficiency equal to that of the “reference” analysis on lepton level. Instead, they are chosen such that the final signal event selection efficiency is the same for all three analyses, as described in the text.

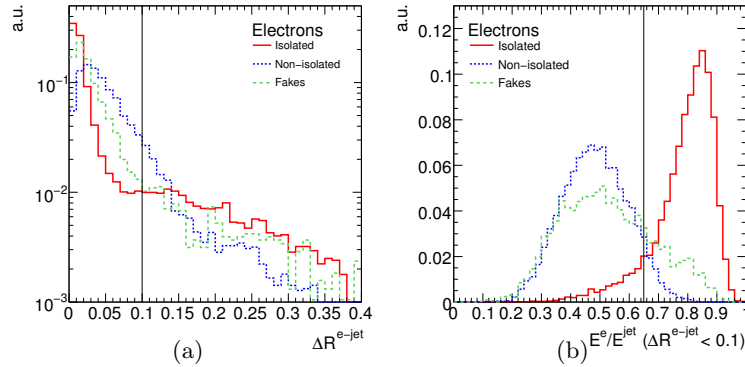


**Figure 6.9:** Angular distance  $\Delta R^{e-jet}$  between reconstructed electrons fulfilling the isolation criteria for the “likelihood tight” selection and the closest reconstructed jet candidate (a) and ratio of the electron cluster energy to the energy of the jet candidate for the cases  $\Delta R^{e-jet} < 0.1$  (b) and  $\Delta R^{e-jet} > 0.1$  (c). The distributions are shown for leptons from  $W$  and heavy quark decays (“isolated” / “non-isolated”) as well as for electron candidates which are caused by other sources than real leptons (“fakes”). Only lepton candidates are considered that satisfy the reconstruction, identification and isolation criteria, as well as the acceptance cuts on  $p_T > 15$  GeV and  $|\eta| < 2.5$ . No kinematic event selection cuts are applied. All distributions are normalized to unity. The lines indicate the cut values for the overlap removal.

muons, jets need to have a minimum  $p_T$  of 15 GeV to be considered<sup>12</sup>. Figure 6.10 shows the resulting  $\Delta R_{\min}^{\text{jet}}$  distributions for signal and background leptons. Following the requirements defined in Ref. [108], muons must be separated from their neighbouring jet by at least  $\Delta R_{\min}^{\text{jet}} = 0.25$ , whereas for electrons a minimum distance of  $\Delta R_{\min}^{\text{jet}} = 0.2$  is demanded.

<sup>12</sup>Occasionally, high energy muon candidates deposit more than the usual 2 GeV to 3 GeV in the calorimeter through hard bremsstrahlung processes, causing very close jet candidates with low  $p_T$ .

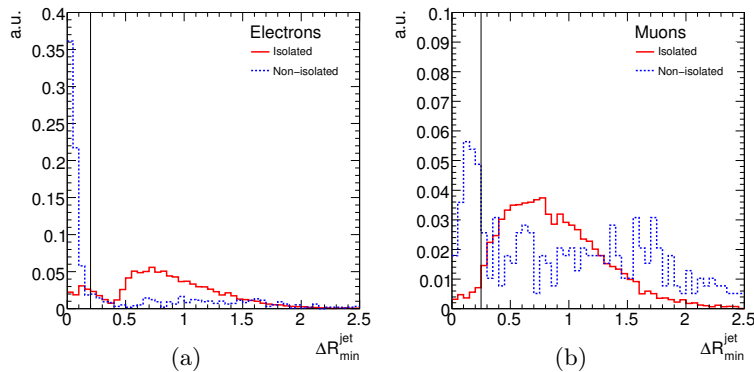


**Figure 6.10:**  $\Delta R_{\min}^{\text{jet}}$  distributions for electrons (a) and muons (b) matching the lepton isolation criteria of the “likelihood tight” analysis and after the removal of electron/jet ambiguities. The distributions are shown for leptons from  $W$  boson decays in the signal sample (“isolated”) and heavy quark decays in the filtered  $t\bar{t}$  dataset (“non-isolated”) and all normalized to unity. The lines indicate the cuts applied to separate signal and background leptons. The two components in the distribution of isolated leptons in (a) is caused by the electron/jet definition procedure described above: The jet clustering algorithm requires a minimum angular distance of  $\Delta R = 0.4$  between two jet candidates. Therefore the  $\Delta R_{\min}^{\text{jet}}$  values are expected to be larger than 0.4 in case the ambiguity was solved correctly. In the case of a smaller values, both, the electron and the jet candidate caused by the electron, are accepted, either because the distance  $\Delta R^{e\text{-jet}}$  is larger than 0.1 or because the ratio  $E_e/E_{\text{jet}}$  is small (tail regions of the distributions for isolated leptons in Figs. 6.9(a) and 6.9(b)).

### 6.4.2 Kinematic event selection

Based on the object selection criteria described above, a pair of like-sign leptons (electrons or muons) and six jets are required. In addition, further event selection criteria are applied to select the desired signal and to reject background events. These are described in the following.

#### 3rd lepton and $Z$ veto

A large fraction of the  $t\bar{t}Z$  background contribution can be rejected by a veto on a third isolated lepton, which in addition ensures that no overlap occurs with a potential analysis of the final state with three leptonic  $W$  boson decays. The accepted events still contain a sizeable fraction of  $t\bar{t}Z$  background events, because the leptons counted by the third lepton veto need to be well isolated. If one of the leptons from the  $Z$  boson decay does not fulfil the isolation requirements or carries too little transverse momentum to be counted, the event is still accepted. Such events can further be suppressed by an explicit veto on the  $Z$  boson mass that includes also non-isolated leptons and leptons with small transverse momenta: events containing a lepton pair of opposite charge and same flavour with an invariant mass  $m_{\ell\ell}$  between 75 GeV and 100 GeV are rejected. This veto includes all leptons above a  $p_T$ -threshold of 6 GeV and inside the Inner Detector acceptance  $|\eta| < 2.5$  that pass the lepton reconstruction and identification criteria, without lepton isolation being required. The dilepton invariant mass distributions in the events passing the 3rd lepton veto in the signal and  $t\bar{t}Z$  for the “reference” and “likelihood tight” analyses are displayed in Fig. 6.11. In the case of the “reference” and “likelihood loose” analyses, the  $Z$  veto decreases the  $t\bar{t}Z$  contribution roughly by another 50%, whereas almost 100% of the signal survive. The impact on the “likelihood tight” analysis is smaller, with only 35% of the background being removed and

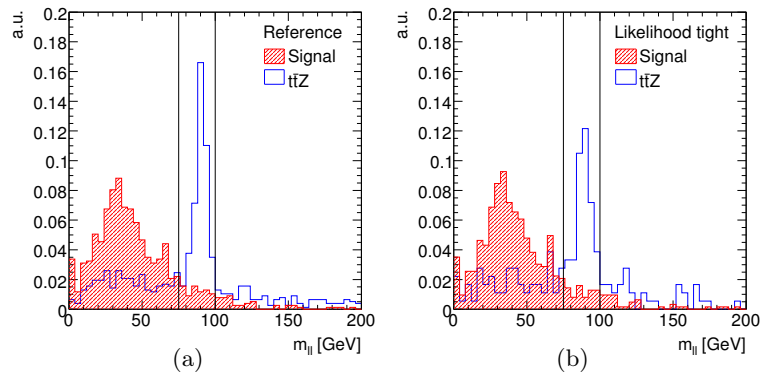


**Figure 6.11:** Invariant mass distributions for oppositely charged lepton pairs in the  $t\bar{t}H$ ,  $H \rightarrow W^+W^-$  and  $t\bar{t}Z$  datasets after the 3rd lepton veto for the “reference” (a) and “likelihood tight” analyses (b). The distributions are normalized to unity. The region between the lines contains the events rejected by the  $Z$  veto.

98% of the signal surviving<sup>13</sup>.

### ***b*-tagging**

Although the  $t\bar{t}$  background contains as many  $b$ -jets as the signal, significant reduction of the  $t\bar{t}$  contribution can be achieved by requiring at least two of the jets to match loose  $b$ -tagging criteria. Since the second lepton in the remaining  $t\bar{t}$  events is usually the product of a semi-leptonic heavy quark decay, but, nevertheless, matches all lepton isolation requirements, the corresponding  $b$ -jet is lost when the ambiguity between electrons and jets is resolved. To be considered a  $b$ -jet, the jets have to be assigned a  $b$ -tag weight larger than three by the combined impact parameter and secondary vertex tagger “IP3D+SV1” [130]. Real  $b$ -jets are identified with an efficiency of about 74% in the signal sample by this requirement. The distribution of weights for  $b$ -,  $c$ - and light jets in the  $t\bar{t}H$ ,  $H \rightarrow W^+W^-$  signal and a comparison of the corresponding selection efficiencies as a function of the cut value are shown in Figs. 6.12(a) and 6.12(b). Figure 6.12(c) shows a comparison of the multiplicity of  $b$ -jet candidates in  $t\bar{t}$  and in signal events after all event selection requirements described so far. At this stage of the analysis, 75% of all signal events contain two jets fulfilling the  $b$ -tagging requirements, whereas less than 10% of all  $t\bar{t}$  events in the pre-filtered sample contain two or more  $b$ -jet candidates.

### **Accepted signal and background cross sections**

A summary of the three different event selections, including the order in which the cuts are actually applied, together with the corresponding accepted cross sections is given in Table 6.6. The total signal selection efficiency of 8% on the filtered signal dataset leads to an accepted cross section of  $(0.84 \pm 0.02)$  fb for  $M_H = 160$  GeV after all cuts. About the same signal efficiency is observed for all other Higgs boson masses, leading to lower accepted cross sections according to the lower production cross sections. Since the  $t\bar{t}W$ ,  $t\bar{t}Z$  and  $t\bar{t}t\bar{t}$  backgrounds are irreducible, the selection efficiencies for these processes, as for the signal, do not differ

<sup>13</sup>This difference is, however, artificial and caused by the order in which the individual cuts are applied in the analysis. Whereas in the former two analyses the muon  $p_T$  cut is applied after the  $Z$ -veto, to be consistent with the analysis in Ref. [108], the tight cut on the likelihood output is applied already in the first steps of the analysis in the latter case, resulting in a tighter lepton selection before the 3rd lepton veto is applied.

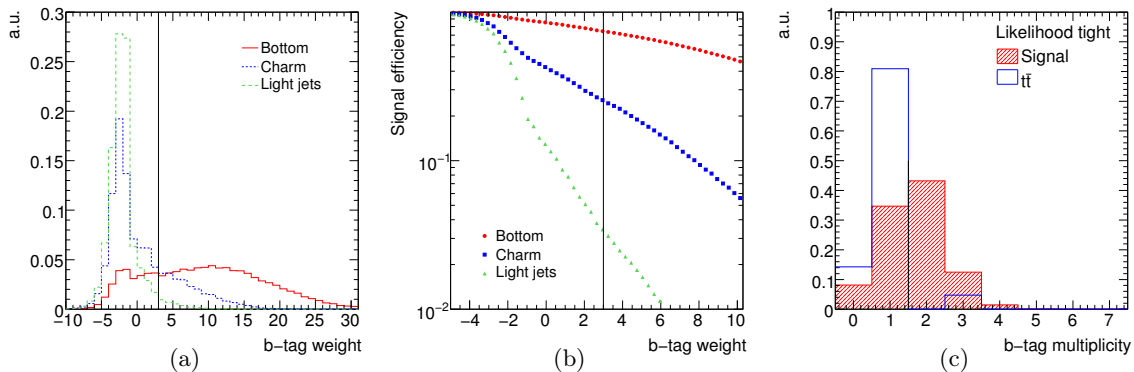


**Figure 6.12:** (a) Distribution of the jet weights provided by the IP3D+SV1 tagger for true  $b$ -,  $c$ - and light jets in  $t\bar{t}H$ ,  $H \rightarrow W^+W^-$ . All distributions are normalized to unity. (b) Selection efficiency of true  $b$ -,  $c$ - and light jets as a function of the cut on the jet weight value. The lines indicate the cut values used for the event selection. (c) Distribution of the  $b$ -jet multiplicity in  $t\bar{t}H$ ,  $H \rightarrow W^+W^-$  and pre-filtered  $t\bar{t}$  events before the requirement of two jets passing the  $b$ -tagging cuts. Only jets inside  $p_T > 20$  GeV and  $|\eta| < 2.5$  are considered.

significantly between the three selections. Considering the expected differences due to different generator level filters or decay modes imposed on the samples, they are furthermore of an order of magnitude comparable to that for the signal. Because of the relatively lower jet multiplicity in  $t\bar{t}W$ , this background passes the requirement of six jets and two leptons with lower probability than the signal and the other irreducible backgrounds. The most effective suppression of  $t\bar{t}Z$  is provided by the 3rd lepton and  $Z$  boson vetoes, as discussed above. The main effect of the event selection is the suppression of reducible backgrounds, the most important of which,  $t\bar{t}$ , is suppressed by about a factor of  $10^7$ . It must be stressed that the  $t\bar{t}$  contribution is underestimated in the pre-filtered dataset and carries a large statistical uncertainty in all  $t\bar{t}$  samples: In the case of the “likelihood tight” analysis, five Monte Carlo events pass the complete event selection criteria in the filtered sample, two of them with negative weight, such that the total accepted cross section in this sample is obtained as the cross section equivalent of one generated event. The same applies for the “no all-hadronic”  $t\bar{t}$  sample, where exactly one Monte Carlo event survives the selection cuts (see the Appendix B.2 for the treatment of MC@NLO event weights). An improved estimate of the total accepted  $t\bar{t}$  cross section is given in Section 6.5 and the total accepted background is calculated in Section 6.7, based on these results.

### 6.4.3 Triggers and trigger efficiencies

All event selection efficiencies given so far do not include possible trigger inefficiencies. Although the signal contains two isolated leptons, which give a clear trigger signature, some loss in the signal selection efficiency due to the trigger requirements is expected. The final state contains well isolated leptons and hence can be triggered by demanding either one isolated high- $p_T$  lepton or two isolated leptons of lower  $p_T$ . The two lepton triggers are not fully implemented in the trigger simulation of the ATLAS reconstruction software release used throughout this thesis. Therefore, only the single high- $p_T$  lepton triggers are discussed briefly here.

Cut	Signal $M_H = 160 \text{ GeV}$	$t\bar{t}W$	$t\bar{t}Z$	$\sigma_{\text{acc}}$ [fb]		$t\bar{t}$ "no all-hadronic"	$t\bar{t}$ (filtered)
				$t\bar{t}t$	$t\bar{t}t\bar{t}$		
0 Initial	8.220±0.062	79.982±0.386	94.800±0.675	1.753±0.010	452314.085±800.000	31985.395±62.656	
<b>"Reference"</b>							
1 $2\ell + 6$ jets	1.562±0.027	3.278±0.084	14.794±0.266	0.239±0.004	431.919±27.306	73.784±3.437	
2 Like-sign leptons	1.554±0.027	1.598±0.059	3.077±0.122	0.096±0.002	63.182±9.436	36.529±2.324	
3 $\Delta R_{\text{min}}^{\text{le}} > 0.25$ ( $\mu$ )	1.452±0.026	1.486±0.057	2.794±0.116	0.087±0.002	44.538±8.221	21.354±1.815	
4 $\Delta R_{\text{min}}^{\text{le}} > 0.2$ ( $e$ )	1.267±0.024	1.297±0.053	2.429±0.108	0.078±0.002	9.322±3.735	6.088±1.040	
5 3rd lepton veto	1.154±0.023	1.168±0.050	2.275±0.105	0.070±0.002	5.179±3.107	2.817±0.698	
6 $Z$ veto	1.152±0.023	1.108±0.049	1.162±0.075	0.056±0.002	5.179±3.107	2.908±0.692	
7 $pr > 20 \text{ GeV}$ ( $\mu$ )	1.131±0.023	1.079±0.048	0.878±0.065	0.052±0.002	5.179±3.107	2.908±0.692	
8 $b$ -tag	0.653±0.018	0.691±0.039	0.475±0.048	0.045±0.002	3.107±1.794	0.545±0.364	
<b>"Likelihood loose"</b>							
1 $2\ell + 6$ jets	1.558±0.027	3.224±0.084	14.928±0.268	0.229±0.004	335.591±24.815	40.345±2.631	
2 Like-sign leptons	1.554±0.027	1.575±0.058	3.115±0.122	0.090±0.002	12.429±4.394	8.996±1.131	
3 $\Delta R_{\text{min}}^{\text{le}} > 0.25$ ( $\mu$ )	1.448±0.026	1.469±0.056	2.856±0.117	0.083±0.002	10.358±4.143	7.269±1.004	
4 $\Delta R_{\text{min}}^{\text{le}} > 0.2$ ( $e$ )	1.263±0.024	1.311±0.053	2.563±0.111	0.076±0.002	4.143±2.072	2.544±0.630	
5 3rd lepton veto	1.157±0.023	1.193±0.051	2.414±0.108	0.068±0.002	3.107±1.794	1.545±0.472	
6 $Z$ veto	1.155±0.023	1.137±0.050	1.190±0.076	0.056±0.002	3.107±1.794	1.636±0.463	
7 $pr > 20 \text{ GeV}$ ( $\mu$ )	1.134±0.023	1.106±0.049	0.888±0.065	0.052±0.002	3.107±1.794	1.636±0.463	
8 $b$ -tag	0.655±0.018	0.710±0.039	0.475±0.048	0.045±0.002	1.036±1.036	0.273±0.240	
<b>"Likelihood tight"</b>							
1 $2\ell + 6$ jets	1.400±0.026	2.862±0.079	13.776±0.257	0.204±0.003	290.017±23.391	34.439±2.444	
2 Like-sign leptons	1.397±0.026	1.383±0.055	2.774±0.115	0.080±0.002	6.215±3.588	6.633±0.940	
3 $\Delta R_{\text{min}}^{\text{le}} > 0.25$ ( $\mu$ )	1.341±0.025	1.338±0.054	2.659±0.113	0.076±0.002	6.215±3.588	6.179±0.900	
4 $\Delta R_{\text{min}}^{\text{le}} > 0.2$ ( $e$ )	1.163±0.023	1.190±0.051	2.376±0.107	0.069±0.002	2.072±1.465	1.817±0.481	
5 3rd lepton veto	1.161±0.023	1.138±0.050	1.200±0.076	0.056±0.002	2.072±1.465	1.908±0.472	
6 $Z$ veto	1.140±0.023	1.110±0.049	0.883±0.065	0.053±0.002	2.072±1.465	1.908±0.472	
7 $b$ -tag	0.652±0.018	0.712±0.039	0.480±0.048	0.046±0.002	1.036±1.036	0.091±0.203	

**Table 6.6:** Event selection criteria and accepted cross sections [fb] for the three analyses for the  $t\bar{t}H$  signal ( $M_H = 160 \text{ GeV}$ ) and the considered background samples. The criteria concerning the jet/lepton characteristics require the event to contain six jets and two leptons (of equal electric charge after the like-sign requirement) matching the criteria given in the "Cut" column. It must be noted that one accepted Monte Carlo  $t\bar{t}$  event corresponds to 1.036 fb for the "no all-hadronic" and to 0.091 fb for the pre-filtered dataset and the numbers given for these samples are plagued with large statistical uncertainties.

The single-lepton triggers studied are listed in Table 6.7. These require either one isolated electron candidate above a threshold of  $p_T = 25$  GeV or an electron candidate that does not have to fulfil isolation requirements, but has a high  $p_T$  threshold of 60 GeV. In the case of the muons, isolated muon candidates with transverse momenta above 20 GeV are required<sup>14</sup>.

	Electrons	Muons
Level-1	L1_EM25I, L1_EM60	L1_MU20, L1_MU40
Level-2	L2_e25i, L2_e60	L2_mu20i
Event Filter	EF_e25i, EF_e60	EF_mu20i

**Table 6.7:** List of the single-lepton triggers used to select  $t\bar{t}H$ ,  $H \rightarrow W^+W^-$  candidate events. The numbers in the labels denote the minimum  $p_T$  required for a trigger decision. L1\_MU20 is sensitive only to the  $p_T$ -range between 20 GeV and 40 GeV. No upper limits are imposed on the transverse momenta of the candidates by all other triggers. An “i” or “T” indicates additional isolation requirements.

The resulting event level trigger efficiencies for the signal at  $M_H = 160$  GeV and for the most relevant backgrounds after the application of the “likelihood tight” event selection criteria are listed in Table 6.8. The requirement of one high- $p_T$  lepton trigger causes only a small loss of 5% in the event rates accepted by the offline selection in the signal as well as in the irreducible backgrounds. The  $t\bar{t}$  dataset is not large enough for a reliable prediction of the loss due to the trigger requirements after all cuts. A higher loss in trigger efficiency than observed in the other backgrounds is expected at least for the fraction of  $t\bar{t}$  background consisting of semi-leptonic  $t\bar{t}$  events. Since the second lepton stems from a heavy quark decay, it tends to have a low transverse momentum and to fail the trigger isolation requirements. Thus, only one lepton can provide the trigger signal and the event is kept with a lower probability.

	$t\bar{t}H$	$t\bar{t}W$	$t\bar{t}Z$	$t\bar{t}t$
Level 1	0.99	0.99	1.00	1.00
Level 2	0.97	0.97	0.99	0.97
Event Filter	0.95	0.95	0.93	0.95

**Table 6.8:** Event level trigger efficiencies after the application of the offline “likelihood tight” event selection requirements for the  $t\bar{t}H$ ,  $H \rightarrow W^+W^-$  signal ( $M_H = 160$  GeV) and the studied background samples. No trigger efficiencies are given for the  $t\bar{t}$  datasets because of the too small number of events in the sample. The efficiencies at the different trigger stages are given as total efficiencies, including the efficiency of previous trigger stages.

Over all, the impact of the trigger requirements on the signal-to-background ratio and also on the discovery significance for the  $t\bar{t}H$ ,  $H \rightarrow W^+W^-$  channel is almost negligible. Moreover, the loss due to the trigger requirements cannot be quantified for all relevant backgrounds. Finally, even higher trigger efficiencies will be achievable with more recent ATLAS reconstruction software versions than used for this study. Especially on the Event Filter level, improvement is expected by more advanced object reconstruction algorithms. In addition, a larger trigger menu than studied here will be available for the data taking. Di-lepton triggers with lower  $p_T$  thresholds are good candidates to catch the events that are lost so far and will be employed for data taking. Therefore, the trigger efficiencies are not accounted for in the results given in the following.

<sup>14</sup>Details on the electron and muon triggers, which, however, may differ slightly between releases and sub-releases of the ATLAS reconstruction software, can be found in Refs. [131, 132].

## 6.5 Estimation of the additional contributions to the $t\bar{t}$ background

The estimation of the  $t\bar{t}$  background from the filtered sample suffers from the fact that sources of background leptons other than semi-leptonic heavy quark decays may be underestimated. Two additional effects need to be considered: Lepton candidates can be caused by other sources than real leptons (“fake” leptons), e.g. by charged hadrons. Moreover, fully leptonic  $t\bar{t}$  events may pass all event selection requirements, if the charge of one of the leptons is assigned incorrectly. The importance of these contributions increases with a more effective a suppression of the semi-leptonic heavy quark decay component. Alternative approaches to estimate the size of these remaining components of the  $t\bar{t}$  background are therefore described in Sections 6.5.1 and 6.5.2. The results are discussed in Section 6.5.3.

### 6.5.1 $t\bar{t}$ background generated by “fake” leptons

One underestimated background component is made up of events with lepton candidates that are mistakenly reconstructed from other objects than real leptons. The number of Monte Carlo events in the “no all-hadronic” sample is not sufficient to give an exact estimate of the fake lepton  $t\bar{t}$  background contribution. In the following the origin and relevance of this background is discussed. A rough estimate of the contribution to the total  $t\bar{t}$  background is obtained in the following.

Figure 6.13 shows the  $p_T$  and  $\eta$  dependence of the fake lepton rates found in the “no all-hadronic”  $t\bar{t}$  sample. These rates are determined as the fraction of fake lepton candidates in a sample of lepton candidates passing the complete set of “likelihood tight” lepton selection requirements, including the cut on  $\Delta R_{\min}^{\text{jet}}$ . The electron fake rates show a strong  $p_T$  dependence, starting at about 1.4% at 15 GeV and decreasing to less than 0.5% for transverse momenta larger than 80 GeV. The fake rates are especially high at  $|\eta| \approx 1.5$ , which are the transition regions between the barrel and endcap parts of the detector. The lowest fake rates are measured in the barrel region. The fake rates for muons are lower by more than an order of magnitude compared with those for electrons. Therefore, only the fake electrons causing  $t\bar{t}$  background are examined in more detail in the following.

In addition to the standard lepton identification criteria, leptons considered for the studied  $t\bar{t}H$  final state must fulfil the very tight isolation criteria introduced in Section 6.4.1. Most of the fake lepton candidates that pass these tight requirements are very untypical and their composition differs significantly from that in samples of electron candidates that are required only to pass the identification criteria (see Ref. [107]). After application of the isolation requirements, they consist mainly of four different types:

- **Charged hadrons:** In rare cases, charged hadrons cause narrow showers with a large fraction of electromagnetic energy deposition. These candidates, in most cases charged pions or kaons, may be reconstructed as electron candidates that pass the electron identification requirements.
- **Hadronically decaying  $\tau$  leptons:** Mainly in fully leptonic  $t\bar{t}$  events,  $\tau$  leptons from  $W$  boson decays cause another source of fake electron candidates, if they decay hadronically. Especially one-prong  $\tau$  lepton decays can resemble electron candidates, if they induce a narrow shower with a large fraction of electromagnetic energy deposition.
- **Internal bremsstrahlung:** In photon radiation processes off  $W$  bosons frequently a well isolated photon is produced, as illustrated in Fig. 6.14. If this photon by chance

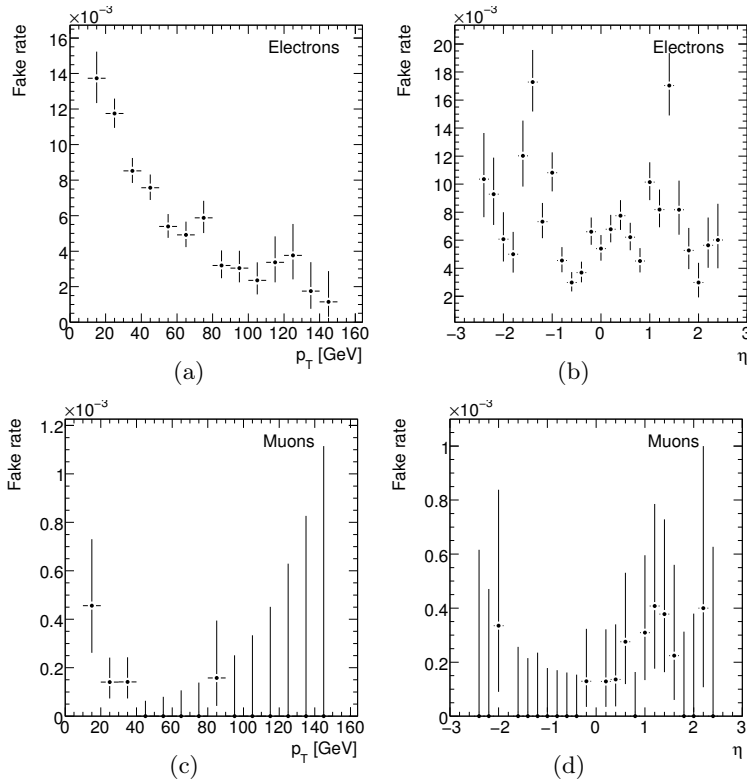


**Figure 6.13:** Fraction of electron (a, b) and muon (c, d) fakes in samples of all electrons/muons passing the lepton selection requirements of the “likelihood tight” event selection in events of the “no all-hadronic”  $t\bar{t}$  sample as a function of  $p_T$  and  $\eta$ . No event selection cuts are applied.

is matched to a track, an electron candidate is faked that is likely to pass all isolation requirements.

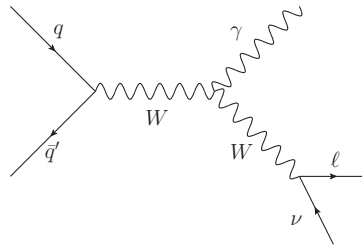


**Figure 6.14:** Feynman diagram for the internal bremsstrahlung process.

- **Background electrons:** Although being real electrons, secondary electrons, mainly from photon conversions or  $\pi^0/\eta$  Dalitz decays, are also classified as fake electron background. These electrons are not only produced in secondary interactions, but often the cluster associated to the electron candidate is not caused by the electron itself, but by the mother photon or  $\pi^0$ .

The composition of the fake electron sample depends strongly on the stage of the event selection. To demonstrate this, the shares of the four types in the sample of fully isolated fake electron candidates from the “no all-hadronic”  $t\bar{t}$  dataset are listed in Table 6.9 at different

stages of the event selection. The numbers are obtained for electron candidates accepted by the “likelihood tight” definition and are given separately for semi-leptonic and fully leptonic events. For comparison, also the real electrons from heavy quark decays are included. Only lepton related event selection requirements are applied, because the sample size is too small to apply also the jet related cuts. Instead, the average jet multiplicities in the selected events are given in addition in the table.

Fake type	Semi-leptonic $t\bar{t}$			Fully leptonic $t\bar{t}$		
	Fraction	Av. $N_{\text{jet}}$	Fraction (tight ID)	Fraction	Av. $N_{\text{jet}}$	Fraction (tight ID)
	Initial					
Charged had.	$0.16 \pm 0.02$	$3.8 \pm 0.1$	$0.00 \pm 0.02$	$0.009 \pm 0.011$	$3.2 \pm 0.7$	$-0.04 \pm 0.04$
Hadronic $\tau$	$0.47 \pm 0.02$	$4.0 \pm 0.1$	$0.24 \pm 0.04$	$0.62 \pm 0.04$	$2.8 \pm 0.1$	$0.22 \pm 0.13$
Int. brems.	$0.24 \pm 0.02$	$4.1 \pm 0.1$	$0.21 \pm 0.04$	$0.31 \pm 0.04$	$2.5 \pm 0.1$	$0.35 \pm 0.13$
Backgr. ele.	$0.031 \pm 0.008$	$3.6 \pm 0.3$	$0.12 \pm 0.04$	$0.004 \pm 0.008$	—	$0.04 \pm 0.07$
Others	$0.012 \pm 0.006$	$4.1 \pm 0.4$	—	$0.018 \pm 0.009$	—	—
HQ decays	$0.085 \pm 0.013$	$3.4 \pm 0.4$	$0.43 \pm 0.05$	$0.04 \pm 0.02$	$2.2 \pm 0.4$	$0.44 \pm 0.13$
	2 leptons					
Charged had.	$0.59 \pm 0.07$	$3.6 \pm 0.2$	$0.06 \pm 0.09$	$0.032 \pm 0.016$	—	—
Hadronic $\tau$	—	—	—	$0.59 \pm 0.05$	$2.9 \pm 0.1$	$0.2 \pm 0.2$
Int. brems.	$0.06 \pm 0.03$	—	$0.17 \pm 0.09$	$0.34 \pm 0.05$	$2.4 \pm 0.2$	$0.4 \pm 0.2$
Backgr. ele.	$0.07 \pm 0.04$	$3.4 \pm 0.7$	$0.17 \pm 0.11$	$0.000 \pm 0.011$	—	$0.00 \pm 0.10$
Others	$0.03 \pm 0.02$	—	—	$0.008 \pm 0.008$	—	—
HQ decays	$0.26 \pm 0.07$	$3.3 \pm 0.3$	$0.61 \pm 0.15$	$0.03 \pm 0.02$	$2.3 \pm 0.4$	$0.39 \pm 0.15$
	Like-sign leptons					
Charged had.	$0.29 \pm 0.13$	$4.6 \pm 0.6$	—	$0.4 \pm 0.2$	—	—
Hadronic $\tau$	—	—	—	$0.3 \pm 0.2$	—	$0.3 \pm 0.3$
Int. brems.	$0.18 \pm 0.09$	—	$0.3 \pm 0.2$	$0.14 \pm 0.13$	—	$0.3 \pm 0.3$
Backgr. ele.	$0.06 \pm 0.09$	—	$0.1 \pm 0.2$	$0.00 \pm 0.13$	—	$0.0 \pm 0.3$
Others	$0.06 \pm 0.09$	—	—	—	—	—
HQ decays	$0.41 \pm 0.15$	$3.6 \pm 0.4$	$0.6 \pm 0.3$	$0.14 \pm 0.13$	—	$0.3 \pm 0.3$

**Table 6.9:** Composition of the fake electron sample and average jet multiplicities in events with fake electrons. Negative fractions or zero fractions with non-zero uncertainty are caused by the MC@NLO event weights. The uncertainties of the efficiencies obtained from weighted event samples are conservatively estimated as described in Appendix B.2.2. Only electron candidates matching the full isolation requirements of the “likelihood tight” selection are considered, including the cut on  $\Delta R_{\text{min}}^{\text{jet}}$ . Definitions of the individual fake classes are given in the text. “Others” are candidates caused by muons or rare candidates that could not be classified. For comparison, also real electrons from heavy quark decays are included (“HQ decays”). The “Fraction (tight)” column gives the fake composition in case tight identification criteria are imposed on the electron candidates. Average jet multiplicities are only given, if at least five events contribute, to ensure a reasonable accuracy. The event selection stages for which the compositions are given correspond to those in Tab 6.6 in Section 6.4, but without the jet related requirements being applied to increase the number of contributing events.

Before any event selection criteria are applied, hadronic  $\tau$  decays and photons from internal bremsstrahlung processes cause the largest fractions of the fake electron sample. Compared with these, the fraction of real electrons from heavy quark decays is about an order of magnitude smaller. As soon as the presence of a pair of isolated lepton candidates is required, the two contributions are significantly reduced in the semi-leptonic  $t\bar{t}$  events. In the case of the events with hadronic  $\tau$  candidates no second lepton exists. In the case of the internal bremsstrahlung events, the photon is in most cases caused by the leptonically decaying  $W$  bo-

son. The probability for the photon to match the isolation criteria is smaller in the vicinity of the hadronically decaying  $W$ . The presence of the photon, on the other hand, prevents the leptons from the  $W$  boson decay from being isolated. Accordingly, no significant decrease is observed for the fully leptonic  $t\bar{t}$  events. A large fraction of these is, however, removed as soon as the two leptons are required to be of equal electric charge. Since for both classes the electron candidates are related to the second  $W$  boson, they tend to carry the charge of the  $W$  boson and hence are rejected. For the same reason, the like-sign requirement removes also a large fraction of fakes caused by charged hadrons in the sample of semi-leptonic events. These hadrons originate preferentially from the hadronization of the quarks from hadronic  $W$  boson decays. This is also supported by the observation that charged hadrons do not play a significant role in the fully leptonic sample at any stage of the analysis.

The fake composition differs significantly between fully and semi-leptonic  $t\bar{t}$  events. Moreover, a correlation between the type of fake found in an event and the average number of jets reconstructed in this event is indicated. The requirement of six jets to be reconstructed is therefore expected to change the composition of the fake lepton sample considerably, compared with the numbers given in the table. Notably, the average jet multiplicities are smallest in events with electrons from heavy quark decays, which certainly causes the importance of fake electrons to be underestimated with respect to these candidates, if only lepton related event selection criteria are considered. Further enhancement of events with fake leptons is expected from the requirement of two jets with large  $b$ -tagging weights. Nevertheless, the size of the  $t\bar{t}$  dataset does not allow for a full application of the event selection requirements. The composition of the fake candidates in  $t\bar{t}$  events passing the complete set of event selection criteria is therefore hard to predict.

Several attempts were made to either factorize the event selection or to scale results of variations of the event selection to obtain a reliable prediction of the accepted cross section. Nevertheless, correlations between jet and lepton related quantities and the above described dependence of the jet multiplicities on the fake type prevent a sensible factorization. Furthermore, a reasonable estimation would require separate treatment of semi- and fully leptonic events and of different fake types, especially of types for which the probability to occur is expected to depend on the number of jets in the event (charged hadrons, background electrons) or not (internal bremsstrahlung, hadronic  $\tau$  leptons). This is impossible with the limited number of events in the “no all-hadronic”  $t\bar{t}$  dataset.

The following approach is therefore employed to obtain an estimate for the fake background contribution: the cross section  $\sigma_{t\bar{t}}^{\text{ni}}$  of the events accepted in the pre-filtered dataset is scaled by the ratio of the probabilities  $P(\geq 6 \text{ jets, f})$  and  $P(\geq 6 \text{ jets, ni})$  that an event is accepted either due to the presence of a lepton fake (“f”) or a non-isolated lepton from a semi-leptonic heavy quark decay (“ni”) in addition to containing at least six jets. In this approach, the fake-induced part of the accepted  $t\bar{t}$  cross section  $\sigma_{t\bar{t}}^{\text{f}}$  is calculated as

$$\sigma_{t\bar{t}}^{\text{f}} = \sigma_{t\bar{t}}^{\text{ni}} \cdot \frac{P(\geq 6 \text{ jets, f})}{P(\geq 6 \text{ jets, ni})} \quad . \quad (6.1)$$

$\sigma_{t\bar{t}}^{\text{ni}}$  is obtained from the events accepted in the pre-filtered dataset, but with the contributions of events with lepton fakes or charge mismeasurement candidates being removed with the help of Monte Carlo generator information, to avoid double counting. Because not sufficient Monte Carlo events are available, the probabilities  $P(\geq 6 \text{ jets, f})$  and  $P(\geq 6 \text{ jets, ni})$  cannot be estimated directly. They are instead expressed by the probabilities  $P(\text{f})$  and  $P(\text{ni})$  to find a lepton fake or a non-isolated lepton in any event and the conditional probabilities  $P(\geq 6 \text{ jets}|\text{ni})$  and  $P(\geq 6 \text{ jets}|\text{f})$  for a minimum of six jets being present in an event with a

non-isolated real lepton or a lepton fake, respectively. Assuming the latter to be equal,  $\sigma_{t\bar{t}}^f$  can be approximated as

$$\sigma_{t\bar{t}}^f = \sigma_{t\bar{t}}^{\text{ni}} \cdot \frac{P(\geq 6 \text{ jets}|\text{f}) \cdot P(\text{f})}{P(\geq 6 \text{ jets}|\text{ni}) \cdot P(\text{ni})} \approx \sigma_{t\bar{t}}^{\text{ni}} \cdot \frac{P(\text{f})}{P(\text{ni})} . \quad (6.2)$$

This approximation is not fully justified, as the average jet multiplicities in events with fakes tend to be higher than in events with leptons from semi-leptonic heavy quark decays, as shown in Table 6.9. Hence, the approximation leads to an underestimation of  $\sigma_{t\bar{t}}^f$ . With two lepton flavours contributing, the cross section is analogously estimated as

$$\sigma_{t\bar{t}}^f \approx \sigma_{t\bar{t}}^{\text{ni}} \cdot \left( f_e \frac{P(\text{f}, e)}{P(\text{ni}, e)} + f_\mu \frac{P(\text{f}, \mu)}{P(\text{ni}, \mu)} \right) . \quad (6.3)$$

The MC@NLO event weights are ignored when determining the fractions  $f_e$  and  $f_\mu$ , because in the case of the “likelihood tight” event selection the net contribution of events where the second lepton is an electron is zero<sup>15</sup>. The probabilities  $P(\text{f})$  and  $P(\text{ni})$  are estimated as the fractions of events passing the lepton requirements due to fake leptons and real leptons from semi-leptonic heavy quark decays. Table 6.10 lists the input values for Eq. (6.3) and the corresponding predictions of the lepton fake contributions to the background calculated according to this procedure.

	“Reference”	“Likelihood loose”	“Likelihood tight”
$\sigma_{t\bar{t}}^{\text{ni}}$ [fb]	$0.363 \pm 0.340$	$0.182^{+0.223}_{-0.182}$	$0.091^{+0.203}_{-0.091}$
$f_e$	$0.43 \pm 0.13$	$0.50 \pm 0.20$	$0.40 \pm 0.22$
$f_\mu$	$0.57 \pm 0.13$	$0.50 \pm 0.20$	$0.60 \pm 0.22$
$P(\text{f}, e)/P(\text{ni}, e)$	$1.00 \pm 0.41$	$1.67 \pm 1.08$	$1.43 \pm 0.86$
$P(\text{f}, \mu)/P(\text{ni}, \mu)$	$0.03 \pm 0.05$	$0.17 \pm 0.13$	$0.10 \pm 0.11$
$\sigma_{t\bar{t}}^f$ [fb]	$0.162^{+0.171}_{-0.162}$	$0.167^{+0.233}_{-0.167}$	$0.057^{+0.135}_{-0.057}$

**Table 6.10:** Estimation of the fake lepton contribution to the  $t\bar{t}$  background for the three analyses according to the estimation procedure described in the text. The cross section  $\sigma_{t\bar{t}}^{\text{ni}}$  for the “likelihood loose” analysis differs from the value given for the pre-filtered  $t\bar{t}$  dataset in Table 6.6 in Section 6.4, because the contribution from events passing the selection requirements due to fake electrons is subtracted from  $\sigma_{t\bar{t}}^{\text{ni}}$ .

As discussed above, this approach underestimates the share of fake electrons. Nevertheless, all numbers entering Eq. (6.3) carry very large statistical uncertainties, which are assumed to cover the systematic uncertainty caused by this treatment. Once more, experience with experimental data is needed to determine lepton fake rates reliably, especially in environments with high jet multiplicity, as in  $t\bar{t}H$ ,  $H \rightarrow W^+W^-$ . More precise estimates of the  $t\bar{t}$  background caused by lepton fakes will be feasible on this basis. If this background turns out to be considerably larger than the prediction of this study, further suppression can be achieved, if tighter identification criteria are required for the electron candidates, as indicated by the numbers in Table 6.9. The shares of electrons faked by charged hadrons, hadronic  $\tau$  leptons and photon radiation are reduced drastically by the tight requirements. The total number of fake electrons decreases by about 85% of the amount in the case of “medium” cuts

<sup>15</sup>Two of the five accepted events contain electrons from heavy quark decays, one of them with a positive, the other with a negative event weight. In consequence of the disregarded weights, the correlation between the  $f_{e/\mu}$  and  $\sigma_{t\bar{t}}^{\text{ni}}$  cannot be determined and has to be neglected for the calculation of the statistical uncertainty on  $\sigma_{t\bar{t}}^f$ .

in the sample, as long as no event selection criteria applied. If a pair of isolated like-sign leptons is required, the decrease is reduced to roughly 50%. Fakes originating from charged hadrons are completely removed from the sample at this stage. Tighter electron selection cuts, however, reduce also the signal selection efficiency. Without adjusting the electron/jet ambiguity removal criteria, a loss of about 15% is observed<sup>16</sup>. Tighter lepton selection cuts will therefore decrease the discovery significance and should only be considered, if the fake background turns out to be very large.

### 6.5.2 Lepton charge mismeasurement

If one of the isolated leptons in fully leptonic  $t\bar{t}$  events is mistakenly assigned the wrong charge sign, the event will pass the event selection, provided there are sufficient additional jets. Especially in the case of electrons, this leads to a non-negligible background contribution. Figure 6.15 shows the  $p_T$  and  $\eta$  dependence of the charge mismeasurement rates in a sample of electrons from  $W$  boson decays in the “no all-hadronic”  $t\bar{t}$  dataset. The mismeasurement rate increases with rising  $p_T$ , as the tracks become stiffer and the direction of the curvature less distinct. The effect is also much stronger in the endcap region of the tracker than in the barrel, due to the limited coverage by the TRT detector only up to  $|\eta| = 2$ . This is reflected in the  $\eta$  dependence that increases rapidly up to more than 1% beyond  $|\eta| = 1.8$ . The effect is two orders of magnitude smaller for the muons, where the curvature measurement of the track segment in the muon system contributes additional information to the charge measurement. The weighted average charge mismeasurement rates obtained from samples of leptons selected by the “likelihood tight” analysis requirements e.g. are  $r_e = (1.51 \pm 0.15) \cdot 10^{-3}$  for electrons and  $r_\mu = (0.016 \pm 0.014) \cdot 10^{-3}$  for muons<sup>17</sup>.

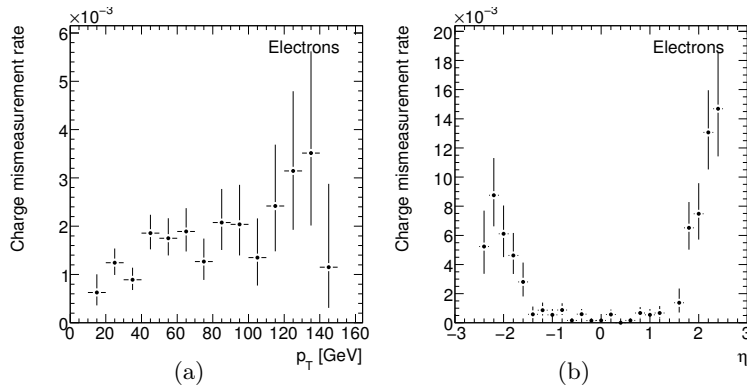


**Figure 6.15:** Charge mismeasurement rates for isolated electrons from  $W$  boson decays in  $t\bar{t}$  events as a function of  $p_T$  (a) and  $\eta$  (b). The rates are obtained as the fraction of reconstructed electrons matched to a generated electron of opposite electric charge in a sample of electrons passing all isolation criteria of the “likelihood tight” analysis, including the angular separation from the closest jet, and matched to  $W$  boson decays.

<sup>16</sup>Tighter electron ID criteria cause more jet candidates to be accepted by the requirements to resolve the electron/jet ambiguities. The loss in  $t\bar{t}$  selection efficiency due to the decreased fake rates may therefore be compensated by artificially increased jet multiplicities due to increased electron contamination, unless stricter requirements are imposed on the jet candidates.

<sup>17</sup>Possible correlations between the kinematics of the two leptons in the event would require an event-by-event weighting approach to obtain an exact estimation. To ignore these correlations can cause a slight underestimation of the actually accepted cross section. Keeping in mind the relatively small size of the  $t\bar{t}$  contribution to the total background and the large statistical uncertainty on the non-isolated and fake lepton parts, it was refrained from following this more complicated approach.

To estimate the lepton charge mismeasurement contribution to the  $t\bar{t}$  background, the event selection was applied to the “no all-hadronic”  $t\bar{t}$  sample, with the two leptons required to carry opposite electric charge. The accepted cross sections are then scaled according to the above quoted charge mismeasurement rates, taking into account the composition of the lepton final states of the selected events according to

$$\sigma_{t\bar{t}}^{\text{cm}} = \sigma_{\text{ev}} \cdot \left( \Delta_{ee} \cdot 2r_e(1 - r_e) + \Delta_{\mu\mu} \cdot 2r_\mu(1 - r_\mu) + \Delta_{e\mu} \cdot (r_e(1 - r_\mu) + r_\mu(1 - r_e)) \right) \quad , \quad (6.4)$$

with  $\sigma_{\text{ev}}$  being the per-event cross section of the “no all-hadronic”  $t\bar{t}$  dataset of 1.036 fb. The  $\Delta_{\ell_1\ell_2}$  denote the effective (weighted) numbers of accepted fully leptonic MC@NLO Monte Carlo events in the final state with the lepton combination  $\ell_1\ell_2$ <sup>18</sup>. The results for the three analyses are summarized in Table 6.11, together with the input quantities of Eq. (6.4).

	“Reference”	“Likelihood loose”	“Likelihood tight”
$r_e$	$(2.17 \pm 0.18) \cdot 10^{-3}$	$(1.51 \pm 0.15) \cdot 10^{-3}$	$(1.51 \pm 0.15) \cdot 10^{-3}$
$r_\mu$	$(0.023 \pm 0.017) \cdot 10^{-3}$	$(0.023 \pm 0.017) \cdot 10^{-3}$	$(0.016 \pm 0.014) \cdot 10^{-3}$
$\Delta_{ee}$	$33 \pm 8$	$23 \pm 6$	$23 \pm 6$
$\Delta_{\mu\mu}$	$55 \pm 10$	$26 \pm 7$	$26 \pm 7$
$\Delta_{e\mu}$	$99 \pm 13$	$56 \pm 10$	$55 \pm 10$
$\sigma_{t\bar{t}}^{\text{cm}}$ [fb]	$0.376 \pm 0.055$	$0.162 \pm 0.030$	$0.160 \pm 0.030$

**Table 6.11:** Estimation of the lepton charge mismeasurement contribution to the  $t\bar{t}$  background for the three analyses according to Eq. (6.4). See the text for an explanation of the quantities listed in the table.

The mismeasurement rates assumed for this estimation are obtained from Monte Carlo datasets that are produced with (almost) perfect alignment of the Inner Detector. In the case of non-perfect alignment, an increase of the mismeasurement rate is expected, causing the accepted cross sections given above to be underestimated. Once there are data, charge mismeasurement rates will be determined with high precision, e.g. from reconstructed  $Z \rightarrow \ell^+\ell^-$  events. The results of this study can then be corrected according to these measurements to obtain a more reliable estimation of the charge mismeasurement contribution from fully leptonic  $t\bar{t}$  background. Should the outcome be considered too large, a large fraction of this background could be suppressed by the rejection of events with electrons measured at large  $|\eta|$ . This will, however, be at the cost of some loss in the signal selection efficiency.

### 6.5.3 Discussion of the total $t\bar{t}$ background

Table 6.12 summarizes the cross sections accepted in the two relevant  $t\bar{t}$  samples and the results obtained by the methods for the estimation of the charge mismeasurement and lepton fake contributions described above. The total  $t\bar{t}$  background ranges from  $(0.900 \pm 0.501)$  fb for the “reference” analysis to  $(0.309^{+0.335}_{-0.157})$  fb for the “likelihood tight” analysis. Fake electrons are an important cause for  $t\bar{t}$  background and their contribution to the background is expected to be on the same order of magnitude as that of leptons from heavy quark decays, if the

<sup>18</sup>This approach neglects the contributions by semi-leptonic events with one lepton candidate being produced in a semi-leptonic heavy quark decay or being a fake lepton. The estimation of  $\sigma_{t\bar{t}}^{\text{nl}}$  from the pre-filtered  $t\bar{t}$  dataset, and hence also the estimation of  $\sigma_{t\bar{t}}^{\text{f}}$  in Section 6.5.1, accounts for the loss of events where the leptons actually carry equal charge, but one being assigned the wrong charge in the reconstruction process. The gain due to the reverse process is not covered and needs to be determined separately. This is, however, neglected, since the number of these kind of events passing the opposite sign event selection is well below the statistical uncertainty of the analysis.

latter are rejected with rates as those achieved by the lepton isolation tools used in this study. The importance of the lepton charge mismeasurement background increases with an improved lepton isolation that suppresses the other two  $t\bar{t}$  background components. Whereas it is of the same order of magnitude as the latter two in the case of the “reference” and “likelihood loose” event selections, the charge mismeasurement contribution is dominant in the case of the “likelihood tight” selection. Instead of just focusing on methods to reject leptons from semi-leptonic heavy quark decays, future analyses therefore must also develop strategies to deal with fake electron and charge mismeasurement background, if further suppression of  $t\bar{t}$  events is desired.

	“Reference”	“Likelihood loose”	“Likelihood tight”
$\sigma_{t\bar{t}}^{\text{acc}}$ (“no all-hadronic”) [fb]	$3.107 \pm 1.794$	$1.036 \pm 1.036$	$1.036 \pm 1.036$
$N_{\text{MC}}^{\text{acc}}$ (“no all-hadronic”)	3	1	1
$\sigma_{t\bar{t}}^{\text{acc}}$ (filtered) [fb]	$0.545 \pm 0.364$	$0.273 \pm 0.240$	$0.091^{+0.203}_{-0.091}$
$N_{\text{MC}}^{\text{acc}}$ (filtered)	16	7	5
$\sigma_{t\bar{t}}^{\text{ni}}$ [fb]	$0.363 \pm 0.340$	$0.182^{+0.233}_{-0.182}$	$0.091^{+0.203}_{-0.091}$
$\sigma_{t\bar{t}}^{\text{f}}$ [fb]	$0.162^{+0.171}_{-0.162}$	$0.167^{+0.234}_{-0.167}$	$0.057^{+0.135}_{-0.057}$
$\sigma_{t\bar{t}}^{\text{cm}}$ [fb]	$0.376 \pm 0.055$	$0.162 \pm 0.030$	$0.160 \pm 0.030$
$\sigma_{t\bar{t}}^{\text{tot}}$ [fb]	$0.900 \pm 0.501$	$0.511^{+0.443}_{-0.368}$	$0.309^{+0.335}_{-0.157}$

**Table 6.12:** Summary of the estimation of the three  $t\bar{t}$  background contributions for the three analyses. The  $\sigma_{t\bar{t}}^{\text{acc}}$  give the accepted cross sections in the “no all-hadronic” and pre-filtered  $t\bar{t}$  samples,  $N_{\text{MC}}^{\text{acc}}$  the unweighted number of MC@NLO Monte Carlo events these cross sections are obtained from. The cross sections  $\sigma_{t\bar{t}}^{\text{ni}}$ ,  $\sigma_{t\bar{t}}^{\text{cm}}$  and  $\sigma_{t\bar{t}}^{\text{tot}}$  give the estimates for the accepted cross section in the three classes of  $t\bar{t}$  background, as obtained by the methods described above.  $\sigma_{t\bar{t}}^{\text{tot}}$  is the sum of all three.

It must be stressed that the estimates for the  $t\bar{t}$  background contributions due to leptons from semi-leptonic heavy quark decays and fake leptons are obtained from only few events passing all event selection criteria and therefore are affected with sizeable statistical uncertainties. Large systematic uncertainties contribute also, in the case of the estimation of the fake lepton contribution. With the available number of Monte Carlo events, no more than giving a 95% confidence limit is justified, which is also difficult because of the event weights (see Appendix B.2.3 for details).

Despite these uncertainties, this study of the  $t\bar{t}$  background shows that there are means to suppress it to a level well below the irreducible background components and demonstrates the importance of  $t\bar{t}$  background contributions other than that caused by semi-leptonic heavy quark decays. Because of the too low number of Monte Carlo events, it is difficult to make a definite prediction of the expected  $t\bar{t}$  background. To guarantee a reasonable inclusion of the  $t\bar{t}$  background in the total background estimation, the total accepted cross sections given in Table 6.12 are nevertheless used as a  $t\bar{t}$  background estimate in the following. Future analyses will then have to focus on developing strategies for a more reliable determination of the  $t\bar{t}$  background from data.

## 6.6 Estimation of the $W$ +jet background

Due to its large cross section,  $W$ +jet production constitutes another potential background.  $W$ +jet events selected by this analysis must contain at least seven high- $p_T$  jets in order to fulfil the requirement of six jets and to provide a second lepton candidate, usually generated by a misidentified additional jet. Hence, the relevant events populate an extreme region of the phase space. This region is expected to be poorly described even by dedicated event generators for final states with many jets. Currently, generators like ALPGEN can handle a maximum of five extra partons in the matrix element calculation. An attempt to estimate the  $W$ +jet background contribution from Monte Carlo will therefore suffer from large uncertainties. Moreover, as very large suppression rates are needed, the restriction to available datasets leads to sizeable statistical uncertainties. Nevertheless, an attempt is made to obtain a rough estimate for an upper limit on the  $W$ +jet background, based on the currently available Monte Carlo datasets, which is described in the following (more details are given in Appendix B.4). The result of the estimation allows the importance of this background to be determined and the necessity of data-driven background estimation approaches to be judged.

### 6.6.1 Validation of the description of the event properties in the release 12 and 14 datasets

The requirement of a large  $W$ +jet Monte Carlo dataset forces the use of samples produced with the fast ATLAS detector simulation ATLFAST-II. These are only available produced with a more recent release of the ATLAS reconstruction software Athena and are generated for a lower centre-of-mass proton–proton collision energy of 10 TeV. Figure 6.16 shows comparisons of the lepton  $p_T$  spectra and multiplicity distributions in the fully simulated release 12 and 14 datasets and the release 14 ATLFAST-II sample with the maximum number of additional partons. No significant differences in the shapes of the transverse momentum distributions are visible in these samples, which are the most relevant ones for this analysis. Deviations in the lepton  $p_T$  spectra show up in the datasets with fewer matrix element partons, which are, however, of lower importance (see Appendix B.4.1). The increased fraction of events with at least one electron in release 14 is therefore not caused by changes in the transverse momentum distributions due to the different centre-of-mass energies, but by the increase of the “medium” electron identification efficiency by roughly 5% for signal electrons. Also the muon reconstruction efficiency has slightly increased in between the releases (see e.g. Refs. [133, 134]). A consistent description of the background lepton shapes is of special importance for a reliable estimation of the background suppression rates from the 10 TeV datasets. This is ensured within the statistical uncertainties, as can be seen in the  $p_T$ -spectra of electrons in the  $W \rightarrow \mu\nu + 5p$  and muons in the  $W \rightarrow e\nu + 5p$  samples. Only background leptons contribute to these distributions. All distributions show good agreement between the fully simulated and ATLFAST-II release 14 datasets.

Comparisons of the jet multiplicities and jet  $p_T$ -spectra, including all jets passing the jet  $p_T$  and  $\eta$  requirements, are shown in Fig. 6.17. The multiplicity in the release 12 dataset is significantly higher than in release 14 in the  $W \rightarrow \mu\nu + 5p$  and  $W \rightarrow e\nu + 5p$  samples, which can be explained by the generator level filter for at least three generator level jets with transverse momenta larger than 30 GeV. No significant difference appears in the case of the  $Wb\bar{b} + 3p$  samples, for which the same filter criteria were applied in both releases. This shows that the decrease in centre-of-mass energy has no influence on the jet multiplicity distributions. Differences can, however, be observed in the transverse momentum distributions, with the jet  $p_T$  being slightly larger also for the  $Wb\bar{b} + 3p$  sample in the case of the 14 TeV centre-

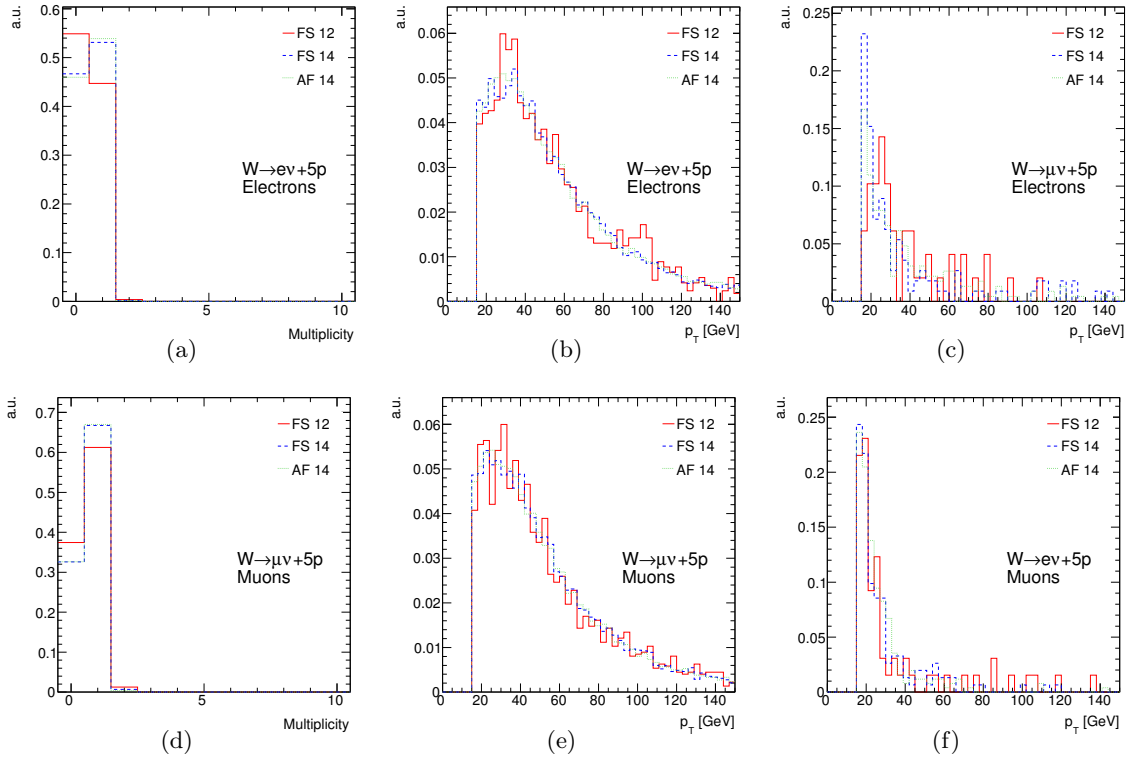


**Figure 6.16:** Comparison of the multiplicity (a) and transverse momentum distribution (b) of electrons in the  $W \rightarrow e\nu + 5p$  samples and  $p_T$  distribution of electron candidates in the  $W \rightarrow \mu\nu + 5p$  samples (c, background electrons). Multiplicity (d) and transverse momentum distribution (e) of muon candidates in the  $W \rightarrow \mu\nu + 5p$  samples and  $p_T$  distribution of muons in the  $W \rightarrow e\nu + 5p$  samples (f, background muons). The samples produced with the full detector simulation are denoted “FS12” and “FS14” for Athena release 12 and 14, respectively. The release 14 ATLFASST-II samples are denoted “AF14”. Only the lepton identification and  $p_T$  and  $\eta$  cuts as described in Section 6.4.1 are applied to the lepton candidates, without any event selection criteria imposed on the contributing events. All distributions are normalized to unity.

of-mass energy. This behaviour might at least partly be attributed to the lower jet seeding energy required by the more recent reconstruction software. This results in an increased jet reconstruction efficiency, especially in the low  $p_T$  region. Nevertheless, the difference in centre-of-mass system energy may as well be a cause. Again, the differences are stronger in datasets with fewer additional matrix element partons (see Appendix B.4.1). Significant deviations in all samples appear in the shapes of the spectra of the first six jets ordered in  $p_T$  (see Fig. B.7 in Appendix B.4.1), but do not affect the jet selection efficiency significantly. Also the description of the jet distributions in ATLFASST-II is in good agreement with the one in fully simulated datasets.

### 6.6.2 Factorization of the event selection

Since no likelihood information for the muon isolation is provided in Athena release 14, the estimation of the  $W$ +jet background has to be done with respect to the “reference” event selection. The cut values for this analysis must be adapted to changes in the shapes of the isolation and  $b$ -tagging variables, which are caused by some major changes in the reconstruction of physics objects (see Appendix B.4.2).

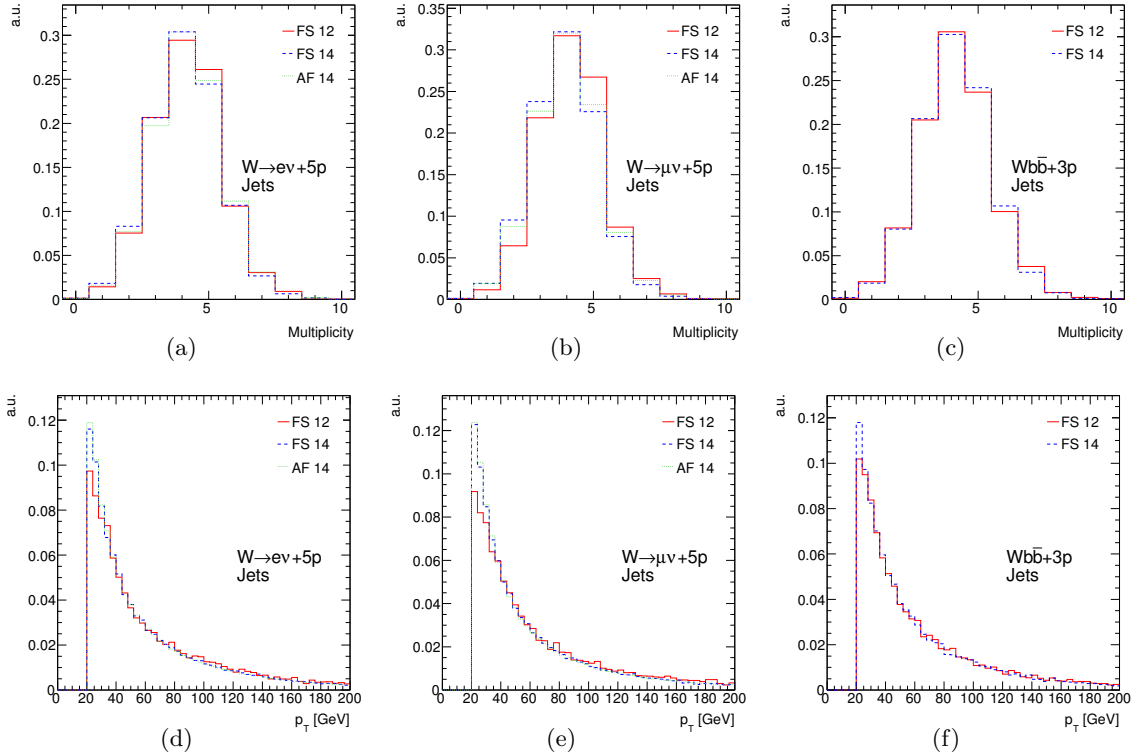


**Figure 6.17:** Comparison of jet multiplicities and transverse momentum distributions in release 12 and 14 full simulation (denoted “FS12” and “FS14”) and release 14 ATLFAS-II (“AF14”) in the  $W \rightarrow e\nu + 5p$  (a, d),  $W \rightarrow \mu\nu + 5p$  (b, e) and  $Wb\bar{b} + 3p$  (c, f) datasets. Only jets passing the jet  $p_T$  and  $\eta$  requirements described in Section 6.4.1 are taken into account and no event selection criteria are required. All distributions are normalized to unity.

Due to very low selection efficiencies, no events pass the complete set of event selection cuts even in the release 14 ATLFAS-II datasets, which contain more than five million events in total. Since in the used samples one Monte Carlo event corresponds to an accepted cross section of up to 0.37 fb (see Table 6.4 in Section 6.3), also the 95% confidence limits that can be derived on the accepted cross sections are large. The event selection has therefore to be factorized to obtain reasonable results. The jet-related event selection criteria are separated from the lepton requirements, still using a consistent object definition for electrons and jets. Nevertheless, an anti-correlation remains between both parts of the event selection. This can be seen in Fig. 6.18, where the average number of jets as a function of the number of isolated leptons per event in the datasets with four additional partons is shown<sup>19</sup>. Events fulfilling the requirement of containing two isolated leptons on average have fewer jets than events with no or one lepton. Splitting the analysis into a lepton and a jet part therefore yields a conservative upper limit to the  $W$ +jet contribution<sup>20</sup>.

<sup>19</sup>The number of Monte Carlo events in the more important five parton samples is too small to observe a reliable anti-correlation.

<sup>20</sup>This behaviour can be tested with the release 12 signal and irreducible background datasets, which contain a sufficiently large number of events to apply the complete event selection and compare the result with the estimation of the factorized approach. The result of the split analysis overrates the accepted cross section in all the cases. The overestimation is the stronger, the less signal-like the considered process is and hence the smaller the total event selection efficiency is. For the signal the factorization approach yields  $(0.70 \pm 0.02)$  fb, compared with  $(0.65 \pm 0.02)$  fb for the full analysis, which corresponds to a small excess of about 8%. The largest deviation is observed in the case of the  $t\bar{t}W + 0p$  sample, where an increase by

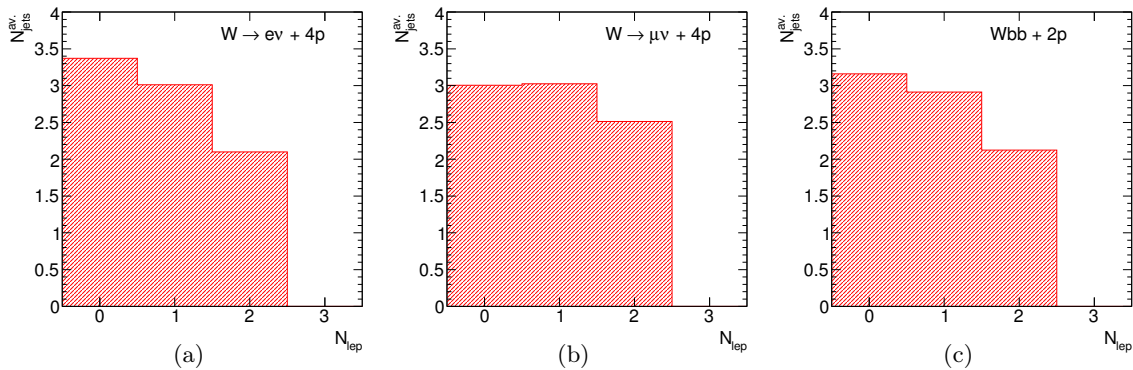


**Figure 6.18:** Average number of jets per event as a function of the number of isolated leptons in the  $W \rightarrow e\nu + 4p$  (a),  $W \rightarrow \mu\nu + 4p$  (b) and  $Wbb + 2p$  (c) datasets. Leptons have to fulfil the isolation and angular separation requirements.

Neglecting the anti-correlation between jet- and lepton based event selection criteria, the cross sections  $\sigma_{lep}$  accepted by the lepton cuts can be scaled by efficiencies  $\epsilon_{jets}$  of the jet-related event selection requirements. In addition, the cross sections need to be scaled from 10 TeV to 14 TeV by factors  $f_{10 \rightarrow 14}$ . This approach ignores possible differences in the distributions of kinematic event variables. This is, however, justified since the most important shapes either do not show significant differences due to the different centre-of-mass energies or the differences do not influence the object selection efficiency. A conservative estimation of the total accepted cross section  $\sigma_{tot}$  per dataset is therefore given by

$$\sigma_{tot} = \sigma_{lep} \cdot \epsilon_{jets} \cdot f_{10 \rightarrow 14} \quad . \quad (6.5)$$

The  $W \rightarrow \tau\nu$  contribution is accounted for by increasing the  $\sigma_{tot}$  by the  $\tau \rightarrow \ell\nu\nu$  ( $\ell = e, \mu$ ) branching ratio of 35.21%<sup>21</sup>. Details on the calculation of the factors  $f_{10 \rightarrow 14}$  are given in Appendix B.4.3.

The results of the  $W$ +jet background calculation are shown in Table 6.13. Summed up, the  $\sigma_{tot}$  for the twelve considered datasets yield an expectation of the total accepted  $W$ +jet cross section of  $(0.07 \pm 0.05)$  fb.

### 6.6.3 Limit on the accepted $W$ +jet cross section

The estimation of the total accepted cross section for the  $W$ +jet background suffers from a very large statistical uncertainty. As indicated by the uncertainties on the individual  $\sigma_{tot}$  in Table 6.13, only few events pass the lepton selection criteria for the datasets that provide the largest contribution to the overall result (one event in the  $W \rightarrow e\nu + 5p$  and  $Wbb + 3p$  and two events in the  $W \rightarrow \mu\nu + 5p$  samples)<sup>22</sup>. Therefore, a 95% upper confidence limit on

---

a factor of 6.5 from  $(0.025 \pm 0.007)$  fb to  $(0.164 \pm 0.007)$  fb is caused by the factorization. These numbers, however, cannot directly be used to correct the result in the  $W$ +jet case, because it is difficult to obtain a reasonable projection for the overestimation factor for the reducible  $W$ +jet process from the behaviour of the irreducible processes.

<sup>21</sup>Because of the non-zero  $\tau$  lepton mass and the on average lower transverse momenta of the daughter lepton with respect to the  $\tau$  because of the two neutrinos, this is a conservative estimate of the  $\tau$  contribution.

<sup>22</sup>The feasibility of further factorization (e.g. loosening the lepton isolation cuts) was tested, but finally was abstained from because all approaches require a minimum number of Monte Carlo events that is not available. Further difficulties arise from the complex classification of the composition of the surviving events and the uncontrollable correlations between leptons and jets.

Dataset	$\sigma_{\text{lep}}$ [fb]	$\epsilon_{\text{jet}}$ [ $10^{-3}$ ]	$f_{10 \rightarrow 14}$	$\sigma_{\text{tot}}$ [fb]
$W \rightarrow e\nu + 2\text{p}$	$22.72 \pm 2.86$	$0.02 \pm 0.00$	1.205	$0.0006 \pm 0.0001$
$W \rightarrow e\nu + 3\text{p}$	$8.34 \pm 1.70$	$0.09 \pm 0.01$	1.169	$0.0011 \pm 0.0003$
$W \rightarrow e\nu + 4\text{p}$	$1.48 \pm 0.74$	$0.72 \pm 0.07$	1.217	$0.0015 \pm 0.0008$
$W \rightarrow e\nu + 5\text{p}$	$0.37 \pm 0.37$	$7.03 \pm 0.40$	1.393	$0.0043 \pm 0.0043$
$W \rightarrow \mu\nu + 2\text{p}$	$25.48 \pm 3.05$	$0.01 \pm 0.00$	1.205	$0.0004 \pm 0.0001$
$W \rightarrow \mu\nu + 3\text{p}$	$11.47 \pm 2.03$	$0.04 \pm 0.01$	1.169	$0.0006 \pm 0.0002$
$W \rightarrow \mu\nu + 4\text{p}$	$3.63 \pm 1.15$	$0.35 \pm 0.05$	1.119	$0.0017 \pm 0.0006$
$W \rightarrow \mu\nu + 5\text{p}$	$0.73 \pm 0.52$	$4.67 \pm 0.32$	1.393	$0.0056 \pm 0.0040$
$W\bar{b}b + 0\text{p}$	$1.32 \pm 0.66$	$0.19 \pm 0.11$	1.224	$0.0003 \pm 0.0002$
$W\bar{b}b + 1\text{p}$	$0.65 \pm 0.46$	$0.65 \pm 0.20$	1.375	$0.0006 \pm 0.0004$
$W\bar{b}b + 2\text{p}$	$0.65 \pm 0.46$	$5.58 \pm 0.79$	1.346	$0.0049 \pm 0.0035$
$W\bar{b}b + 3\text{p}$	$0.32 \pm 0.32$	$80.20 \pm 3.84$	1.724	$0.0445 \pm 0.0446$
Sum				$0.0661 \pm 0.0451$
95% CL				0.236

**Table 6.13:** Summary of the estimation of the  $W$ +jet background using the factorized event selection as described in the text.  $\sigma_{\text{lep}}$  gives the cross sections accepted by the lepton-related event selection cuts in the individual datasets,  $\epsilon_{\text{jet}}$  the corresponding event selection efficiency for the jet related requirements and  $f_{10 \rightarrow 14}$  the factor for scaling the result from 10 TeV to 14 TeV. The total cross section per sample is given as  $\sigma_{\text{tot}} = \sigma_{\text{lep}} \cdot \epsilon_{\text{jet}} \cdot f_{10 \rightarrow 14}$ , with a correction for the leptonic  $\tau$  decay branching ratio.

the accepted cross section is calculated, assuming a Poisson distribution with the number of accepted Monte Carlo events as the expectation value, rather than providing an expectation value for the cross section itself. The combination of the limits obtained from several datasets is performed, using a toy Monte Carlo experiment, as described in Appendix B.4.4. Only the six most important datasets are considered, because the expectation values obtained from the remaining ones are negligibly small. Such, a combined limit of 0.236 fb is obtained.

It must be stressed that this limit suffers from large uncertainties. The most important one is the limited description of high jet multiplicity events by the Monte Carlo generator. Additional uncertainties are introduced by the factorization of the event selection requirements. Smaller contributions result from differences in the physics objects selection between different Athena releases and the choice of the cut values for  $b$ -tagging and lepton isolation. Also the use of datasets that were generated for a centre-of-mass energy of 10 TeV is a non-negligible source of uncertainties. Wherever possible, it is ensured not to underestimate the accepted cross sections to obtain a conservative limit. The use of ATLFast-II datasets, however, compensates part of the conservative estimation of the  $W$ +jet background. The shower parameterization of ATLFast-II is based on average lepton and hadron candidates. Therefore, in particular the lepton fake candidates that pass the stringent lepton isolation criteria required in Section 6.4 and hence are very untypical cannot be described in as much detail as with the full detector simulation.

The estimated limit of 0.236 fb on the accepted  $W$ +jet cross section must be considered very conservative. Nevertheless, it is much smaller than the total accepted  $t\bar{t}$  cross section, which is 0.900 fb in the case of the “reference” analysis. The  $W$ +jet background is finally expected to decrease drastically, probably in a way comparable to the reduction in the  $t\bar{t}$  contribution, if the likelihood is applied for the selection of leptons. The impact of the  $W$ +jet background is discussed together with the results for all other backgrounds in the next section.

## 6.7 Summary of the accepted signal and background cross sections

This section summarizes all results and provides the basis for pile-up and systematics studies as well as for the prediction of the discovery significances and corresponding accuracies for a measurement of  $\sigma \times \text{BR}$ . Table 6.14 lists the accepted signal and background cross sections for the three analyses and the study published in Ref. [108]. In the most favourable case of a Higgs boson mass of 160 GeV, the signal cross section accepted by all three analyses is  $(0.65 \pm 0.02)$  fb, quickly decreasing to 0.14 and 0.34 fb for  $M_H = 120$  GeV and 200 GeV, respectively. Assuming an integrated luminosity of  $30 \text{ fb}^{-1}$ , the expected number of signal events reaches a maximum of 20 for  $M_H = 160$  GeV and drops to four for  $M_H = 120$  GeV and ten for  $M_H = 200$  GeV, as illustrated in Fig. 6.19.

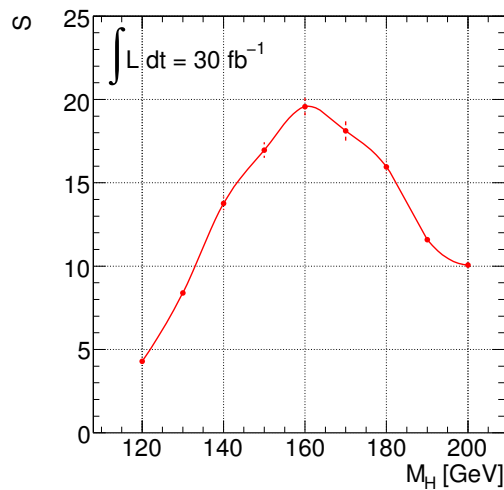


**Figure 6.19:** Number of expected signal events  $S$  for an integrated luminosity of  $30 \text{ fb}^{-1}$  as a function of the Higgs boson mass (“likelihood tight” analysis). The signal cross sections are scaled to the leading order values as used for Table 6.14. The error bars indicate the statistical uncertainty of the Monte Carlo estimation.

The accepted cross sections for the signal and the irreducible backgrounds are about the same for all three analyses of this study, as expected due to the choice of the lepton isolation cut values (see Section 6.4). In contrast, the  $t\bar{t}$  background components caused by semi-leptonic heavy quark decays and fake leptons decrease significantly due to the use of the dedicated isolation likelihoods. The total  $t\bar{t}$  contribution to the background varies between 43% and 20% for the three analyses of this study, making the dominant background contributions being the irreducible ones. Accordingly, the signal-to-background ratios for  $M_H = 160$  GeV vary between 0.31 for the “reference” and 0.42 for the “likelihood tight” analysis. Compared with the published study, where more than 70% of the total background consisted of  $t\bar{t}$ , the background could be reduced by more than a factor of 20 at the cost of about two third of the accepted signal.

Figures 6.20(a) and 6.20(b) show the statistical significances, assuming Poisson distributed signal and background expectations, of the observed signal as a function of  $M_H$  for the three signal selections and an assumed integrated luminosity of  $30 \text{ fb}^{-1}$ , together with the corresponding signal-to-background ratios<sup>23</sup>. A maximum significance of 2.7 is reached in

<sup>23</sup>Appendix B.6 contains a list of the signal and background expectations and the signal-to-background ratios

	$\sigma^{\text{acc}}$ [fb]			
	Published	“Reference”	“Likelihood loose”	“Likelihood tight”
Signal (120 GeV)	$0.45 \pm 0.01$	$0.139 \pm 0.005$	$0.140 \pm 0.005$	$0.143 \pm 0.005$
Signal (130 GeV)	—	$0.269 \pm 0.008$	$0.272 \pm 0.008$	$0.280 \pm 0.008$
Signal (140 GeV)	—	$0.452 \pm 0.014$	$0.455 \pm 0.014$	$0.459 \pm 0.014$
Signal (150 GeV)	—	$0.545 \pm 0.015$	$0.557 \pm 0.016$	$0.565 \pm 0.016$
Signal (160 GeV)	$1.85 \pm 0.03$	$0.653 \pm 0.018$	$0.655 \pm 0.018$	$0.652 \pm 0.018$
Signal (170 GeV)	—	$0.595 \pm 0.019$	$0.604 \pm 0.019$	$0.604 \pm 0.019$
Signal (180 GeV)	—	$0.517 \pm 0.012$	$0.529 \pm 0.013$	$0.532 \pm 0.013$
Signal (190 GeV)	—	$0.384 \pm 0.010$	$0.389 \pm 0.010$	$0.386 \pm 0.010$
Signal (200 GeV)	$0.95 \pm 0.01$	$0.329 \pm 0.009$	$0.334 \pm 0.009$	$0.336 \pm 0.009$
$t\bar{t}$ non-isolated	$7.4 \pm 1.1$	$0.363 \pm 0.340$	$0.182^{+0.233}_{-0.182}$	$0.091^{+0.203}_{-0.091}$
$t\bar{t}$ fakes	—	$0.162^{+0.171}_{-0.162}$	$0.167^{+0.234}_{-0.167}$	$0.057^{+0.135}_{-0.057}$
$t\bar{t}$ charge mismeas.	—	$0.376 \pm 0.055$	$0.162 \pm 0.030$	$0.160 \pm 0.030$
$t\bar{t}W$	$1.70 \pm 0.05$	$0.691 \pm 0.039$	$0.710 \pm 0.039$	$0.712 \pm 0.039$
$t\bar{t}Z$	$1.14 \pm 0.07$	$0.475 \pm 0.048$	$0.475 \pm 0.048$	$0.480 \pm 0.048$
$t\bar{t}t\bar{t}$	$0.06 \pm 0.00$	$0.045 \pm 0.002$	$0.045 \pm 0.002$	$0.046 \pm 0.002$
<b>Total BG</b>	$10.3 \pm 1.1$	$2.111 \pm 0.505$	$1.741^{+0.448}_{-0.373}$	$1.546^{+0.341}_{-0.169}$
$t\bar{t}W$ (AcerMC)	—	$0.460 \pm 0.051$	$0.465 \pm 0.051$	$0.443 \pm 0.050$
$W$ +jet (95% CL)	—	0.236	—	—

**Table 6.14:** Accepted signal and background cross sections [fb] for the three analyses. The numbers in the “Published” column are quoted from Ref. [108]. It should be noted that different cross section normalization factors were applied for some of the datasets in the publication, notably for the signal, which was normalized to the NLO values. The accepted cross section in the filtered  $t\bar{t}$  sample was scaled by a factor 1.15 to account for the losses due the use of the filter.

the most favoured case of  $M_H = 160$  GeV by the “likelihood tight” analysis. To demonstrate the variations allowed by the current statistical uncertainty on the background expectation, Figs. 6.20(c) and 6.20(d) display the curves for the “likelihood tight” analysis, together with the respective curves obtained taking the  $\pm 1\sigma$  background variations due to the statistical uncertainty on the Monte Carlo estimation into account.

The same curves are shown in Fig. 6.21, but with the NLO cross section values used to normalize the signal, as was done in the publication. If only the statistical significances are considered, the use of the “likelihood tight” selection requirements causes only a small increase in the significance. Nevertheless, the signal-to-background ratios are increased almost by a factor of three with respect to the published analysis (see Fig. 6.21(b)), which causes the “likelihood tight” event selection to be very robust against uncertainties of the background estimation, as discussed in Section 6.9.5. The “likelihood tight” analysis is therefore used as a reference in the following, unless stated otherwise.

In addition to the estimation of the  $t\bar{t}W$  contribution that is obtained from the ALPGEN samples, Table 6.14 gives the accepted cross sections in the AcerMC sample. As expected, these are roughly 35% smaller than the ALPGEN values. The comparison of the results obtained from both samples gives a hint on the order of magnitude of the systematic uncertainties due to the choice of the Monte Carlo generator (see Section 6.9.3).

The  $W$ +jet background contribution has only been estimated for the “reference” analysis. The conservative upper limit that is determined for this case is about 20% of the  $t\bar{t}$  background and only 10% of the total background. Furthermore, the limit corresponds to less than half of

---

and expected significances displayed in the figures, including the NLO signal cross section expectations.

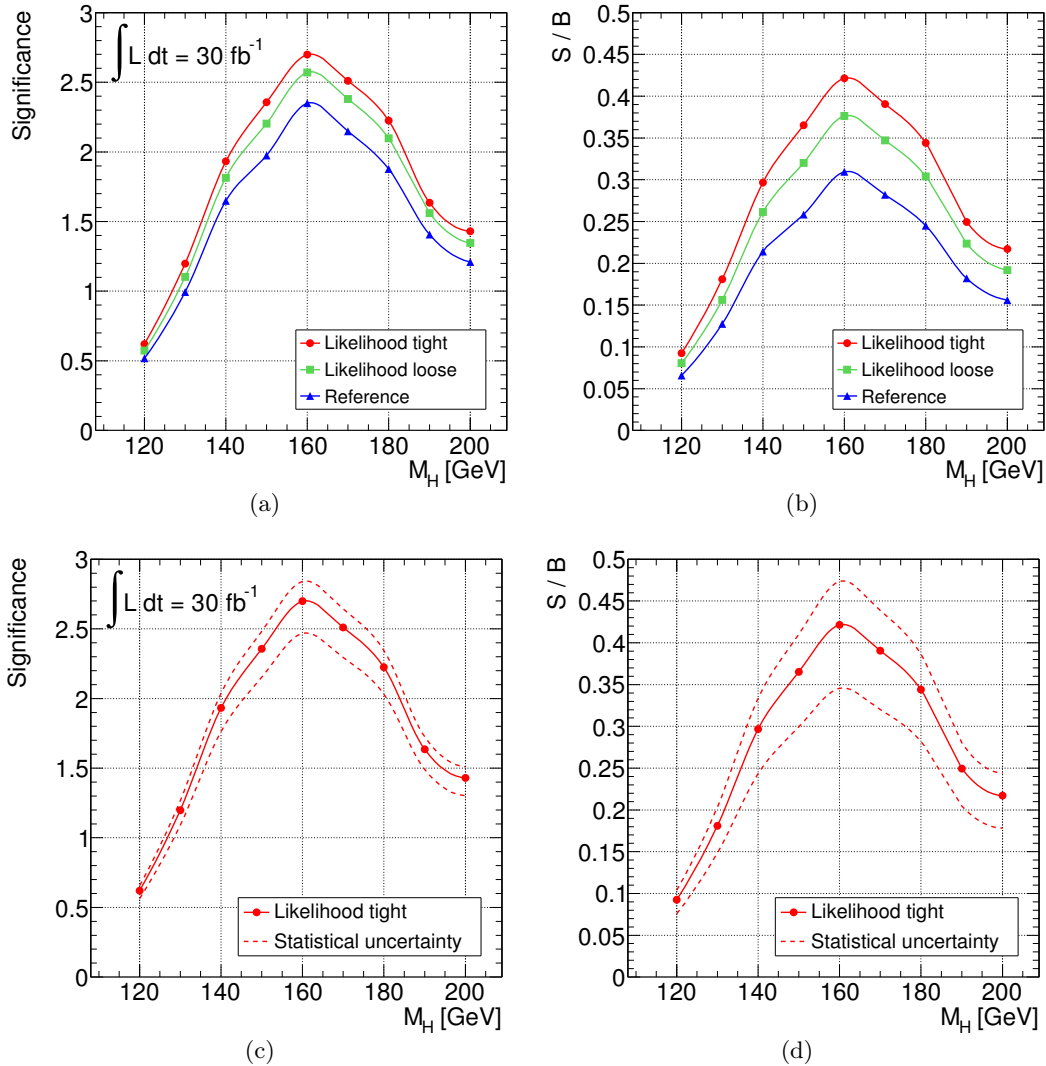


**Figure 6.20:** Expected statistical significance (a) and signal-to-background ratio (b) as a function of the Higgs boson mass for the three analyses described in Section 6.4. The curves are repeated for the “likelihood tight” analysis in (c) and (d), together with the band corresponding to the  $\pm 1\sigma$  background variations due to the statistical uncertainty on the Monte Carlo estimation. LO signal cross sections are assumed in all figures.

the  $\pm 1\sigma$  band of the statistical uncertainty of the background and hence would not change the significance and signal-to-background ratio significantly, if included in the total background. The impact of this upper limit on the expected significance and signal-to-background ratio is shown in Fig. 6.22. Even in this conservative scenario, the  $W$ +jet background does not reduce the significance for an observation of  $t\bar{t}H$ ,  $H \rightarrow W^+W^-$  drastically. An even smaller contribution to the total background can be expected for the analyses using the dedicated likelihoods for lepton isolation, where the reducible backgrounds contribute even less to the total background expectation. It can therefore be concluded, that the irreducible background components will dominate the total background, if the lepton isolation performs on the experimental data as expected. Very likely, the actual expectation for the accepted  $W$ +jet cross section lies far below the  $t\bar{t}$  estimation.  $W$ +jet is therefore not included in the calculation of the total background expectation. Since this prediction is based upon Monte Carlo samples

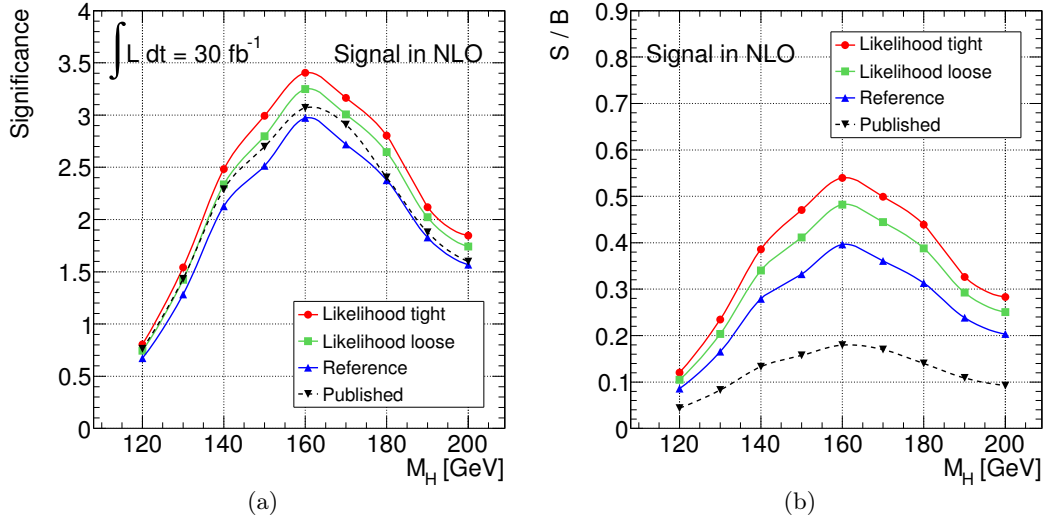


**Figure 6.21:** Statistical significance (a) and signal-to-background ratio (b) as a function of the Higgs boson mass for the three analyses described in Section 6.4 and the analysis published in Ref. [108]. The signal cross sections are scaled to the next-to-leading order values used in the publication.

with a too small number of events, as for  $t\bar{t}$ , further studies should anyhow aim to confirm these conclusions on the  $W$ +jet background on data.

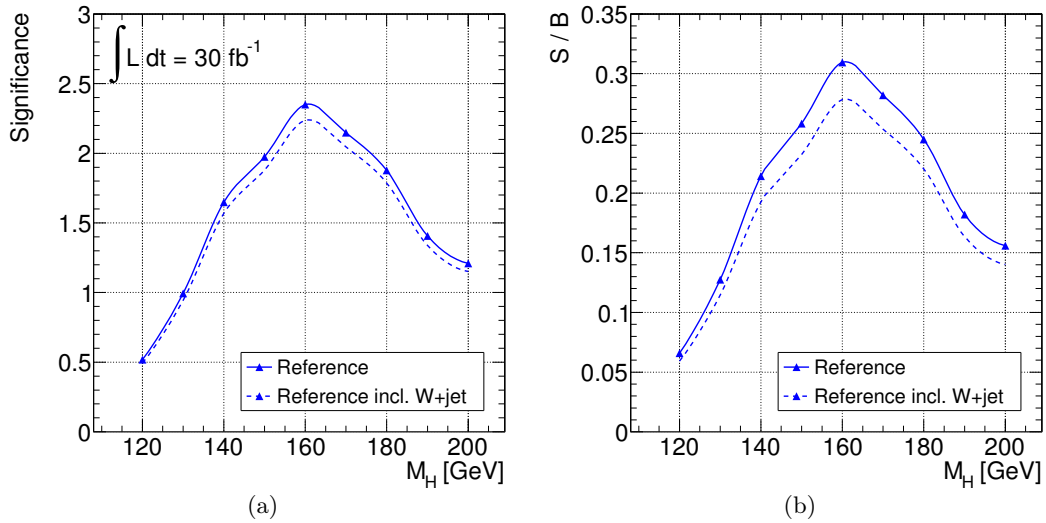


**Figure 6.22:** Statistical significance (a) and signal-to-background ratio (b) as a function of  $M_H$ , including the 95% confidence upper limit on the expectation of the  $W$ +jet background for the “reference” analysis.

## 6.8 Impact of pile-up on the signal and background selection

In the high-intensity conditions at hadron colliders, pile-up of multiple collisions per beam crossing will occur. Furthermore, a cloud of slow neutrons from earlier collisions constitutes the so-called “cavern background” in the muon spectrometer. These effects are expected to affect the analyses even of the “low-luminosity” data that are going to be collected in the first years of data taking. Both cause extra activity in the detector and therefore influence the event selection. Not all of the relevant background datasets were produced with overlaid pile-up and cavern background. The full analysis therefore had to be performed without taking these contributions into account. Nevertheless, for the signal at a Higgs boson mass of 160 GeV as well as for  $t\bar{t}$  “no all-hadronic” and  $t\bar{t}W$ , pile-up samples exist with, however, a smaller number of events than generated without pile-up. They are produced from subsets of the generated events used for the production of the corresponding samples without pile-up (see Table 6.4 in Section 6.3 of this chapter for details). The average number of minimum-bias collisions in these samples is 2.3 per event, corresponding to a luminosity of  $10^{33} \text{ cm}^{-2}\text{s}^{-1}$ , as assumed for the first three years of data taking.

The study of these samples can only provide an idea of what has to be expected for an analysis of experimental data under pile-up conditions. Pile-up Monte Carlo samples exist only for some of the relevant background processes. Furthermore, the effect on the jet energy scale will be corrected by suited recalibration methods and the lepton identification and isolation strategies will be adapted to more active environments. The main goal of this study is therefore to demonstrate the robustness of the event selection strategy under the influence of pile-up, rather than to give definite projections for accepted signal and background cross sections. Pile-up influences every step in the event selection. In order to understand and quantify the pile-up effects, Table 6.15 summarizes the changes in the lepton, jet selection and event selection. In the case of the  $t\bar{t}$  datasets, which are too small to give a reasonable value for the total accepted cross section, the accepted cross sections are compared separately for the jet and lepton related parts of the event selection.

The lepton reconstruction and identification efficiencies remain largely unaffected by the impact of pile-up for both lepton flavours. The effectiveness of the lepton isolation variables, however, is expected to degrade. The calorimeter based isolation variables suffer more than track based variables, because the latter can be protected against pile-up contamination by cuts on the track parameters, as discussed in Section 5.2 of Chapter 5. Figure 6.23 compares the distributions of the isolation variables in the signal samples with and without additional minimum-bias events. Almost no difference is visible in the distribution of  $p_{\text{T}}^{\text{max trk}}(0.2)$ . In contrast, the  $E_{\text{T}}^{\text{cone}}(0.2)$  distribution, and therefore also the distribution of the likelihood output value, show the expected tendency towards less isolated leptons. With the cut value used for the “likelihood tight” event selection, however, no significant loss in the electron isolation efficiency results. A significant loss is caused on the isolated muon selection efficiency. The effect is the larger, the less isolated the candidates already are due to the jet multiplicity in the event itself: the decrease in the selection efficiency for pairs of isolated leptons is much higher in  $t\bar{t}$  than in the signal and the irreducible backgrounds.

The extra activity caused by pile-up leads to an increase mainly in the multiplicity of low- $p_{\text{T}}$  jets. Furthermore, the jet energy scale is systematically overestimated in the studied samples<sup>24</sup>, and the measurement of the jet directions and resolutions are affected. Figure 6.24(a)

<sup>24</sup>The change in the jet energy scale can be corrected by a recalibration taking into account the pile-up contribution to the energy measurements in the calorimeter. This is, however, not applied to the jets in the available pile-up Monte Carlo datasets.

	No pile-up	Pile-up	Difference	
	Electron selection efficiency			
Reconstruction	$0.907 \pm 0.002$	$0.906 \pm 0.003$	—	
ID	$0.718 \pm 0.004$	$0.713 \pm 0.004$	-1%	
“Likelihood tight”	$0.626 \pm 0.004$	$0.618 \pm 0.004$	-1%	
	Muon selection efficiency			
Reconstruction	$0.936 \pm 0.002$	$0.933 \pm 0.002$	—	
“Likelihood tight”	$0.718 \pm 0.004$	$0.696 \pm 0.004$	-3%	
	Average jet multiplicity			
Signal	$5.681 \pm 0.011$	$5.739 \pm 0.014$	+1%	
$t\bar{t}W$	$4.572 \pm 0.008$	$4.659 \pm 0.011$	+2%	
$t\bar{t}$	$3.994 \pm 0.002$	$4.071 \pm 0.005$	+2%	
	Fraction of events with $\geq 6$ jets			
Signal	$0.533 \pm 0.004$	$0.531 \pm 0.004$	—	
$t\bar{t}W$	$0.309 \pm 0.002$	$0.326 \pm 0.002$	+6%	
$t\bar{t}$	$0.134 \pm 0.001$	$0.163 \pm 0.001$	+22%	
	Accepted cross sections [fb]			
Signal	$0.652 \pm 0.018$	$0.594 \pm 0.018$	-9%	
$t\bar{t}W$	$0.712 \pm 0.039$	$0.651 \pm 0.048$	-9%	
$t\bar{t}$ (lepton cuts)	$53 \pm 8$	$82 \pm 28$	+55%	compatible with 0
$t\bar{t}$ (jet cuts)	$(60.7 \pm 0.3) \cdot 10^3$	$(73.5 \pm 0.8) \cdot 10^3$	+20%	
$t\bar{t}$ charge mis.	$0.160 \pm 0.030$	$0.154 \pm 0.052$	-8%	compatible with 0

**Table 6.15:** Overview on the changes caused by the presence of pile-up in the low-luminosity scenario, assuming an average of 2.3 minimum-bias collisions per event. The “electron/muon selection efficiency” gives the efficiencies for the selection of leptons from  $W$  boson decays in the signal datasets after the reconstruction and application of the ID and isolation criteria without any event selection criteria applied. The “Average jet multiplicities” and “Fraction of events with  $\geq 6$  jets” are compared in the signal,  $t\bar{t}W$  and “no all-hadronic”  $t\bar{t}$  sample ( $t\bar{t}$ ), also without application of event selection cuts. Finally, the accepted cross sections for the event selection on the signal,  $t\bar{t}W$  and “no all-hadronic”  $t\bar{t}$  datasets are given. The  $t\bar{t}$  dataset is too small to give a reasonable value for the total accepted cross section. The accepted cross sections are therefore given separately for the jet and lepton related parts of the event selection (“lepton cuts” and “jet cuts”). The  $t\bar{t}$  contribution due to charge mismeasurement is obtained from the  $t\bar{t}$  sample overlayed with pile-up events using the “opposite-sign” analysis method as introduced in Section 6.5.2. The samples with and without pile-up are not statistically independent due to the use of the same generated events.

shows a comparison of the jet  $p_T$  distributions of jets in the signal samples with and without pile-up and the ratio of both is shown in Fig. 6.24(b). The latter is significantly larger than one for transverse jet momenta smaller than 30 GeV and levels off at one for higher  $p_T$ . Figure 6.25 shows comparisons of the resulting jet multiplicity distributions for the signal and the two background processes. The average multiplicity of jets with  $p_T > 20$  GeV increases only slightly, as can be seen from the numbers given in Table 6.15. More important for the event selection efficiency is the fraction of events with six or more jets. No change in this fraction is observed in the case of the signal. In contrast, the fraction increases by 7% for  $t\bar{t}W$  and 22% for  $t\bar{t}$ , because the average jet multiplicities are lower than six for both backgrounds and the six jets requirement cuts into the steeply falling tails of the multiplicity spectra.

The increase of the jet multiplicity is further enhanced by the loss in the lepton isolation efficiency, which are correlated through the procedure to resolve the electron/jet ambiguities. In the  $t\bar{t}$  sample, the changes in the attribution of electrons and jets actually cause the largest part of the total increase of the event selection efficiency. The presence of additional jets also

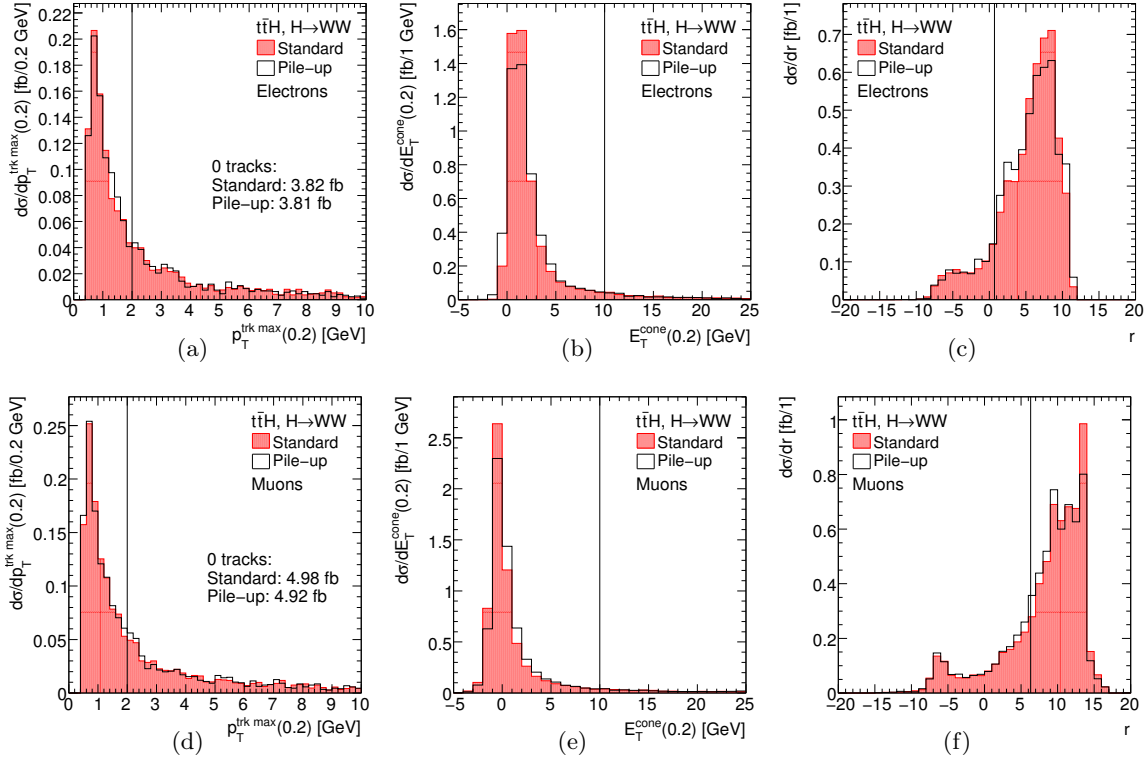


**Figure 6.23:** Distributions of  $p_T^{\text{max trk}}(0.2)$  (a, d),  $E_T^{\text{cone}}(0.2)$  (b, e) and the likelihood output value  $r$  (c, f) for electrons (upper row) and muons (lower row). The distributions are compared in the  $t\bar{t}H, H \rightarrow W^+W^-$  signal for  $M_H = 160$  GeV with and without pile-up overlayed. The lines correspond to the cuts applied in the “reference” and “likelihood tight” event selections.

influences the separation of jets and leptons. The distributions of the distance between leptons and the closest jet in the signal are shown in Figs. 6.26(a) and 6.26(b). Both distributions show a small tendency towards closer jets, which reflects in a significant decrease of the efficiency of the angular distance requirement by several per cent.

No difference is visible in the distributions of the  $b$ -tag weights in samples with and without pile-up, shown in Fig. 6.27. This is in accordance with the expectation of the  $b$ -tagging efficiencies being almost unaffected by the impact of low-multiplicity pile-up. Since the selected events contain at least six jets and hence a very distinct primary vertex, the probability for a misidentification of the vertex due to pile-up tracks is very low. Nevertheless, if applied in the event selection, the  $b$ -tag requirement leads to a small efficiency loss of a few per cent.

All reported effects result in a net change of the event selection efficiency. Its actual size and direction depends strongly on the event topology of the individual processes. A rough estimate of the impact of pile-up on the accepted number of background events can be made as follows: The signal and the irreducible  $t\bar{t}W$  background suffer a loss of 9% each, so it can be assumed that the other irreducible backgrounds  $t\bar{t}Z$  and  $t\bar{t}t\bar{t}$  will also be reduced by about 10%. The  $t\bar{t}$  charge mismeasurement background must be considered an irreducible background, too, due to the two real isolated leptons. Applying the strategy outlined in Section 6.5.2 for the estimation of the charge flip contribution to the  $t\bar{t}$  background yields a loss of 8%, which is also in agreement with the numbers above.<sup>25</sup> It is more difficult to make

<sup>25</sup> Assuming statistical independence, this also compatible with zero within the statistical errors, though.

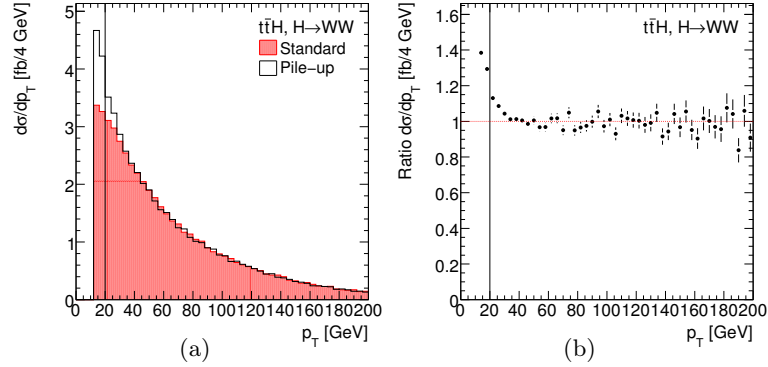


**Figure 6.24:** (a)  $p_T$  distribution of jets in the signal sample with and without pile-up. Jets are selected according to the requirements of the “likelihood tight” event selection, as described in Section 6.4.1, except for the cut on  $p_T$ . (b) Ratio of the histograms on the left. The error bars in (b) are slightly overestimated, since the samples are treated as statistically independent.

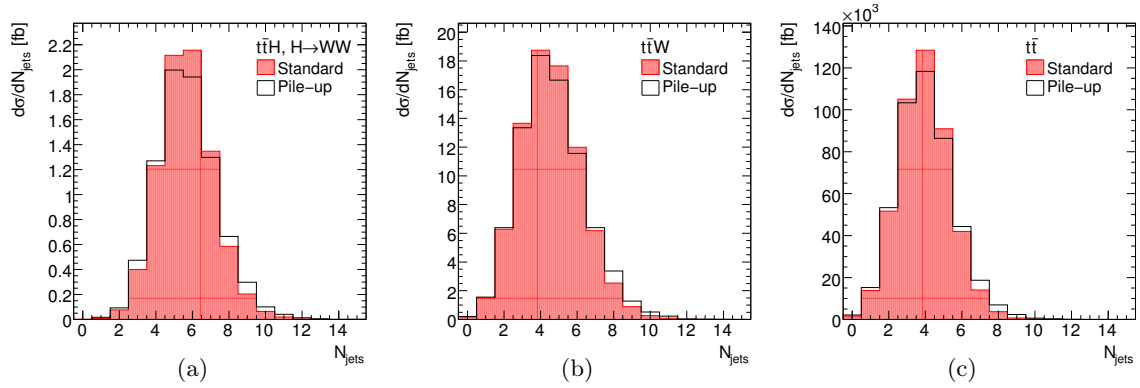
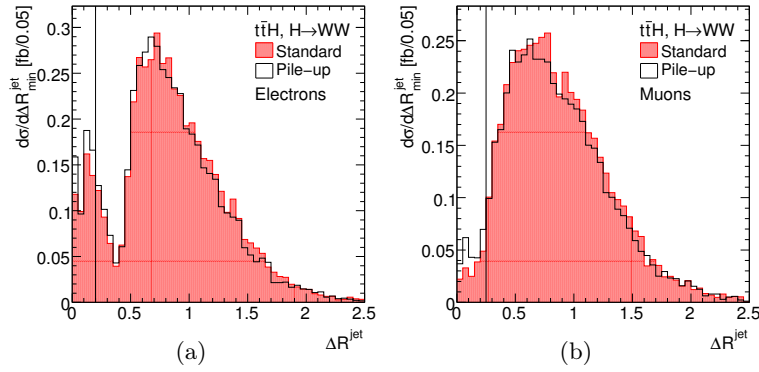


**Figure 6.25:** Jet multiplicities in the  $t\bar{t}H$ ,  $H \rightarrow W^+W^-$  signal for  $M_H = 160$  GeV (a),  $t\bar{t}W$  (b) and  $t\bar{t}$  (c) with and without pile-up. Only jets passing all jet selection criteria of the “likelihood tight” event selection in Section 6.4.1, including the requirement of a minimum  $p_T$  of 20 GeV, are included.

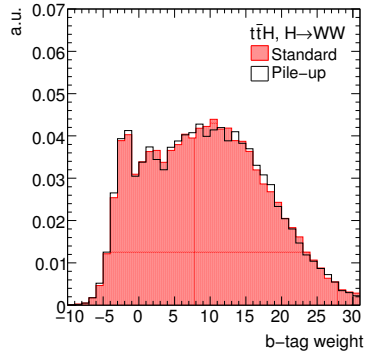
a projection for the reducible components of the  $t\bar{t}$  background. Nevertheless, these make up only small contributions to the total background. Taking into account that lepton- and jet related effects are anti-correlated, the assumption is justified, that the 20% increase observed for the jet selection can be considered a reasonable upper limit on the expected pile-up effect for the purpose of this estimation.

Table 6.16 lists the estimated signal and background expectations under these assumptions. Since the contribution of the reducible  $t\bar{t}$  components to the total background is small, the signal-to-background ratio remains almost unchanged. The statistical significance of the observed signal is moderately decreased by 6%. The uncertainty on the projection of the reducible backgrounds has hardly any impact on the overall result<sup>26</sup>. A slightly smaller loss in the signal selection efficiency can be expected for the “reference” and “likelihood loose” event selections, which depend less on the lepton isolation. On the other hand, for these analyses the impact of the enhancement in the reducible backgrounds is expected to be accordingly larger. Nevertheless, the requirement of a minimum jet  $p_T$  of 20 GeV makes all three analyses relatively robust against the influence of pile-up and only small effects are expected.

<sup>26</sup>Even a 100% increase would decrease the significance only by 10% instead of 6%.



**Figure 6.26:** Distance to the closest jet  $\Delta R_{\min}^{\text{jet}}$  for electrons (a) and muons (b) from  $W$  boson decays in the signal without and in the presence of pile-up.



**Figure 6.27:** Distribution of the  $b$ -tag weights for real  $b$ -jets with and without pile-up.

Sample	No pile-up [fb]	Pile-up [fb]	Comment
Signal	$0.652 \pm 0.018$	$0.594 \pm 0.018$	Pile-up dataset available
$t\bar{t}W$	$0.712 \pm 0.039$	$0.651 \pm 0.048$	Pile-up dataset available
$t\bar{t}Z$	$0.480 \pm 0.048$	$0.432 \pm 0.043$	Assumption $-10\%$
$t\bar{t}\bar{t}$	$0.046 \pm 0.002$	$0.041 \pm 0.002$	Assumption $-10\%$
$t\bar{t}$ (charge mismeasurement)	$0.160 \pm 0.030$	$0.154 \pm 0.052$	Pile-up dataset available
$t\bar{t}$ ( $b \rightarrow \ell\nu$ )	$0.091^{+0.203}_{-0.091}$	$0.109^{+0.244}_{-0.109}$	Assumption $+20\%$
$t\bar{t}$ (fakes)	$0.057^{+0.135}_{-0.057}$	$0.068^{+0.164}_{-0.068}$	Assumption $+20\%$
Total background	$1.546^{+0.341}_{-0.169}$	$1.456^{+0.409}_{-0.203}$	
$S/B$	0.42	0.41	
Significance	2.70	2.53	

**Table 6.16:** Prediction of the accepted signal and background cross sections, signal-to-background ratios and statistical significance under the influence of pile-up and comparison to the values obtained for the standard scenario.

## 6.9 Estimation of systematic uncertainties on the accepted signal and background cross sections

The significance that can be achieved to claim an observation of the Higgs boson in the  $t\bar{t}H, H \rightarrow W^+W^-$  channel and the accuracy of a subsequent measurement of  $\sigma_{t\bar{t}H} \times \text{BR}(H \rightarrow W^+W^-)$  depend strongly on the precision of the background estimation and the prediction of expected signal rates. Various sources of systematic uncertainties limit the predictions of signal and background expectations. Among them are the uncertainty of the detector performance and the measurement of the luminosity, as well as uncertainties of the theoretical description of the relevant physics processes.

A reconstruction of the Higgs boson is difficult in the studied channel and will at most yield a broad mass peak, such that sidebands will be of little use. Determining the background from data is therefore challenging and no strategy has been established to date. An estimation of the uncertainty on the Monte Carlo based predictions on the number of expected signal and background events is therefore presented in the following. Furthermore, the dependence of the significance of the observed signal on the background uncertainty is studied. These give a hint on the precision future data driven background estimation strategies must provide to allow for a study of the process with reasonable accuracy.

### 6.9.1 Detector performance uncertainties

The first considered source of uncertainty is the limited knowledge of the detector performance. It includes the lepton identification and isolation efficiencies, the lepton and jet energy and  $p_T$  reconstruction and the  $b$ -tagging efficiencies and background rejections. The expected precisions to which these quantities can be determined from data have been estimated by the ATLAS collaboration in the course of the publication of Ref. [28] for consistent use throughout different analyses [49]<sup>27</sup>. According to the suggestions for the  $10 \text{ fb}^{-1}$  scenario in Ref. [49], the impact of the uncertainties of the lepton and jet momenta and energies is studied by variations of their respective quantities. Efficiency uncertainties are modelled by random removal or, in the case of the  $b$ -tagging uncertainties also addition, of extra objects from or to the selected lepton and jet samples<sup>28</sup>. An overview of all applied modifications is given in Table 6.17. The resulting uncertainties of the accepted cross sections are obtained from a comparison of the outcome of the event selection using the modified objects with the standard selection efficiencies. The variations are applied one after the other, neglecting possible small correlations between individual changes.

This approach is not suited to determine the uncertainties on the non-isolated lepton and fake  $t\bar{t}$  background contributions<sup>29</sup>. Their statistical uncertainties are extremely large and single Monte Carlo events correspond to cross sections much higher than the expected uncertainties on the total cross section that are to be determined. Hence, the variations are applied either only to the lepton- or to the jet related part of the event selection to estimate

<sup>27</sup>These numbers have been confirmed to be conservative, but reasonable estimations by recent analyses of the data (see e.g. Refs. [135, 136]).

<sup>28</sup>To estimate the impact of the uncertainties on lepton selection efficiencies, actually both, a decrease and an increase, need to be considered. The latter, however, is difficult to implement, because the basic object selection is performed in the very beginning, whereas the systematic variations are applied later in the analysis. While random removal of objects can easily be applied in this later step, random addition of jets or leptons cannot. Therefore, only the impact of a loss is determined here and it is assumed that the relative changes in positive and negative direction are equal. This is justified, because the uncertainties of the selection efficiencies of real leptons and jets are small, whereas the total efficiencies are high.

<sup>29</sup>The definitions of the three components of the  $t\bar{t}$  background are given in Section 6.5.

the uncertainties on  $\sigma_{t\bar{t}}^{\text{ni}}$  and  $\sigma_{t\bar{t}}^{\text{f}}$ . The total accepted cross sections determined in Section 6.5 are then scaled according to the observed variation in the relevant part of the event selection. This approach implies that the correlations between the lepton- and jet related selection criteria do not vary with the varied event selection requirements. These can safely be assumed as long as the variations are small and do not particularly affect background leptons, which are strongly connected to the jet sample.

The results are listed in Table 6.17. The lepton properties can be determined with high precision and hence they cause only negligible uncertainties far below 1%, both on the accepted signal and background cross sections. The uncertainties on the jet energy scale, the  $b$ -tagging efficiency and the light jet rejection rates all result in uncertainties of about 5% on the accepted signal cross section and somewhat higher uncertainties of about 7% on the background cross sections. Added in quadrature, this results in an estimated detector performance uncertainty of roughly 9% on the signal and 11% on the background.

	Variation	Signal	Total background
Electron reconstruction and ID efficiency	-0.2%	-0.3%	—
Electron $p_{\text{T}}$ resolution	+5%	-0.1%	-0.1%
Electron $p_{\text{T}}$ scale	+0.1%	+0.1%	—
Electron $p_{\text{T}}$ scale	-0.1%	-0.1%	—
Muon reconstruction efficiency	-0.1%	-0.1%	—
Muon $p_{\text{T}}$ resolution	+1%	+0.1%	+0.3%
Muon $p_{\text{T}}$ scale	+0.1%	+0.1%	—
Muon $p_{\text{T}}$ scale	-0.1%	—	—
Jet energy resolution	+10%	+0.3%	-0.5%
Jet energy scale	+5%	+5.9%	+7.3%
Jet energy scale	-5%	-5.5%	-6.9%
$b$ -tagging efficiency	+5%	+5.3%	+6.4%
$b$ -tagging efficiency	-5%	-6.1%	-7.3%
Light jet mistag rate	+20%	+4.8%	+2.9%
Light jet mistag rate	-20%	-4.2%	-6.0%
Total detector performance uncertainty		$\pm 9\%$	$\pm 11\%$

**Table 6.17:** Overview of the systematic uncertainties on the signal and background predictions due to the uncertainties on the prediction of the detector performance. All contributions are determined according to the descriptions in Ref. [49], with the exception of the light jet mistag rate. The uncertainty of 10% quoted there is considered too optimistic and hence replaced by a more reasonable value of 20%, which could by now also be backed by measurements [136]. Relative uncertainties are given for the efficiencies and mistag rates. A dash indicates that no change in the number of selected events could be observed. The total uncertainties are obtained by adding the individual contributions in quadrature. The average of the two values is used if increase and decrease are treated separately (details on the individual background components are given in Appendix B.7).

### Lepton isolation

Probably the most important source of experimental uncertainties in the case of the  $t\bar{t}H$ ,  $H \rightarrow W^+W^-$  channel is the uncertainty of the lepton isolation. The uncertainty on the signal selection efficiency can easily be determined from data, e.g. in the study of  $Z \rightarrow e^+e^-$  or  $Z \rightarrow \mu^+\mu^-$  events. In contrast, selecting sufficiently clean background samples of leptons associated to heavy quark decays to determine the uncertainty of the background rejection is a challenge. Hence, no reasonable way to determine the lepton selection uncertainties for the cuts on the

lepton isolation variables could be established so far. This certainly is one of the important problems to be solved by future analyses. Nevertheless, it is clear that in the case of very tight isolation requirements, as applied in this analysis, especially variations in the background rejection are expected to contribute a sizeable share to the overall experimental uncertainty.

To get at least an idea of the impact of the isolation uncertainties, the change in the accepted signal and background cross sections as a function of a variation of the isolation efficiencies of real isolated signal leptons for the “likelihood tight” electron and muon selection are shown in Fig. 6.28. Again, the reducible  $t\bar{t}$  background components are treated by factorization of the event selection criteria. The accepted signal and background cross sections are strongly correlated, leaving the signal-to-background ratio unaffected. A decrease of the efficiency by 5%, which probably is a conservative guess of the obtainable precision, causes a loss of roughly 4% in  $\sigma^{\text{acc}}$  for both lepton flavours.

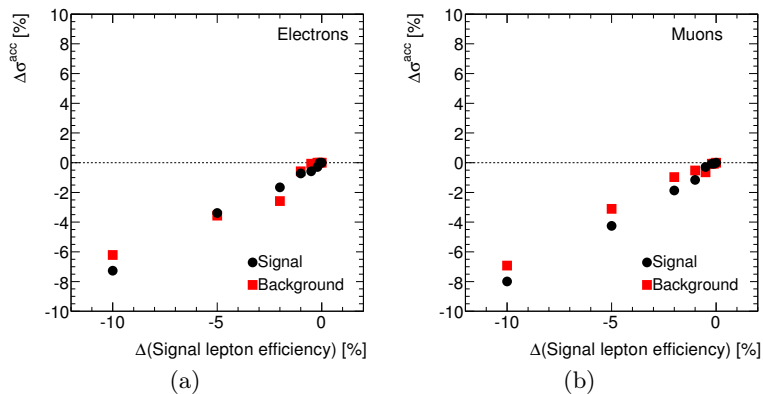


**Figure 6.28:** Influence of a variation of the isolated lepton signal selection efficiencies on the accepted signal and background cross sections. The curves are obtained by systematically removing a given fraction of signal electrons (a) and muons (b) passing the isolation criteria for the “likelihood tight” event selection. No error bars are shown for the sake of clarity.

Random removal or addition of further non-isolated background leptons can easily be applied to the signal and the irreducible backgrounds. Even changes of up to several hundred per cent have almost no effect on the accepted cross sections in these samples. In contrast, sizeable impact is expected on the accepted  $t\bar{t}$  cross section. Nevertheless, the factorization approach is no longer feasible for the evaluation of the uncertainties due to the background lepton rejections. The uncertainties on the non-isolated background lepton rejections are expected to be high, 50% or more probably being a reasonable estimate. Such variations change the composition of the accepted leptons in a reducible background sample significantly and via the electron/jet ambiguity also the accepted jets. The assumption of a constant correlation between the lepton- and jet related event selection requirements is therefore no longer justified and the impact of variations in the background lepton rejection cannot be determined.

Although the event selection has been optimized such that  $t\bar{t}$  is no longer the dominant background contribution, large experimental uncertainties on this background component can still have an impact on the total accepted background. A change in  $(\sigma_{t\bar{t}}^{\text{mi}} + \sigma_{t\bar{t}}^{\text{f}})$  of  $\pm 50(100)\%$  results in a change of the total accepted background cross section of roughly  $\pm 5(10)\%$  for the “likelihood tight” event selection. The dependence is expected to be even stronger in the case of the “likelihood loose” and “reference” analyses, where  $t\bar{t}$  contributes a larger fraction of the total background. With 50% uncertainty being a reasonable, the background lepton

rejection uncertainty is expected to be of the same order of magnitude as the other three relevant sources of experimental uncertainties identified above.

### 6.9.2 Luminosity

The measurement of the luminosity that will be delivered by the LHC is expected to add an uncertainty of  $\pm 3\%$  on the prediction of the accepted signal and background event yields [108].

### 6.9.3 Theory uncertainties

As worked out in Section 2.2.3, Monte Carlo driven predictions suffer also from theory uncertainties of the inclusive and differential signal and background cross sections.

#### Factorization and renormalization scale

The choice of the factorization and renormalization scales used in the perturbative cross section calculations causes an uncertainty on the result, which can roughly be estimated by scaling the chosen scale up and down by a factor of two. The scale uncertainties on the NLO calculation on the  $t\bar{t}H$  production cross section have been estimated in Ref. [47] to vary between  $(_{-9.3}^{+5.9})\%$  and  $(_{-10.0}^{+6.8})\%$  for Higgs boson masses between 120 GeV and 200 GeV. For the  $t\bar{t}Z$  background a scale uncertainty of  $\pm 11\%$  in NLO is reported in Ref. [46]. The scale uncertainties on the  $t\bar{t}$  production cross section are reduced to  $\pm 6\%$  by the NLL corrections included in the calculation in Ref. [123]. No NLO calculations and corresponding uncertainties exist for the other two relevant backgrounds  $t\bar{t}W$  and  $t\bar{t}t\bar{t}$ . In the following, it is assumed that NLO calculations will exist for all relevant backgrounds once  $t\bar{t}H$  production is studied on data, although not being available to date. Furthermore, the order of magnitude of the scale uncertainties obtained in NLO for the signal and the  $t\bar{t}Z$  background is used as an estimate also for the remaining background, which mainly consists of  $t\bar{t}W$  production. Therefore, a total scale uncertainty of  $\pm 10\%$  is assumed for the background cross section in the following.

#### Parton distribution functions

Further uncertainties on inclusive cross section calculations are caused by the limited knowledge of the underlying PDFs used for cross section calculations. For the NLO calculation of the signal cross section, a PDF uncertainty between  $\pm 8.8\%$  and  $\pm 9.4\%$  has been calculated for Higgs boson masses between 120 GeV and 200 GeV in Ref. [47]. A total uncertainty of  $\pm 15\%$ , including the  $\pm 11\%$  scale uncertainty and the PDF uncertainty, is given for the NLO  $t\bar{t}Z$  cross section calculation in Ref. [46]. The PDF uncertainty of this calculation must therefore be  $\pm 10\%$ . The PDF contribution to the  $\pm 12\%$  total uncertainty on the NLO+NLL calculation of the  $t\bar{t}$  cross section is also  $\pm 10\%$  [127, 123]. Again, a similar uncertainty of roughly  $\pm 10\%$  is assumed for the other background processes.

#### Description of exclusive final states

Theory uncertainties do not only affect the normalization of the inclusive cross sections, but also influence the selection efficiencies obtained from Monte Carlo samples. These uncertainties are especially important for analyses of complex final states, which select extreme phase space regions of the background processes, such as  $t\bar{t}H$ . In particular the region with the required large number of jets is only poorly described by current Monte Carlo programs. This results in large uncertainties on all background processes, with the effect being the larger, the more of the jets are not covered by the matrix element calculation but need to be modelled

by the parton shower. The problem could be overcome by the development of Monte Carlo generators that are capable to include a sufficiently large number of additional partons in their matrix element calculations for all relevant background processes. In contrast to the inclusive cross section calculations, where NLO results for all relevant background cross section can be expected to be ready once the  $t\bar{t}H$ ,  $H \rightarrow W^+W^-$  channel is to be studied, it is unlikely that such generators will be available in time. Therefore, the uncertainty must be taken into account as a serious contribution to the uncertainty of Monte Carlo based predictions also in the future.

One way to get a rough estimate of the uncertainty is the comparison of different generators. As mentioned in Section 6.3.3,  $t\bar{t}W$  production is the only relevant background process for which at least two different samples of reasonable size are available. One is generated with ALPGEN, the other with AcerMC. Both were produced generating the same  $W$  boson decays and applying the same generator level filters. Hence, the selection efficiencies observed in the two samples can directly be compared with obtain a hint on the uncertainties on the event selection efficiencies that can be caused by the choice of the generator<sup>30</sup>. The efficiency found in the AcerMC dataset is 0.40%, whereas the total selection efficiency obtained from the combination of the three  $t\bar{t}W$  ALPGEN samples is 0.89%, mainly due to the differences in the tails of the jet multiplicity distribution in both samples (see Fig. 6.4(b) in Section 6.3.3). This corresponds to a difference of more than 50% with respect to the ALPGEN value used for this study.

This result probably overestimates the actual uncertainty. In the case of the  $t\bar{t}W$  background the choice of the generator used for the analysis has been discussed in detail in Section 6.3.3 and ALPGEN is considered to be better suited for this analysis. Furthermore, a large fraction of the background is made up of  $t\bar{t}Z$  production, which, as discussed in Section 6.3.3, is expected not to be as sensitive to the choice of the generator as  $t\bar{t}W$ . On the other hand  $t\bar{t}$ , which is certainly a candidate to suffer seriously from the limited description of multi-jet final states, constitutes only a small fraction of the total background selected by the “likelihood tight” analysis. Furthermore, also a future improvement of the Monte Carlo description by comparison with data from multijet final states in  $t\bar{t}W$  and  $t\bar{t}Z$  production events seems feasible. In the following discussion, an uncertainty of  $\pm 30\%$  is assumed<sup>31</sup>.

#### 6.9.4 Summary of systematic uncertainties

All uncertainties discussed above are summarized in Table 6.18. As pointed out before, most of the numbers in the table are only rough estimates. Some of the contributions, e.g. the detector and luminosity uncertainties or the PDF uncertainty are (at least partly) correlated among the signal and the backgrounds. Part of the uncertainties therefore do not affect the signal-to-background ratios but can have some impact on the significance expectations. Adding the individual contributions in quadrature yields a total uncertainty of about  $\pm 16\%$  for the signal and  $\pm 36\%$  for the background. Although these numbers are partly obtained from rough estimations, they still show that although the experimental uncertainty is high, certainly the largest part of the current total uncertainty of the background is caused by the exclusive use of Monte Carlo samples to predict the background. This uncertainty is not only large, but also hard to estimate more precisely than done here. This reveals once more

<sup>30</sup>In contrast, the accepted cross sections for the two datasets in Table 6.14 cannot be compared directly. Both are normalized to the inclusive cross sections of their respective generators and hence to different values.

<sup>31</sup>A very small effect is expected also on the signal, where additional partons can also enhance the signal selection efficiency. The impact is, however, considered negligible.

the urgent need for strategies to use data to determine the background expectation and its uncertainty with better accuracy in future analyses.

	Signal	Total background
Detector performance uncertainty	$\pm 9\%$	$\pm 11\%$
Likelihood efficiency	$\pm 4\%$	$\pm 4\%$
Likelihood rejection	—	$\pm 5\%$
Luminosity $\pm 3\%$	$\pm 3\%$	$\pm 3\%$
Factorization and renormalization scale	$(\begin{smallmatrix} +6 \\ -10 \end{smallmatrix})\%$	$\pm 10\%$
PDFs	$\pm 9\%$	$\pm 10\%$
Exclusive final state	—	$\pm 30\%$
Total uncertainty	$(\begin{smallmatrix} +15 \\ -17 \end{smallmatrix})\%$	$\pm 36\%$

**Table 6.18:** Summary of the systematic uncertainties affecting the prediction of the accepted signal and background cross sections in this analysis. It must be noted that the  $\pm 30\%$  uncertainty on the description of the final state is only a rough estimation (details are given in the text).

### 6.9.5 Impact of systematic uncertainties on the signal significance

In the following, the impact of systematic uncertainties on the background estimation on the significance of a measurement is examined. For this purpose, the expected significance is scanned as a function of the relative background uncertainty  $\Delta B/B$ . The choice of the distribution underlying the background measurement is crucial for the calculation of significances in presence of systematic uncertainties. Many studies assume a Poisson distribution, which is correct, if the background is estimated with one subsidiary measurement, e.g. in a sideband. This is presumably not feasible in the case of  $t\bar{t}H$ ,  $H \rightarrow W^+W^-$ . A Gaussian distribution is therefore insinuated here. The expected significance is estimated from the predicted number of accepted signal and background events using a profile likelihood ratio with a Gaussian background expectation uncertainty. A test of the compatibility with the background-only hypothesis is made (no assumptions are made on the signal + background hypothesis). The significance expectations are evaluated with an Asimov dataset (see Appendix B.5 for details).

Figure 6.29 shows the dependence of the significance on the background uncertainty for the three analyses. For comparison with the results from the study published in Ref. [108], the curves are also shown for the signal normalized to the NLO  $t\bar{t}H$  production cross section. The slope of the curves is the smaller, the tighter the event selection is and therefore the larger the signal-to-background ratio. Hence, the results of the tighter event selection criteria are more robust against background estimation uncertainties. The best expected significance over a wide range is provided by the “likelihood tight” event selection. The 36% uncertainty estimated for the Monte Carlo based background prediction in this thesis result in a significance of about  $1\sigma$  for the “likelihood tight” analysis<sup>32</sup>. It is expected, that this uncertainty can be reduced with a data driven background estimation.

Finally, since  $t\bar{t}H$ ,  $H \rightarrow W^+W^-$  is certainly not a candidate channel for a discovery of the Higgs boson, not only the significance of an observation of a signal is of interest. As outlined in Section 1.5, studies of the channel will aim at a measurement of the product of the production cross section times the branching ratio of the Higgs boson decay into two

<sup>32</sup>As the 36% are dominated by one source of uncertainty that is not Gaussian, the Gaussian assumption is certainly not correct in this case.

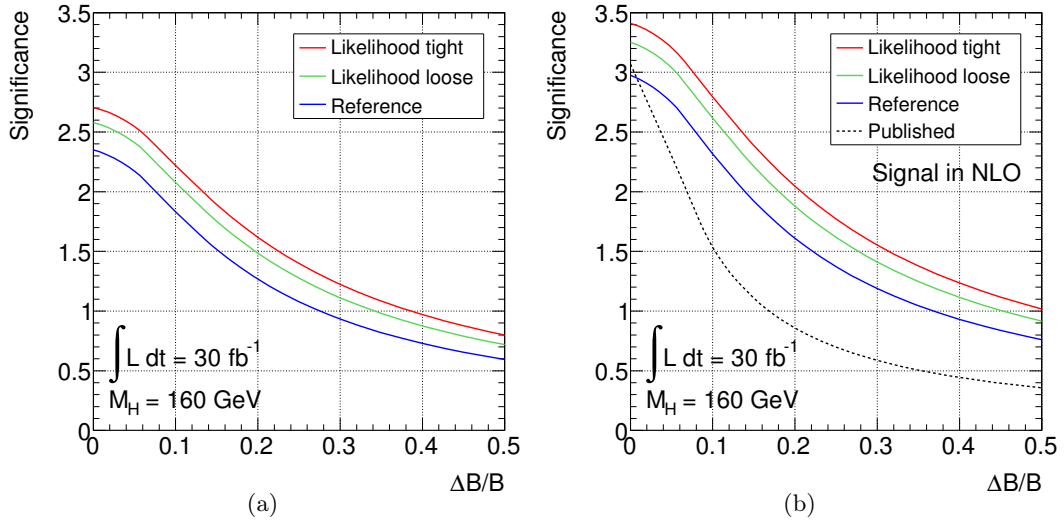


**Figure 6.29:** Comparison of the influence of the relative systematic background estimation uncertainty  $\Delta B/B$  on the expected significance of the observed signal for the three event selection strategies and a Higgs boson mass of  $M_H = 160$  GeV. The scans are shown for the results obtained with the leading order normalization of the accepted signal cross sections (a) and with NLO normalization to be comparable to the published results of Ref. [108], which are shown in addition in (b).

$W$  bosons  $\sigma_{t\bar{t}H} \times \text{BR}(H \rightarrow W^+W^-)$ . The  $\Delta B$  dependence of the accuracy that can be achieved in a measurement of  $\sigma_{t\bar{t}H} \times \text{BR}(H \rightarrow W^+W^-)$  is discussed in Chapter 6.12.

## 6.10 Summary and Outlook

### 6.10.1 Summary

One of the main goals of the ATLAS experiment is the search for the Higgs boson. Should a Higgs boson candidate be found, the next step would be to determine its properties. The  $t\bar{t}H, H \rightarrow W^+W^-$  process is considered a candidate to access the top Yukawa coupling at the LHC. The study of this channel is challenging and requires an accurate description of the detector performance, which is essential for reliable predictions of the reducible backgrounds. Part of the work done in the course of this thesis contributed to the first study of the channel using a full detector simulation, which was published in Ref. [108]. The study presented in this thesis extends this work in several ways, including an improved event selection strategy and thorough estimations of the reducible  $t\bar{t}$  and  $W$ +jet backgrounds.

A promising strategy for the selection of  $t\bar{t}H, H \rightarrow W^+W^-$  events in the final state with two like-sign leptons has been established in the course of this thesis, involving the application of  $b$ -tagging requirements and much tighter lepton isolation criteria than proposed in the publication. This selection provides a still reasonable estimated signal event yield of about 19 events in  $30 \text{ fb}^{-1}$  of data and at an excellent signal-to-background ratio larger than 0.4 in the preferred Higgs boson mass range close to 160 GeV. The study shows that, as expected, the channel cannot provide sufficient signal significance to claim a discovery of the Higgs boson with the first  $30 \text{ fb}^{-1}$  at the LHC. Nevertheless, at least for Higgs boson masses in a broad mass range around the  $W$  pair mass, the chances are good to observe a significant excess of events, which can be used to further study the properties of the Higgs boson. A tight likelihood based lepton isolation allows the reducible  $t\bar{t}$  background to be suppressed to a level where it is no longer the most important contribution to the overall background. The remaining small  $t\bar{t}$  background is furthermore no longer dominated by events that pass the event selection criteria due to leptons produced in heavy quark decays. Instead, also events with leptons being mimicked by non-lepton background and especially real isolated leptons with wrongly attributed charge sign play an important role.  $W$ +jet production, which so far has been considered no serious contribution to the background without further investigation, was studied as a background to the  $t\bar{t}H, H \rightarrow W^+W^-$  process for the first time and could indeed be ruled out as a source of serious background. Moreover, the study reveals that the results are robust against the influence of pile-up. Almost no degradation in the performance is observed in the low-luminosity scenario studied in this thesis. The signal-to-background ratio reaches a level that tolerates also a relatively large systematic uncertainty on the background estimation. Determining this background from data turns out to be mandatory, but no reliable strategy could yet be established. This task is left to future studies.

One of two big challenges is the investigation of the  $t\bar{t}$  and  $W$ +jet backgrounds with the Monte Carlo datasets provided by the ATLAS collaboration. The  $t\bar{t}H, H \rightarrow W^+W^-$  production occurs with a small cross section and large rejection factors are required for the reducible backgrounds. These backgrounds furthermore require the study of Monte Carlo events generated with a full detector simulation to investigate the subtle features of those mostly atypical background event candidates surviving even very strict event selection requirements. The available  $t\bar{t}$  and  $W$ +jet Monte Carlo datasets are roughly a factor 100 too small, compared with the required suppression rates for these backgrounds. To overcome this deficit, the event selection was factorized, but the results are still limited by sizeable statistical uncertainties. Additionally, difficult to estimate uncertainties are introduced by the factorization approach due to correlations between the separately treated jet- and lepton-related parts of the event selection. The results on the  $t\bar{t}$  and  $W$ +jet background contributions are therefore conser-

vatively estimated, wherever the influence of such correlations remains undetermined. The other large source of uncertainties is the theoretical description of the background events. For the most relevant backgrounds, higher order calculations are needed to provide the final states with the large number of high- $p_T$  jets that are required by the event selection criteria. To date, no generators are able to describe the required number of extra partons for the major backgrounds. Furthermore, for some relevant backgrounds, such as  $t\bar{t}W$  and  $t\bar{t}t\bar{t}$ , not even inclusive NLO cross section calculations exist, which can lead to large uncertainties also in the normalization of the expected contributions. The uncertainties arising from the theory description are difficult to estimate and there is no way to ensure a conservative treatment of these issues.

Nevertheless, due to the good signal-to-background ratio, the chances are good to solve both problems in future studies with background estimation from data. Future studies have furthermore the potential to enhance the sensitivity through the use of event reconstruction techniques to further reduce the  $t\bar{t}W$  and  $t\bar{t}Z$  backgrounds and through combination of the studied two like-sign lepton final state with the final state involving three leptons. Finally, the analysis of data obtained in later high-luminosity runs, using an adapted event selection strategy, might allow the sensitivity to be increased. These options are briefly discussed in the following.

### 6.10.2 Further suppression of the $t\bar{t}W$ and $t\bar{t}Z$ backgrounds

After successful suppression of the  $t\bar{t}$  process, the irreducible  $t\bar{t}W$  and  $t\bar{t}Z$  production and the lepton charge mismeasurement contribution of  $t\bar{t}$  are the largest background contributions to the two like-sign lepton final state of  $t\bar{t}H$ ,  $H \rightarrow W^+W^-$ . All three contain pairs of well isolated leptons of the same charge, so further optimization of the lepton isolation requirements will not help to further increase the signal-to-background ratio. Instead, dedicated methods have to be applied to separate the signal from the irreducible backgrounds. If the signal process could be reconstructed, i.e. the jets and leptons could be attributed to the respective Higgs boson or the two top quarks, a Higgs boson mass peak could be reconstructed or the differences in the event kinematics of the signal and background could be used for further background suppression. One such approach is a kinematic fit, which takes all measured quantities in the event and varies them within their experimental uncertainties, with constraints imposed by the  $W$  boson and top quark masses. The approach provides the missing neutrino four-momenta and improved energies and momenta for the observed final state particles. Such a fit was attempted in the ATLFAST study in Ref. [128]. The result was an enhancement of the signal-to-background ratio by a factor of two, still keeping a reasonable signal yield. Alternatively, for Higgs boson masses not too far above  $M_H = 160$  GeV, the final state can be reconstructed analytically, under the assumption that both  $W$  boson daughters of the Higgs boson decay at rest in the Higgs boson rest frame. This approach was tried and gives promising first results but the studies are limited by the available number of Monte Carlo events for the signal and irreducible backgrounds, which are too small to allow for the use of multivariate analysis techniques (see Appendix B.8).

Such attempts are, however, challenging because of the limited resolutions of the jet properties and  $\cancel{E}_T$ , the large number of combinations and the high probability to miss part of the final state objects even in the case of signal events. Invariant mass peaks that can be reconstructed with these methods are therefore broad and do not contain clean signal-free regions that allow the background to be determined from sidebands (see Ref. [25] for a comparable analysis). The same can be expected for any other variable that might be suited to

distinguish signal from background events. There are good chances, though, to reduce the background and enhance the signal-to-background ratio with the help of the reconstructed event properties, applying cuts on e.g. the reconstructed Higgs boson mass, a  $\chi^2$ , quantifying the deviation of the invariant masses of the reconstructed object candidates from their nominal masses, or the output of a likelihood or neural network trained with variables characterizing the reconstructed event. The results of both above mentioned attempts look promising and encourage further studies. The analytic reconstruction, although very preliminary, indicates that signal-to-background ratios of one or better are possible, thus backing the results of the ATLFast analysis. Such attempts presume a very good understanding of their impact on the backgrounds, which needs to be accounted for when determining the background expectations. Given that, event reconstruction techniques will probably be a powerful means for further background suppression.

### 6.10.3 The three lepton final state

Apart from the two like-sign lepton final state, also the final state with three isolated leptons is a good candidate to observe a  $t\bar{t}H$ ,  $H \rightarrow W^+W^-$  signal. This final state, which was also considered in Refs. [108, 128, 137], consists of three leptons and four jets, two being  $b$ -jets. The relevant background processes are the same as in the case of the two lepton final state. The  $t\bar{t}Z$  background becomes more important with respect to the two lepton final state and an efficient  $Z$  boson veto is therefore very important. Again, lepton isolation is crucial to suppress the  $t\bar{t}$  background, which, in contrast to the two lepton final state, mainly consists of fully leptonic events, but again with an additional lepton candidate from a heavy quark decay. Due to the three leptonically decaying  $W$  bosons, the signature is much cleaner than that of the two lepton final state and reducible backgrounds are less important. On the other hand, there are three neutrinos to be reconstructed, which are too many unknowns for an attempt to reconstruct the signal in a kinematic fit or with the assumption that two  $W$  bosons decay at rest, as discussed above. The above mentioned studies found a signal yield of roughly half of that in the two lepton final state. Also the background contributions are smaller, resulting in slightly better signal-to-background ratios compared with the two lepton analyses. The signal significances and consequently also the accuracies of physics quantity measurements are lower than in the two lepton final state. Nevertheless, they are large enough that a combination of both channels substantially increases the significance and the accuracies. A detailed analysis of the three lepton final state is beyond the scope of this thesis, but is certainly worth being considered in future studies.

### 6.10.4 High-luminosity run at the LHC

The original schedule for the LHC consisted of a low-luminosity running phase of three years, with the plan to collect a total integrated luminosity of  $30 \text{ fb}^{-1}$  at an instantaneous luminosity of about  $10^{-33} \text{ cm}^{-2}\text{s}^{-1}$ . Later, the luminosity should be raised by a factor of ten and data taking should go on for some more years. The high-luminosity conditions do not allow the results of this study just to be scaled up by a factor of ten to get a prediction of what could be achieved analysing data from this phase. The pile-up effects discussed in Section 6.8 will increase to a level where they are no longer negligible. To still obtain reasonable results, tighter event selection requirements will be necessary. The studies in Refs. [128, 137] also included high-luminosity conditions, assuming three years of LHC running at  $10^{-34} \text{ cm}^{-2}\text{s}^{-1}$ . These conditions will require stricter selection criteria on the jet transverse momenta and force a lower  $b$ -tagging efficiency to retain the light jet background rejection. Stricter trigger conditions will furthermore have some impact on the leptons. Gains in the order of two or

more in the number of selected signal events can be expected in both final states, resulting in increased statistical significance expectations. At the same time, the signal-to-background ratios are expected to be slightly degraded with respect to those obtained in the low-luminosity running. Reconstructing the event will become more difficult under the high-luminosity conditions. Not only will the increase in activity result in a dilution of the measured jet momenta and  $\cancel{E}_T$ . In addition, a substantial decrease in the number of accepted signal jets is expected, if the minimum jet  $p_T$  is raised to 30 GeV. In consequence, the fraction of signal events where all six jets pass the jet selection criteria, which is already small with a minimum jet  $p_T$  requirement of 20 GeV (see Appendix B.8), will further decrease. Also the number of jets falsely attributed to the event will decrease, but probably not fast enough such that the result of the two effects is a net increase of the fraction of selected events with the full set of correct jets. The event selection criteria applied in this thesis require already higher minimum transverse jet momenta than the two studies mentioned, so the effect of the tighter jet selection criteria will be smaller.

## 6.11 Comparison with previous studies

The  $t\bar{t}H$ ,  $H \rightarrow W^+W^-$  channel has already been studied by three other groups in the past. These are

- the ATLAS full simulation study published in 2009 in Ref. [108], which is used as a basis for the study established in this thesis,
- an earlier ATLAS analysis, performed with the fast detector simulation ATLFAST and published as an ATLAS report in 2002 [128],
- and the parton level study published in Ref. [137].

No comparable study is known from the CMS experiment. The results of the three studies are discussed and compared with the results of this thesis in the following.

The loosest event selection criteria are applied in the full simulation study. Therefore, they result in the highest signal event yield and the statistical significance of the predictions, neglecting systematic uncertainties on the background expectation, is relatively high. On the other hand, the signal-to-background ratio is low compared with all other analyses and the background is clearly dominated by top quark pair production. Under such conditions, the significance or the accuracy of any measurement of a physical quantity that should be performed on the selected signal events drops quickly with the uncertainty of the background measurement. This requires a very accurate determination of the background contribution. Ignoring the  $t\bar{t}$  background, the relative composition of the irreducible backgrounds in the study presented in this thesis is still very much the same as in the published study.

The ATLFAST study is the analysis best comparable in terms of accepted signal and background events to this study. Nevertheless, the event selection criteria are somewhat looser, probably due to the lower minimum jet  $p_T$ . Accordingly, and also because the signal was normalized to the NLO calculation, the signal expectation is larger by more than 50%. Assuming NLO normalization also for the signal expectations in this thesis, the signal-to-background ratios obtained in both analyses are comparable. The total background is larger by 25% in the ATLFAST study. This is basically caused by the considerably larger  $t\bar{t}W$  and  $t\bar{t}\bar{t}$  contributions. The  $t\bar{t}$  and  $t\bar{t}Z$  backgrounds are about the same in both studies. Also the  $t\bar{t}W$  contributions obtained with AcerMC match well in both analyses. Nevertheless, the final  $t\bar{t}W$  contribution given in the ATLFAST study, including the production of an additional parton with the CompHEP generator, is larger than the result obtained with ALPGEN in this thesis, although up to two additional partons are generated here. The  $t\bar{t}\bar{t}$  background is larger by approximately a factor of four in the ATLFAST study. This is explained by the difference in the inclusive cross section values used for the normalization in the two studies, which also differ by a factor of four. The factorization and renormalization scales used for the calculations are not reported in the ATLFAST study, but probably the discrepancy is an effect of the large scale sensitivity of the  $t\bar{t}\bar{t}$  production process. The use of more sophisticated means to suppress background leptons from  $t\bar{t}$  is proposed but refrained from in the study, because reliable predictions are difficult without taking into account the calorimeter shower shapes. Finally, a kinematic fit was applied, which provides a gain in signal significance and enhances the signal-to-background ratio by a factor of two at the cost of 30% of the signal. The backgrounds are about halved with the exception of the dominant  $t\bar{t}W$  background, which is reduced to one fifth of its original size.

The signal expectation predicted by the parton level study is 25% smaller than that of this study, which is presumably due to the strict  $b$ -tagging requirements. The reported signal-to-

background ratio is larger than one. The background contributions from  $t\bar{t}Z$  and  $t\bar{t}W$  are much smaller than those found in this thesis. Especially the  $t\bar{t}Z$  contribution is very small, also with respect to the  $t\bar{t}W$  contribution obtained in the same analysis. These large discrepancies in the  $t\bar{t}W$  and  $t\bar{t}Z$  backgrounds can probably be explained by the method used to scale these backgrounds obtained with the LO generator MadGraph up to account for the extra jets. Only for  $t\bar{t}t\bar{t}$  production, the expectation is of the same size as in this study, although a veto on more than two  $b$ -tagged jets was applied to reduce this background. Probably this is another hint that the scales for the inclusive cross section calculation used for the normalization of the  $t\bar{t}t\bar{t}$  results in this thesis are chosen such that the result is relatively low. Finally, the parton level analysis yields a non-negligible  $t\bar{t}WW$  contribution to the background. This relatively large contribution compared with the  $t\bar{t}t\bar{t}$  process can probably be explained by an underestimation of the  $t\bar{t}W$  and  $t\bar{t}Z$  backgrounds in combination with the fact that the  $b$ -jet veto reduces the contribution of  $t\bar{t}t\bar{t}$  but not that of  $t\bar{t}WW$ . The ATLFASST study included also an attempt to reproduce the results of the parton level analysis. The  $t\bar{t}W$  background was found to be larger by a factor 2.5 and the  $t\bar{t}Z$  background larger by a factor of seven than in the parton level study, which backs the assumption that the procedure to normalize these backgrounds leads to an underestimation. In addition, the  $t\bar{t}$  background to be expected with the event selection criteria applied in the parton level study was estimated in the ATLFASST study and was found to increase the total background almost by a factor of ten.

It must be kept in mind that, except for the study in Ref. [108], which follows a slightly different approach compared with all others, the other studies are not based on a realistic detector description. Especially for the estimation of the  $t\bar{t}$  contribution, detector effects are of vital importance and reliable predictions of this background can hardly be obtained without taking these effects into account. The studies are therefore very difficult to compare. Nevertheless, the comparison of the other backgrounds reveals once more the crucial role of the Monte Carlo description of additional jets in the most important background processes  $t\bar{t}W$ ,  $t\bar{t}Z$  and  $t\bar{t}$ , which leads to large differences in the total predicted background. It also suggests that  $t\bar{t}t\bar{t}$  production needs to be kept in mind as a potential source of background in the future. Once NLO calculations or background measurements from data are available, they will decide if the outcome of this study, that this background can be neglected, holds or not. In the latter case, a  $b$ -jet veto as in the parton level study should be considered to reduce the influence of the background from  $t\bar{t}t\bar{t}$  production.

## 6.12 Measuring the top Yukawa coupling

Once a Higgs boson has been discovered, measurements of its properties will be necessary in order to distinguish between different theoretical models with Higgs bosons involved. The  $t\bar{t}H$ ,  $H \rightarrow W^+W^-$  channel is not suited for a discovery of the Higgs boson. Instead, the study of the complex final state is motivated by its potential to access the Yukawa coupling constant  $g_t$ , parameterizing the strength of the Higgs boson coupling to the top quark.

### 6.12.1 Accuracy of a $\sigma_{t\bar{t}H} \times \text{BR}(H \rightarrow W^+W^-)$ measurement

Input for all  $g_t$  measurements is the product  $\sigma_{t\bar{t}H} \times \text{BR}(H \rightarrow W^+W^-)$  of the Higgs boson production cross section  $\sigma_{t\bar{t}H}$  in the  $t\bar{t}H$  channel and the branching ratio  $\text{BR}(H \rightarrow W^+W^-)$  for its subsequent decay into a pair of  $W$  bosons. With  $N$  being the number of measured events passing the event selection requirements, this product can be determined without further theory assumptions according to

$$\sigma \times \text{BR} = C \cdot \frac{N - B}{\mathcal{L} \cdot \epsilon} \quad . \quad (6.6)$$

Here,  $B$  is the background contribution, obtained from some subsidiary measurement. Signal events are selected with an efficiency  $\epsilon$  (including a detector acceptance factor) and  $\mathcal{L}$  denotes the total integrated luminosity. The combinatorial factor  $C$  scales the selected lepton and jet final state up to the total  $H \rightarrow W^+W^-$  branching ratio.

Using the estimation  $N = S + B$  in Eq. (6.6), with  $S$  and  $B$  being the signal and background expectations obtained in a Monte Carlo study, and estimating the statistical uncertainty as  $\Delta N = \sqrt{N} = \sqrt{S + B}$ , the expected relative uncertainty on  $\sigma_{t\bar{t}H} \times \text{BR}(H \rightarrow W^+W^-)$  is given as

$$\left( \frac{\Delta(\sigma \times \text{BR})}{\sigma \times \text{BR}} \right)^2 = \frac{S + B}{S^2} + \left( \frac{\Delta B}{S} \right)^2 + \left( \frac{\Delta \epsilon}{\epsilon} \right)^2 + \left( \frac{\Delta \mathcal{L}}{\mathcal{L}} \right)^2 \quad . \quad (6.7)$$

The relative uncertainty on the luminosity measurement at the ATLAS experiment is expected to be  $\Delta \mathcal{L} / \mathcal{L} = \pm 3\%$ . The  $\pm 9\%$  experimental event selection efficiency uncertainty as obtained from the Monte Carlo study in this thesis (see Section 6.9.1) are rounded up to  $\pm 10\%$  to account for a possible, but so far unknown, contribution of the lepton isolation efficiency. The background measurement uncertainty  $\Delta B$  is unknown as well. Figure 6.30 therefore shows the  $\Delta B / B$  dependence of the relative uncertainty of a measurement of  $\sigma_{t\bar{t}H} \times \text{BR}(H \rightarrow W^+W^-)$  for the three different event selection strategies outlined in Section 6.4 and a Higgs boson mass of  $M_H = 160$  GeV. LO and NLO signal normalization are shown for comparison with the results of the published ATLAS full simulation study [108]. The uncertainties are dominated by the statistical uncertainty and the systematic uncertainty on the background estimation, whereas the contributions of  $\Delta \epsilon$  and  $\Delta \mathcal{L}$  are almost negligible. Total accuracies better than  $\pm 50\%$  are possible with the likelihood based event selection strategies only for a background uncertainty of less than  $\pm 10\%$ . Uncertainties better than  $\pm 100\%$  can be achieved by the ‘‘likelihood tight’’ analysis for background uncertainties almost up to  $\pm 40\%$ . In the case of the ‘‘likelihood tight’’ event selection, the size of the background estimation uncertainty reaches that of the statistical uncertainty at about  $\Delta B / B = \pm 30\%$ .

Figure 6.31 shows the relative uncertainty on  $\sigma_{t\bar{t}H} \times \text{BR}(H \rightarrow W^+W^-)$  for different values of  $\Delta B / B$  in the range from 0% to  $\pm 50\%$  as a function of the Higgs boson mass. Without background uncertainty, the precision is about  $\pm 50\%$  for Higgs boson masses between 140 GeV and 180 GeV. For smaller  $M_H$ , it quickly rises to more than  $\pm 150\%$  at  $M_H = 120$  GeV. At  $\Delta B / B \approx \pm 30\%$ , where the statistical and systematic background estimation uncertainties

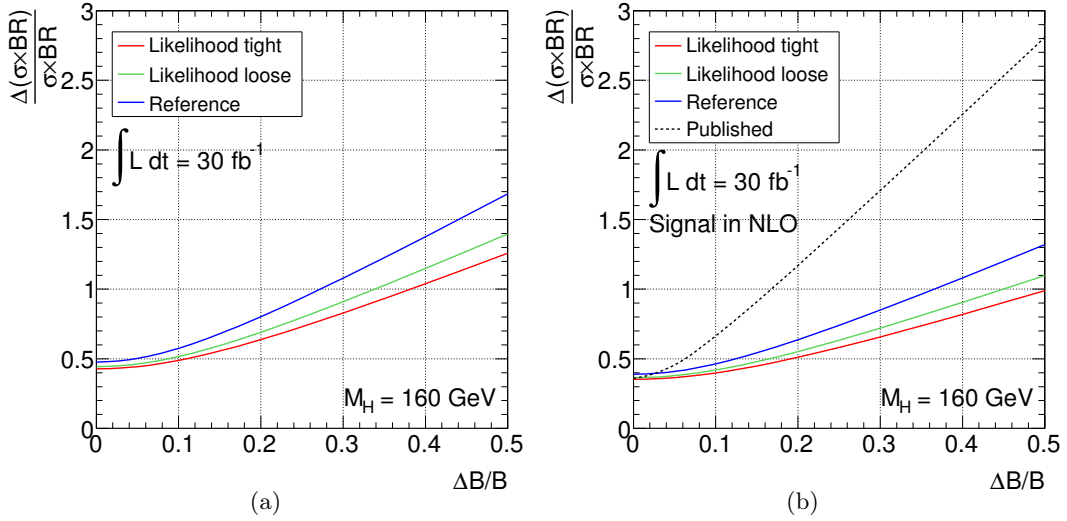


**Figure 6.30:** Relative uncertainty of a measurement of  $\sigma_{t\bar{t}H} \times \text{BR}(H \rightarrow W^+W^-)$  as a function of the relative systematic background uncertainty  $\Delta B/B$  for the three event selection strategies presented in this thesis and a Higgs boson mass of  $M_H = 160 \text{ GeV}$  (calculated according to Eq. (6.7), with  $\Delta\epsilon/\epsilon = \pm 10\%$  and  $\Delta\mathcal{L}/\mathcal{L} = \pm 3\%$ ). The scans are shown for the results obtained with the leading order normalization of the accepted signal cross sections (a) and with NLO normalization to be comparable to the results of Ref. [108], which are shown in addition in (b).

are about equal, the total uncertainty on  $\sigma \times \text{BR}$  is about  $\pm 100\%$  for the Higgs boson mass range between 140 GeV and 180 GeV.

### 6.12.2 Coupling measurements

If a direct, model-independent, measurement of  $g_t$  is to be derived from such a measurement of  $\sigma_{t\bar{t}H} \times \text{BR}(H \rightarrow W^+W^-)$ , e.g. as in Ref. [39] (see Section 1.5), it must be combined with an independent measurement of the branching ratio  $\text{BR}(H \rightarrow W^+W^-)$  (which is, though, not possible at the LHC). The total accuracy  $\Delta g_t/g_t$  is then determined not only by the  $\sigma_{t\bar{t}H} \times \text{BR}(H \rightarrow W^+W^-)$  measurement, but also by the branching ratio measurement and the theoretical prediction of  $\sigma_{t\bar{t}H} \times \text{BR}(H \rightarrow W^+W^-)$ . Nevertheless, very likely the uncertainty on the  $\sigma_{t\bar{t}H} \times \text{BR}(H \rightarrow W^+W^-)$  measurement will be by far the dominant contribution. Since  $\sigma_{t\bar{t}H} \times \text{BR}(H \rightarrow W^+W^-)$  is proportional to the square of  $g_t$ , the relative uncertainty on  $g_t$  will then be about half that on  $\sigma_{t\bar{t}H} \times \text{BR}(H \rightarrow W^+W^-)$ .

More relevant for the LHC is the determination of Higgs boson coupling constants in combined fits, using input from all accessible Higgs boson production and decay channels. Introducing successive assumptions on the underlying physics model, first ratios of squared coupling constants and later squares of absolute values can be determined, as performed in Refs. [33, 34] (see Section 1.5). These studies are based on input from various ATLFEST studies, among them that published in Ref. [128] for the  $t\bar{t}H$ ,  $H \rightarrow W^+W^-$  channel. As discussed in Section 6.11, for the two like-sign lepton channel, these results are comparable to those obtained in this thesis, though perhaps being a bit too optimistic. Furthermore, if some model dependence is accepted and it is assumed that no non-Standard Model particles contribute to the top quark loop, the  $t\bar{t}H$ ,  $H \rightarrow W^+W^-$  process contributes only weakly to the precision of the determination of  $g_t^2/g_{WWH}^2$  and  $g_t^2$ . It can therefore be assumed that the precisions shown in Fig. 6.32 are backed by the results of this study.

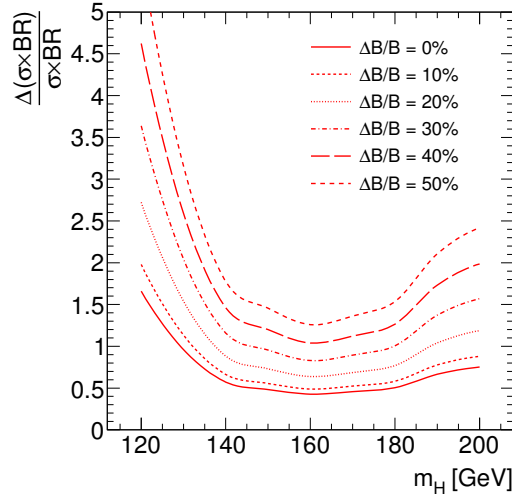


**Figure 6.31:** Higgs boson mass dependence of the relative precision of a measurement of  $\sigma_{t\bar{t}H} \times \text{BR}(H \rightarrow W^+W^-)$  in the like-sign two lepton final state (“likelihood tight” event selection) with an integrated luminosity of  $30 \text{ fb}^{-1}$  at the ATLAS experiment for different relative background measurement uncertainties  $\Delta B/B$  between 0% and  $\pm 50\%$  (calculated according to Eq. (6.7), with  $\Delta\epsilon/\epsilon = \pm 10\%$  and  $\Delta\mathcal{L}/\mathcal{L} = \pm 3\%$ ).

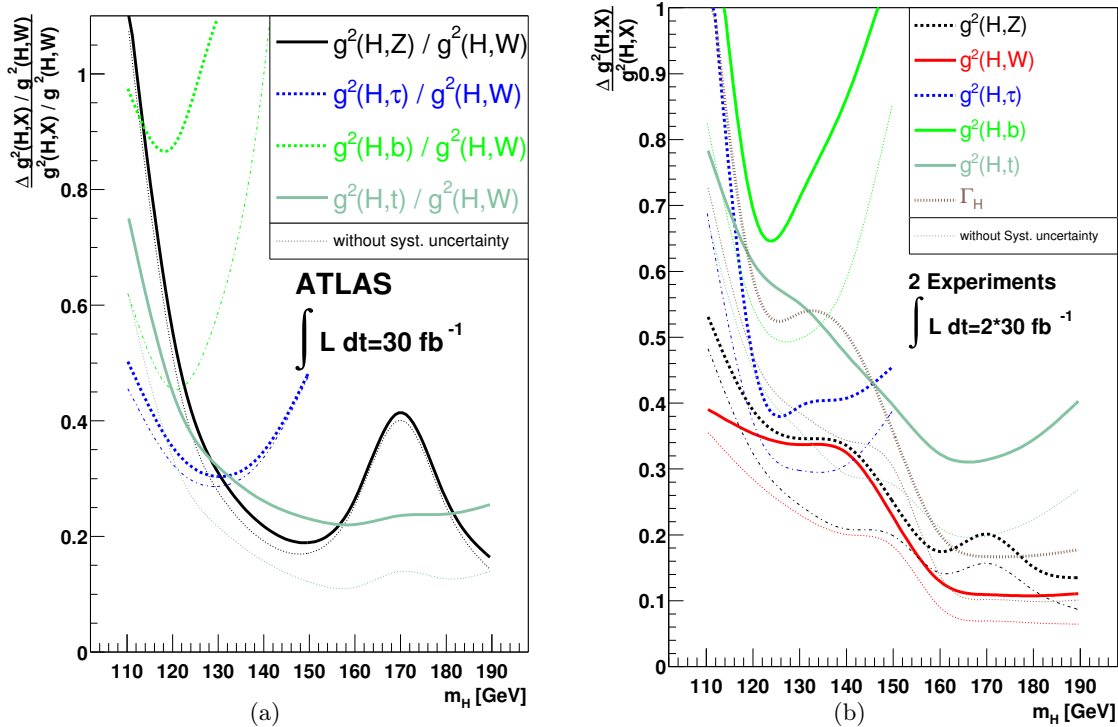


**Figure 6.32:** Expected relative accuracy for a measurement of relative Higgs boson coupling parameters at the ATLAS experiment with an integrated luminosity of  $30 \text{ fb}^{-1}$  (a) and expected relative uncertainty for a measurement of the squared coupling constants using data from two LHC experiments (b) (taken from Refs. [33] (a) and [34] (b); details on the underlying theoretical assumptions are given therein).



# Summary

The first part of this thesis was a contribution to the construction of the ATLAS Semiconductor Tracking detector (SCT). About 200 SCT endcap modules were assembled at the University of Freiburg. Before shipping to the endcap assembly sites, each module was subject to thorough testing in order to ensure their functionality within the ATLAS specifications. A large part of these tests concerned the electrical functionality of the readout electronics and the bias current behaviour of the sensors. The responsibility for the electrical characterization of the Freiburg modules was part of this thesis. The leakage currents of the sensors and their capability for operation at high bias voltages after the type inversion expected after a few years of heavy irradiation were tested in measurements of the  $I - V$  curves of the sensors. Digital tests of the hybrid comprised the verification of correct clock and command reception and configurability of the readout chips as well as tests of the redundancy links on the hybrid, the bypassing of individual chips in the case of a failure and tests of the functionality and efficiency of the pipelines. Since the charge information from the sensor is converted into binary information directly on the readout chips, the analogue properties of the ATLAS SCT modules had to be determined in threshold scans. A given calibration pulse was for this purpose injected several times and the resulting signal rate was determined as a function of the threshold to obtain an S-shaped curve, from which offset, gain and input and output noise of each readout channel were determined. The detector noise occupancy was measured in a dedicated scan, as were the adjustability of the offsets of individual channels to guarantee minimum spread when operated at a common threshold and time-walk scans to ensure the delays of the signals generated by different test pulses to lie well within the maximum window of 25 ns. Also the long-term stability of the noise and leakage currents and the power consumption of the hybrids were monitored. Except for some problems with the breakdown and noise behaviour of some modules equipped with sensors by the supplier CiS, most of the modules were well within the specifications and could be delivered in time to the endcap assembly sites in Amsterdam and Liverpool. The assembly and testing was finalized in autumn 2005. Since late in 2009, the ATLAS experiment is taking data very successfully and the SCT detector has proved its functionality in full operation, contributing to a variety of first physics results.

To be suited for the analysis of physics processes, the signals measured in the detector need to be transferred into particle four-momenta, requiring the reconstruction and identification of different particle types. This thesis contributes to the physics object identification by an extended study of methods to separate isolated electrons from real electron background produced in the decays of heavy quarks. The latter are accompanied by energy deposits in the calorimeter and additional tracks from the rest of the heavy quark jets. A large number of potential variables were tested and compared for their ability to distinguish signal and background. The most powerful isolation variables that could be identified are sums of the transverse momenta of additional tracks in certain cones around the electron candidate as well as the energy deposit in these cones after subtraction of the energy of the electron cluster. Some further separation power is provided by the impact parameter of the electron track itself. The optimal choice of the cone size depends crucially on the signal to be studied. In very clean signal topologies, such as  $Z \rightarrow e^+e^-$ , large cones can be exploited and provide

an excellent background rejection at high signal selection efficiencies. If the signal topology is more complex, large cone sizes pick up too much contamination from other objects in the event and lead to a significant decrease in the signal selection efficiency. For signals such as e.g. top quark pair production, smaller cone sizes are therefore better suited, even at the cost of some background rejection power. Apart from this restriction, very good and robust signal and background separation can be achieved for a variety of different signal event types with a standard set of four variables, combined in a projective likelihood estimator with the input PDFs determined from electrons selected only in one type of signal and background events ( $Z \rightarrow e^+e^-$  and  $t\bar{t}$ , respectively). A cut on the output value of the likelihood estimator is meant to be applied on top of the ATLAS electron ID criteria, which are optimized to reject non-electron background. Typical rejection factors that can be reached without significant loss in the signal selection efficiency in clean signals are of the order  $10^3$ , depending on the  $p_T$  and  $\eta$  of the candidate. Rejections of up to  $10^4$  can be achieved at still reasonable total signal selection efficiencies. In less clean signals and with smaller cone sizes, rejection factors of up to about  $5 \cdot 10^3$  are realistic. The isolation likelihood tool, including a PDF set obtained from suited Monte Carlo datasets, was made available in the official ATLAS reconstruction software package. Later, the algorithm was extended to allow for more flexibility in the variable and PDF choice and also for use for further non-electron background rejection and for the isolation of photon signals. Now, that ATLAS has collected some  $\text{fb}^{-1}$  of data, PDFs could be obtained from suited signal and background samples, thus reducing the uncertainties on the shapes of the variables due to the modelling of the detector response. Furthermore, a more reliable description of the discriminating variables and the large numbers of available events may allow to take advantage of the correlations among the variables and the use of more advanced multivariate analysis tools, both of which are expected to increase the separation power.

The isolation likelihood tool is a powerful ingredient to the study of the  $t\bar{t}H$ ,  $H \rightarrow W^+W^-$  channel, for which it has also been extended to muons. The most promising final state in this channel consists of a pair of equally charged leptons, accompanied by six jets. One of the most important backgrounds are semi-leptonically decaying  $t\bar{t}$  events (i.e.  $t\bar{t} \rightarrow bjj b\ell\nu$ ), which are produced abundantly at the LHC. The second lepton selected in these events is most likely the product of a heavy quark decay. Based on a first full simulation study of the channel, which was published together with a group from Marseille and Beijing in 2009, an event selection strategy was established in the course of this thesis, involving  $b$ -tagging requirements on the jets and very tight lepton isolation criteria. Whereas in the published study the final background was dominated by top quark pair production, it could be shown that it is possible to suppress this background to a level where it is no longer the largest contribution, with a still reasonable estimated signal event yield of about 19 events in  $30 \text{ fb}^{-1}$  of data and at an excellent signal-to-background ratio larger than 0.4 in the preferred Higgs boson mass range close to 160 GeV. The remaining background is irreducible and is dominated by  $t\bar{t}W$  and  $t\bar{t}Z$  production. The study involves also a detailed analysis of the lepton charge mismeasurement and electron fake contributions to the  $t\bar{t}$  background, which were neglected in the published study due to the use of a filtered  $t\bar{t}$  dataset. It was found that, at the  $t\bar{t}$  background suppression level reached with the tight lepton isolation applied in this study, all three contribute significantly to the remaining small  $t\bar{t}$  background, with fully leptonic  $t\bar{t}$  events with one of the lepton charges assigned wrongly being the largest contribution. Another background candidate that was not considered in the publication is  $W$  boson production in association with jets. This background was also studied in detail in the course of this thesis and a conservative limit could be set on its contribution that proves that indeed this source of background is negligible. All these results suffer from two large uncertainties: The

statistical uncertainties of the  $t\bar{t}$  and  $W$ +jet backgrounds are large due to the combination of the requirements for large background suppression rates and the use of Monte Carlo events generated with the full detector simulation, which were provided by the ATLAS collaboration only in a limited number. Moreover, the theoretical description of the relevant background processes leads to large uncertainties. All of them involve two or more additional partons that can only poorly be predicted by current Monte Carlo generators. Background estimation from data will therefore be mandatory for future studies of the channel. The channel is, however, not suited for a discovery of the Higgs boson. Besides the fact that other channels are much easier to access in the relevant Higgs boson mass range, a sufficiently narrow Higgs boson mass reconstruction will certainly not be feasible and the significance obtained in a simple counting experiment is not sufficient for a  $5\sigma$  discovery. Hence, the channel is of interest only, once a Higgs boson has been discovered in another channel. Given the mass of the Higgs boson turns out not to be too far away from 160 GeV, it can provide valuable information on the top Yukawa coupling, in particular for model-independent measurements.



# A Addendum on the electron isolation

## A.1 Additional discriminating variables

Apart from the isolation variables discussed in Chapter 5, more candidates were tested for their separation power in the course of this thesis. Most of these extra candidates are related to the shower shape and track match quantities that are already exploited by the electron identification cuts (see Section 3.3.3). Some of them still show substantial differences in the shapes for signal and background electrons and could be used for isolation purposes. A list of candidates is given in the following and the signal and background distributions for some of them are shown in Fig. A.1:

- The number of additional tracks  $N^{\text{trk}}(0.2)$  and  $N^{\text{trk}}(0.4)$ , measured in cones of  $\Delta R < 0.2$  and  $0.4$  around the electron cluster (Figs. A.1(a) and A.1(b)).
- The fraction  $E^1/E$  of the total EM cluster energy reconstructed in the first EM calorimeter layer.
- $[E^1(\pm 3) - E^1(\pm 1)]/E^1(\pm 1)$ , with  $E^1(\pm n)$  being the energy measured in the first EM calorimeter layer, summed up in  $n$  cells in both directions from the cell with the largest energy deposit.
- The shower width  $w_{\text{tot}}^1$  measured from 40 strips in the first EM calorimeter layer.
- The ratio  $E_{233}/E_{277}$  of uncalibrated energies measured in  $3 \times 3$  and  $7 \times 7$  cells in the second EM calorimeter layer (Fig. A.1(c)).
- The transverse energy  $E_{\text{T}}^{\text{had}}$  measured in the first sampling of the hadronic calorimeter (Fig. A.1(d)).
- $E_{\text{T}}^{\text{had}}/(E_{\text{T}}^{\text{EM}} + E_{\text{T}}^{\text{had}})$ , the fraction of the total transverse energy measured in the first sampling of the hadronic calorimeter (Fig. A.1(e)).
- The ratio of the cluster energy and the track momentum  $E/p$  (Fig. A.1(f)).
- The angular distances  $\Delta\eta$  and  $\Delta\phi$  between the cluster position measured in the second EM sampling and the associated track in  $\phi$  and  $\eta$ .

None of these candidates are further considered. Their separation power is much weaker than that of the variables listed in Section 5.2 and hence their contribution to the combined performance if combined in a projective likelihood estimator is almost negligible. Some even degrade the performance due to anti-correlations with other variables. Furthermore, their shapes strongly depend on the identification cuts (e.g. if “tight” electrons are used instead of “medium” electrons). Thus, not exploiting them allows for more flexibility, which is mandatory for an official Athena tool to satisfy the needs of a variety of different analyses.

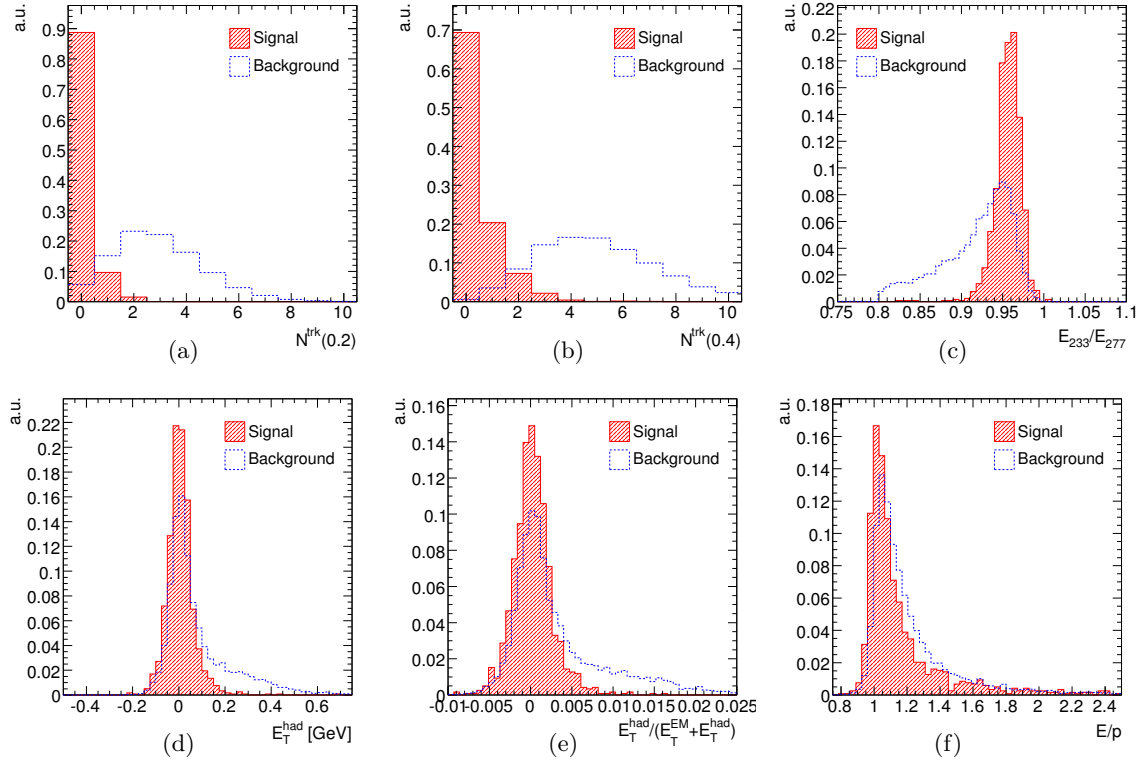


**Figure A.1:** Comparison of the signal and background distributions of some of the additional isolation variables in the bin  $19 \text{ GeV} < p_T^{\text{rec}} < 27 \text{ GeV}$ ,  $|\eta^{\text{rec}}| < 1.37$  (example). The definitions of the variables are given in the text. All distributions are normalized to unity, including overflows.

## A.2 Pile-up conditions

To study the impact of pile-up on the electron isolation, a sample of  $Z \rightarrow e^+e^-$  events is available overlaid with minimum-bias events. It assumes an average of 2.3 minimum-bias events per event, corresponding to a luminosity of  $10^{33} \text{ cm}^{-2}\text{s}^{-1}$  at a collision rate of 40 MHz, comparable to the low luminosities that are expected in the first period of data taking. No samples for higher-luminosity scenarios are available.

### Tracking based isolation variables

Pile-up leads to multiple collisions per beam crossing, resulting in a higher overall detector activity. The tracking performance is degraded by hits from additional tracks, which are mistakenly assigned to the tracks of the main event. Furthermore, tracks from minimum-bias vertices may be falsely assigned to the primary vertex of the event of interest. These effects can reduce the separation power of the tracking based isolation variables but can be reduced by suitably chosen requirements on the tracks included in the calculation of the quantities. The “standard quality cuts” defined for the tracking studies in Ref. [71] are used as a reference in the following to test the potential of several track selection criteria to reduce the sensitivity of the isolation variables against pile-up. The two candidates that are prone to higher detector activity are the longitudinal impact parameter and the track  $p_T$  distribution. Variations of the cuts on the transverse impact parameter and the hit requirements for the tracks on the other hand show no significant influence on the separation power.

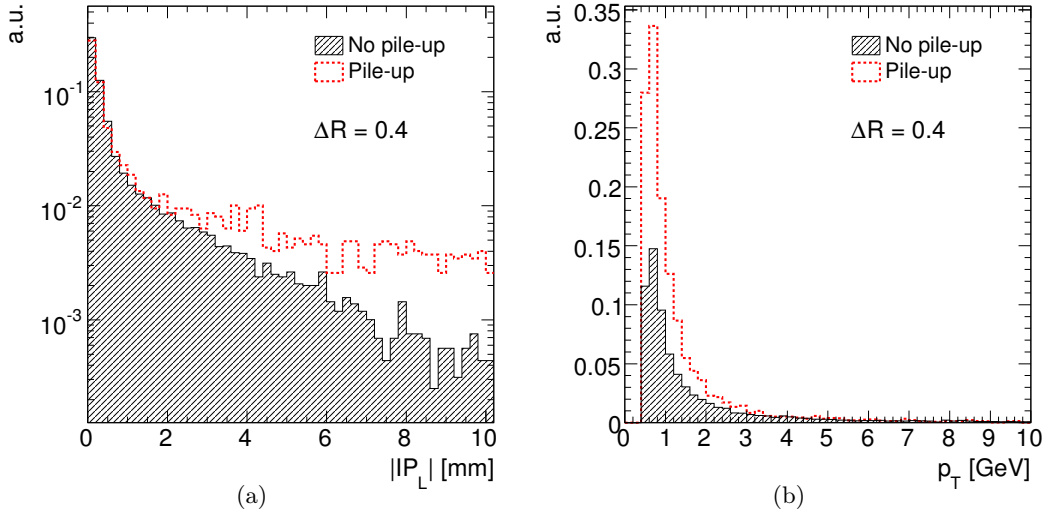
Figure A.2(a) shows a comparison of the distributions of the longitudinal impact parameter  $IP_L$  of the tracks found in a cone of  $\Delta R = 0.4$  around electron candidates with and without pile-up. The distribution indicates that the 10 mm cut already allows a large fraction of tracks from minimum-bias events to pass. The requirement is therefore tightened to  $|IP_L| < 2 \text{ mm}$ . A comparison of the  $p_T$  distributions of the same tracks with and without pile-up is shown in Fig. A.2(b). It indicates that a relatively high cut on  $p_T$  would also help to reduce the contamination by pile-up tracks. Nevertheless, the separation power of the corresponding isolation variables is the higher, the lower the  $p_T$  threshold is chosen. The benefit of gathering as many tracks as possible outweighs the reduction of pile-up contamination and therefore the minimum  $p_T$  is lowered to  $0.5 \text{ GeV}$ <sup>1</sup>.

Figure A.3 shows the impact of both requirements on the performance curves obtained with signal electrons from the pile-up dataset as defined in Section 5.4. Because of the lack of a better suited background sample, these are still obtained with respect to the rejection of background electrons in the  $t\bar{t}$  sample as used before. Figure A.3(a) indicates that even on pile-up events raising the minimum required track- $p_T$  from 0.5 to 1 GeV leads to a small loss in performance. Varying the cuts on the longitudinal impact parameter on the other hand does not influence the performance, as can be seen in Fig. A.3(b).

### Impact on the separation power

Similar effects as described in the case of the high jet multiplicity environments in Sections 5.2 and 5.4 are caused by pile-up events, which play a non-negligible role from the very beginning of data taking in ATLAS. Pile-up could not be considered in this study, since no suited background Monte Carlo dataset with a sufficiently large number of events is available. To get a rough idea of the impact of pile-up on the performance of the `IsolationLikelihood`,

<sup>1</sup>This no longer applies for later versions of the ATLAS reconstruction software due to changes in the tracking algorithms. Here, the use of tracks with a minimum  $p_T$  of 1 GeV is the better choice (see Ref. [111]).



**Figure A.2:** Longitudinal  $IP_L$  (a) and  $p_T$  (b) of tracks in a cone of opening angle  $\Delta R = 0.4$  around signal electrons in  $Z \rightarrow e^+e^-$  with and without pile-up. All distributions are normalized to the number of contribution electron candidates, including the overflow.

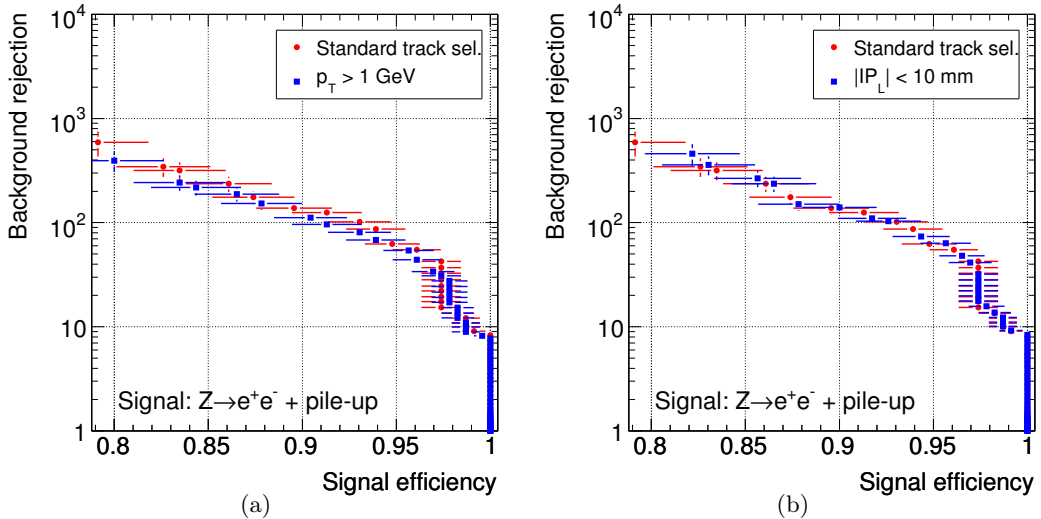


**Figure A.3:** Comparison of the background rejection as a function of the signal selection efficiency for different track selection cuts on signal samples from the pile-up  $Z \rightarrow e^+e^-$  sample in the example bin  $19 \text{ GeV} < p_T^{\text{rec}} < 27 \text{ GeV}$ ,  $|\eta^{\text{rec}}| < 1.37$ . The standard track selection ( $p_T > 0.5 \text{ GeV}$ ,  $IP_L < 2 \text{ mm}$ ) is compared with selections with  $p_T > 1 \text{ GeV}$  (a) and  $IP_L < 10 \text{ mm}$  (b) in the bin  $19 \text{ GeV} < p_T < 27 \text{ GeV}$  and  $0 < |\eta| < 1.37$ . Background electrons are still selected from the  $t\bar{t}$  dataset without pile-up.

Figs. A.4 and A.5 show the total performance curves for signal electrons in the pile-up  $Z \rightarrow e^+e^-$  sample. Background electrons are still taken from the  $t\bar{t}$  dataset without pile-up. Since the efficiency for the selection of background electrons decreases in the same way as it does in the case of signal electrons under the influence of pile-up, this overestimates the loss in the performance. The curves can therefore be regarded as upper limits to the expected degradations.

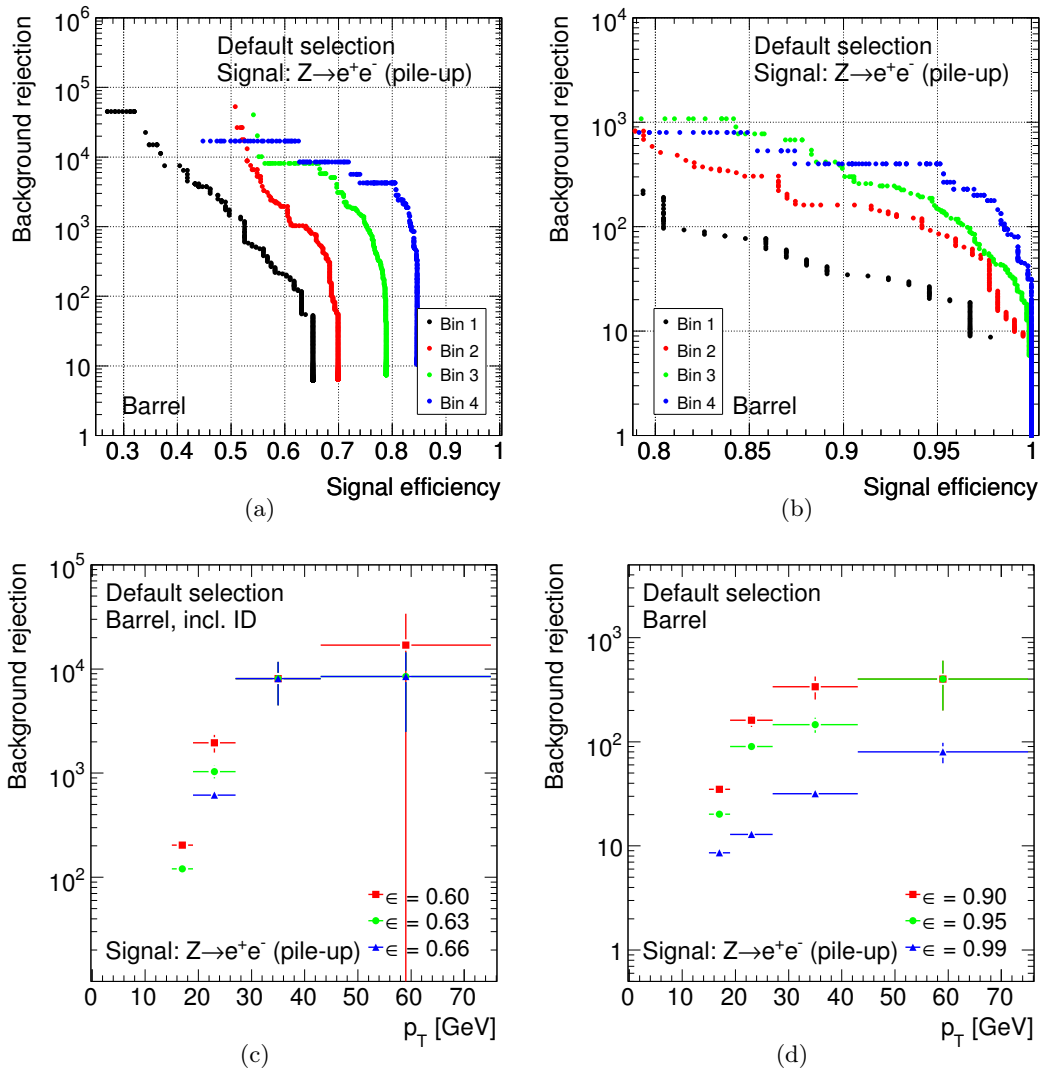


**Figure A.4:** Performance of the likelihood tool in the barrel region of the ATLAS detector on signal electrons from the  $Z \rightarrow e^+e^-$  dataset overlaid with minimum-bias events. Background electrons are selected from the  $t\bar{t}$  sample without pile-up. The curves on the left include the electron ID signal selection efficiencies and background rejections as listed in Tables 5.3 and 5.4, whereas the curves on the right do not. The curves in (a) and (b) are given in bins of  $p_T^{\text{gen}}$  and  $\eta^{\text{gen}}$ . The corresponding  $p_T$  dependence of the background rejections at given signal selection efficiencies is shown in (c) and (d). For the definition of the bins, see Table 5.2 in Section 5.1. Error bars are not displayed in (a) and (b) for the sake of clarity.

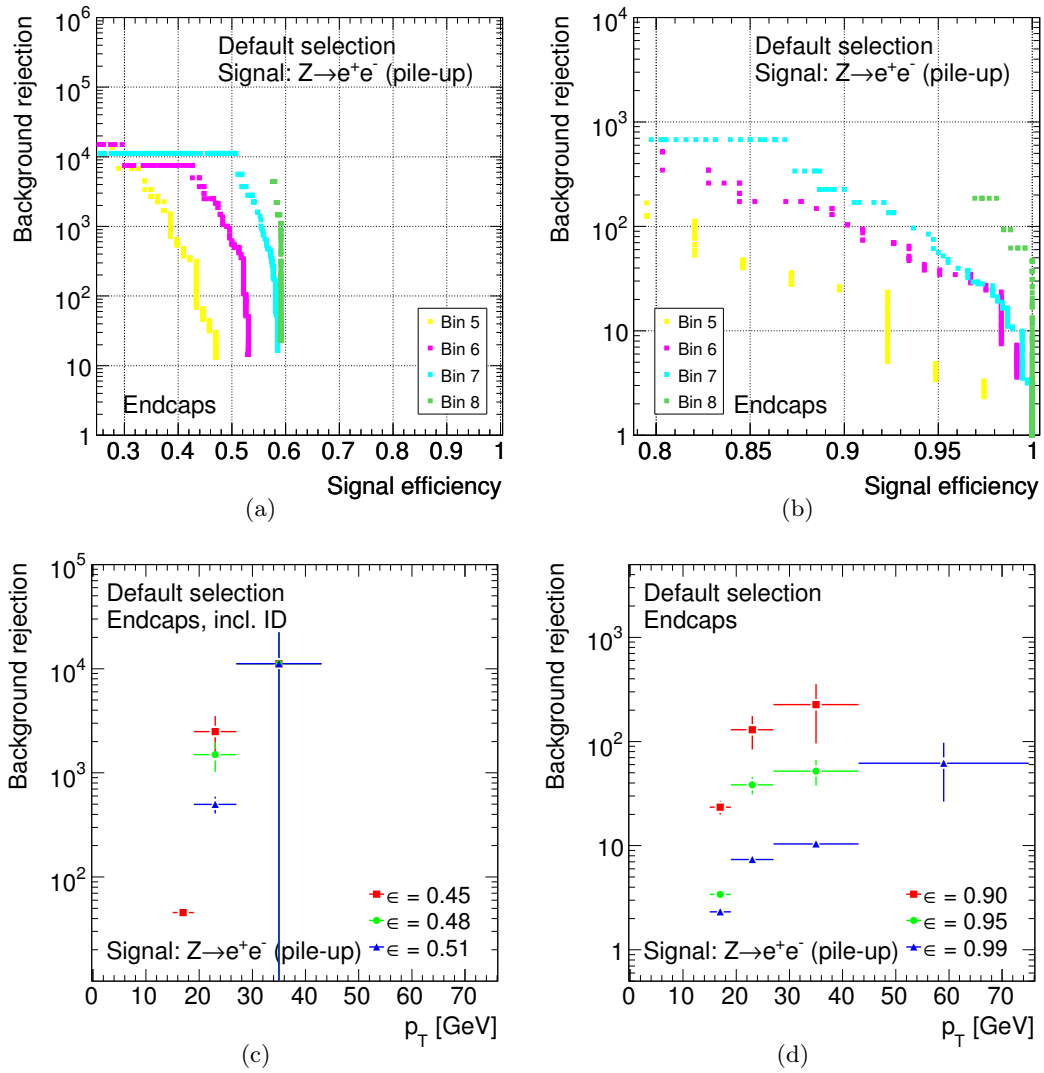
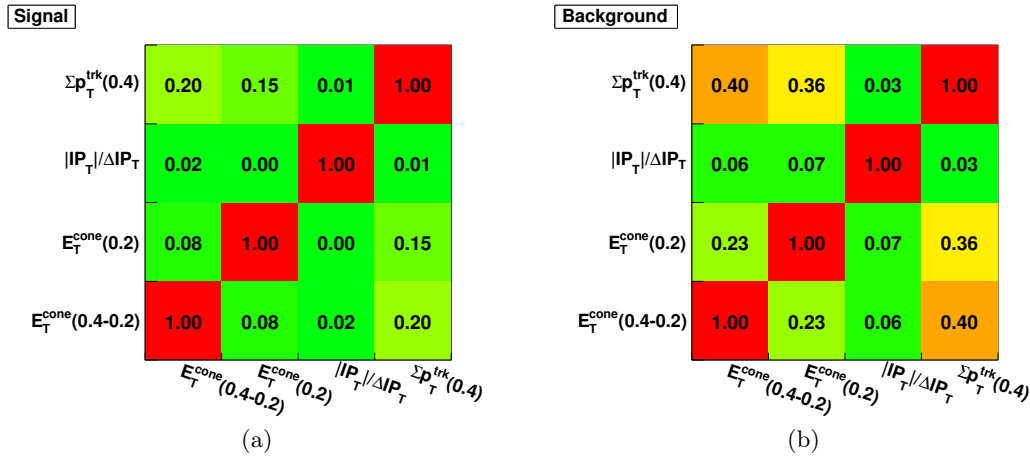


Figure A.5: The same as in Fig. A.4, but for the endcaps of the ATLAS detector.

### A.3 Correlations

The isolation variables are correlated among each other. Figure A.6 shows the correlation coefficients between the input variables of the “default” selection in one example bin of  $p_T$  and  $\eta$  for signal and background. As the example shows, there are strong correlations of up to about 40% in the background between  $E_T^{\text{cone}}(0.4 - 0.2)$  and  $\Sigma p_T^{\text{trk}}(0.4)$ , whereas the corresponding correlations in the signal are much smaller. These correlations can be exploited for the separation of signal and background e.g. if multi dimensional PDFs are used to obtain the likelihood ratio. Nevertheless, this requires sufficiently large training datasets and is hence impossible with the available Monte Carlo samples.



**Figure A.6:** Correlation coefficients between the input variables of the “default” selection (transformed for the use as input variables for the `IsolationLikelihood` as described in Section 5.3) in the signal (a) and background (b). The bin  $19 \text{ GeV} < p_T < 27 \text{ GeV}$  and  $0 < |\eta| < 1.37$  is shown as an example.

## A.4 Overview of the discriminating variables

Variable	Cone size	Transformation	Range	Selection
$E_T^{\text{cone}}(0.2)$	0.2	$y = \ln(x[\text{GeV}] + 1.01)$	-5...7	“default” “highJetMulti”
$E_T^{\text{cone}}(0.4)$	0.4	$y = \ln(x[\text{GeV}] + 1.01)$	-5...7	
$E_T^{\text{cone}}(0.4 - 0.2)$	0.4	$y = \ln(x[\text{GeV}] + 1.01)$	-5...7	“default”
$\Sigma p_T^{\text{trk}}(0.2)$	0.2	$y = \ln(x[\text{GeV}] - 0.49) + 5.5$	0...13	“highJetMulti”
$\Sigma p_T^{\text{trk}}(0.4)$	0.4	$y = \ln(x[\text{GeV}] - 0.49) + 5.5$	0...13	“default”
$\Sigma p_T^{2\text{trk}}(0.2)$	0.2	$y = \ln(x[\text{GeV}^2] - 0.24) + 5.5$	0...17	
$\Sigma p_T^{2\text{trk}}(0.4)$	0.4	$y = \ln(x[\text{GeV}^2] - 0.24) + 5.5$	0...17	
$p_T^{\text{max trk}}(0.2)$	0.2	$y = \ln(x[\text{GeV}] - 0.49) + 5.5$	0...13	
$p_T^{\text{max trk}}(0.4)$	0.4	$y = \ln(x[\text{GeV}] - 0.49) + 5.5$	0...13	
$\Sigma(p_T^{\text{trk}}/\Delta R)(0.2)$	0.2	$y = \ln(x[\text{GeV}] - 2.45) + 3$	0...15	
$\Sigma(p_T^{\text{trk}}/\Delta R)(0.4)$	0.4	$y = \ln(x[\text{GeV}] - 1.2) + 3$	0...15	
$ IP_T /\Delta IP_T$	-	$y = \ln(x)$	-7...5	“default” “highJetMulti”

**Table A.1:** Overview on the considered discriminating variables. The “Cone size” refers to the opening angle  $\Delta R$  around the electron candidate in which calorimeter and track information is summed up. The functions in the column denoted “Transformation” give the transformation functions used to map the raw distribution of the variable onto distribution that approximately follows a Gaussian (see Section 5.3). The numbers in the “Range” column give the range of the x-axis of the corresponding histogram provided in the Athena implementation of the `IsolationLikelihood` tool. Possible outliers are mapped onto the lowest/highest bin of the histogram. The “Selection” column indicates if the variable is contained in one of the standard variable sets that are defined in Section 5.4.

## A.5 Choice of the “default” and “highJetMulti” variable sets and performance of the input variables

To evaluate the separation power of individual variables and to select the best performing variable sets to be used in physics analyses, the performance curves (as defined in Section 5.4) are compared for different combinations of variables to select the one providing the largest background rejection over an as large as possible efficiency range. In the following, the “default” selection of variables serves as a reference to discuss the performance of different isolation variables.

The choice of the size of the cones in which the input variables are calculated has a big influence on the performance of the likelihood. Since the tracks belonging to heavy quark jets can spread widely, it is safest to use cone sizes of the order of magnitude that are used by the jet algorithms in order to gather as much as possible of the energy deposited by the jet or all tracks associated to it. On the other hand, the probability to pick up tracks or energy not related to the electron candidate or its mother heavy quark jet increases with the cone size. Figure A.7(a) shows the comparison of the “default” likelihood configuration with configurations using varying cone sizes, as well as the single-variable performances of calorimeter variables calculated in different cones. The performance is best for the large cones of  $\Delta R = 0.4$  in the case of the  $Z \rightarrow e^+e^-$  signal sample, where the largest loss in separation power appears if  $\Sigma p_{\text{T}}^{\text{trk}}(0.4)$  is replaced by  $\Sigma p_{\text{T}}^{\text{trk}}(0.2)$ . The degradation of the performance observed by the exchange of any of this variables is stronger in the endcaps than in the barrel. The benefit of using 0.4-cones is no longer given for signal electrons in  $t\bar{t}$ , as shown in Section 5.4. The single variable scans in Fig. A.7(b) show that separately exploiting the energy close to the cluster ( $E_{\text{T}}^{\text{cone}}(0.2)$ ) and farther away ( $E_{\text{T}}^{\text{cone}}(0.4 - 0.2)$ ) provides a slightly better separation power than if only  $E_{\text{T}}^{\text{cone}}(0.4)$  is used. This is due to additional information on the distribution of the total energy in the large cone, which is exploited if the energy deposit in the two regions is used separately. This is the case especially in the endcap bins, where even  $E_{\text{T}}^{\text{cone}}(0.4 - 0.2)$  alone provides better separation power than  $E_{\text{T}}^{\text{cone}}(0.4)$  does.

The information on additional tracks is combined in different ways as sums of the  $p_{\text{T}}$  of all tracks with varying weights. Figure A.7(d) shows the performance curves for the “default” likelihood configuration in case  $\Sigma p_{\text{T}}^{\text{trk}}(0.4)$  is exchanged by the sums weighted as described. Figure A.7(c) compares the separation powers of each sum of its one. Though the differences in the single variable scans are small, the unweighted  $p_{\text{T}}$ -sum serves best in all kinematic regions. The variable performing worst in the barrel is  $p_{\text{T}}^{\text{max trk}}(0.4)$  and the sum weighted with  $1/\Delta R$  in the endcaps. No significant difference can be observed in the performance curves with  $\Sigma p_{\text{T}}^{\text{trk}}(0.4)$  being replaced by any of these variables to appear consistently over the whole kinematic range.

The “default” variable set, containing the variables  $E_{\text{T}}^{\text{cone}}(0.2)$ ,  $E_{\text{T}}^{\text{cone}}(0.4 - 0.2)$ ,  $\Sigma p_{\text{T}}^{\text{trk}}(0.4)$  and  $|IP_{\text{T}}|/\Delta IP_{\text{T}}$ , is the one providing the best performance over the largest kinematic range for signal samples with moderate jet activity, like e.g.  $Z \rightarrow e^+e^-$ . The combination of  $E_{\text{T}}^{\text{cone}}(0.2)$ ,  $\Sigma p_{\text{T}}^{\text{trk}}(0.2)$  and  $|IP_{\text{T}}|/\Delta IP_{\text{T}}$  is shown to be the best suited choice in the case of high jet-multiplicity events like  $t\bar{t}$  in similar tests.

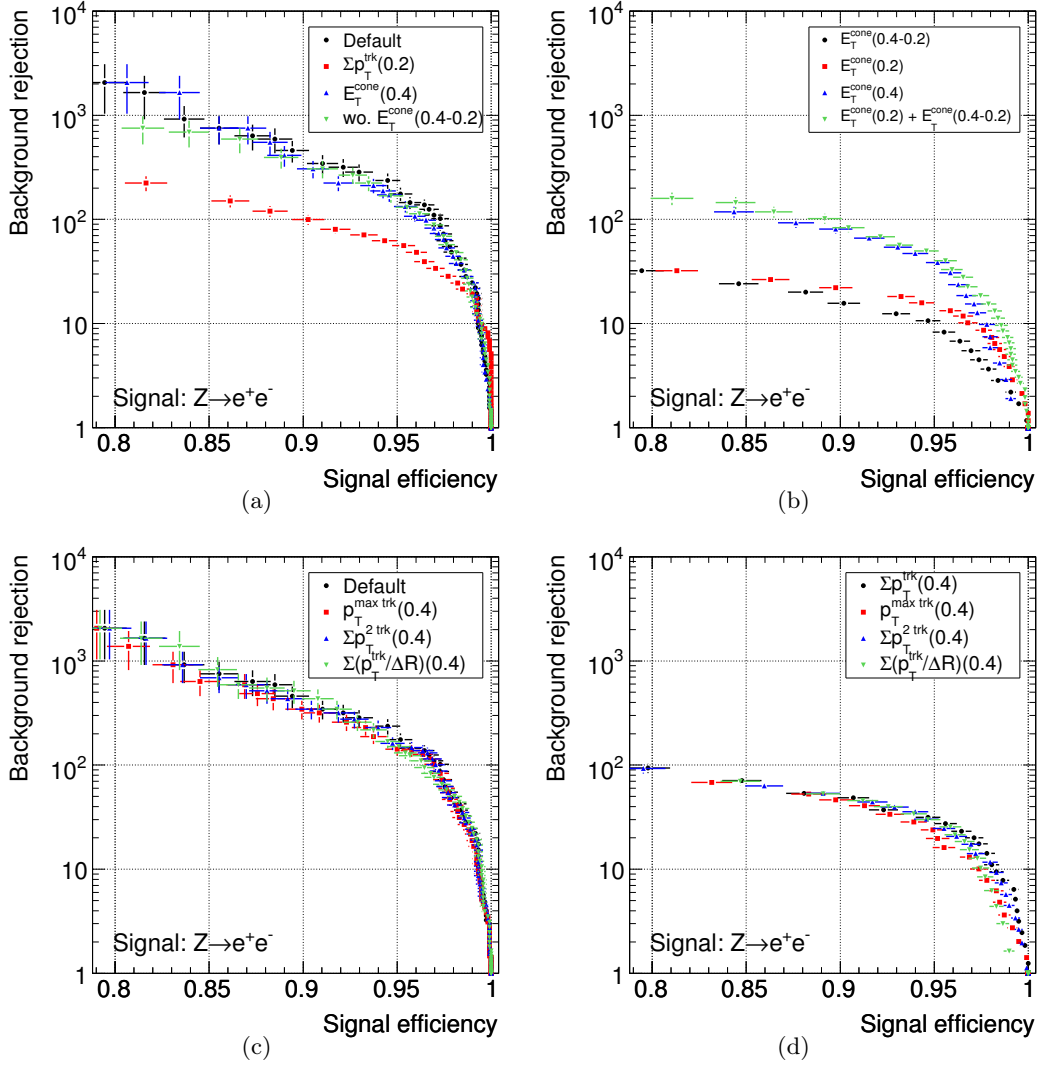


**Figure A.7:** Comparison of the background rejection as a function of the signal efficiency for different sets of input variables. Figures (a, b) show a comparison of isolation variables calculated in different cones in the bin  $19 \text{ GeV} < p_T < 27 \text{ GeV}$  and  $0 < |\eta| < 1.37$ . (a) “Default” configuration and configuration obtained by the exchange of  $\Sigma p_T^{\text{trk}}(0.4)$  by  $\Sigma p_T^{\text{trk}}(0.2)$ ,  $E_T^{\text{cone}}(0.4-0.2)$  and  $E_T^{\text{cone}}(0.2)$  by  $E_T^{\text{cone}}(0.4)$  and without  $E_T^{\text{cone}}(0.4-0.2)$ . (b) Performance curves of the individual variables indicated in the legend. Figures (c, d) show comparisons of differently weighted  $p_T$ -sums in the bin  $19 \text{ GeV} < p_T < 27 \text{ GeV}$  and  $0 < |\eta| < 1.37$ . (c) Standard configuration and configurations with  $\Sigma p_T^{\text{trk}}(0.4)$  being exchanged by the variables indicated in the legend and (d) each of the variables on their own.

## A.6 $\eta$ and $p_T$ dependence of the signal selection efficiency and background rejection without electron identification efficiencies included

The curves shown to demonstrate the  $\eta$  and  $p_T$  dependence of the separation power of the `IsolationLikelihood` in Section 5.4 include the signal selection efficiencies and background rejection factors of the electron identification requirements given in Tables 5.3 and 5.4 in Section 5.1. The combined efficiency and rejection is, what one will normally use to adjust the cuts on the likelihood output value to the needs of individual physics analyses, since the electron identification efficiencies and background rejections themselves vary strongly, depending on the kinematic region. Nevertheless, to demonstrate the contribution of the `IsolationLikelihood` to this combined performance, the curves shown in the following do not take the contribution of the electron identification criteria into account. Figures A.8 and A.9 show the performance curves and the  $p_T$  dependent background rejections at fixed signal efficiencies for “medium” signal electrons in  $Z \rightarrow e^+e^-$  and  $t\bar{t}$  datasets. Figures A.10 and A.11 shows the corresponding curves for “loose” and “tight” electrons in  $Z \rightarrow e^+e^-$  events.

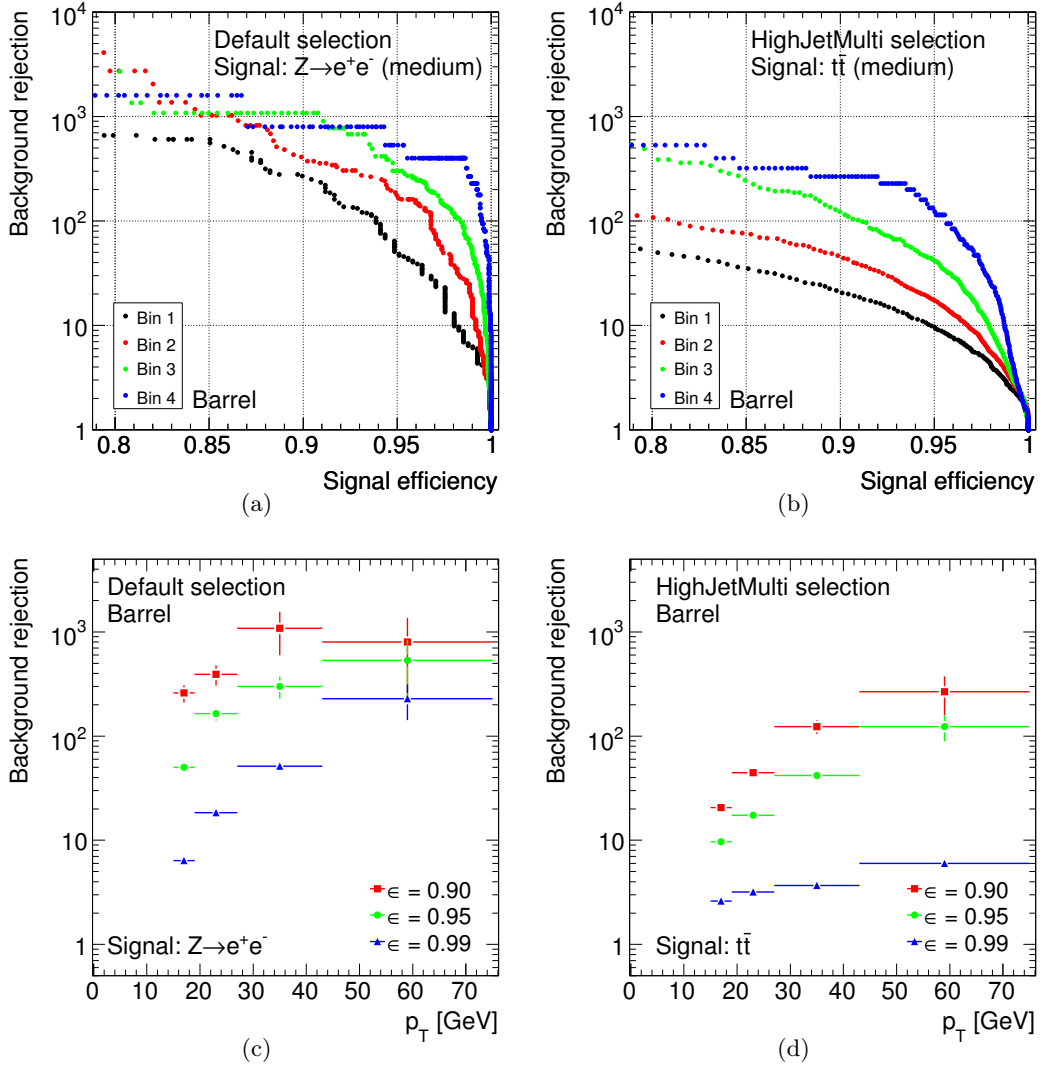


**Figure A.8:** Performance of the likelihood tool on signal electrons from the  $Z \rightarrow e^+e^-$  (a, c) and  $t\bar{t}$  (b, d) datasets (barrel region). Background electrons are selected from the  $t\bar{t}$  sample in all scans. The “default” variable set is used for signal electrons from  $Z \rightarrow e^+e^-$ , whereas the likelihood is trained with the “highJetMulti” variable set for signal electrons from  $t\bar{t}$ . The curves in (a) and (b) are given in bins of  $p_T^{\text{gen}}$  and  $\eta^{\text{gen}}$ . The corresponding  $p_T$  dependence of the background rejections at given signal selection efficiencies is shown in (c) and (d). The curves do not include the electron ID signal selection efficiencies and background rejections as listed in Tables 5.3 and 5.4. The corresponding curves obtained including these efficiencies are shown in Section 5.4 (Fig. 5.11). For the definition of the bins, see Table 5.2 in Section 5.1. Error bars are not displayed in (a) and (b) for the sake of clarity.

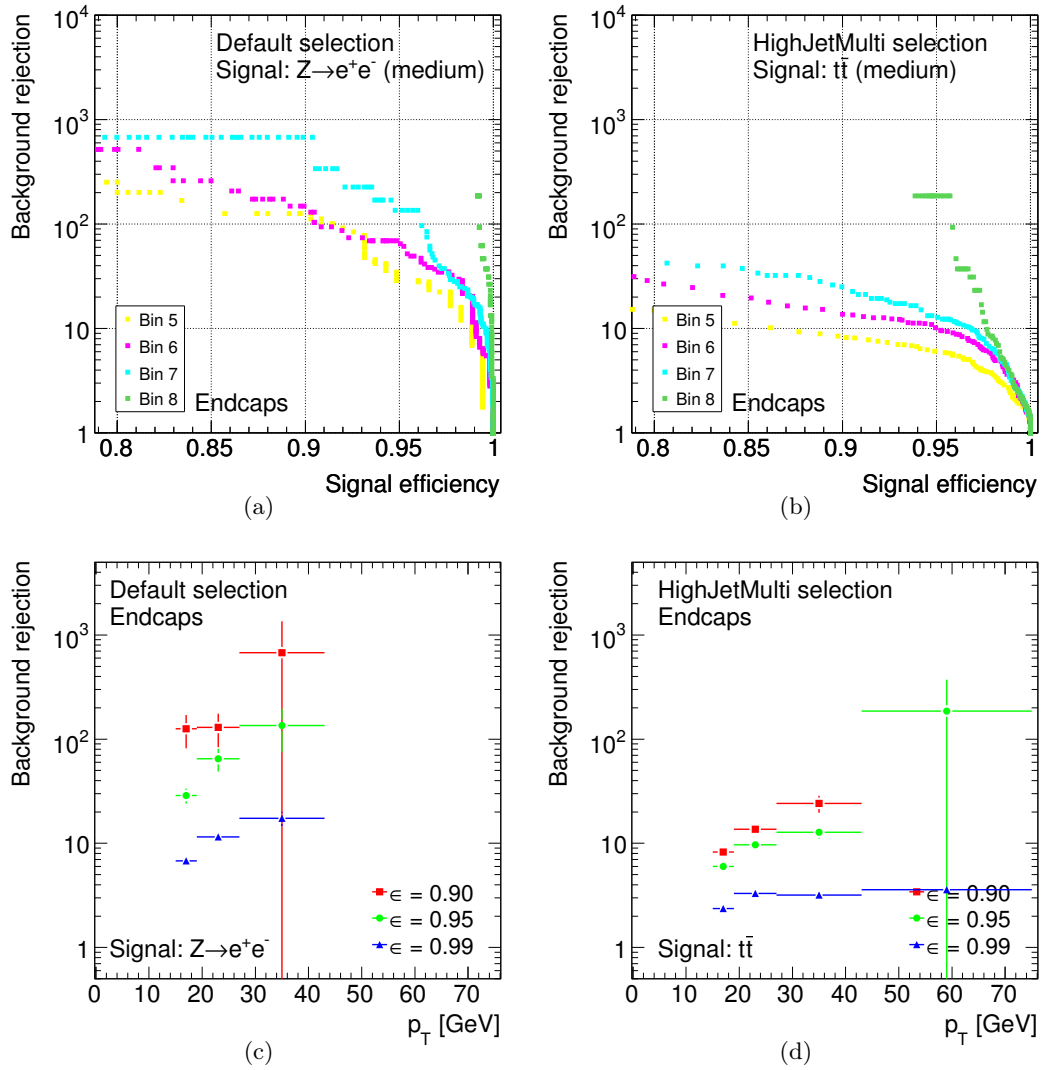


**Figure A.9:** The same as in Fig. A.10, but for the endcap regions of the ATLAS detector. The corresponding curves obtained including the electron ID efficiencies are shown in Section 5.4 (Fig. 5.12).

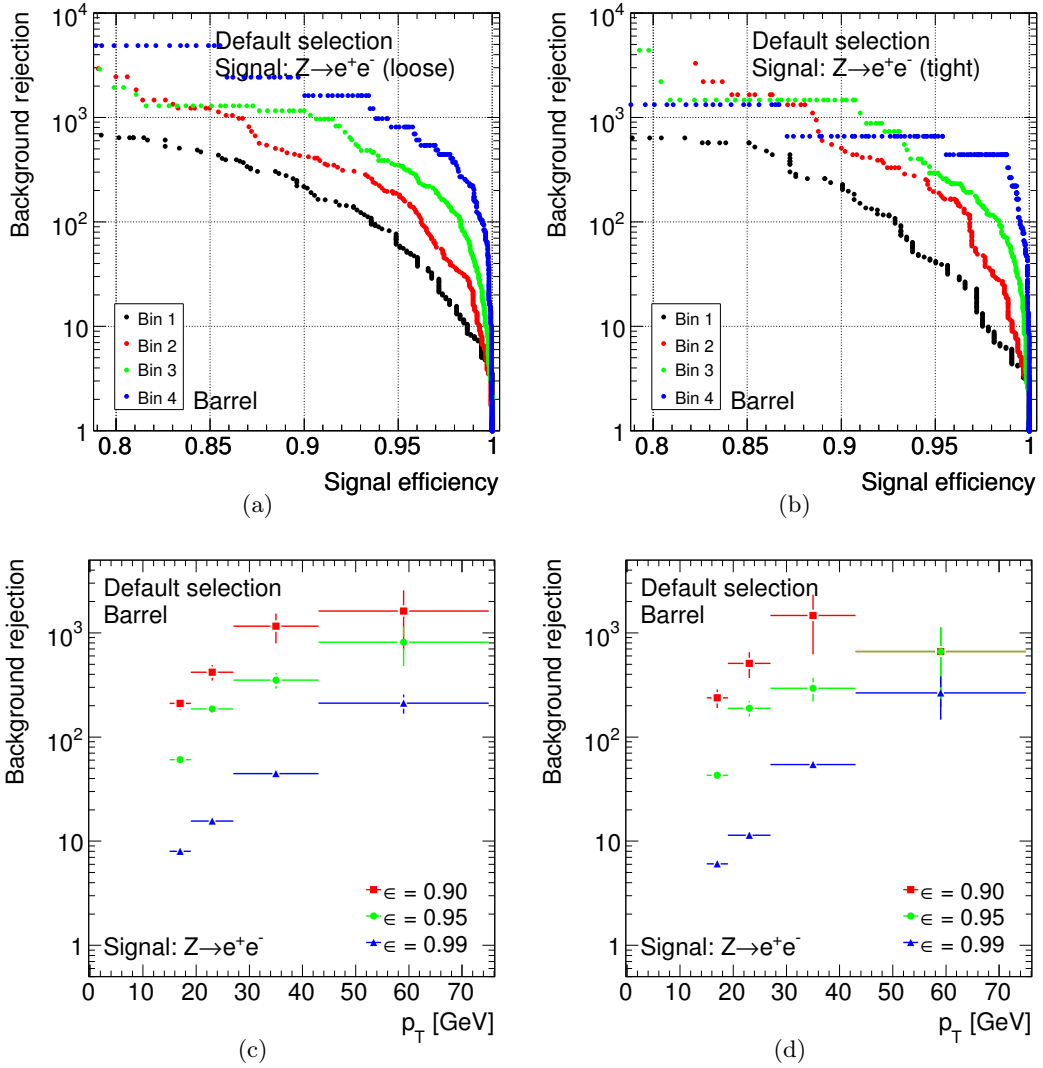


**Figure A.10:** Performance of the likelihood tool on “loose” (a, c) and “tight” signal electrons (b, d) from the  $Z \rightarrow e^+e^-$  dataset (barrel region). Background electrons are selected from the  $t\bar{t}$  sample. The curves in (a) and (b) are given in bins of  $p_T^{\text{gen}}$  and  $\eta^{\text{gen}}$ . The corresponding  $p_T$  dependence of the background rejections at given signal selection efficiencies is shown in (c) and (d). The curves do not include the electron ID signal selection efficiencies and background rejections as listed in Tables 5.3 and 5.4. The corresponding curves including these efficiencies are shown in Section 5.4 (Fig. 5.13). For the definition of the bins, see Table 5.2 in Section 5.1. Error bars are not displayed in (a) and (b) for the sake of clarity.

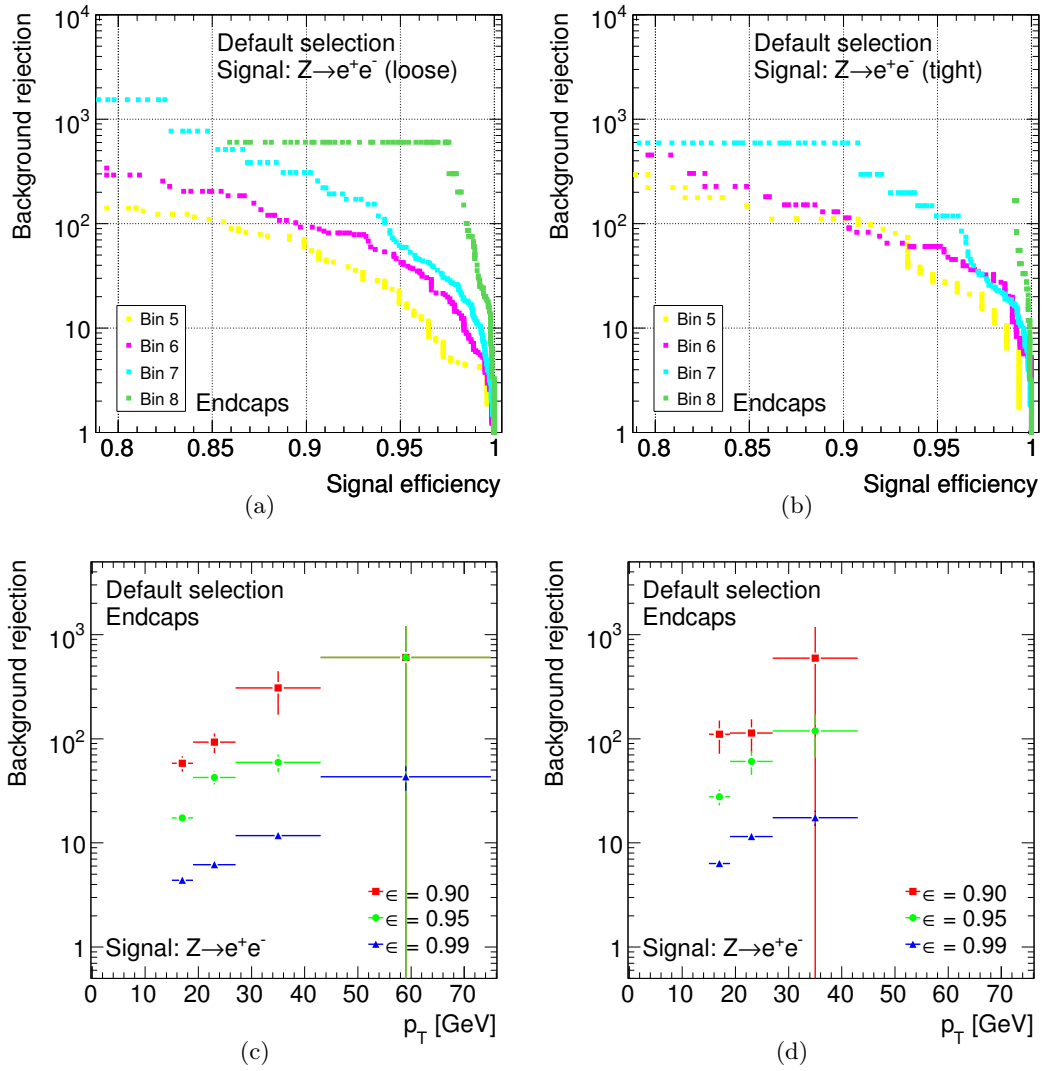


**Figure A.11:** The same as in Fig. A.10, but for the endcap regions of the ATLAS detector. The corresponding curves including the electron ID efficiencies are shown in Section 5.4 (Fig. 5.14).

## A.7 Choice of the training samples

Some improvement in the performance is expected, if the PDFs are produced from dedicated training samples that are obtained under the same conditions as the electrons to be tested. Figure A.12 shows a comparison of the performance curves for PDFs using either signal electrons from the  $Z \rightarrow e^+e^-$  or from the  $t\bar{t}$  dataset as training samples. In both cases, the test sample consists of signal electrons obtained from the  $t\bar{t}$  dataset. The gain is small in the case of the “highJetMulti” selection (Fig. A.12(a)), but a considerable improvement is observed if the “default” variable set is used (Fig. A.12(b)).

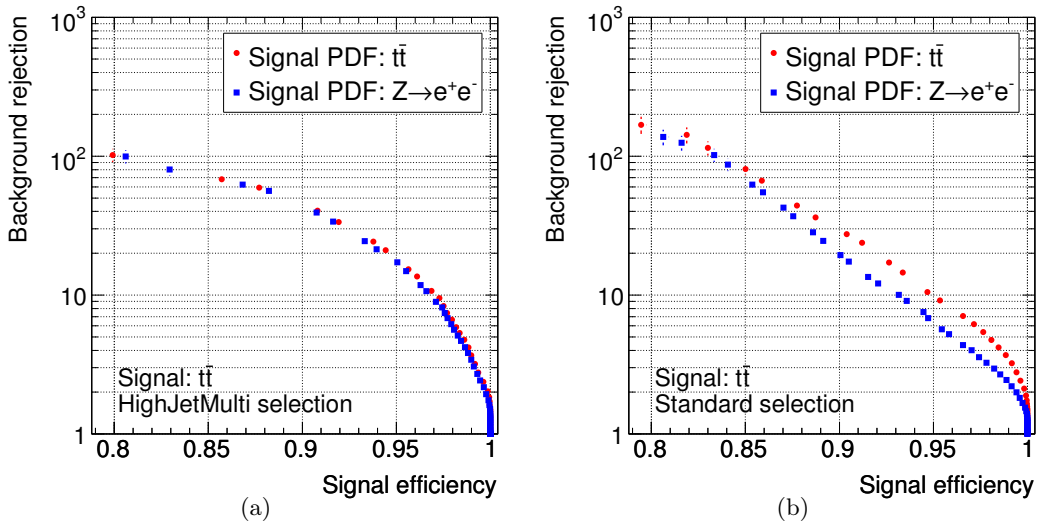


**Figure A.12:** Comparison of the performance curves obtained with PDFs determined either on a sample of signal electrons in the  $Z \rightarrow e^+e^-$  or in the  $t\bar{t}$  dataset. The signal electrons for the test sample are always selected from  $t\bar{t}$  events. The “highJetMulti” set of input variables is used in (a), whereas the “default” selection is used in (b). All curves are shown for the example bin  $19 \text{ GeV} < p_T^{\text{rec}} < 27 \text{ GeV}$ ,  $|\eta^{\text{rec}}| < 1.37$ .

Figure A.13 shows comparisons of the performance curves obtained on test samples of “loose” (Fig. A.13(a)) and “tight” (Fig. A.13(b)) electron candidates, obtained with PDFs determined from training samples either of “medium” or of electrons selected according to the same requirements as applied on the test electrons. No significant differences are observed in this case.

Therefore, PDFs are provided only obtained from training samples of “medium” electrons in  $Z \rightarrow e^+e^-$  events in the Athena implementation of the `IsolationLikelihood`, to be used also for analyses requiring “loose” or “tight” electron identification criteria. Furthermore, the difference in the case of signal electrons from the  $t\bar{t}$  sample is negligible, if the “highJetMulti” set of input variables is used, as is recommended for the case of high-activity signals. To minimize the complexity of the tool, the Athena implementation therefore does not offer a high jet multiplicity option for the training. In contrast,  $t\bar{t}$  events are used to train the likelihoods for the  $t\bar{t}H$ ,  $H \rightarrow W^+W^-$  analysis presented in Chapter 6 of this thesis.

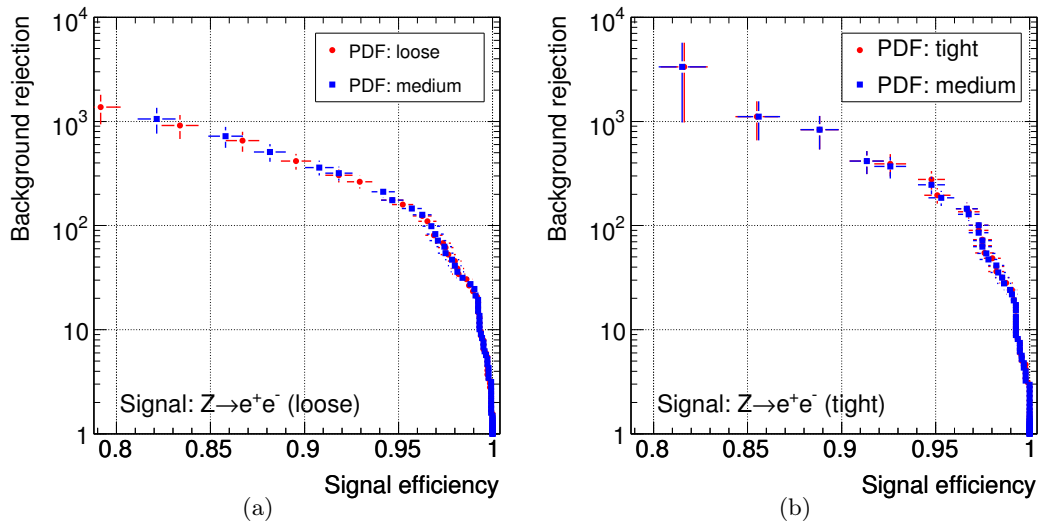


**Figure A.13:** Comparison of the performance curves obtained with PDFs determined either from the standard “medium” electron candidate sample or from samples of “loose” (a) / “tight” (b) electron candidates from the  $Z \rightarrow e^+e^-$  dataset. The signal electrons for the test sample are required to fulfil the “loose” (a) / “tight” (b) electron identification requirements. All curves are shown for the example bin  $19 \text{ GeV} < p_T^{\text{rec}} < 27 \text{ GeV}$ ,  $|\eta^{\text{rec}}| < 1.37$ .



## B Addendum on the $t\bar{t}H, H \rightarrow W^+W^-$ study

### B.1 Impact of the use of the `WZtoLeptonFilter` for the generation of the filtered $t\bar{t}$ dataset

Due to the lack of time in the course of the activities for the publication of Ref. [108], the production of the filtered dataset had to be done with the Athena code that was already in the official release at that time. The best suited code was the `WZtoLeptonFilter`, originally provided for the  $WH, H \rightarrow W^+W^-$  signal sample generation. This filter could be configured such that it selected events containing pairs of like-sign leptons fulfilling  $p_T < 13 \text{ GeV}$  and  $|\eta| < 2.6$ , but with a small reservation affecting events that contain three or more leptons: in fully leptonic  $t\bar{t}$  events, leptons other than those from the  $W$  boson decays were only considered for the like-sign check in the case the  $W$  boson decay candidates did not both fulfil  $p_T > 30 \text{ GeV}$  and  $|\eta| < 1.3$  or  $1.7 < |\eta| < 2$  in the case of electrons and  $p_T > 15 \text{ GeV}$  and  $|\eta| < 1.05$  or  $1.45 < |\eta| < 1.8$  in the case of muons. Re-running the filter on the unfiltered “no all-hadronic” and “all-hadronic”  $t\bar{t}$  samples showed that about 6% of all events (21% of all fully leptonic events) passing a like-sign filter are lost by this extra condition. The effect of this selection on the  $p_T$  and  $\eta$  distributions of the leptons from  $W$  boson decays can clearly be spotted for the example of electrons in Fig. B.1, which shows that the lost events tend to contain leptons with larger transverse momenta and more central leptons than the events passing the filter.

Nevertheless, the effect of this criterion on the events that are relevant for the two lepton analysis is negligible. Except for lepton charge mismeasurement candidates, which need to be estimated separately in any case, fully leptonic  $t\bar{t}$  events hardly contribute to the accepted sample. This is ensured on the one hand by the jet multiplicity, which is lower in fully leptonic events than in semi-leptonic ones (see Fig. B.2), such that about 16% of the semi-leptonic  $t\bar{t}$  events contain six or more jets compared with less than 3.5% of the fully leptonic ones. Further reduction of the fully leptonic contribution to the overall result is guaranteed by the veto on a third isolated lepton. If only the lepton selection criteria are applied to the unfiltered “no all-hadronic”  $t\bar{t}$  dataset, but no requirements on the number of jets for the sake of better statistical reliability, roughly 15% of all events passing the lepton cuts because of a semi-leptonic heavy quark decay are fully leptonic ones. On the level of the few events out of the pre-filtered dataset that pass the complete event selection, no contribution from fully leptonic events is expected, even if this overestimated ratio is assumed. The bias due to the extra conditions of the `WZtoLeptonFilter` can therefore safely be considered as fully covered by the large statistical uncertainty of the result and hence be neglected.

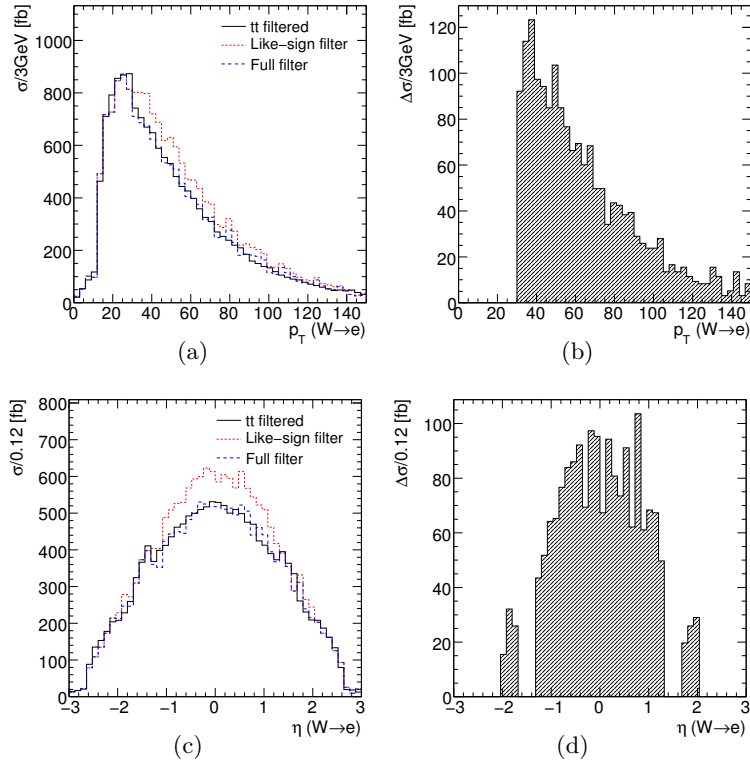


**Figure B.1:** Influence of the “WZToLeptonFilter”-bias on the  $t\bar{t}$  like-sign lepton filter:  $p_T$  (a) and  $\eta$  distributions (c) of the electrons (the distributions for muons look similar) from  $W$  boson decays in the pre-filtered  $t\bar{t}$  dataset (“ $t\bar{t}$  filtered”), together with the impact of a like-sign (“Like-sign filter”) and the WZToLeptonFilter (“Full filter”) on the full  $t\bar{t}$  datasets. (b, d) Distribution of the events that pass the like-sign filter, but are rejected by the WZToLeptonFilter.

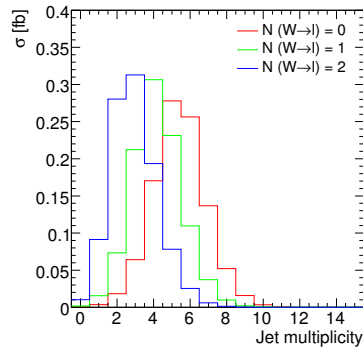


**Figure B.2:** Number of good jets (including  $p_T$ -cuts) for fully hadronic, semi-leptonic and fully leptonic  $t\bar{t}$  events. All distributions are normalized to unity.

## B.2 Calculation of results obtained with MC@NLO datasets

Events produced with MC@NLO are generated with positive and negative weights (see Section 2.3.1). These weights always have to be taken into account, if physical observables (e.g. cross sections, transverse momentum distributions, invariant masses) are to be calculated. They can be neglected, if geometric or reconstruction-related properties are to be determined (e.g. acceptances, object-level selection efficiencies). In the following, a summary is given of the mathematical treatment of MC@NLO event weights in this thesis.

### B.2.1 Cross sections

The expectation of the accepted cross section  $\sigma^{\text{acc}}$  for  $n_{\pm}$  events with weight  $+1/-1$  passing all selection cuts is calculated according to

$$\sigma^{\text{acc}} = \sigma^{\text{ev}} \cdot (n_+ - n_-) \quad . \quad (\text{B.1})$$

The corresponding statistical error is

$$\delta\sigma^{\text{acc}} = \sigma^{\text{ev}} \cdot \sqrt{n_+ + n_-} \quad . \quad (\text{B.2})$$

Since physics forbids negative cross section values, the uncertainty is limited from below by the cross section value itself. Therefore, asymmetric errors are given in the case  $\delta\sigma^{\text{acc}} > \sigma^{\text{acc}}$ .

The per-event cross section  $\sigma^{\text{ev}}$  is determined as

$$\sigma^{\text{ev}} = \frac{\sigma^{\text{in}}}{n_+^0 - n_-^0} \quad (\text{B.3})$$

from the nominal input cross section  $\sigma^{\text{in}}$  for the dataset, consisting of  $n_+^0$  events with positive and  $n_-^0$  events with negative weight.

### B.2.2 Efficiencies

Efficiencies obtained from a MC@NLO dataset are calculated as

$$\epsilon = \frac{n_+ - n_-}{n_+^0 - n_-^0} \quad . \quad (\text{B.4})$$

The expression can be re-written in terms of the efficiencies  $\epsilon_+$  and  $\epsilon_-$  obtained individually in the positive and negative weight samples as

$$\epsilon = \frac{n_+^0 \epsilon_+ - n_-^0 \epsilon_-}{n_+^0 - n_-^0} \quad . \quad (\text{B.5})$$

With propagation of the errors one then obtains

$$\delta\epsilon = \frac{\sqrt{n_+(1-\epsilon_+) + n_-(1-\epsilon_-)}}{n_+^0 - n_-^0} \quad (\text{B.6})$$

as the uncertainty on  $\epsilon$ , if  $\epsilon_+$  and  $\epsilon_-$  are not too close to zero or one. The numbers in this thesis are obtained with this approximation although the efficiencies are sometimes low. In such cases it is ensured that the influence on the error of the final result is small, such that the calculation of asymmetric errors is unnecessary.

### B.2.3 Limits

The difference of two Poisson distributed random variables with expectation values  $m_1$  and  $m_2$  follows the Skellam distribution [138]. It gives the probability to observe a difference of  $n$  as

$$P(n|m_1, m_2) = e^{-(m_1+m_2)} \cdot \left(\frac{m_1}{m_2}\right)^{\frac{n}{2}} \cdot I_n(2\sqrt{m_1 m_2}) \quad . \quad (\text{B.7})$$

Here,  $I_n$  denotes the  $n$ th order modified Bessel function. The expectation value of  $P(n|m_1, m_2)$  is  $m = m_1 - m_2$  and can take negative values. The variance of the distribution is  $\sigma^2 = m_1 + m_2$ .

To obtain a confidence limit on the parameters  $m_1$  and  $m_2$  from a measurement, their ratio

$$r \equiv \frac{m_2}{m_1} \quad (\text{B.8})$$

needs to be known. Then, Eq. (B.7) can be rewritten as

$$P(n|m_1, r) = e^{-m_1(1+r)} \cdot \left(\frac{1}{r}\right)^{\frac{n}{2}} \cdot I_n(2m_1\sqrt{r}) \quad . \quad (\text{B.9})$$

If a difference of  $n = n_1 - n_2$  events is observed, the 95% upper limit on the expectation value  $m_1$  is given by the value  $m_1^{95}$ , for which

$$1 - 0.95 = \sum_{n'=-\infty}^n P(n'|m_1^{95}, r) \quad (\text{B.10})$$

is fulfilled.

Figure B.3 shows the dependence of the limit on the non-isolated lepton contribution of the  $t\bar{t}$  background as a function of the expectation value  $n$  for the three analyses described in Sections 6.4 and 6.5. The observed ratio of events with negative and positive weights is used as an estimate for the expected ratio  $r$ . The 95% confidence limits  $m^{95}$  on the expected difference

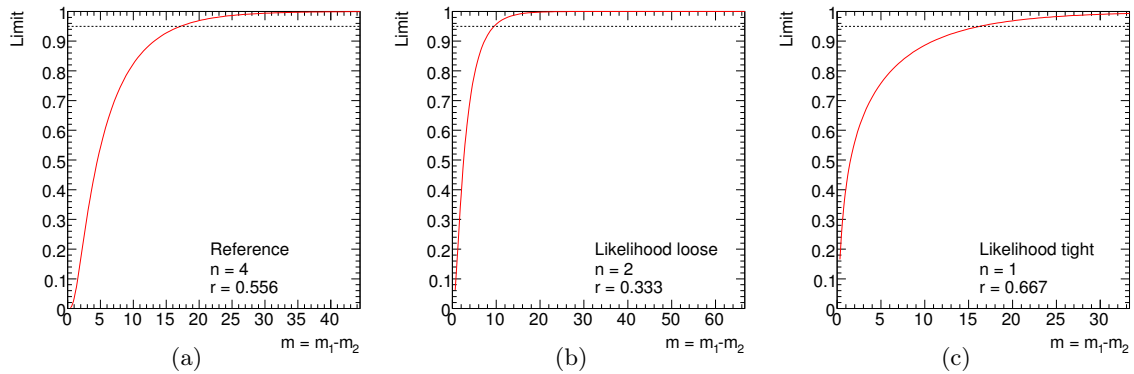


**Figure B.3:** Limits as a function of the expectation value  $m$  for the “reference” (a), “likelihood loose” (b) and “likelihood tight” (c) analyses. The dashed line marks the 95% limit.

$m$  can be read from the curves. The resulting limits  $m^{95}$  and the corresponding cross sections are summarized in Table B.1. Figure B.4 shows the estimated probability density  $P(n|m_1^{95}, r)$  for the three analyses, if the 95% confidence limit is used as the expectation value  $m$ . For the “reference” analysis, a limit of about 1.547 fb is obtained. The result is similar in the case of the “likelihood tight” analysis with 1.474 fb. In the case of the “likelihood loose” analysis,

where the observed  $r$  is smallest, the cross section is predicted to be no larger than 0.865 fb at the 95% confidence level. This shows the strong sensitivity of the limits on the input value of  $r$ , which is very poorly estimated by the observed value because it suffers from a large statistical error. For this reason, giving limits on the accepted  $t\bar{t}$  cross sections is abstained from.

	“Reference”	“Likelihood loose”	“Likelihood tight”
Observed $n$	4	2	1
Observed $r$	$\frac{5}{9}$	$\frac{2}{4}$	$\frac{2}{3}$
$m^{95}$	17	9.5	16.2
$\sigma_{t\bar{t}}^{\text{ni}, 95}$ [fb]	1.547	1.474	0.865
$m_{\text{Poisson}}^{95}$	9.15	6.30	4.74
$\sigma_{t\bar{t}, \text{Poisson}}^{\text{ni}, 95}$ [fb]	8.3	5.7	4.3

**Table B.1:** Summary of the estimation of 95% limits on  $\sigma_{t\bar{t}}^{\text{ni}}$ . The observed  $n$  and  $r$  give the weighted number of Monte Carlo events and the respective ratio of events with negative and positive weight accepted by the three analyses. Using the observed ratio as an estimate for the true ratio  $r$ , the 95% limits  $m^{95}$  on the expected difference and  $\sigma_{t\bar{t}}^{\text{ni}, 95}$  on the expectation for the accepted cross section for  $t\bar{t}$  events with leptons from semi-leptonic heavy quark decays are obtained with the procedure described in the text. For comparison, the corresponding Poisson limits are given, which are obtained from the net number of accepted events.

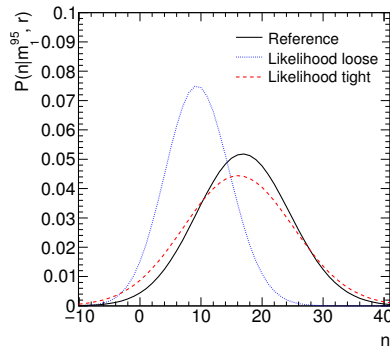


**Figure B.4:** Probability distributions  $P(n|m_1^{95}, r)$  for the three analyses, obtained with the estimated  $r$  values and 95% limits on the expectation values for  $m$  given in Table B.1.

### B.3 Event selection and background cross sections in the published study

A study of the signal and background conditions in the  $t\bar{t}H, H \rightarrow W^+W^-$  channel was published in the course of this thesis in collaboration with the Marseille/Beijing ATLAS group [108]. This analysis served as a starting point for the study presented here. The result of this study in the two lepton final state was an accepted signal of  $(1.85 \pm 0.03)$  fb at a signal-to-background ratio smaller than 0.2 for  $M_H = 160$  GeV and the dominant background contribution being  $t\bar{t}$ . Table B.2 shows the published accepted cross sections for the signal and the considered backgrounds.

Sample	$\sigma_{Total} \cdot BR$	Basic sel.	Calo iso.	Track iso.	Cone iso.	Like-sign	Z-veto	$p_T^\mu$
$t\bar{t}H$ ( $2L^{truth}$ , 120 GeV)	3.9	1.05	0.80	0.65	0.52	0.52	0.51	$0.45 \pm 0.01$
$t\bar{t}H$ ( $2L^{truth}$ , 160 GeV)	11.1	4.01	3.02	2.57	2.09	2.09	2.04	$1.85 \pm 0.03$
$t\bar{t}H$ ( $2L^{truth}$ , 200 GeV)	4.7	1.83	1.43	1.24	1.05	1.04	1.02	$0.95 \pm 0.01$
$t\bar{t}b\bar{b}$ (EW)	259.0	15.8	4.1	0.9	0.3	0.2	0.2	$0.11 \pm 0.07$
$t\bar{t}b\bar{b}$	2360.	177.	31.7	6.3	1.8	0.9	0.9	$0.5 \pm 0.2$
$t\bar{t}$	833000.	6170.	1970.	870.	500.	16.0	16.0	$7.4 \pm 1.1$
$t\bar{t}t\bar{t}$	2.68	0.65	0.33	0.26	0.20	0.07	0.07	$0.06 \pm 0.00$
$t\bar{t}W + 0j$	61.1	1.17	0.46	0.30	0.19	0.10	0.10	$0.09 \pm 0.01$
$t\bar{t}W + 1j$	50.5	2.09	0.93	0.66	0.48	0.23	0.23	$0.21 \pm 0.02$
$t\bar{t}W + \geq 2j$	76.9	8.6	4.9	4.1	3.3	1.58	1.54	$1.40 \pm 0.05$
$t\bar{t}Z$	110.	25.7	20.5	18.1	13.7	1.6	1.2	$1.14 \pm 0.07$
$Wb\bar{b}$	66721.	1.6	0.14	-	-	-	-	-
<b>Total background</b>								$10.3 \pm 1.1$

**Table B.2:** Cut flow and expected cross sections [fb] for the  $t\bar{t}H$  ( $2L$ ) analysis. The errors presented are statistical only. Some backgrounds, such as  $W$ +jets,  $b\bar{b}$  and  $t\bar{t}jj$  have not been included. The table is copied from Ref. [108]; ‘‘Calo iso.’’, ‘‘Track iso.’’ and ‘‘Cone iso.’’ refer to the cuts on  $E_T^{\text{cone}}(0.2)$ ,  $p_T^{\text{max trk}}(0.2)$  and  $\Delta R_{\text{min}}^{\text{jet}}$ , respectively.

The most important differences in the event selection and prediction of the accepted background cross sections between the published study and the contents of this thesis will be summarized in the following:

- **Minimum transverse momentum for jets**

The published analysis required six jets with a minimum transverse momentum of 15 GeV. This threshold is raised to 20 GeV for the present analysis, since the higher cut value reduces the contamination by pile-up jets drastically, as is shown in Section 6.8. In addition, it brings along some safety for the use of the ALPGEN  $t\bar{t}W$  background dataset, which is produced with a minimum parton level jet  $p_T$  of 15 GeV.

- **$b$ -tagging**

No  $b$ -tagging was applied in the published analysis. This requirement, together with the demand for 20 GeV jets, is the main cause for the reduction of the accepted signal cross section by more than a factor of two compared with the published results. On the other hand, it downsizes the importance of  $t\bar{t}$  as a source of background.

- **Muon  $p_T$  requirement**

A cut on  $p_T > 20$  GeV was introduced for muons, because after application of the  $E_T^{\text{cone}}(0.2)$  and  $p_T^{\text{max trk}}(0.2)$  requirements it turned out that the suppression of the muon background from semi-leptonic heavy quark decays was much lower than that of the electron background. Since the transverse momenta of background leptons tend to be much lower than those of leptons from  $W$  boson decays, the minimum  $p_T$  requirement helps to reduce the background. The extra muon  $p_T$  cut is applied as the last step in the

event selection and is not taken into account by the requirements on the event topology and kinematics executed before.

- **Track selection for the calculation of track isolation variables**

The requirements tracks had to fulfil to be included in the calculation of the track isolation variables were: a minimum angular distance of  $\Delta R = 0.01$  from the lepton candidate,  $IP_T < 2$  mm and  $IP_L < 1.5$  mm for the impact parameters and a minimum of four hits in the SCT and Pixel Detectors, of which at least one had to be measured in the Pixel Detector. These requirements were stricter than those used for this study (see Section 5.2) and thus the tracker isolation cut on  $p_T^{\text{max trk}}(0.2) < 2$  GeV was less effective than it is in the present analysis.

- **Electron/jet ambiguities and angular electron/jet separation**

The electron/jet ambiguity removal was done in one step together with the requirement of a minimum separation of the electron from the closest jet: Electrons passing the identification requirements, with no further isolation requirements, were considered further only if they matched either  $\Delta R_{\text{min}}^{\text{jet}} > 0.2$  or  $\Delta R_{\text{min}}^{\text{jet}} < 0.1$  and  $E_{\text{ele}}/E_{\text{jet}} > 0.65$ . Jets closer than  $\Delta R_{\text{min}}^{\text{jet}} = 0.2$  to such an electron candidate were removed from the jet sample. Electrons that did not satisfy these criteria were discarded, whereas the corresponding jet was kept.

- **Treatment of duplicate electron clusters**

Electrons that were mistakenly reconstructed twice by the clustering algorithm were not rejected. This results in two different near-by electron candidates with almost identical transverse momenta. If such candidates are well isolated, they constitute a good like-sign lepton pair candidate and hence contribute especially to the reducible  $t\bar{t}$  background. The  $t\bar{t}$  background in the published study is dominated by real leptons from semi-leptonic heavy quark decays. Therefore, this effect did not significantly influence the resulting accepted cross sections, but becomes a serious contribution if this source of  $t\bar{t}$  background is further suppressed.

- **Correction of the bias due to the use of the filtered  $t\bar{t}$  dataset**

To compensate the loss of  $t\bar{t}$  events due to the use of the filtered dataset, another  $(15 \pm 10)\%$  were added to the accepted cross sections determined from the filtered sample. This number was obtained by the Marseille/Beijing group from a comparison of the filtered and standard sample at the level of the requirement of exactly two well isolated like-sign leptons in the event selection of the published analysis. It must be assumed that this comparison suffered from the too small size of the “no all-hadronic”  $t\bar{t}$  dataset. The necessary correction for the loss of events with charge mismeasurement and “fake” leptons (see Sections 6.5.1 and 6.5.2 of this thesis) was therefore probably underestimated.

- **Signal normalization**

All accepted signal cross section were normalized to the NLO cross section values and Higgs boson decay branching ratios given in Ref. [119].

- **$t\bar{t}Z$  cross section**

The NLO calculation from Ref. [46] was used to scale the accepted cross sections, which is somewhat smaller than the LO generator value that is used in this thesis (see Section 6.3.3).

- **$Wb\bar{b}$  background**

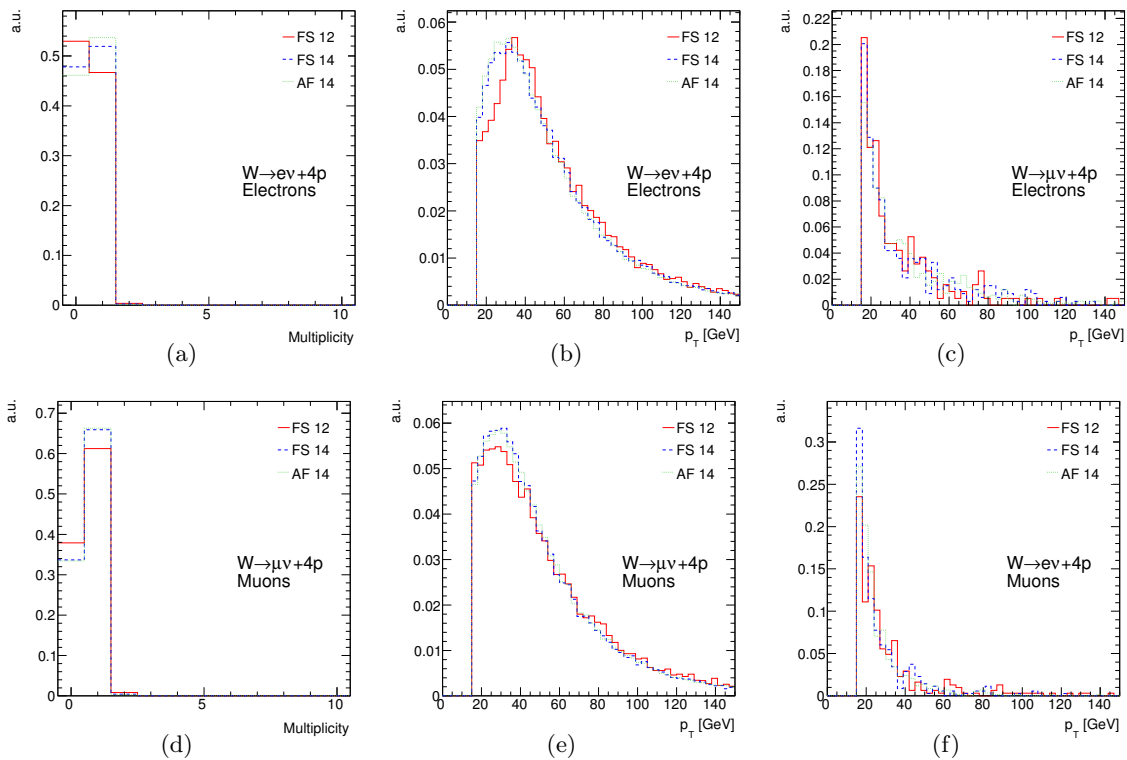
The  $Wb\bar{b}$  background was estimated with the help of a ALPGEN dataset, which was customly produced for the  $t\bar{t}H, H \rightarrow W^+W^-$  analysis with the same generator level filter as the pre-filtered  $t\bar{t}$  dataset. Apart from the still too small size of the sample, it was generated with the  $Wb\bar{b} +0p$  inclusive generator setting, i.e. without the treatment of the production of additional light jets in the matrix element calculation. This probably causes a serious underestimation of the high jet multiplicity contribution to  $Wb\bar{b}$ .

## B.4 Details on the estimation of the $W$ +jet background contribution

### B.4.1 Comparison of the lepton and jet $p_T$ spectra in the 10 TeV and 14 TeV datasets

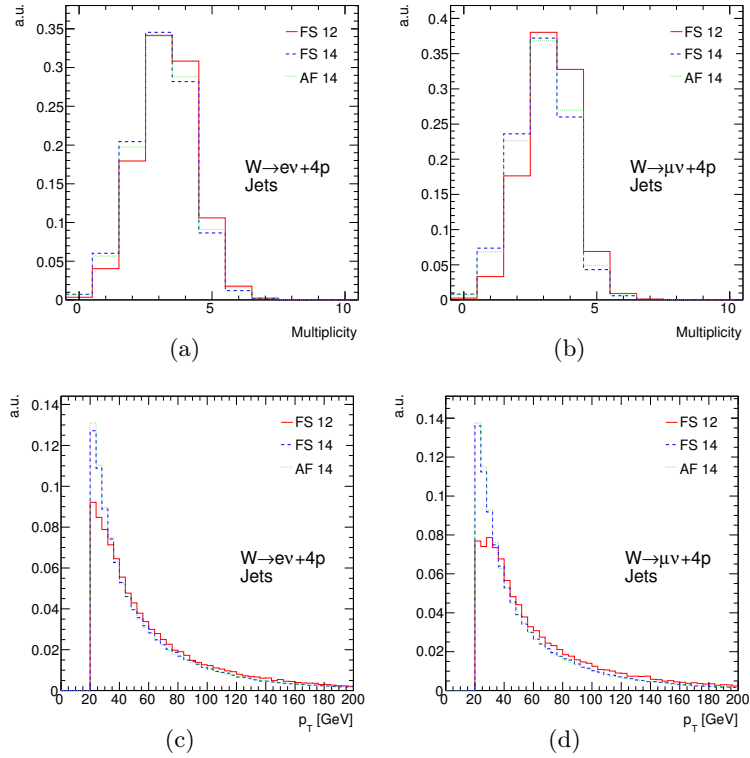
In addition to the lepton multiplicities and transverse momentum spectra in the  $W$ +jet datasets with the maximum number of five additional matrix element partons shown in Fig. 6.16 in Section 6.6.1, Fig. B.5 shows the corresponding distributions in the four parton datasets. While in the five parton samples no significant deviations occur in the  $p_T$  spectra, the maxima of the distributions are shifted with respect to each other in the four parton samples. This indicates that in the samples with lower number of additional jets the lepton selection efficiency is not only influenced by the changes in the identification criteria, but also by the acceptance of the kinematic cuts. The samples with four or fewer extra partons, however, provide a much smaller contribution to the total  $W$ +jet background than the five parton datasets and therefore, these deviations in the shape are not corrected for in the analysis.

Figure B.6 shows the jet multiplicity and  $p_T$  distributions of jets in the  $W \rightarrow e\nu + 4p$ ,  $W \rightarrow \mu\nu$



**Figure B.5:** Comparison of the multiplicity (a) and transverse momentum distribution (b) of electron candidates in the  $W \rightarrow e\nu + 4p$  samples and transverse momentum distribution of electrons in the  $W \rightarrow \mu\nu + 4p$  samples (c, background electrons). Multiplicity (d) and transverse momentum distribution (e) of muon candidates in the  $W \rightarrow \mu\nu + 4p$  samples and transverse momentum distribution of muons in the  $W \rightarrow e\nu + 4p$  samples (f, background muons). The samples produced with the full detector simulation are denoted “FS12” and “FS14” for Athena release 12 and 14, respectively. The release 14 ATLFAS-II samples are denoted “AF14”. Only the lepton identification and acceptance cuts, but no event selection criteria, are applied to the lepton candidates. All distributions are normalized to unity.

+4p and  $Wb\bar{b}+2p$  samples. The increase of the deviations of the transverse jet momenta becomes obvious, if compared with the corresponding distributions in the five parton samples shown in Fig. 6.17 in Section 6.6.1. Nevertheless, since the result is dominated by the five parton contributions and the deviations in the shapes are irrelevant compared with the large generator uncertainties mentioned above, no PDF reweighting is applied to correct the shapes for the analysis.



**Figure B.6:** Comparison of jet multiplicities and  $p_T$  distributions in release 12 and 14 full simulation (denoted “FS12” and “FS14”) and release 14 ATLFast-II (“AF14”) in the  $W \rightarrow e\nu + 4p$  (a, d) and  $W \rightarrow \mu\nu + 4p$  (b, e) datasets. Only jets passing the acceptance cuts are taken into account and no event selection criteria are required. All distributions are normalized to unity.

Significant differences between the releases can also be observed if not the total  $p_T$  spectra are considered, but the spectra are compared separately for the first six jets ordered in  $p_T$ , as shown in Fig. B.7 for the  $W \rightarrow \mu\nu + 5p$  and  $Wb\bar{b} + 3p$  datasets. The largest difference is visible in the  $p_T$  distribution of the first jet and affects the position of the maximum of the distribution. The shift of the maximum is, however, safely above the jet  $p_T$  threshold in both cases and therefore is not expected to influence the jet selection efficiency significantly.

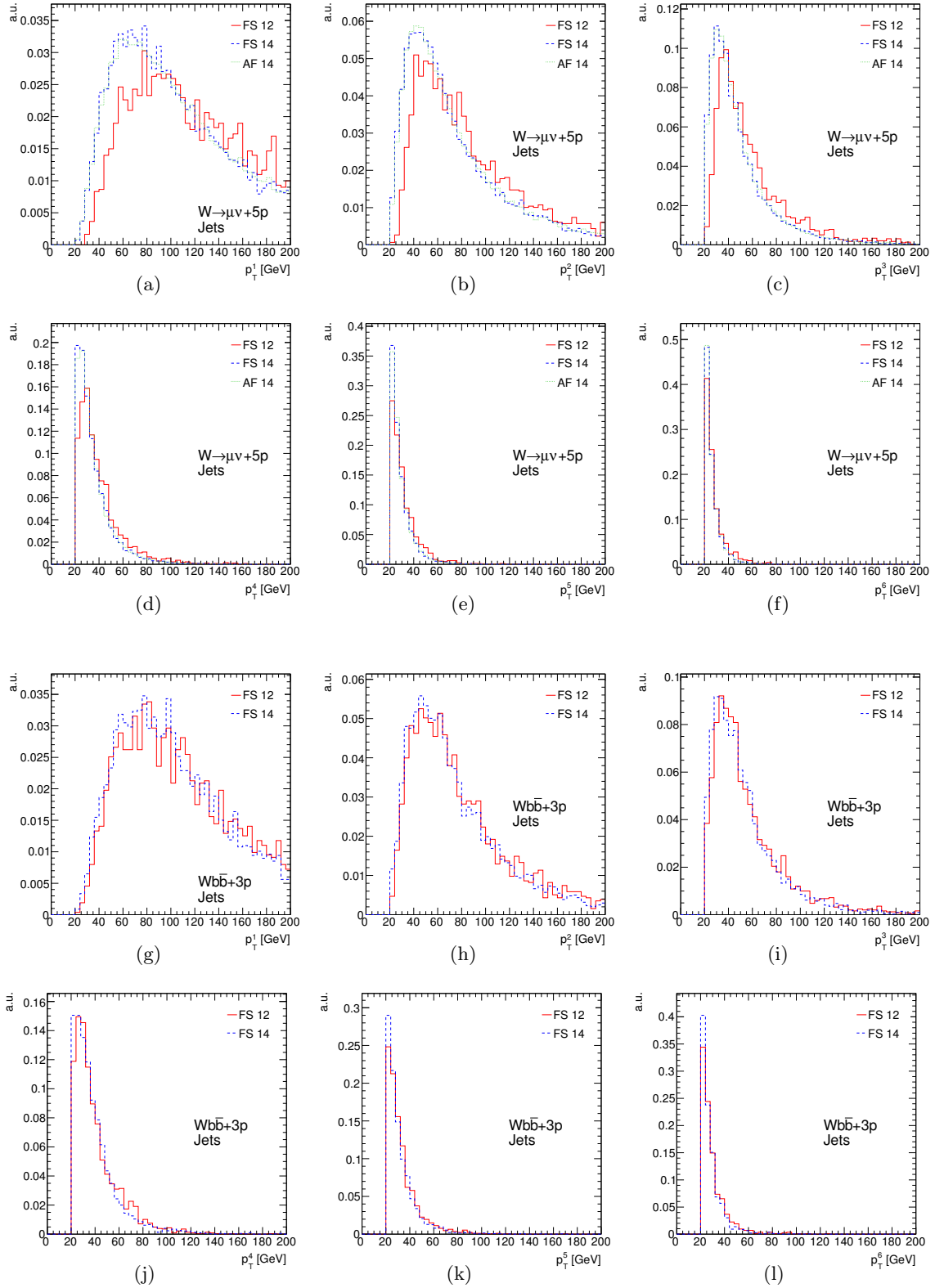


**Figure B.7:** Comparison of the transverse momentum distributions, separately for the first six jets, ordered in  $p_T$ , in release 12 and 14 full simulation (denoted “FS12” and “FS14”) and release 14 ATLFAS-II (“AF14”) in the  $W \rightarrow \mu\nu + 5p$  (a - f) and  $Wb\bar{b} + 3p$  (g - l) datasets. Only jets passing the acceptance cuts are taken into account and no event selection criteria are imposed. All distributions are normalized to unity.

### B.4.2 Differences in the Athena release 12 and 14 object reconstruction and event selection for the release 14 analysis

Since there have been some changes in the reconstruction of physics objects, there are large differences in the shapes of the isolation variables (see Fig. B.8), notably in  $E_T^{\text{cone}}(0.2)$  of the muons, where the subtraction of the muon energy deposition is treated differently. Also the distribution of the  $b$ -tag weights for the jets, which is shown in Fig. B.9, changed from one release to the other. The comparison of full and fast simulation in Athena 14, on the other hand, shows very good agreement in all properties.

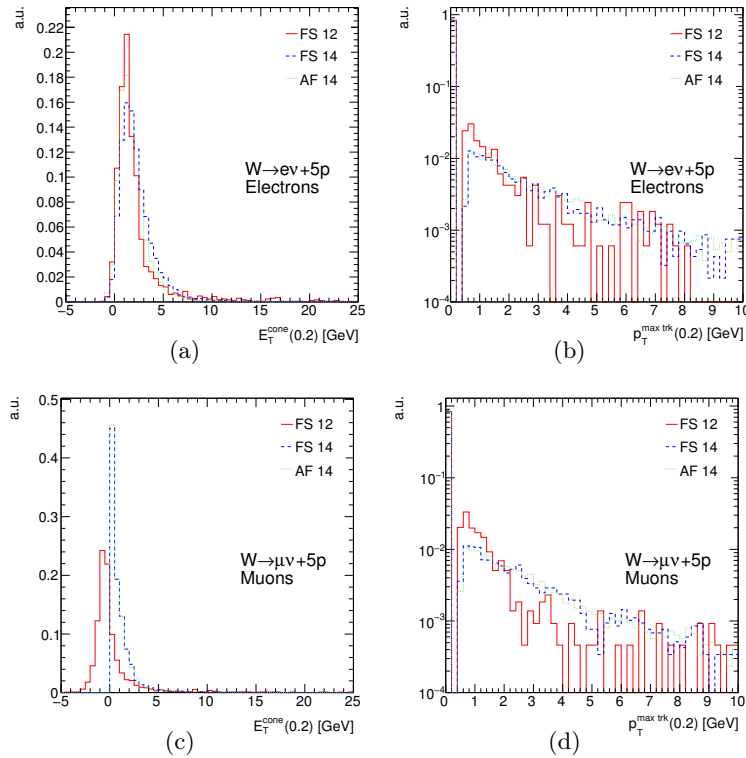


**Figure B.8:** Comparison of the distributions of the lepton isolation variables in full detector simulation in Athena release 12 (“FS12”) and 14 (“FS14”) and in ATLFAST-II (“AF14”). Shown are  $E_T^{\text{cone}}(0.2)$  for electrons (a) and muons (c) and  $p_T^{\text{max trk}}(0.2)$  for electrons (b) and muons (d). All distributions are obtained for leptons matched to the decays of  $W$  bosons on generator level and are normalized to unity. No event selection criteria are applied.

To account for the changes in the shapes of the cut variables, the cuts on the  $E_T^{\text{cone}}(0.2)$  and  $p_T^{\text{max trk}}(0.2)$  variables are adapted such, that the lepton level selection efficiencies for leptons from  $W$  boson decays in the release 12 and 14  $W \rightarrow e\nu + 5p$  and  $W \rightarrow \mu\nu + 5p$  samples are the same. The isolation cuts are not adapted to correct also the losses in the efficiency of the lepton identification criteria. Hence, despite the changes in the cuts on the isolation variables, the resulting total lepton level selection efficiencies are different<sup>1</sup>. In analogy to the procedure for the lepton isolation cuts, the value for the cut on the  $b$ -jet weight is chosen such that the tagging efficiency for true  $b$ -jets is the same in a mixture of the  $W \rightarrow e\nu + 5p$  and  $W \rightarrow \mu\nu + 5p$  samples in Athena 12 and 14. Lacking  $t\bar{t}H, H \rightarrow W^+W^-$  signal samples produced with release 14, this procedure is the best possible approximation to the optimal adaption

<sup>1</sup>A correction for agreement of the total lepton selection efficiency would require to relax the isolation cuts, which can cause uncontrollable loss in background rejection by several orders of magnitude.

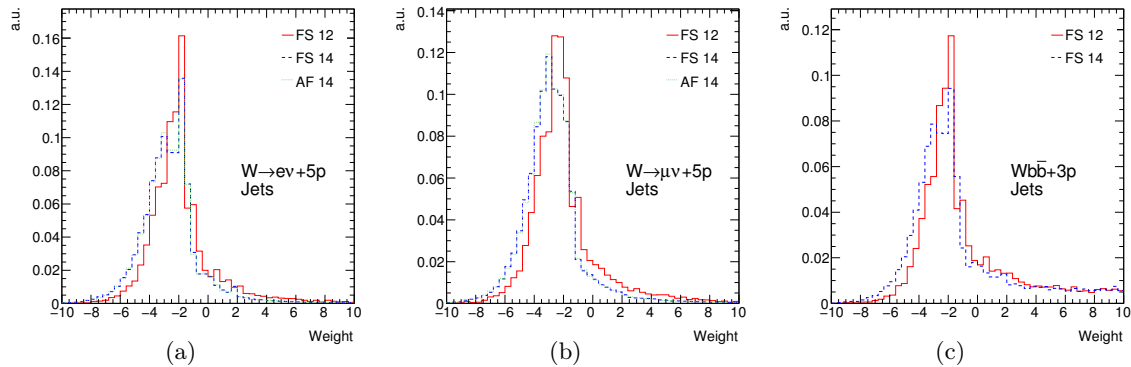


**Figure B.9:** Comparison of the jet weight distributions as obtained with full detector simulation in release 12 (“FS12”) and 14 (“FS14”) and with the fast simulation ATLFASST-II in release 14 (“AF14”) in the  $W \rightarrow e\nu + 5p$  (a),  $W \rightarrow \mu\nu + 5p$  (b) and  $Wb\bar{b} + 3p$  (c) samples. All distributions are normalized to unity. No event selection criteria are applied.

of the cuts, which would be to adapt the cut values for equal  $t\bar{t}H$ ,  $H \rightarrow W^+W^-$  signal event selection efficiency in the two releases<sup>2</sup>. By the approach chosen for this analysis, the signal selection efficiency differs by a few per cent due to the different lepton identification efficiencies and the arbitrary choice of a dataset to obtain the values of the isolation cuts from. A difference of this order of magnitude can be accepted, keeping in mind that this analysis is only meant to give a rough estimate of the  $W$ +jet background. Given a reasonable background suppression can be achieved in release 14 with the selection criteria used for this study of the release 14 samples, a possible signal loss of this order of magnitude decreases the signal significance a bit, but does not prevent the observation of  $t\bar{t}H$ ,  $H \rightarrow W^+W^-$ . Furthermore, as the application of the electron identification criteria in more recent releases of Athena than version 12 is accompanied by an increased background suppression rate (see e.g. a comparison of the numbers given in Refs. [107, 139]), an analysis completely performed on samples reconstructed with a more recent software release can afford to operate at a higher signal selection efficiency with the background still being under control, such that a possible signal loss can be compensated simply by a relaxation of the event selection cuts.

The dependence of the lepton selection efficiencies for the two isolation variables and the angular distance of the leptons from their closest jets as a function of the cut value for the two releases is compared in Fig. B.10. No significant difference between release 12 and 14 can be observed for the latter variable, such that the release 12 cut value can be kept for the release 14 analysis. Figure B.11 shows the selection efficiencies for  $b$ -,  $c$ - and light jets as a function of the value for the cut on the  $b$ -tag weights in release 12 and 14, together with the cut values used for the respective analyses. While the efficiencies for the selection of  $b$ -jets are equal, the corresponding selection efficiencies for charm and light jets are smaller in release 14 by about a factor of two with respect to the release 12 efficiencies, due to changes in the  $b$ -tagging and tracking algorithms between the releases. This leads to a reduction of the estimation of the  $W$ +jet background. An overview of all cut values that are changed for the release 14 analysis

<sup>2</sup>Since no signal sample is available in release 14, the cuts have to be adjusted on a more or less arbitrarily chosen dataset. The choice of the samples to adjust the cuts significantly changes the cut values and hence the finally accepted cross sections. Furthermore, in the case of the track isolation cuts, the selection of the tracks to be considered is done with the same track quality criteria as applied in release 12. Especially the  $p_T^{\max \text{ trk}}$  (0.2)-criterion is quite sensitive to changes in the track quality criteria. The assumption that the adapted cut values still provide the same signal selection efficiency on event level in release 14 as in release 12 hence causes a sizeable uncertainty on the final result.

is given in Table B.3.

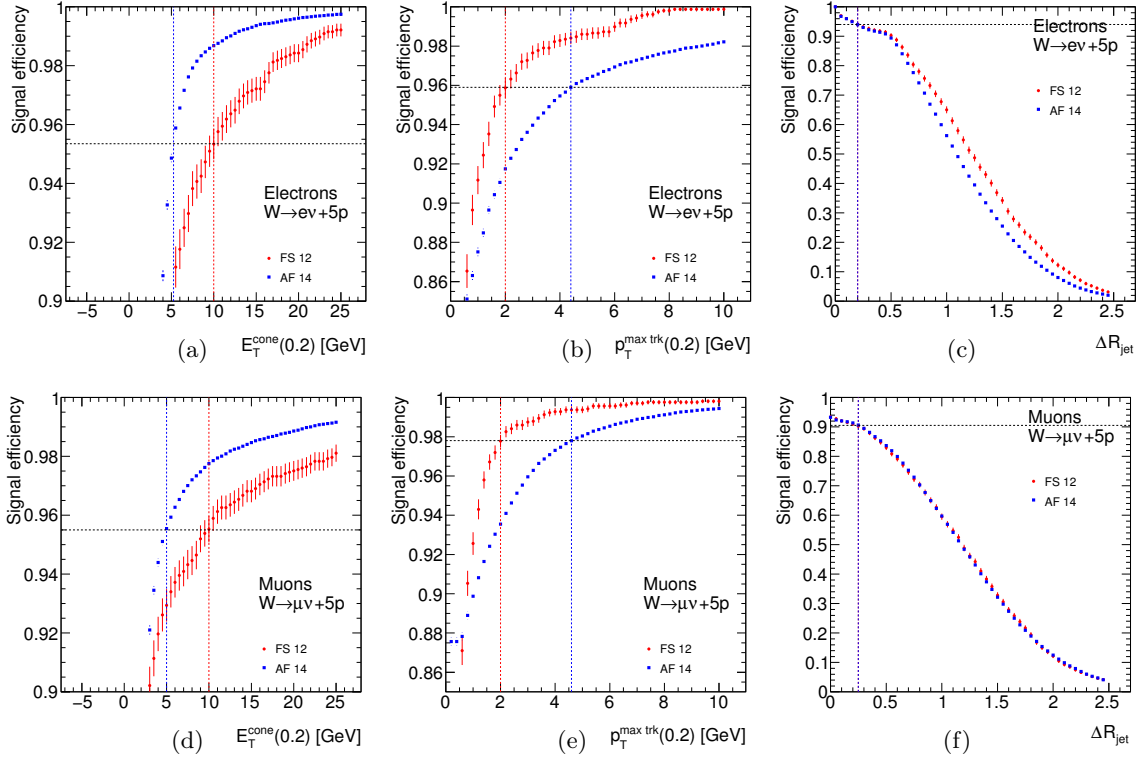


**Figure B.10:** Comparison of the dependence of the signal lepton selection efficiencies on the cut value on  $E_T^{\text{cone}}(0.2)$  (a, d),  $p_T^{\text{max trk}}(0.2)$  (b, e) and  $\Delta R_{\text{min}}^{\text{jet}}$  (c, f) for electrons in the  $W \rightarrow e\nu + 5p$  (upper row) and muons in the  $W \rightarrow \mu\nu + 5p$  sample (lower row), both matched to leptons from the decays of  $W$  bosons on generator level. The lines indicate the target lepton level efficiency for the adaption of the cut value and the corresponding cut values for the release 12 (full simulation) and 14 (ATLFAST-II) analyses. The (adapted) cut on  $E_T^{\text{cone}}(0.2)$  is applied for the  $p_T^{\text{max trk}}(0.2)$  curve and both isolation cuts are applied for  $\Delta R_{\text{min}}^{\text{jet}}$ .

Variable	$\epsilon_{\text{sig}}$	Release 12	Release 14
Electron $E_T^{\text{cone}}(0.2)$	0.95	10.0	5.25
Muon $E_T^{\text{cone}}(0.2)$	0.96	10.0	5.0
Electron $p_T^{\text{max trk}}(0.2)$	0.96	2.0	4.4
Muon $p_T^{\text{max trk}}(0.2)$	0.98	2.0	4.6
Jet weight	0.68	3.0	1.1

**Table B.3:** Target lepton and  $b$ -jet selection efficiencies  $\epsilon_{\text{sig}}$  and corresponding cut values for the release 12 and 14 event selections. The efficiencies  $\epsilon_{\text{sig}}$  are calculated with respect to the number of identified objects passing all cuts except that on the variable in question, i.e. the lepton isolation cuts are not adapted to compensate differences in the lepton identification efficiency.

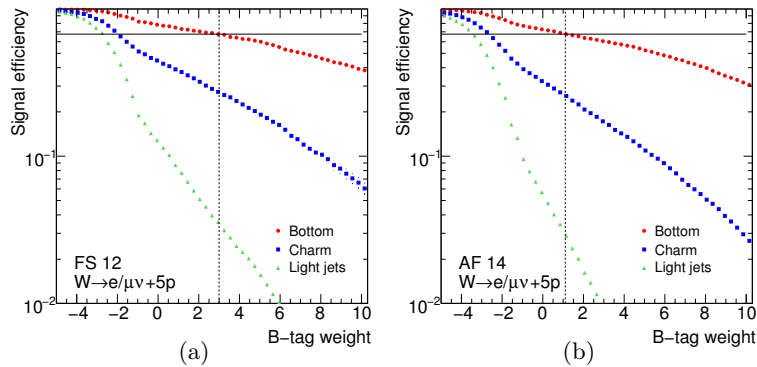


**Figure B.11:** Comparison of the selection efficiencies of  $b$ -,  $c$ - and light jets as a function of the cut value on the  $b$ -tagging weights in a mixture of the  $W \rightarrow e\nu + 5p$  and  $W \rightarrow \mu\nu + 5p$  datasets in full detector simulation in Athena 12 (a) and in the fast simulation ATLFast-II in release 14 (b).

### B.4.3 Correction of the centre-of-mass energy

The Athena 14 datasets used to estimate the  $W$ +jet background to  $t\bar{t}H$ ,  $H \rightarrow W^+W^-$  are produced at a lower centre-of-mass energy of 10 TeV than the samples used to study the signal and all other backgrounds, which assume an energy of 14 TeV. The shapes of the lepton and jet distributions in the release 12 and 14 datasets are in sufficient agreement, as discussed in Section 6.6.1. Therefore, the results obtained at 10 TeV are corrected by simple multiplication with constant scaling factors  $f_{10 \rightarrow 14}$  (see Section 6.6.2). These factors are obtained from a comparison of the 10 TeV and 14 TeV cross sections, without adjusting the shapes by PDF reweighting. The release 12 and 14 datasets that are compared in Section 6.6 were produced with different generator level filters. Therefore, the corresponding release 14 cross sections cannot be simply scaled to the release 12 values. Instead, the ALPGEN cross sections  $\sigma_{\text{tot}}$  are used together with the MLM matching efficiencies  $\epsilon_{\text{MLM}}$  (see Table 6.4 in Section 6.3 for the determination of cross sections in ALPGEN) to obtain the scaling factors according to

$$f_{10 \rightarrow 14} = \frac{\epsilon_{\text{MLM}}^{14} \cdot \sigma_{\text{tot}}^{14}}{\epsilon_{\text{MLM}}^{10} \cdot \sigma_{\text{tot}}^{10}}, \quad (\text{B.11})$$

with the 10 TeV numbers taken from Ref. [126] and the 14 TeV numbers from Refs. [125, 140]. All numbers and the resulting scaling factors are listed in Table B.4.

Sample	$\sigma_{\text{tot}}^{10}$ [pb]	$\epsilon_{\text{MLM}}^{10}$	$\epsilon_{\text{MLM}}^{10} \cdot \sigma_{\text{tot}}^{10}$ [pb]	$\sigma_{\text{tot}}^{14}$ [pb]	$\epsilon_{\text{MLM}}^{14}$	$\epsilon_{\text{MLM}}^{14} \cdot \sigma_{\text{tot}}^{14}$ [pb]	$f_{10 \rightarrow 14}$
$W \rightarrow e\nu + 2\text{p}$	2499.00	0.27	674.73	2032.00	0.40	812.80	1.205
$W \rightarrow e\nu + 3\text{p}$	1099.40	0.18	197.89	771.00	0.30	231.30	1.169
$W \rightarrow e\nu + 4\text{p}$	431.30	0.13	56.07	273.00	0.25	68.25	1.217
$W \rightarrow e\nu + 5\text{p}$	141.50	0.12	16.98	91.00	0.26	23.66	1.393
$W \rightarrow \mu\nu + 2\text{p}$	2498.60	0.27	674.62	2032.00	0.40	812.80	1.205
$W \rightarrow \mu\nu + 3\text{p}$	1099.70	0.18	197.95	771.00	0.30	231.30	1.169
$W \rightarrow \mu\nu + 4\text{p}$	431.50	0.13	56.09	273.00	0.23	62.79	1.119
$W \rightarrow \mu\nu + 5\text{p}$	141.50	0.12	16.98	91.00	0.26	23.66	1.393
$Wb\bar{b} + 0\text{p}$	6.82	0.75	5.12	–	–	6.26	1.224
$Wb\bar{b} + 1\text{p}$	11.52	0.44	5.07	–	–	6.97	1.375
$Wb\bar{b} + 2\text{p}$	10.40	0.28	2.91	–	–	3.92	1.346
$Wb\bar{b} + 3\text{p}$	5.95	0.27	1.61	–	–	2.77	1.724

**Table B.4:** Calculation of the scaling factors for the adaption of the  $W$ +jet cross sections from 10 TeV to 14 TeV.  $\sigma_{\text{tot}}^{10}$  and  $\sigma_{\text{tot}}^{14}$  give the ALPGEN cross sections for 10 TeV and 14 TeV,  $\epsilon_{\text{MLM}}^{10}$  and  $\epsilon_{\text{MLM}}^{14}$  the respective MLM matching efficiencies. The scaling factors  $f_{10 \rightarrow 14}$  are calculated according to Eq. (B.11).

#### B.4.4 Combined limit on the $W$ +jet background

The  $W$ +jet dataset is too small for a reliable prediction of the accepted cross section itself. Hence, a 95% upper limit is set on this value instead. This requires the combination of the results from several separate datasets, because the  $W$ +jet Monte Carlo sample is split into several sub-samples, each with a different input cross section. A Bayesian approach is used to obtain this combined 95% confidence limit for the  $W$ +jet contribution to the background. The probability  $P(m|n)$  for an expected value of  $m$ , if  $n$  events are observed, can be expressed according to Bayes as

$$P(m|n) = \frac{P(n|m) \cdot P(m)}{P(n)} = \frac{P(n|m) \cdot P(m)}{\int dm P(n|m) \cdot P(m)} \quad . \quad (\text{B.12})$$

The probability  $P(n|m)$  follows a Poisson distribution. Assuming a constant prior  $P(m)$ ,  $P(m|n)$  obeys the same distribution

$$P(m|n) = P(n|m) = \frac{e^{-m} \cdot m^n}{n!} \quad . \quad (\text{B.13})$$

Accordingly, each of a number of  $N$  experiments that are to be combined fulfils

$$P(m_i|n_i) = \frac{e^{-m_i} \cdot m_i^{n_i}}{n_i!} \quad . \quad (\text{B.14})$$

The total probability  $P(\sigma|n_1, \dots, n_N)$  for the expectation value of the accepted cross section

$$\sigma_{\text{tot}}^{\text{exp}} = \sum_{i=1}^N m_i \cdot \sigma_i^{\text{ev}} \quad , \quad (\text{B.15})$$

with  $\sigma_i^{\text{ev}}$  being the cross section per event in sample  $i$ , can be estimated from the individual  $P(m_i|n_i)$  by performing a large number of pseudo-experiments. Samples of  $(m_1, \dots, m_N)$  are generated in a hit-and-miss procedure according to the distribution in Eq. (B.14) for the given values of the  $n_i$ . The corresponding values of  $\sigma_{\text{tot}}^{\text{exp}}$  are calculated according to Eq. (B.15) and histogrammed. The resulting histogram contains the desired distribution  $P(\sigma_{\text{tot}}^{\text{exp}})$  by which

the 95% confidence limit  $\sigma_{\text{tot}}^{95}$  for the combined distribution is given as the value of  $\sigma_{\text{tot}}^{\text{exp}}$ , where

$$\int_0^{\sigma_{\text{tot}}^{95}} d\sigma_{\text{tot}}^{\text{exp}} P(\sigma_{\text{tot}}^{\text{exp}}) = 0.95 \quad . \quad (\text{B.16})$$

The resulting amounts of selected events in the relevant datasets for the  $W$ +jet analysis are listed in Table B.5. In addition, the limits that can be derived from each individual dataset are given. The combined 95% confidence limit on the expected  $W$ +jet cross section according to the procedure described above is  $\sigma_{\text{tot}}^{95} = 0.236$  fb. The corresponding probability distribution for the expectation value of the accepted cross section is shown in Fig. B.12.

Dataset	$N_{\text{MC}}$	$N^{95}$	$\sigma^{95}$ [fb]
$Wbb+3p$	1	4.74	0.211
$Wb\bar{b}+2p$	2	6.30	0.015
$W \rightarrow \mu\nu+5p$	2	6.30	0.018
$W \rightarrow \mu\nu+4p$	10	16.96	0.003
$W \rightarrow e\nu+5p$	1	4.74	0.020
$W \rightarrow e\nu+4p$	4	9.15	0.003
Combined			0.236

**Table B.5:** 95% confidence limits  $\sigma^{95}$  for the six most important  $W$ +jet background samples and combined limit  $\sigma_{\text{tot}}^{95}$ . The column denoted  $N_{\text{MC}}$  gives the number of Monte Carlo events passing all lepton selection criteria per dataset,  $N^{95}$  the corresponding 95% confidence limit. The limit  $\sigma^{95}$  for each dataset is given by  $N^{95}$ , scaled by the effective per-event cross section in the respective sample. The combination is performed according to the toy Monte Carlo procedure described in the text.

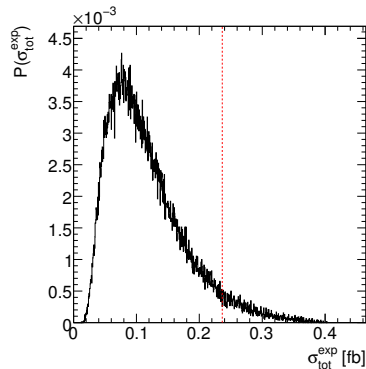


**Figure B.12:** Probability distribution for the expectation value of the accepted  $W$ +jet cross section as obtained from the combination of the six most important datasets with the help of toy Monte Carlo experiments. The line marks the 95% confidence limit.

## B.5 Calculation of significance expectations

In number counting experiments, claims for an observation of physics beyond the Standard Model expectation are usually quantified by the so-called “significance” of the effect. Especially if uncertainties of a subsidiary background measurement need to be incorporated, various approaches exist to determine the significance. Many of them have been introduced and their performance compared in Ref. [141]. Throughout this thesis, the profile likelihood method is used, since it is expected to provide stable results over a large range of parameters and can easily be implemented. A Gaussian uncertainty is assumed for the subsidiary background measurement. In the following, the calculation of significances with this approach is described in the simplest case of one channel and only one single background measurement. The description follows those in Refs. [141, 142] and Ref. [26], the latter covering also the more general case.

### B.5.1 $p$ -value and significance

Quoting significances means to quantify the level of agreement (or better: disagreement) of an experimental result with some hypothesized expectation. A measure of such an incompatibility is the  $p$ -value of the experimental result, which is the probability of finding a result as compatible or less with the hypothesis to be tested. In the case of a number counting experiment as in this thesis, the hypothesis in question is the “background-only” hypothesis, which assumes only the known Standard Model processes to occur. A significant excess of counts with respect to this hypothesis can then be attributed to new physics beyond the Standard Model. The  $p$ -value of a measurement  $n$ , assumed to be drawn from a distribution  $f(n, \text{some parameters})$  is then given as the sum

$$p = \sum_{n'=n}^{\infty} f(n', \text{some parameters}) \quad , \quad (\text{B.17})$$

or, in the case of a continuous  $n$

$$p = \int_n^{\infty} dn' f(n', \text{some parameters}) \quad . \quad (\text{B.18})$$

In the common case of a Poisson background distribution with expectation value  $b$ , the  $p$ -value of a measurement of  $n$  counts is simply given by

$$p_b = \sum_{m=n}^{\infty} \frac{b^m}{m!} e^{-b} \quad . \quad (\text{B.19})$$

The “significance”  $Z$  of a measurement is derived from its  $p$ -value as

$$Z = \sqrt{2} \operatorname{erf}^{-1}(1 - p) \quad . \quad (\text{B.20})$$

It gives the number of standard deviations at which a Gaussian random variable of zero mean and a standard deviation of one would give a one-sided tail area equal to  $p$ . By definition, a “discovery” can be claimed, if  $Z$  is larger than five, which corresponds to a  $p$ -value of  $p = 2.87 \cdot 10^{-7}$ .  $Z = 3$  still corresponds to  $p = 1.35 \cdot 10^{-3}$ .

### B.5.2 Treatment of background uncertainties: profile likelihood ratio

If the background expectation  $b$  is not known precisely but carries its own uncertainty  $\sigma$ , this reduces the significance of an experimental result. There is no definite way to account for a background uncertainty in the calculation of  $Z$ . Several methods that differ in their results have been established. The method considered to be most suited for this analysis is a profile likelihood ratio as described in the following.

Assume a measurement yields a number of  $n$  events. The event yield  $n$  follows a Poisson distribution with expectation value  $\mu s + b$ , where  $b$  is the expectation of a measurement of background only and  $s$  is the signal expectation. The “strength parameter”  $\mu$  parameterizes the degree of agreement with either the background-only hypothesis ( $\mu = 0$ ) or the predicted signal ( $\mu = 1$ )<sup>3</sup>. The background is not known exactly, but is estimated by an additional measurement  $m$  or from a Monte Carlo prediction. Here,  $m$  is assumed to follow a Gaussian distribution with expectation value  $b$ . Its width  $\sigma$  is assumed to be known exactly. The likelihood to obtain  $n$  events in the main measurement and  $m$  events in a subsidiary measurement is then given by

$$L(b, \mu) = \frac{(\mu s + b)^n}{n!} e^{-(\mu s + b)} \frac{1}{\sqrt{2\pi}\sigma} e^{-\frac{1}{2}\left(\frac{m-b}{\sigma}\right)^2} . \quad (\text{B.21})$$

To test the compatibility of a value of  $\mu$  with the measurement, the profile likelihood ratio

$$\lambda(\mu) = \frac{L(\mu, \hat{b})}{L(\hat{\mu}, \hat{b})} \quad (\text{B.22})$$

is constructed. The parameters  $\hat{\mu}$  and  $\hat{b}$  are the unconditional maximum-likelihood estimators of  $\mu$  and  $b$ , whereas  $\hat{b}$  maximizes  $L$  under the condition of  $\mu$  being fixed to the value to be tested. The closer the likelihood ratio is to one, the better is the agreement of the data with the hypothesis. Small values of  $\lambda(\mu)$  correspond to little compatibility of the measurement with the hypothesis. Equivalently, the variable

$$q_\mu = -2 \ln \lambda(\mu) \quad (\text{B.23})$$

can be calculated, which is more convenient to use than the profile likelihood itself. The value  $q_\mu$  follows a distribution  $f(q_\mu|\mu)$ , from which the  $p$ -value of a measurement  $q_\mu^{\text{obs}}$  under the hypothesis  $\mu$  can be calculated according to

$$p = \int_{q_\mu^{\text{obs}}}^{\infty} dq_\mu f(q_\mu|\mu) . \quad (\text{B.24})$$

In the simple case studied here,  $\ln L(\mu, b)$  can be minimized analytically. The estimator  $\hat{\mu}$  must thereby be constrained to  $\hat{\mu} \geq 0$ , since only positive values of  $\mu$  are sensible. Such, one obtains the unconditional estimators

$$\hat{\mu} = \begin{cases} \frac{n-m}{s} & n > m \\ 0 & \text{else} \end{cases} \quad (\text{B.25})$$

<sup>3</sup>The parameterization through  $\mu$  and  $s$  is employed here to be consistent with the common notation, which is also used in two of the above mentioned references. The appearance of a signal expectation  $s$  is somewhat misleading, though, since it suggests, that the significance of a result is only defined for a certain signal hypothesis. Actually,  $s$  appears only in a product with  $\mu$ , so the choice of  $s$  is arbitrary.

and

$$\hat{b} = \begin{cases} m & n > m \\ \frac{1}{2}(m - \sigma^2 + \sqrt{(m - \sigma^2)^2 + 4n\sigma^2}) & \text{else} \end{cases} \quad (\text{B.26})$$

The conditioned estimator for  $b$  under the background-only hypothesis  $\mu = 0$  is given as

$$\hat{\hat{b}} = \frac{1}{2}(m - \sigma^2 + \sqrt{(m - \sigma^2)^2 + 4n\sigma^2}) \quad (\text{B.27})$$

### B.5.3 Wilks' approximation

Determining the probability distribution  $f(q_\mu|\mu)$  is the crucial step in the significance calculation. It can e.g. be done by sampling the distribution with a large enough number of pseudo-experiments. To save computing time, the distribution can alternatively be approximated. According to Wilks' theorem,  $f(q_\mu|\mu)$  approaches a  $\chi^2$  distribution for one degree of freedom for sufficiently large  $n$ . It can therefore be parameterized as

$$f(q_\mu|\mu) \approx \frac{1}{2}\delta(q_\mu) + \frac{1}{2}\chi_1^2(q_\mu) \quad (\text{B.28})$$

For this distribution the significance is given as

$$Z = \sqrt{q_\mu^{\text{obs}}} \quad (\text{B.29})$$

Figure B.13 demonstrates the validity of the Wilks' approximation for the background-only hypothesis of the "likelihood tight" analysis and an assumed relative background uncertainty of 20%. The outcome of  $10^6$  pseudo-experiments is displayed in Fig. B.13(a). Figure B.13(b) shows a comparison of the corresponding distribution of  $f(q_\mu|\mu)$  and the approximation of Eq. (B.28). Both show good agreement, as they did also in a couple of tests with other numbers relevant for this analysis. For  $\sigma \rightarrow 0$  the significances obtained with this method

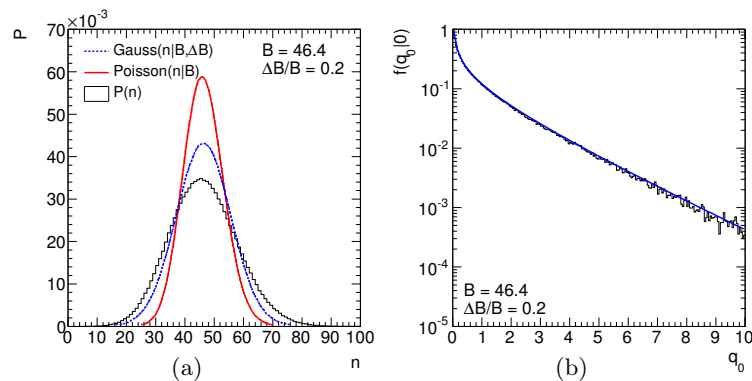


**Figure B.13:** Test of Wilks' theorem for the significance calculation. (a) Sampling  $f(q_0|0)$  with the help of pseudo-experiments: The blue dashed line shows the distribution of the generated background measurements  $m$  (Gaussian with the expectation value  $B$  as obtained for the "likelihood tight" event selection and width  $\Delta B = 0.2B$ ). The black histogram is the result of  $10^6$  pseudo-experiments drawn from a Poisson distribution with an expectation value varying randomly according to the Gaussian. For comparison: the red line shows the distribution of the measurements  $n$  under the background only hypothesis  $\mu = 0$  in the case of an exactly known expectation value  $B$  (Poisson with expectation value  $B$ ). (b) Corresponding distribution of the test statistic  $q_0$  (black histogram) and approximation of  $f(q_0|0)$  according to Eq. (B.28) (blue curve).

approach that of Eq. (B.19). In the case of zero background uncertainty, the significance is therefore obtained by setting  $\sigma/b = 10^{-5}$  in this thesis. Thus, problems can be avoided that are caused by the direct implementation of Eq. (B.19) in the case of non-integer values of  $n$ , as they occur when calculating significance expectations as described in the following.

### B.5.4 Expected significances

To quantify the potential to discover a hypothesized signal in advance of data taking, it is common to give the median significance obtained under the assumption of the signal hypothesis. The calculation of the median significance requires to perform a large number of pseudo-experiments to sample the distribution of  $Z$ . This time consuming procedure can be avoided by the use of an approximation, which is referred to as the use of an ‘‘Asimov dataset’’ in Ref. [26]. With good precision, the median can be estimated by replacing the data values  $m$  and  $n$  by their expectation values  $b$  and  $\mu s + b$  under the signal hypothesis  $\mu = 1$  in the formalism above. Checks of this approach with some of the numbers relevant for this analysis justify the use of the Asimov assumption. Figure B.14 shows the distributions of  $n$ ,  $q_0$  and  $Z$  obtained from  $10^7$  pseudo-experiments for the example of the ‘‘likelihood tight’’ signal and background expectations and an assumed relative background uncertainty of 20%. The median significance and its Asimov estimate differ by less than 1% in this and all other tested cases. All significance expectations in this thesis are therefore obtained using the Asimov approximation.

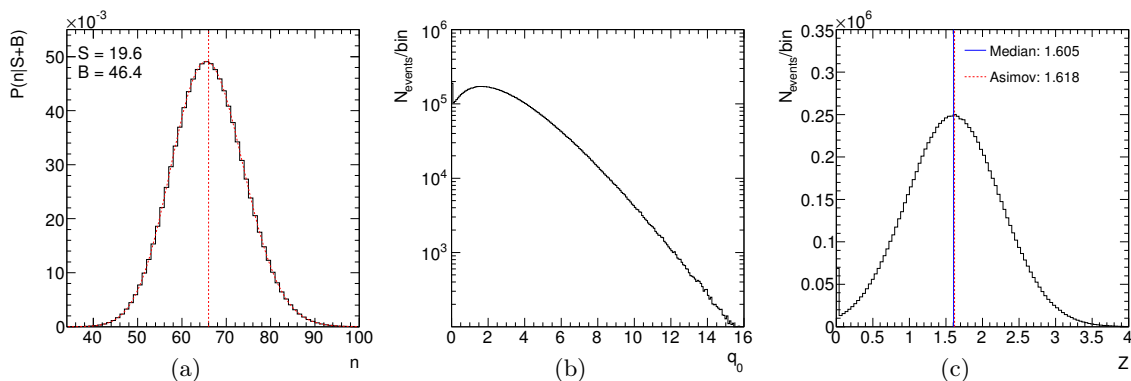


**Figure B.14:** Test of the Asimov approximation to calculate significance expectations. (a) Distribution of the outcome  $n$  of  $10^7$  pseudo-experiments following a Poisson distribution with expectation value  $\mu s + b$  under the signal hypothesis  $\mu = 1$ . The test case is the signal and background expectation  $S$  and  $B$  obtained with the ‘‘likelihood tight’’ analysis. (b) Distribution of the test statistic  $q_0$  (background only hypothesis) for the events in (a), assuming a background uncertainty  $\Delta B/B$  of 20%. (c) Corresponding distribution of the significance  $Z$ . The lines indicate the median of the distribution and the estimate of the expected  $Z$  using the Asimov dataset. The excesses at zero in the distributions of  $q_0$  and  $Z$  are due to cases, where  $m > n$  and hence  $\lambda(0) = 1$ .

## B.6 Signal expectations and significances for different Higgs boson masses

$M_H$ [GeV]	Signal				Background		$S/B$	$S/B$	$Z$	$Z$
	$\sigma^{\text{acc}}$ [fb]	$\sigma_{\text{NLO}}^{\text{acc}}$ [fb]	$S$	$S_{\text{NLO}}$	$\sigma^{\text{acc}}$ [fb]	$B$		NLO		NLO
<b>Likelihood tight</b>										
120	0.143	0.186	4.3	5.6	1.546	46.4	0.092	0.120	0.62	0.80
130	0.280	0.363	8.4	10.9	1.546	46.4	0.181	0.235	1.20	1.54
140	0.459	0.597	13.8	17.9	1.546	46.4	0.297	0.386	1.93	2.48
150	0.565	0.728	16.9	21.8	1.546	46.4	0.365	0.471	2.36	2.99
160	0.652	0.835	19.6	25.0	1.546	46.4	0.422	0.540	2.70	3.41
170	0.604	0.772	18.1	23.2	1.546	46.4	0.391	0.499	2.51	3.16
180	0.532	0.679	16.0	20.4	1.546	46.4	0.344	0.439	2.23	2.80
190	0.386	0.505	11.6	15.2	1.546	46.4	0.250	0.327	1.64	2.12
200	0.336	0.438	10.1	13.1	1.546	46.4	0.217	0.283	1.43	1.85
<b>Likelihood loose</b>										
120	0.140	0.182	4.2	5.5	1.741	52.2	0.080	0.105	0.57	0.74
130	0.272	0.354	8.2	10.6	1.741	52.2	0.156	0.203	1.10	1.42
140	0.455	0.592	13.7	17.8	1.741	52.2	0.261	0.340	1.81	2.33
150	0.557	0.716	16.7	21.5	1.741	52.2	0.320	0.411	2.20	2.80
160	0.655	0.839	19.7	25.2	1.741	52.2	0.376	0.482	2.57	3.25
170	0.604	0.773	18.1	23.2	1.741	52.2	0.347	0.444	2.38	3.01
180	0.529	0.675	15.9	20.2	1.741	52.2	0.304	0.388	2.10	2.65
190	0.389	0.509	11.7	15.3	1.741	52.2	0.223	0.292	1.56	2.02
200	0.334	0.436	10.0	13.1	1.741	52.2	0.192	0.250	1.35	1.74
<b>Reference</b>										
120	0.139	0.181	4.2	5.4	2.111	63.3	0.066	0.086	0.52	0.67
130	0.269	0.349	8.1	10.5	2.111	63.3	0.127	0.165	0.99	1.28
140	0.452	0.589	13.6	17.7	2.111	63.3	0.214	0.279	1.65	2.13
150	0.545	0.701	16.4	21.0	2.111	63.3	0.258	0.332	1.97	2.51
160	0.653	0.836	19.6	25.1	2.111	63.3	0.309	0.396	2.35	2.97
170	0.595	0.761	17.8	22.8	2.111	63.3	0.282	0.360	2.15	2.72
180	0.517	0.661	15.5	19.8	2.111	63.3	0.245	0.313	1.88	2.38
190	0.384	0.503	11.5	15.1	2.111	63.3	0.182	0.238	1.41	1.83
200	0.329	0.429	9.9	12.9	2.111	63.3	0.156	0.203	1.21	1.57

**Table B.6:** Accepted signal and background cross sections  $\sigma^{\text{acc}}$  [fb] for the three analyses (see Table 6.14 for their uncertainties). The columns denoted  $S$  and  $B$  contain the number of signal and background events expected with an integrated luminosity of  $30 \text{ fb}^{-1}$ . The  $S/B$  columns give the corresponding signal-to-background ratios and  $Z$  the expected significance, calculated as described in Appendix B.5. All numbers are given with the signal expectations normalized to the LO calculation. In addition, they are given in NLO normalization, for comparison with the results published in Ref. [108].

## B.7 Details on the estimation of detector systematics uncertainties

To determine the impact of uncertainties on the physics objects reconstruction and efficiencies on the estimation of the accepted signal and background cross sections, the respective quantities are varied according to their expected uncertainties. When the event selection is then applied to the manipulated sample, the comparison with the nominal result can be used to quantify the desired uncertainty. The resolution that can be achieved by this approach depends on the number of Monte Carlo events passing the event selection criteria. Except for  $t\bar{t}$ , which had to be factorized to obtain a reasonable result,  $t\bar{t}Z$  is the limiting background component. 100 Monte Carlo events are selected in this case, which corresponds to a resolution of the order of 1%.

Table B.7 summarizes the impact of all tested variations on the individual background components. Details on the implementation of the estimation of the detector uncertainties are given in Ref. [49]. To obtain an estimate for the uncertainties on the  $t\bar{t}$  background, either only the lepton- or the jet related event selection criteria are studied because of the lack of sufficient Monte Carlo events for the full analysis. The filtered  $t\bar{t}$  dataset is used to obtain the uncertainties caused by the uncertainties on the lepton related quantities, whereas the impact of the uncertainties on the jet related quantities is studied on the “no all-hadronic” sample. The table also indicates which dataset and event selection is used to study each source of systematic uncertainty.

	Signal	$t\bar{t}W$	$t\bar{t}Z$	$t\bar{t}t$	$t\bar{t}$ jet cuts	$t\bar{t}$ lepton cuts	$t\bar{t}$ unlike-sign	Total BG
Electron reconstruction and ID efficiency $-0.2\%$	$-0.3\%$	—	$-1.0\%$	—	—	$-0.2\%$	—	—
Electron $p_T$ resolution (width of $E_T$ increased by 5%)	$-0.1\%$	—	—	—	—	$-0.4\%$	$-1.0\%$	$-0.1\%$
Electron $p_T$ scale $+0.1\%$	$+0.1\%$	—	—	$+0.3\%$	—	$+0.2\%$	—	—
Electron $p_T$ scale $-0.1\%$	$-0.1\%$	—	—	—	—	—	—	—
Muon reconstruction efficiency $-0.1\%$	$-0.1\%$	—	—	—	—	—	—	—
Muon $p_T$ resolution (width of $1/ p_T $ increased by 1%)	$+0.1\%$	$-1.2\%$	$+3.0\%$	$-0.3\%$	—	$+0.6\%$	$-1.9\%$	$+0.3\%$
Muon $p_T$ scale $+0.1\%$	$+0.1\%$	—	—	$+0.3\%$	—	$+0.2\%$	—	—
Muon $p_T$ scale $-0.1\%$	—	—	—	—	—	—	—	—
Jet energy resolution (width of $E$ increased by 10%)	$+0.3\%$	$+0.7\%$	$-2.0\%$	$-0.4\%$	$-0.1\%$	—	$-1.4\%$	$-0.5\%$
Jet energy scale $+5\%$	$+5.9\%$	$+8.6\%$	$+6.0\%$	$+0.8\%$	$+9.1\%$	—	$+5.8\%$	$+7.3\%$
Jet energy scale $-5\%$	$-5.5\%$	$-6.8\%$	$-5.0\%$	$-2.8\%$	$-9.2\%$	—	$-11.6\%$	$-6.9\%$
$b$ -tagging efficiency $+5\%$	$+5.3\%$	$+7.5\%$	$+4.0\%$	$+2.7\%$	$+7.3\%$	—	$+9.2\%$	$+6.4\%$
$b$ -tagging efficiency $-5\%$	$-6.1\%$	$-5.5\%$	$-10.0\%$	$-3.1\%$	$-6.8\%$	—	$-9.7\%$	$-7.3\%$
Light jet mistag rate $+20\%$	$+4.8\%$	$+2.5\%$	$+2.0\%$	$+1.3\%$	$+4.7\%$	—	$+5.8\%$	$+2.9\%$
Light jet mistag rate $-20\%$	$-4.2\%$	$-5.8\%$	$-8.0\%$	$-1.5\%$	$-3.6\%$	—	$-3.9\%$	$-6.0\%$

**Table B.7:** Detailed overview of the systematic uncertainties on the signal and background predictions due to the uncertainties on the prediction of the detector performance. All contributions are determined according to the description in Ref. [49], with the exception of the light jet mistag rate. The uncertainty of 10% quoted there is considered too optimistic and hence replaced by a more realistic value of 20%, which by now could be confirmed by measurements [136]. All values given for the efficiency and mistag rate uncertainties are to be understood as relative values. A dash indicates that no change in the number of selected events could be observed.

## B.8 Outlook on a reconstruction of the signal

The study presented in this thesis shows that an event selection strategy can be established that efficiently suppresses the reducible backgrounds to the considered  $t\bar{t}H$ ,  $H \rightarrow W^+W^-$  final state. Thereafter, the background is dominated by processes that generate the same lepton signature as the signal and misidentification of objects does no longer play an important role in the generation of background. For further background suppression, it is therefore no longer sufficient to study the properties of individual jets and leptons. Instead, the complete topology of the event must be exploited instead.

The like-sign lepton final state of  $t\bar{t}H$ ,  $H \rightarrow W^+W^-$  allows the complete event to be reconstructed. This means to attribute the observed charged leptons and jets to the Higgs boson and top quark decay products and to reconstruct the four-momenta of the neutrinos produced in the leptonic  $W$  boson decays. The final state comprises four  $W$  bosons, two of them decaying leptonically, the other two hadronically, and two  $b$ -jets. The two leptonically decaying  $W$  bosons are forced to carry the same charge by the like-sign lepton requirement. This ensures that one of the  $W$  bosons from the Higgs boson decay decays leptonically, whereas the other decays into a pair of quarks. In consequence, also one of the top quarks must produce a  $W$  boson decaying into leptons and the other one that decays into a pair of quarks. Hadronic  $W$  boson candidates can be formed as pairs of light jets. The two neutrinos have to be reconstructed from the balance of the transverse momenta and the measured missing transverse energy. This could be done in a kinematic fit, as has been attempted in Ref. [128]. Alternatively, the final state allows for a fully analytic reconstruction, if the assumption is made that both  $W$  bosons from the Higgs boson decay decay at rest in the rest frame of the Higgs boson. This approach is applied in the following.

### B.8.1 Analytic reconstruction of the final state

The reconstruction is based on the assumption that the two  $W$  bosons produced in the decay of the Higgs boson are at rest in the Higgs boson rest frame. The Higgs boson rest frame is then defined by the rest frame of the hadronically decaying  $W$  boson, in which the two jets are produced back-to-back. The other  $W$  boson is at rest in the same system, so the sum of the four-vectors of the charged lepton from the Higgs boson decay and its partner neutrino have to add up to a  $W$  boson at rest in this reference frame. The four-vector of the neutrino from the Higgs boson decay can such be reconstructed unambiguously.

The transverse momentum  $p_{\text{T}}^{\nu}$  of the second neutrino, which is attributed to the leptonic top quark decay, can then be calculated from the measured  $\cancel{E}_{\text{T}}$  and  $p_{\text{T}}^{\ell}$ , by subtracting the energy and the transverse momentum of the neutrino assigned to the Higgs boson decay. Finally, the invariant mass of the charged lepton/neutrino system is constrained to the  $W$  boson mass. Hence, the longitudinal component  $p_z^{\nu}$  of the second neutrino is obtained by solving

$$M_W^2 = (E^{\ell} + E^{\nu})^2 - (p_{\text{T}}^{\ell} + p_{\text{T}}^{\nu})^2 - (p_z^{\ell} + p_z^{\nu})^2 \quad , \quad (\text{B.30})$$

where  $E^{\ell}$ ,  $p_{\text{T}}^{\ell}$  and  $p_z^{\ell}$  are the energy, transverse and longitudinal momentum of the charged lepton assigned to the top quark decay. The equation is quadratic in  $p_z^{\nu}$ , which means that two possible solutions must be considered later. Due to the limited accuracy of the  $\cancel{E}_{\text{T}}$  measurement, it may happen that there is no real solution to the equation. In this case, the imaginary part of the solution is dropped.

The assumption of resting Higgs boson daughters is exactly fulfilled only for Higgs boson masses up to  $2M_W$ . For substantially larger Higgs boson masses, the assumption is no

longer valid and the reconstructed Higgs boson mass peak becomes broader, as illustrated in Fig. B.15.

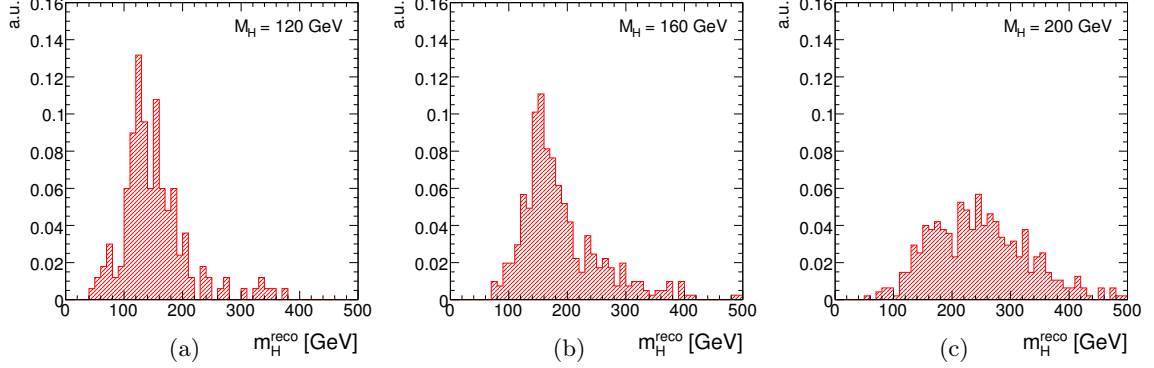


**Figure B.15:** Reconstructed Higgs boson mass distribution obtained in the  $t\bar{t}H, H \rightarrow W^+W^-$  Monte Carlo datasets for Higgs boson masses of 120 GeV (a), 160 GeV (b) and 200 GeV (c). Only combinations that are identified as the correct ones by matching with the Monte Carlo generator information contribute to the distributions. All distributions are normalized to unity.

## B.8.2 Combinatorial background

The calculations above are done for all possible combinations of reconstructed leptons and jets. Among these, the correct one has to be chosen in the next step. To restrain the number of possible combinations, only the two jets with the highest  $b$ -tag weights are treated as  $b$ -jets. All others are considered light jets for the pairing, even if their  $b$ -tag weight is larger than three. With that restriction and assuming that Eq. (B.30) has two solutions for each combination, the minimum number of possible combinations to be considered is 48. Often, additional jets are present in the signal due to initial and final state radiation. The average number of combinations to be tested in signal events is therefore larger than 200.

One approach to select one of the combinations to be considered the “correct” one is to calculate a  $\chi^2$  that quantifies the deviation of the invariant masses of the reconstructed object candidates from their nominal masses  $M_t$  and  $M_W$  according to

$$\chi^2 = \left( \frac{m_{bjj}^{\text{had.}t} - M_t}{\sigma(m_{bjj}^{\text{had.}t})} \right)^2 + \left( \frac{m_{\text{lep.}t}^{\text{lep.}t} - M_t}{\sigma(m_{\text{lep.}t}^{\text{lep.}t})} \right)^2 + \left( \frac{m_{jj}^H - M_W}{\sigma(m_{jj}^H)} \right)^2 + \left( \frac{m_{\text{lep.}W}^H - M_W}{\sigma(m_{\text{lep.}W}^H)} \right)^2. \quad (\text{B.31})$$

Here,  $m_{bjj}^{\text{had.}t}$  and  $m_{\text{lep.}t}^{\text{lep.}t}$  are the invariant masses of the reconstructed hadronic and leptonic top quark candidates, whereas  $m_{jj}^H$  and  $m_{\text{lep.}W}^H$  denote the invariant masses of the hadronic and leptonic  $W$  boson candidates attributed to the Higgs boson decay. The  $\sigma$  denote the respective resolutions of the mass peaks<sup>4</sup>. The widths must be determined e.g. from fits to the invariant mass distributions of the correct combinations obtained from Monte Carlo datasets, which are shown in Fig. B.16. The Gaussian mass peaks are diluted by the uncertainties on the jet and  $\cancel{E}_T$  measurement and by losses due to final state radiation. This needs to be accounted for in the fits. To calculate the  $\chi^2$  variable, the widths  $\sigma(m_{bjj}^{\text{had.}t}) = 25$  GeV,  $\sigma(m_{\text{lep.}t}^{\text{lep.}t}) = 35$  GeV,

<sup>4</sup>This approach can be chosen, if the Higgs boson mass is not too far away from 160 GeV (which is also assumed by the strategy to reconstruct the neutrino four-momenta described above) and the two  $W$  bosons from its decay can be considered to be produced on-shell. Alternatively, for known Higgs boson mass also the deviation of the Higgs boson itself could be used instead of the two  $W$  bosons.

$\sigma(m_{jj}^H) = 10 \text{ GeV}$  and  $\sigma(m_{\text{lep.}W}^H) = 35 \text{ GeV}$  are used in the following. So far, no pre-selection cuts on the reconstructed invariant masses are applied, but might be worth considering in the future to reduce the number of combinations to be tested.

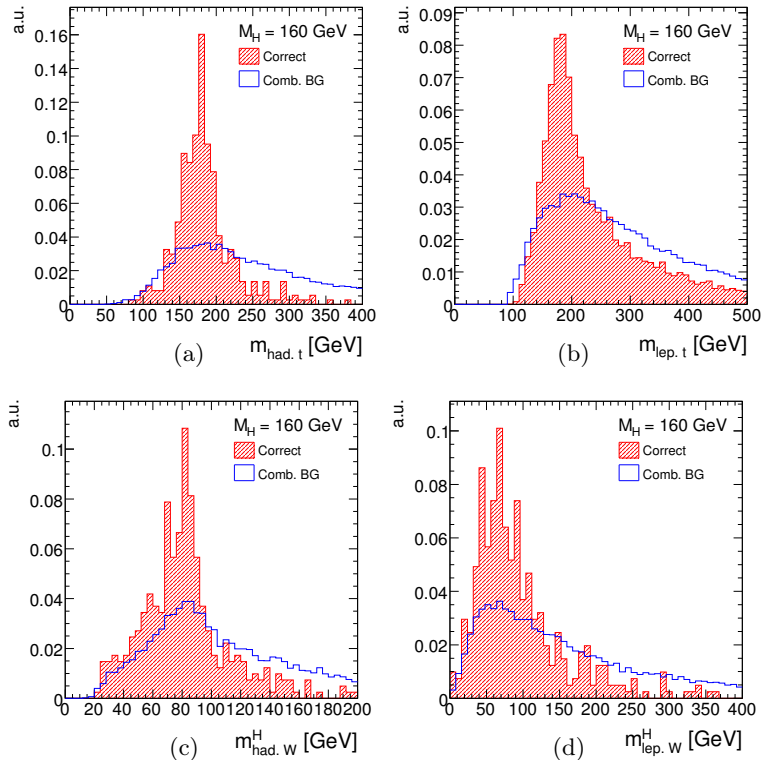


**Figure B.16:** Invariant mass distributions of the reconstructed hadronic top quark (a), leptonic top quark (b) and the hadronic (c) and leptonic (d)  $W$  bosons attributed to the Higgs boson decay. The mass distributions are shown for the correct combination and the combinatorial background, all obtained from the  $t\bar{t}H$ ,  $H \rightarrow W^+W^-$  Monte Carlo sample for  $M_H = 160 \text{ GeV}$ . All distributions are normalized to unity, including the overflows.

To evaluate the quality of the event reconstruction (e.g. to determine the probability to get the correct combination when choosing the one with the smallest  $\chi^2$ ), a reliable matching of reconstructed objects and generator level particles is essential. Especially assigning jets to their mother particles requires some care. In the approach used for this study, jets are assigned to their closest generator level quark or gluon within a cone of opening angle  $\Delta R < 0.3^5$ .

Figure B.17(a) shows the distributions of the  $\chi^2$  values for the combination found to be the correct one with this matching procedure and the combinatorial background in the  $M_H = 160 \text{ GeV}$  signal sample. A clear separation is visible, with the correct combination leading to a  $\chi^2$  smaller than 10 in most of the cases. Nevertheless, both distributions are normalized to unity, and a large number of wrong combinations contribute to the background normalization. It is therefore likely that the combination with the minimum  $\chi^2$  value is not the correct one.

<sup>5</sup>This results in a fraction of about 7% jet candidates that could not be attributed to a quark or gluon. A generated lepton is found in close vicinity of the reconstructed jet in most of these cases, which could have falsely caused a jet candidate. The assignment could, however, also have failed because the parton is missed due to the choice of a too small cone for the matching procedure, especially if final state radiation dilutes the jet angles. Furthermore, FSR could also require to match several jets to the same parton. These issues still deserve more studies.

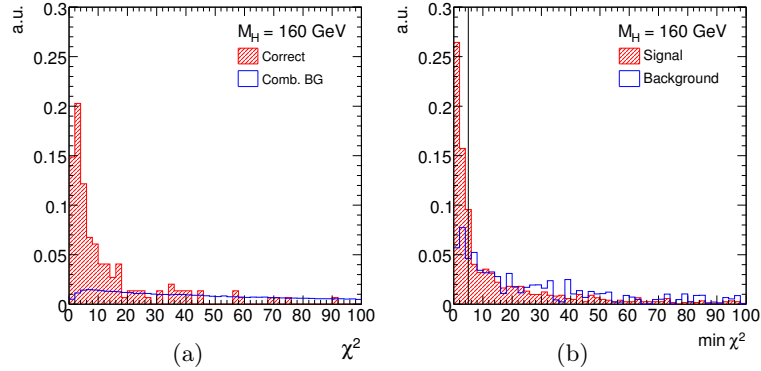


**Figure B.17:** (a) Distributions of the  $\chi^2$  calculated according to Eq. (B.31) for the correct combination and the combinatorial background in the  $M_H = 160$  GeV signal sample. (b) Distribution of the minimum  $\chi^2$  obtained for signal events and for the  $t\bar{t}W$ ,  $t\bar{t}Z$  and  $t\bar{t}t\bar{t}$  background events passing all event selection criteria. The line indicates the cut on  $\chi_{\min}^2 < 5$ , which is applied in the following. All distributions are normalized to unity, including the overflows.

Only in about 6% of all selected signal events the full set of leptons and jets can be assigned to the generator information by the matching procedure. In larger fractions of the events at least parts of the final state are correctly attributed (both top quarks in 18% and the complete Higgs boson in 26% of all events). Therefore, the  $\chi_{\min}^2$  has a large probability to determine at least a combination that is close to the correct one. Those events where all leptons and jets can be assigned allow the probability to be determined that the combination with the smallest  $\chi^2$  is the correct one. This is the case in only 32% of all events. In another 23%, the correct combination results in the second smallest and in about 13% in the third smallest value of  $\chi^2$ . In total, the correct combination is among those three with the smallest  $\chi^2$  values in roughly two thirds of all events.

### B.8.3 Suppression of irreducible backgrounds

Although the minimum  $\chi^2$  value  $\chi_{\min}^2$  is only of limited use to select the correct combination in signal events, it is useful to distinguish between the signal and the irreducible backgrounds  $t\bar{t}W$ ,  $t\bar{t}Z$  and  $t\bar{t}t\bar{t}$ . A comparison of the  $\chi_{\min}^2$  distributions in the signal and these backgrounds is shown in Fig. B.17(b). The signal distribution is peaked at low values, whereas the distribution has a large tail in the backgrounds. The effect of a requirement  $\chi_{\min}^2 < 5$  is demonstrated in Fig. B.18<sup>6</sup>, which shows the signal and background distributions obtained from the lowest  $\chi^2$  combination before and after a cut on  $\chi^2$ . The requirement decreases the expected signal yield by 58% to 8.2 events at  $30 \text{ fb}^{-1}$ , but at the same time reduces the total irreducible background by 87%. Accordingly, the signal-to-background ratio rises from 0.53 to 1.75. The resulting mass distribution is much narrower in both, signal and background, which demonstrates the sensitivity of the background shapes are to the event reconstruction strategy and the definition of the  $\chi^2$ . A reliable way must be found to take this into account in background estimation strategies. Future studies will also need to optimize the calculation of  $\chi^2$  and the choice of the cut value.

<sup>6</sup>The figures and the numbers given in the following include only the irreducible backgrounds. Top quark pair production is not considered here, since its contribution is relatively small and the results obtained from the factorization approaches in Section 6.5 are not suited for an event reconstruction. Considering also  $t\bar{t}$  production would result in an even larger relative decrease of the background, since the event reconstruction is expected to work the more efficient the less signal-like a background process is.

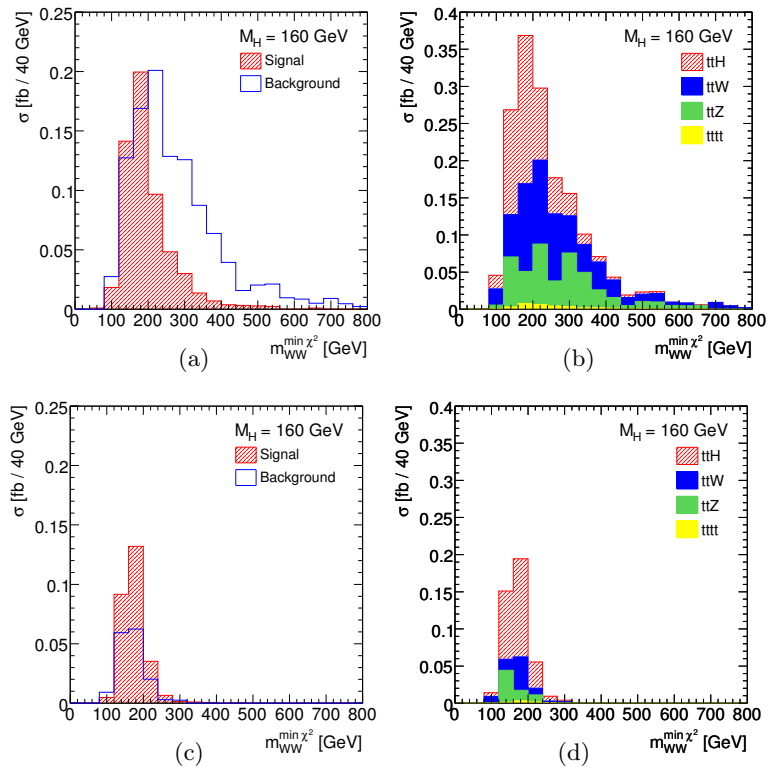


**Figure B.18:** Higgs boson mass distributions obtained from the combination with minimum  $\chi^2$  in the signal and the backgrounds. The distributions in the lower row are obtained after an additional cut on  $\chi_{\min}^2 < 5$ . Figures (a) and (c) show the distributions obtained in the signal sample at  $M_H = 160$  GeV and the total background from  $t\bar{t}W$ ,  $t\bar{t}Z$  and  $t\bar{t}t\bar{t}$  production. Figures (b) and (d) show the same distributions stacked and with the contributions of the individual background processes illustrated. The assumption of the  $W$  bosons decaying at rest and the definition of the  $\chi^2$  variable favours  $W$  boson candidates close to  $M_W$ , which is reflected in the narrow Higgs boson candidate mass distribution in the backgrounds after the  $\chi^2$  cut.

### B.8.4 Multivariate methods

Better suppression of combinatorial and physics backgrounds can probably be achieved, if not only the invariant masses, but also other properties of the reconstructed event are exploited, e.g. by a (combinatorial) likelihood or a neural network. The training of such a tool, however, requires a sufficiently large number of fully reconstructed signal events. In the current signal Monte Carlo dataset ( $M_H = 160$  GeV), these are only 82 candidates. This number is too small to obtain reasonable results in tests of different multivariate methods. Hence, no indication of the performance can be given here. Figure B.19 shows a number of variables that might, together with the mass distributions shown above, be promising candidates as input to multivariate methods. Some of these depend on the Higgs boson mass and hence require input from other channels that can measure the Higgs boson mass with sufficient precision. Furthermore, variables characterizing the Higgs boson rest frame might be of interest and also jet charge information should be tested for their potential. Such variables could be supplemented with variables whose distributions differ in the signal and the physics background (but not in combinatorial background), either in the same classifier or in an extra step that takes the output value of the first step as one of the inputs (as in the analyses in Ref. [25]). Candidates are the measured  $\cancel{E}_T$ , jet multiplicities and the transverse momenta of the jets. In

Ref. [128], also the total visible mass, the minimum distance between any lepton and any jet in the event and the  $p_T$  of the leptons are proposed as potential candidates. Such techniques should be considered as soon as sufficiently large datasets are available.

### **B.8.5 Summary**

The preliminary results obtained here show that a reconstruction of the event can certainly help to reduce irreducible background. Nevertheless, good understanding of the whole reconstruction procedure is mandatory for a reliable prediction of the remaining background. Future studies will first have to prove that this can be achieved. Finally, if the reconstruction of the whole event turns out to be too difficult to obtain reasonable results, also exploiting only well reconstructed parts of the event might be worth considering.

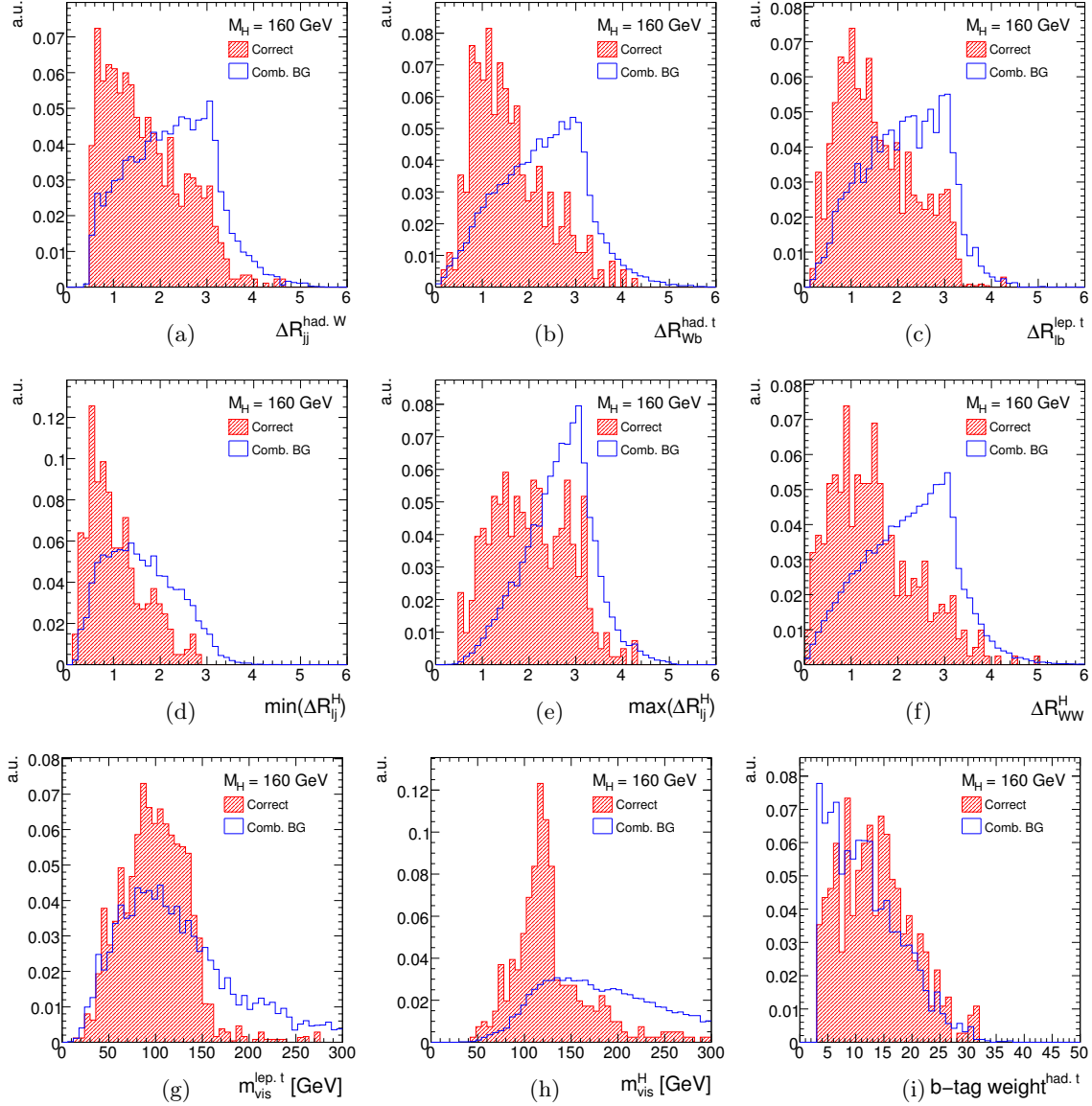


**Figure B.19:** Distributions of potential input variables for a multivariate analysis, shown for the correct combination and the combinatorial background:  $\Delta R_{jj}^{\text{had}, W}$  between the two jets assigned to a hadronic  $W$  candidate (a),  $\Delta R_{Wb}^{\text{had}, t}$  between the  $W$  boson and  $b$ -jet assigned to the hadronic top quark candidate (b),  $\Delta R_{lb}^{\text{lep}, t}$  between the charged lepton and  $b$ -jet assigned to the leptonic top quark candidate (c),  $\min(\Delta R_{lj}^H)$  and  $\max(\Delta R_{lj}^H)$  between the lepton and each of the two jets assigned to the Higgs boson candidate (d, e),  $\Delta R_{WW}^H$  between the two reconstructed  $W$  bosons attributed to the Higgs boson decay (f), visible invariant masses  $m_{\text{vis}}^{\text{lep}, t}$  and  $m_{\text{vis}}^H$  of the leptonic top and the Higgs boson candidate (g, h) and weight  $b$ -jet assigned to the hadronic top quark decay (i). All distributions are obtained from the  $t\bar{t}H$ ,  $H \rightarrow W^+W^-$  signal sample for  $M_H = 160$  GeV and normalized to unity.



# List of Figures

1.1	The Higgs potential . . . . .	8
1.2	Theoretical bounds on $M_H$ as a function of $\Lambda$ . . . . .	10
1.3	Tevatron Standard Model Higgs boson exclusion limits . . . . .	11
1.4	Indirect LEP2 upper limit on the Higgs boson mass . . . . .	12
1.5	Main Higgs boson production Modes at the LHC . . . . .	13
1.6	Higgs boson production cross sections at the LHC and branching ratios . . . . .	14
1.7	Total decay width of the Standard Model Higgs boson . . . . .	14
1.8	ATLAS Higgs boson discovery potential . . . . .	15
1.9	ATLAS and CMS Standard Model Higgs boson exclusion limits . . . . .	16
1.10	Expected accuracies for coupling measurements at the LHC . . . . .	18
2.1	Feynman diagrams for $t\bar{t}H$ production . . . . .	21
2.2	MSTW 2008 NLO proton PDFs for $Q^2 = 10 \text{ GeV}^2$ and $Q^2 = 10^4 \text{ GeV}^2$ . . . . .	22
2.3	Scale dependence of the $t\bar{t}H$ and $t\bar{t}Z$ production cross section calculations . . . . .	23
2.4	PDF dependence of the inclusive $t\bar{t}$ production cross section . . . . .	24
3.1	Total integrated luminosity and peak luminosity per day in ATLAS . . . . .	30
3.2	Schematic view of the CERN accelerator complex . . . . .	31
3.3	Cross sections and production rates for some important processes . . . . .	32
3.4	Cut-away view of the ATLAS detector . . . . .	33
3.5	Cut-away view of the ATLAS Inner Detector . . . . .	34
3.6	Plan view of a quarter-section of the Inner Detector . . . . .	35
3.7	ID material distribution . . . . .	37
3.8	Cut-away view of the ATLAS calorimeter system . . . . .	38
3.9	Sketch of a LAr EM calorimeter barrel module . . . . .	39
3.10	Cut-away view of the ATLAS muon system . . . . .	41
3.11	Schematic view of the ATLAS trigger system . . . . .	42
4.1	Fully equipped SCT endcap disk . . . . .	52
4.2	The three types of ATLAS SCT endcap modules . . . . .	53
4.3	Exploded view of the SCT endcap module layout . . . . .	53
4.4	Endcap module spine and fan-ins . . . . .	54
4.5	Microscopic view of Hamamatsu and CiS SCT sensors . . . . .	55
4.6	Sensor strip layouts: CiS vs. Hamamatsu . . . . .	56
4.7	Type inversion: dependence of $N_{\text{eff}}$ and $V_{\text{dep}}$ on $\Phi_{\text{eq}}$ . . . . .	57
4.8	Time dependence of the different annealing contributions . . . . .	58
4.9	Endcap module hybrid . . . . .	59
4.10	Chips and connectors on the endcap module hybrid . . . . .	60
4.11	Data flow and clock and command signal distribution on the hybrid . . . . .	61
4.12	Patch card . . . . .	62
4.13	Schematic view of the SCT endcap module testing system . . . . .	63
4.14	$I - V$ curves of ATLAS SCT endcap modules . . . . .	66

4.15	$I - V$ training curves . . . . .	67
4.16	Analysis of analogue properties in a binary system with threshold-scans . . . . .	68
4.17	$vt50$ as a function of the injected charge (response curve) . . . . .	69
4.18	Time-walk . . . . .	69
4.19	Long-term test results . . . . .	71
4.20	Typical $vt50$ , gain, offset and input noise monitoring result . . . . .	72
4.21	Response curve and gain and noise as a function of the input charge . . . . .	73
4.22	Short circuit on a Inner module sensor . . . . .	74
4.23	Noise bumps on a CiS module . . . . .	74
4.24	Noise occupancy threshold scan . . . . .	75
4.25	Bad channel distribution of Freiburg CiS Inner modules . . . . .	76
4.26	Average gain, noise, offset and bad channels on disk 6c . . . . .	77
4.27	Leakage current distributions at 150 V and 350 bias voltage . . . . .	78
4.28	Average noise occupancy and average electronic noise . . . . .	78
4.29	Distribution of the number of bad channels . . . . .	78
5.1	Generated signal and background electrons: $p_T$ and $\eta$ distributions . . . . .	82
5.2	Transverse momentum resolutions . . . . .	83
5.3	Calorimeter based isolation variables . . . . .	84
5.4	Tracking based isolation variables . . . . .	86
5.5	Signal distributions in $Z \rightarrow e^+e^-$ and $t\bar{t}$ . . . . .	87
5.6	Result of the smoothing procedure . . . . .	90
5.7	$r$ distribution . . . . .	92
5.8	Efficiency vs. rejection for the “default” and “highJetMulti” configurations . . . . .	92
5.9	Separation power and impact of the “default” selection variables . . . . .	93
5.10	Comparison of tracking and calorimeter variables . . . . .	94
5.11	$p_T$ and $\eta$ dependence of the total background rejection for signal electrons from $Z \rightarrow e^+e^-$ and $t\bar{t}$ (barrel) . . . . .	95
5.12	$p_T$ and $\eta$ dependence of the total background rejection for signal electrons from $Z \rightarrow e^+e^-$ and $t\bar{t}$ (endcaps) . . . . .	96
5.13	$p_T$ and $\eta$ dependence of the total background rejection for “loose” and “tight” signal electrons (barrel) . . . . .	97
5.14	$p_T$ and $\eta$ dependence of the total background rejection for “loose” and “tight” signal electrons (endcaps) . . . . .	98
6.1	Signal and semi-leptonic $t\bar{t}$ background signatures . . . . .	102
6.2	Cross sections and branching ratios for $t\bar{t}H$ , $H \rightarrow W^+W^-$ production . . . . .	104
6.3	LO Feynman diagrams for $t\bar{t}$ production . . . . .	109
6.4	Parton level jet distributions in $t\bar{t}Z$ and $t\bar{t}W$ . . . . .	111
6.5	Feynman diagrams for $t\bar{t}Z$ and $t\bar{t}W$ production . . . . .	112
6.6	Feynman diagrams for $t\bar{t}t\bar{t}$ production . . . . .	112
6.7	Lepton isolation variables: distributions . . . . .	116
6.8	Lepton isolation variables: background rejection vs. signal efficiency . . . . .	117
6.9	Variables for the electron/jet ambiguity removal . . . . .	118
6.10	Angular separation of leptons and jets . . . . .	119
6.11	Invariant di-lepton mass distributions in $t\bar{t}H$ , $H \rightarrow W^+W^-$ and $t\bar{t}Z$ . . . . .	120
6.12	$b$ -jet identification . . . . .	121
6.13	Lepton fake rates in $t\bar{t}$ events . . . . .	125
6.14	Feynman diagram for the internal bremsstrahlung process . . . . .	125

6.15	Electron charge mismeasurement rates in $t\bar{t}$ events . . . . .	129
6.16	Lepton multiplicity and $p_T$ distributions in $W \rightarrow e\nu + 5p$ and $W \rightarrow \mu\nu + 5p$ . . .	133
6.17	Jet multiplicity and $p_T$ distributions in $W \rightarrow e\nu + 5p$ , $W \rightarrow \mu\nu + 5p$ and $Wb\bar{b} + 3p$	134
6.18	Correlation of $N_{lep}$ and $N_{jets}$ in $W$ +jet . . . . .	135
6.19	Signal expectation as a function of $M_H$ . . . . .	137
6.20	Expected significance and $S/B$ as a function of $M_H$ (LO) . . . . .	139
6.21	Expected significance and $S/B$ as a function of $M_H$ (NLO) . . . . .	140
6.22	Statistical significance and $S/B$ , including the upper limit on $W$ +jet . . . . .	140
6.23	Comparison of the isolation variables with and without pile-up . . . . .	143
6.24	Comparison of the $p_T$ distribution of jets with and without pile-up . . . . .	144
6.25	Comparison of the jet multiplicities with and without pile-up . . . . .	144
6.26	Comparison of the $\Delta R_{min}^{jet}$ distributions with and without pile-up . . . . .	145
6.27	Comparison of the $b$ -tag weight distribution with and without pile-up . . . . .	145
6.28	Influence of a variation of the isolated lepton selection efficiencies . . . . .	148
6.29	Influence of systematic uncertainties on the signal significance . . . . .	152
6.30	Influence of the systematic background uncertainty on a measurement of $\sigma_{t\bar{t}H} \times$ $BR(H \rightarrow W^+W^-)$ . . . . .	160
6.31	$M_H$ dependence of the relative accuracy on $\sigma_{t\bar{t}H} \times BR(H \rightarrow W^+W^-)$ . . . . .	161
6.32	Expected accuracies for coupling measurements at the LHC . . . . .	161
A.1	Additional isolation variables . . . . .	168
A.2	Pile-up: $IP_L$ and $p_T$ of tracks in $Z \rightarrow e^+e^-$ . . . . .	170
A.3	Pile-up: influence of track selection cuts . . . . .	170
A.4	Pile-up: $p_T$ and $\eta$ dependence of the total background rejection (barrel) . . .	171
A.5	Pile-up: $p_T$ and $\eta$ dependence of the total background rejection (endcaps) . .	172
A.6	Correlations of the discriminating variables . . . . .	173
A.7	Selection of input variables . . . . .	176
A.8	$p_T$ and $\eta$ dependence of the total background rejection for signal electrons from $Z \rightarrow e^+e^-$ and $t\bar{t}$ (barrel, no electron ID) . . . . .	178
A.9	$p_T$ and $\eta$ dependence of the total background rejection for signal electrons from $Z \rightarrow e^+e^-$ and $t\bar{t}$ (endcaps, no electron ID) . . . . .	179
A.10	$p_T$ and $\eta$ dependence of the total background rejection for “loose” and “tight” signal electrons (barrel, no electron ID) . . . . .	180
A.11	$p_T$ and $\eta$ dependence of the total background rejection for “loose” and “tight” signal electrons (endcaps, no electron ID) . . . . .	181
A.12	Comparison: signal PDFs obtained from $Z \rightarrow e^+e^-$ and $t\bar{t}$ . . . . .	182
A.13	Comparison: signal PDFs obtained from “loose” and “tight” electrons . . . . .	183
B.1	Influence of the “WZToLeptonFilter”-bias on the $t\bar{t}$ like-sign lepton filter . . .	186
B.2	Jet multiplicities in $t\bar{t}$ events . . . . .	186
B.3	MC@NLO weights: limits as a function of the expectation value $m$ . . . . .	188
B.4	MC@NLO weights: 95% probability distributions $P(n m_1^{95}, r)$ . . . . .	189
B.5	Lepton multiplicity and $p_T$ distributions $W \rightarrow e\nu + 4p$ and $W \rightarrow \mu\nu + 4p$ . . . . .	193
B.6	Jet multiplicity and $p_T$ distributions in $W \rightarrow e\nu + 4p$ , $W \rightarrow \mu\nu + 4p$ and $Wb\bar{b} + 2p$	194
B.7	Jet $p_T$ distributions for the for the first six jets, ordered in $p_T$ . . . . .	195
B.8	Distribution of isolation variables in release 12 and 14 . . . . .	196
B.9	Jet weight distributions in release 12 and 14 . . . . .	197
B.10	Comparison of lepton efficiencies in the Athena 12 and 14 $W$ +jet samples . .	198
B.11	Comparison of jet efficiencies in the Athena 12 and 14 $W$ +jet samples . . . . .	199

---

B.12 Calculation of a combined 95% CL: Toy Monte Carlo . . . . .	201
B.13 Test of Wilks' theorem for the significance calculation. . . . .	204
B.14 Test of the Asimov approximation to calculate significance expectations . . .	205
B.15 Mass dependence of the reconstructed Higgs boson mass distribution . . . . .	210
B.16 Reconstructed top quark and $W$ boson mass distributions . . . . .	211
B.17 Signal reconstruction: $\chi^2$ distributions . . . . .	212
B.18 Higgs boson mass distributions reconstructed from the $\chi^2_{\min}$ combination . . .	213
B.19 Potential input variables for a multivariate analysis . . . . .	215

# List of Tables

1.1	Overview on the Standard Model fermions . . . . .	4
1.2	Overview on the Standard Model gauge bosons . . . . .	5
1.3	Electroweak quantum numbers of the Standard Model fermions . . . . .	6
3.1	LHC design parameters . . . . .	30
3.2	Track parameter resolutions . . . . .	44
5.1	Monte Carlo samples for isolation studies . . . . .	80
5.2	Bin definitions and electron candidate sample sizes . . . . .	80
5.3	Signal electron identification efficiencies . . . . .	81
5.4	Background electron rejections . . . . .	81
6.1	Classification of the $t\bar{t}H$ , $H \rightarrow W^+W^-$ final states . . . . .	101
6.2	Signal Monte Carlo samples . . . . .	105
6.3	Production cross sections for potential background processes . . . . .	106
6.4	Background Monte Carlo samples . . . . .	108
6.5	Lepton selection efficiencies . . . . .	118
6.6	Accepted signal and background cross sections . . . . .	122
6.7	Trigger selection for $t\bar{t}H$ , $H \rightarrow W^+W^-$ candidate events . . . . .	123
6.8	Event level trigger efficiencies for the single-lepton triggers . . . . .	123
6.9	Composition of the fake electron sample . . . . .	126
6.10	Estimation of the fake lepton contribution to $t\bar{t}$ . . . . .	128
6.11	Estimation of the lepton charge mismeasurement contribution to $t\bar{t}$ . . . . .	130
6.12	Summary of the $t\bar{t}$ background contributions . . . . .	131
6.13	Estimation of the $W$ +jet background . . . . .	136
6.14	Overview: accepted signal and background cross sections . . . . .	138
6.15	Changes caused by pile-up . . . . .	142
6.16	Pile-up: accepted signal and background cross sections . . . . .	145
6.17	Overview of the detector performance uncertainties . . . . .	147
6.18	Summary of the systematic uncertainties . . . . .	151
A.1	Overview on the discriminating variables . . . . .	174
B.1	MC@NLO weights: estimation of 95% limits on $\sigma_{t\bar{t}}^{\text{ni}}$ . . . . .	189
B.2	Cut flow and expected cross sections for the published $t\bar{t}H$ analysis . . . . .	190
B.3	Release 14 event selection cut values . . . . .	198
B.4	Scaling factors for the correction of the centre-of-mass energy . . . . .	200
B.5	95% CL for the accepted $W$ +jet cross sections . . . . .	201
B.6	Signal and background expectations, $S/B$ and expected significances . . . . .	206
B.7	Detailed overview of the detector performance uncertainties . . . . .	208



# Bibliography

- [1] S. L. Glashow, Nucl. Phys. **22** (1961) 579.
- [2] S. Weinberg, Phys. Rev. Lett. **19** (1967) 1264.
- [3] A. Salam and J. C. Ward, Phys. Lett. **13** (1964) 168.
- [4] M. E. Peskin and D. V. Schroeder, *An Introduction to quantum field theory* (Westview, 1995).
- [5] F. Halzen and A. D. Martin, *Quarks and Leptons: An Introductory Course in Modern Particle Physics* (Wiley, 1984).
- [6] A. Pich (2007), hep-ph/0705.4264.
- [7] Y. Fukuda et al. (Super-Kamiokande), Phys. Rev. Lett. **81** (1998) 1562.
- [8] Q. R. Ahmad et al. (SNO), Phys. Rev. Lett. **87** (2001) 071301.
- [9] K. Nakamura et al. (Particle Data Group), J. Phys. **G37** (2010) 075021.
- [10] G. Arnison et al. (UA1), Phys. Lett. **B122** (1983) 103.
- [11] G. Arnison et al. (UA1), Phys. Lett. **B126** (1983) 398.
- [12] N. Cabibbo, Phys. Rev. Lett. **10** (1963) 531.
- [13] M. Kobayashi and T. Maskawa, Prog. Theor. Phys. **49** (1973) 652.
- [14] P. W. Higgs, Phys. Lett. **12** (1964) 132.
- [15] P. W. Higgs, Phys. Rev. Lett. **13** (1964) 508.
- [16] P. W. Higgs, Phys. Rev. **145** (1966) 1156.
- [17] F. Englert and R. Brout, Phys. Rev. Lett. **13** (1964) 321.
- [18] G. S. Guralnik, C. R. Hagen and T. W. B. Kibble, Phys. Rev. Lett. **13** (1964) 585.
- [19] I. Torchiani, *Search for Higgs Bosons and Supersymmetric Particles in Tau Final States in Proton–Antiproton Collisions at 1.96 TeV*, Ph.D. thesis, Universität Freiburg (2008).
- [20] A. Djouadi, Phys. Rept. **457** (2008) 1.
- [21] T. Hambye and K. Riesselmann, Phys. Rev. **D55** (1997) 7255.
- [22] R. Barate et al. (LEP Working Group for Higgs boson searches), Phys. Lett. **B565** (2003) 61.
- [23] Tevatron New-Phenomena and Higgs Working Group (2011), hep-ex/1107.5518.

- [24] LEP Electroweak Working Group (2011), <http://lepewwg.web.cern.ch/LEPEWWG/plots/summer2011/>.
- [25] G. Aad et al. (ATLAS collaboration), CERN-OPEN-2008-020 (2009) 1333.
- [26] G. Aad et al. (ATLAS collaboration), CERN-OPEN-2008-020 (2009) 1480.
- [27] J. F. Gunion and X.-G. He, Phys. Rev. Lett. **76** (1996) 4468.
- [28] G. Aad et al. (ATLAS collaboration), CERN-OPEN-2008-020 (2009).
- [29] G. L. Bayatian et al. (CMS), J. Phys. **G34** (2007) 995.
- [30] CMS collaboration, CMS-PAS-HIG-11-022 (2011).
- [31] ATLAS collaboration, ATLAS-CONF-2011-135 (2011).
- [32] E. Accomando et al. (2006), [hep-ph/0608079](http://arxiv.org/abs/hep-ph/0608079).
- [33] M. Dürrssen, ATL-PHYS-2003-030 (2003).
- [34] M. Dürrssen et al., Phys. Rev. **D70** (2004) 113009.
- [35] R. Lafaye et al., JHEP **08** (2009) 009.
- [36] J. A. Aguilar-Saavedra et al. (ECFA/DESY LC Physics Working Group) (2001).
- [37] G. Aarons et al. (ILC) (2007), [hep-ph/0709.1893](http://arxiv.org/abs/hep-ph/0709.1893).
- [38] A. Gay, Eur. Phys. J. **C49** (2007) 489.
- [39] K. Desch and M. Schumacher, Eur. Phys. J. **C46** (2006) 527.
- [40] J. M. Campbell, J. W. Huston and W. J. Stirling, Rept. Prog. Phys. **70** (2007) 89.
- [41] G. Altarelli and G. Parisi, Nucl. Phys. **B126** (1977) 298.
- [42] A. D. Martin, W. J. Stirling, R. S. Thorne and G. Watt, Eur. Phys. J. **C63** (2009) 189.
- [43] J. C. Collins and D. E. Soper, Ann. Rev. Nucl. Part. Sci. **37** (1987) 383.
- [44] J. C. Collins, D. E. Soper and G. F. Sterman, Adv. Ser. Direct. High Energy Phys. **5** (1988) 1.
- [45] W. Beenakker et al., Phys. Rev. Lett. **87** (2001) 201805.
- [46] A. Lazopoulos, T. McElmurry, K. Melnikov and F. Petriello, Phys. Lett. **B666** (2008) 62.
- [47] S. Dittmaier et al. (LHC Higgs Cross Section Working Group), CERN-2011-002 (2011).
- [48] A. D. Martin, W. J. Stirling, R. S. Thorne and G. Watt, <http://projects.hepforge.org/mstwpdf/>.
- [49] G. Aad et al. (ATLAS collaboration), CERN-OPEN-2008-020 (2009) 3.
- [50] S. Frixione and B. R. Webber, JHEP **06** (2002) 029.
- [51] V. V. Sudakov, Sov. Phys. JETP **3** (1956) 65.

- [52] G. Altarelli, Phys. Rept. **81** (1982) 1.
- [53] T. Sjostrand, S. Mrenna and P. Skands, JHEP **05** (2006) 026.
- [54] G. Corcella et al., JHEP **01** (2001) 010.
- [55] J. Alwall et al., JHEP **09** (2007) 028.
- [56] B. P. Kersevan and E. Richter-Was, Comput. Phys. Commun. **149** (2003) 142.
- [57] M. L. Mangano et al., JHEP **07** (2003) 001.
- [58] J. Alwall et al., Eur. Phys. J. **C53** (2008) 473.
- [59] S. Jadach, Z. Was, R. Decker and J. H. Kuhn, Comput. Phys. Commun. **76** (1993) 361.
- [60] E. Barberio and Z. Was, Comput. Phys. Commun. **79** (1994) 291.
- [61] X. Artru and G. Mennessier, Nucl. Phys. **B70** (1974) 93.
- [62] J. M. Butterworth, J. R. Forshaw and M. H. Seymour, Z. Phys. **C72** (1996) 637.
- [63] L. Evans and P. Bryant (editors), JINST **3** (2008) S08001.
- [64] G. Aad et al. (ATLAS collaboration), JINST **3** (2008) S08003.
- [65] ATLAS collaboration, *2011 pp Collisions*, <https://twiki.cern.ch/twiki/bin/view/AtlasPublic/LuminosityPublicResults>.
- [66] C. Lefèvre (CERN), CERN-Brochure-2009-003-Eng (2009).
- [67] C. Lefèvre (CERN), CERN-DI-0812015 (2008).
- [68] ATLAS collaboration, CERN-LHCC-99-14 and CERN-LHCC-99-15 (1999).
- [69] ATLAS collaboration, CERN-LHCC-2005-022 (2005).
- [70] *ROOT*, <http://root.cern.ch>.
- [71] G. Aad et al. (ATLAS collaboration), CERN-OPEN-2008-020 (2009) 16.
- [72] Z. Marshall, ATL-SOFT-PROC-2008-001 (2008).
- [73] S. Agostinelli et al., Nucl. Instrum. Meth. **A506** (2003) 250.
- [74] E. Richter-Was, D. Froideveaux and L. Poggioli, ATL-PHYS-98-131 (1998).
- [75] K. Assamagan et al., ATL-COM-SOFT-2008-024 (2008).
- [76] M. Dürrssen, ATL-PHYS-INT-2008-043 (2008).
- [77] A. Abdesselam et al., Nucl. Instrum. Meth. **A575** (2007) 353.
- [78] A. Ahmad et al., Nucl. Instrum. Meth. **A578** (2007) 98.
- [79] ATLAS collaboration, CERN-LHCC-97-16 and CERN-LHCC-97-17 (1997).
- [80] S. Haywood, ATL-INDET-2001-007 (2001).

- [81] Hamamatsu Photonics Co. Ltd., Hamamatsu (Japan), <http://www.hamamatsu.com>.
- [82] CiS Institut für Mikrosensorik GmbH, Erfurt (Germany), <http://www.cismst.org>.
- [83] T. Ohsugi et al., Nucl. Instrum. Meth. **A383** (1996) 166.
- [84] F. G. Hartjes, Nucl. Instrum. Meth. **A552** (2005) 168.
- [85] M. Moll, *Radiation Damage in Silicon Particle Detectors*, Ph.D. thesis, Universität Hamburg (1999).
- [86] G. Lindström et al., Nucl. Instrum. Meth. **A466** (2001) 308.
- [87] F. Campabadal et al., Nucl. Instrum. Meth. **A552** (2005) 292.
- [88] P. Abbon et al., CERN-LHCC-97-015 (1997).
- [89] C. Ketterer, *Entwicklung von Silizium-Streifen-Detektormodulen für den ATLAS SCT-Detektor*, Ph.D. thesis, Universität Freiburg (2004).
- [90] A. Abdesselam et al., ATL-INDET-PUB-2007-0011 (2006).
- [91] D. J. White et al., Nucl. Instrum. Meth. **A457** (2001) 369.
- [92] M. D’Onofrio et al., ATL-INDET-2003-004 (2003).
- [93] J. Butterworth, D. Hayes, J. Lane and M. Postranecky, CERN-99-09 (1999) 336.
- [94] M. Morrissey, *SLOG* (1999), <http://hepwww.rl.ac.uk/atlas-sct/mm/Slog/slog.pdf>.
- [95] A. Greenall, *ATLAS SCT AERO* (2003), [http://hep.ph.liv.ac.uk/~ashley/ATLAS\\_AERO.html](http://hep.ph.liv.ac.uk/~ashley/ATLAS_AERO.html).
- [96] M. Morrissey, *MuSTARD* (1998), <http://sct-testdaq.home.cern.ch/sct-testdaq/sctdaq/www/mustard.html>.
- [97] E. Górnicki, P. Malecki and S. Koperny, CERN-2000-010 (2000) 376.
- [98] P. Malecki et al., CERN-2001-005 (2001) 363.
- [99] L. Eklund, J. Hill, G. Moorhead and P. Phillips, *Atlas SCT Test DAQ Online Documentation*, <http://sct-testdaq.home.cern.ch/sct-testdaq/sctdaq/sctdaq.html>.
- [100] A. Clark et al., ATL-INDET-2002-015 (2002).
- [101] C. Lacasta, ATL-IS-EN-0008 (2002).
- [102] Z. Dolezal, ATL-IS-QA-0004 (2004).
- [103] T. Jones, *Private communication* (2005).
- [104] M. Wiesmann, *Private communication* (2005).
- [105] V. A. Mitsou, IEEE Trans. Nucl. Sci. **53** (2006) 729.
- [106] [http://pjd.home.cern.ch/pjd/Assembly/Disk6/Disk6\\_Average.html](http://pjd.home.cern.ch/pjd/Assembly/Disk6/Disk6_Average.html).

- [107] G. Aad et al. (ATLAS collaboration), CERN-OPEN-2008-020 (2009) 72.
- [108] G. Aad et al. (ATLAS collaboration), CERN-OPEN-2008-020 (2009) 1364.
- [109] K. S. Cranmer, *Comput. Phys. Commun.* **136** (2001) 198.
- [110] D. W. Scott, *Multivariate Density Estimation* (Wiley, 1992).
- [111] J. Hartert and I. Ludwig, ATL-PHYS-INT-2010-052 (2010).
- [112] O. Brandt, A. J. Barr and P. Brückman de Rentstrom, ATL-PHYS-INT-2008-023 (2008).
- [113] W. Beenakker et al., *Nucl. Phys.* **B653** (2003) 151.
- [114] S. Dawson, L. H. Orr, L. Reina and D. Wackerroth, *Phys. Rev.* **D67** (2003) 071503.
- [115] S. Dawson et al., *Phys. Rev.* **D68** (2003) 034022.
- [116] L. Reina and S. Dawson, *Phys. Rev. Lett.* **87** (2001) 201804.
- [117] L. Reina, S. Dawson and D. Wackerroth, *Phys. Rev.* **D65** (2002) 053017.
- [118] M. Spira (1995), [hep-ph/9510347](#).
- [119] G. Aad et al. (ATLAS collaboration), CERN-OPEN-2008-020 (2009) 1198.
- [120] J. Pumplin et al., *JHEP* **07** (2002) 012.
- [121] A. Djouadi, J. Kalinowski and M. Spira, *Comput. Phys. Commun.* **108** (1998) 56.
- [122] M. Spira, *Fortsch. Phys.* **46** (1998) 203.
- [123] R. Bonciani, S. Catani, M. L. Mangano and P. Nason, *Nucl. Phys.* **B529** (1998) 424.
- [124] B. P. Kersevan and E. Richter-Was (2004), [hep-ph/0405247](#).
- [125] G. Aad et al. (ATLAS collaboration), CERN-OPEN-2008-020 (2009) 870.
- [126] A. Shibata et al., ATL-COM-PHYS-2009-334 (2009).
- [127] M. Beneke et al. (2000), [hep-ph/0003033](#).
- [128] J. Levêque, J. B. de Vivie, V. Kostioukhine and A. Rozanov, ATL-PHYS-2002-019 (2002).
- [129] S. Hassani et al., *Nucl. Instrum. Meth.* **A572** (2007) 77.
- [130] G. Aad et al. (ATLAS collaboration), CERN-OPEN-2008-020 (2009) 398.
- [131] G. Aad et al. (ATLAS collaboration), CERN-OPEN-2008-020 (2009) 619.
- [132] G. Aad et al. (ATLAS collaboration), CERN-OPEN-2008-020 (2009) 647.
- [133] G. Aad et al. (ATLAS collaboration), CERN-OPEN-2008-020 (2009) 162.
- [134] D. Adams et al., ATL-PHYS-INT-2009-110 (2009).
- [135] ATLAS collaboration, ATL-COM-CONF-2011-116 (2011).

- [136] ATLAS collaboration, ATLAS-CONF-2011-089 (2011).
- [137] F. Maltoni, D. L. Rainwater and S. Willenbrock, Phys. Rev. **D66** (2002) 034022.
- [138] J. G. Skellam, Journ. Roy. Statist. Soc. Series A **109** (1946) 296.
- [139] ATLAS collaboration, ATLAS-CONF-2010-005 (2010).
- [140] W. Verkerke, *Private communication* (2009).
- [141] R. D. Cousins, J. T. Linnemann and J. Tucker, Nucl. Instrum. Meth. **A595** (2008) 480.
- [142] G. Cowan and E. Gross, *Comparison of significance from profile and integrated likelihoods* (2008), <http://www.pp.rhul.ac.uk/~cowan/stat/notes/PLvsInt.pdf>.

# Acknowledgements

After so many pages of thesis I have hardly any words left to say thank you to all the people contributing to this thesis (directly or indirectly) during the last seven years. But I'll try... I'd like to say a **BIG THANK YOU**:

First of all to Karl Jakobs for giving me the opportunity to become a tiny part of the big ATLAS collaboration and to participate in the exciting things they do at CERN (something I have dreamt of for a long time before starting this PhD). For the advice and many fruitful discussions in all those years and for never losing the faith in me and the  $t\bar{t}H$ ,  $H \rightarrow W^+W^-$  channel, even in times when it seemed that both of us might be buried under an overwhelmingly large background from  $W$ +jet production.

To all my unofficial co-supervisors: Michael Heldmann for the introduction to multivariate analysis techniques and the encouragement to get my stuff into Athena and CSC. Michael Dührssen, who guided my first steps into Higgs physics and always came up with some good advice. And the world-best plusquam-postdoc Christian (Super-)Weiser, who contributed not only with his brilliant ideas, developed in many extended discussions on the  $t\bar{t}H$  issue, but also with his constant advice on the correct use of German grammar and his sense of humour, which, applied in the right moment, could always significantly reduce the  $t\bar{t}$  background and other annoying stuff.

To Markus Schumacher and Giacinto Piacquadio for their interest in my work and lots of valuable comments on the analysis.

To the members of the ATLAS collaboration, especially Daniel Froidevaux and Dirk Zerwas for their support with the electron isolation studies, Louis Fayard, Leandro Nisati, Bill Murray and Isabel Trigger for their patience and support during the CSC adventure and Huaqiao Zhang, Lian-You Shan, Feng Lu, Emmanuel Monnier and Benjamin Ruckert for the collaboration on the note.

Once again, to Michael and Michael for bequeathing me with their respective analysis frameworks, both reflecting so incredibly the personality of their respective author and both equipped with various stunning and amiable little features. Furthermore, M&M and Jörg Mechnich for various "Advanced C++" lessons, including the patient correction of my humble exercises.

To the various computing administrators in our group, for taking care of the queue (almost) never to stand still, even on Sundays and on Christmas, and for always accepting my "NO!!!" when circulating lists of release 12 datasets to be deleted.

To Peter Wienemann for assisting me in generating a 2 TB (much at that time!) dataset in the early BFG days and to Hans-Gunther Borrmann for the successful effort to prevent these data from getting lost somewhere in the depths of the BFG.

To the people with whom I had the pleasure to share the work on the SCT modules: Uli Parzefall, Harald Fox, Maxim Titov, Jens Meinhardt, Dieter Joos, Ines Messmer, Olga Kotrbova and especially Simon Eckert, who never got tired introducing me to every single special feature of the SCT testing system.

To Karl Jakobs, Xavier Portell, Ralf Bernhard, Markus Schumacher, Michael Dührssen, Georges “the ATLAS collaboration” Aad, Matti Werner, Luzie Weithofer, Uli Parzefall, Christian Weiser and especially Sebastian Weber (who finally worked through all of it!) for patiently fighting through the draft of this thesis.

To Christina Skorek, the best secretary in the world, who always found an easy solution for complicated problems.

In addition to all those Freiburg people I have mentioned above also to (more or less sorted according to their current and former distribution among various offices): Ingo Torchiani, Andrea Dahlhoff, Henrik Nilsen, Olav Mundal, Frank Meisel, Björn Penning, Sascha Thoma, Urban Bitenc, Evelyn Schmidt, Susanne Kühn, Andreas Zwerger, Matti Werner (yep, I know, I mention you twice), Johanna Bronner, Jochen Hartert, Stefan Winkelmann, Mirjam Fehling-Kaschek, Julian Glatzer, Kristin Lohwasser 🍷!, Manuela Venturi, Michel Janus, Christoph Anders, Romain Madar and all the others for sharing work, life, fun, office, kitchen, beer and everything else...

The truly irreplaceable haco51 for his constant fidelity and tenacity until the very end.

All my friends and family members who supported me during this PhD (I won’t put names here – but if you happen to read this one day: yes, I mean you).

Last but not most, to Sebastian Weber, the superhero who supplied me patiently with all that a girl needs when finishing her PhD, including hope and faith sufficient for us two, encouragement and distraction after many long days of hard work, precision-positioning of figures, high-performance backup of data, nourishment, a bed to sleep and finally even a spare computer, when mine decided that it needs an immediate break (two days before I had to finish this).